Molecular Ruthenium based Water Oxidation Catalysts and their Immobilization on Electrode Surfaces

Dissertation
for the award of the degree
"Doctor rerum naturalium"
of the Georg-August-Universität Göttingen

within the doctoral program of chemistry
of the Georg-August University School of Science (GAUSS)

submitted by
Sheida Rajabi
from Tehran, Iran

Göttingen
2021

Thesis committee

Prof. Dr. Franc Meyer
Institut für Anorganische Chemie, Georg-August-Universität Göttingen

Prof. Dr. Inke Siewert
Institut für Anorganische Chemie, Georg-August-Universität Göttingen

Prof. Dr. Christian Jooß
Institut für Materialphysik, Georg-August-Universität Göttingen

Members of the Examination Board

Reviewer: Prof. Dr. Franc Meyer
Institut für Anorganische Chemie, Georg-August-Universität Göttingen

Second Reviewer: Prof. Dr. Inke Siewert
Institut für Anorganische Chemie, Georg-August-Universität Göttingen

Third Reviewer: Prof. Dr. Christian Jooß
Institut für Materialphysik, Georg-August-Universität Göttingen

Further members of the Examination Board:

Jun.-Prof. Dr. Anna Krawczuk
Institut für Anorganische Chemie, Georg-August-Universität Göttingen

Jun.-Prof. Dr. Johannes Walker
Institut für Organische und Biomolekulare Chemie, Georg-August-Universität Göttingen

Dr. Michael John
Institut für Organische und Biomolekulare Chemie, Georg-August-Universität Göttingen

Date of the oral examination: 14. December 2021

for Shahriar

Contents

1 Introduction

The global energy demand is severely influenced by the strong economic growth and world population over the last decades. The global average temperature is gradually rising due to the excessive consumption of fossil fuels which release significant amounts of anthropogenic greenhouse gases such as carbon dioxide (CO_2) to the earth's atmosphere. The Intergovernmental Panel on Climate Change (IPCC) announced that the generation of the CO_2 gas driven by human activities must be limited to net-zero by 2050 to maintain the global long-term temperature at 1.5°C above the pre-industrial level.[1] Depletion of the limited fossil fuel resources as well as the catastrophic consequences of CO_2 emission on the environment,[2,3] make it obligatory to expand sustainable and eco-friendly energy conversion schemes.

Renewable energy sources such as solar, biomass, hydropower, tidal, and wind power can meet modern society's energy demand with minimum damage to the environment. Contribution of the clean energies in electricity generation is growing steadily in the coming decades and beyond, especially in the developed countries. For example, by 2025, 40 to 45% of the electricity consumption in Germany will be supplied by renewable energies.[4] Among these, wind and solar energy are the most prominent resources. The energy provided by the sun can be harvested in several ways: solar cells in photovoltaic systems, thermal power plants, and solar collectors.[5] In the latter case, the radiation from the sun is converted directly into thermal energy which can be used for heating water and space heating purposes. However, the sun's intensity is quite low at the earth's surface,[6] and challenges associated with the collection, storage, and transportation on a large scale limit its application as a universal energy source for all societies.

In nature, a large fraction of sunlight captured by photosynthetic organisms is converted into chemical energy in the form of carbohydrates. Reduction of CO_2 to energy-rich components requires the reducing equivalents which can be provided by sunlight-driven H_2O splitting. However, the oxidation of water to dioxygen involving the transfer of four electrons and four protons is a thermodynamically uphill conversion in this process.[7,8] In recent years, extensive scientific research has been focused on understanding the fundamental steps relevant to

natural photosynthesis in order to develop artificial photosynthetic systems, mimicking analogous conditions.

1.1 Natural Photosynthesis

The conversion of water and carbon dioxide into the organic molecules of biomass (mostly carbohydrates) using sunlight energy is called oxygenic photosynthesis (eq. 1.1). This biochemical process which takes place in the plants, green algae, and cyanobacteria is composed of several steps: light-harvesting, charge separation, electron transfer, catalytic water oxidation, and assimilation of CO_2 into chemical energy.[9] The photo-oxidation of water to dioxygen is accompanied by the evolution of two protons and two electrons (per water molecule) which are further used to generate the energy carriers in the form of adenosine triphosphate (ATP) and the reduced nicotinamide adenine dinucleotide phosphate (NADPH).[10]

$$CO_2 + H_2O \xrightarrow{light} (CH_2O)_n + O_2 \quad (1.1)$$
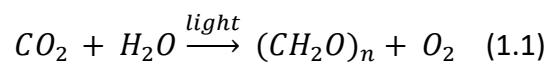
The electron and proton transfer chain of oxygenic photosynthesis in the thylakoid membrane can be summarized in the Z-scheme (Scheme 1.1). In the first step, the solar energy captured by the antenna pigments is transferred to the primary charge separation center (photosystem II). Although the photosynthetic organisms can capture all wavelengths of light energy, but only two photons are required to accomplish the water splitting and CO_2 reduction reactions. Upon light excitation in the PSII, the excited P680* transfers an electron to the pheophytin molecule to form the radical pair state P680$^{\cdot+}$ which has a sufficient oxidation potential to drive the water splitting reaction. The electrons accumulated in PSII are shuttled toward PSI through plastoquinone (Q_A and Q_B), cytochrome b_6f, and plastocyanin (PC).[11–13] The cytochrome b_6f complex also contributes to pump the protons from one side of the thylakoid membrane (stroma) to another side (lumen) to provide a proton gradient for ATP synthase to generate the energy-rich molecule adenosine triphosphate (ATP).[14] Similar light-driven excitation is also observed in PSI by a chlorophyll P700. The electrons in PSI moves to ferredoxin (FD) to finally reduce NADP with one H$^+$ to NADPH by ferredoxin-NADP$^+$ reductase (FNR). The produced reducing equivalents are eventually used to store the solar energy into chemical energy mainly in form of carbohydrates.[9,15]
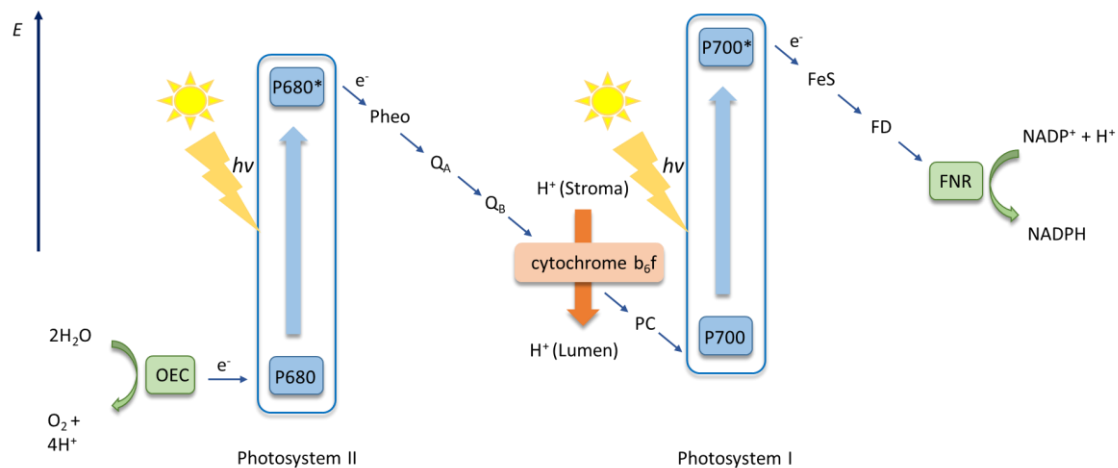
Scheme 1.1. Simplified Z-scheme of the light-driven reactions of natural photosynthesis. The energy of two photons is required to extract the electrons from the oxygen evolving complex (OEC). The electrons are subsequently absorbed by PSII and PSI to produce the strong oxidizing species $P680^+$ and $P700^+$, respectively. The generated NADPH in the PSI is used to convert CO_2 to carbohydrates. The scheme also demonstrates the electron transfer chain from OEC to FNR. (Pheo: pheophytin, Q: plastoquinone, PC: plastocyanin, FeS: Iron-sulfur cluster, FD: ferredoxin, and FNR: ferredoxin-NADP+ reductase).[16]

Photosystem II is composed of an acceptor where the charge separation occurs through oxidation of the P680 to the most oxidizing agent $P680^+$ and the donor site where the electrons are generated during the oxygen evolution reaction (OER). The structure of PSII was confirmed by the *Ferreira* group in 2004.[17] The central unit of the OEC is a disordered cubane-like cluster, in which the three Mn and one Ca are linked by μ-oxo ligands. The fourth dangling Mn is connected to the cubane via two oxo bridges (Figure 1.1).[18–20] The refined crystal structure of OEC with higher resolution (1.9 Å) was reported later by the *N.Kamiya* group which provided a more detailed description of the cluster arrangement as well as the surrounding environment.[21]

Kok and co-workers proposed a catalytic cycle for the formation of dioxygen at the OEC, known as "S-states".[22] This process includes five intermediates (S_0 to S_4), where S_0 is the most reduced state and S_4 is the most oxidized one. The sequential oxidation of the Mn_4Ca cluster of the OEC leads to the accumulation of four oxidative equivalents, which subsequently are reduced in the last step by the electrons derived from the oxygen evolution reaction. All the transitions except $S_4 \rightarrow S_0$ are light dependent and proceed via excitation and charge separation at P680.[9,12]
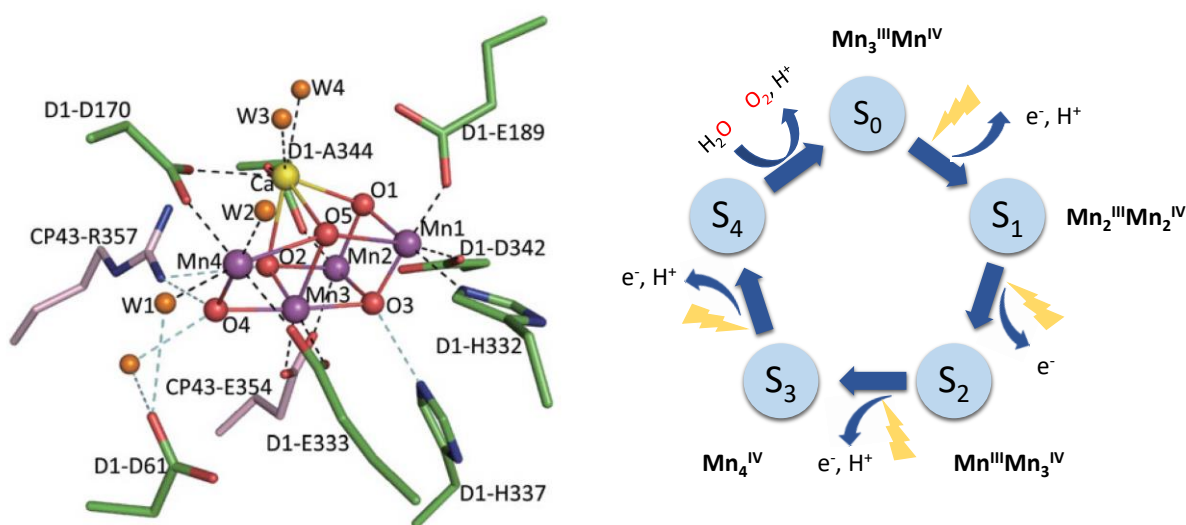
Figure 1.1. Structure of the Mn_4CaO_5 cluster in OEC. The distances between the atoms are given in Ångstrom. (Manganese: purple, oxygen: red, calcium: yellow, and water: orange). Reprinted with the permission of copyright © 2011, Nature publishing group.[21] (Left). Schematic catalytic cycle of the OEC presented by Kok *et.al.*,[22] involving five oxidation steps from S_0 to S_4 (Right).

1.2 Artificial Photosynthesis

The amount of solar radiation captured by the earth's surface is larger than the worldwide energy consumption by humans. However, due to the fluctuation of the sun's intensity on the earth (depending on the location and weather condition) as well as its intermittent and diffuse nature, it is challenging to ensure that the human's needs can be met. In addition, efficient storage, conversion, and distribution of solar energy in the form of energy carriers are highly required.

The concept of solar energy conversion in chemical bonds can be used in the design and assembly of artificial photosynthesis (AP) systems, which mimic the functionality of PSI and PSII.[23–25] Light-driven water splitting to generate hydrogen gas as a clean energy source, and

CO_2 reduction to produce carbon-based fuels like methanol, methane, formaldehyde, formate, etc. are the primary investigated reactions in AP. Fuel generation via artificial photosynthesis requires the orchestration of multi-step processes such as 1) light harvesting by a photosensitizer (PS) 2) charge separation 3) accumulation of the electrons at the reduction catalyst to reduce either protons or CO_2 and, 4) oxidation of water to dioxygen.

Two types of devices can be used in AP, a photoelectrochemical cell (PEC), and a photovoltaic-coupled electrolyzer (PVE).[26] The PEC cell comprises of two compartments, a photoanode (oxidative part) and a photocathode (reductive part), which are physically separated by a proton exchange membrane (PEM). An appropriate light absorption unit has to be coupled to at least one of the electrodes. Upon illumination, the protons generated at the photoanode are transferred to the hydrogen evolving catalyst (HEC) loaded on the photocathode to reduce the reactants to chemical fuels. The WOC and HEC can be applied in a homogenous phase or anchored to an electrode surface.[24] A schematic overview of a PEC cell for water splitting is demonstrated in Scheme 1.2.
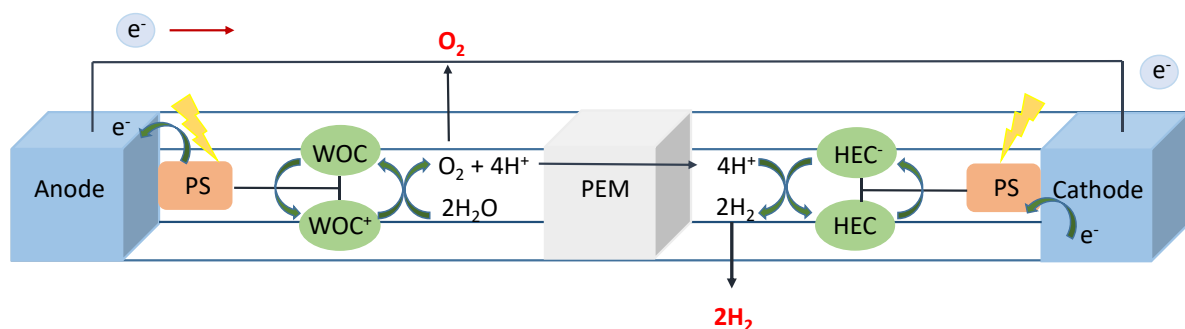
Scheme 1.2. Simplified representation of a photoelectrochemical cell (PEC) for light-driven water splitting containing photosensitizer (PS), water oxidation catalyst (WOC), proton exchange membrane (PEM), and hydrogen evolving catalyst (HEC).[24]

Light harvesting by light absorbing materials containing chromophores is the first step of artificial photosynthesis. These components are capable of inducing the electron transfer from the low energy valance band to the higher energy orbital upon illumination, generating a charge-separated state. Molecular dye-sensitized TiO_2[27,28] or n-type semiconductors such as $BiVO_4$,[29] which has a suitable valance band gap, can be used as photo-absorbers in the photoanode. An ideal light absorber unit requires long-term stability of the excited state, a broad absorption in the visible spectrum, high photochemical stability, and appropriate

potential to drive the photo-catalytic reactions. [Ru(bpy)$_3$]$^{2+}$-type complexes are one of the well-studied molecular photosensitizers, capable of absorbing sunlight for charge separation processes. Upon irradiation, the electron in the t$_{2g}$ orbital of the ruthenium center undergoes a metal-to-ligand charge transfer (MLCT), forming the lowest excited singlet state ^{1}[Ru(bpy)$_3$]$^{2+*}$, which has a short excited-state lifetime and rapidly converts to the long-lived state ^{3}[Ru(bpy)$_3$]$^{2+*}$ via intersystem crossing (ISC).[30–32] This triplet excited level has enough potential to mediate the photo-oxidation as well as the photo-reduction.

1.3 Water Oxidation Catalysis

1.3.1 Water Oxidation Reaction

The oxidation of water to molecular dioxygen appears to be a straightforward reaction at a first sight. However, compared to the majority of the reactions in nature which are only single- or two-electron redox processes, the removal of four electrons and four protons is necessary for the liberation of dioxygen gas according to eq. 1.2. This thermodynamically and kinetically demanding reaction is considered as the bottleneck in the development of artificial photosynthesis. To accomplish this conversion a Gibbs free energy (ΔG^o) of 237.18 kJ·mol^{-1} (25°C, 1 bar) is required. This value can be converted to the electrochemical potential of 1.23 V $vs.$ NHE (at standard conditions)[33,34] using the $Nernst$ equation (eq. 1.3), where n is the number of transferred electrons and F is the $Faraday$ constant.

$$2H_2O \rightarrow O_2 + 4H^+ + 4e^- \quad E^0 = 1.23 \text{ V } vs. \text{ NHE} \quad (1.2)$$
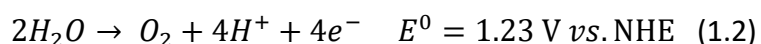
$$\Delta G° = nFE° \quad (1.3)$$

In addition, this reaction is associated with a large kinetic barrier ($\eta \geq 400$ mV), originating from the coupling of two oxygen atoms and the orchestration of 4H$^+$ and 4e$^-$ transfer.[35] These call for a catalyst capable of reducing this overpotential and accelerating the rate of overall water splitting reaction. Therefore, an efficient catalyst must be able to lower the activation energy at low potentials in order to facilitate the multistep charge transfer processes. Consequently, the metal centers in WOCs should have easy access to high oxidation states before undergoing any side reactions. The robustness of the catalysts especially under harsh oxidizing conditions is another important feature that has to be taken into account. In some systems, complete loss of the ligand under catalytic conditions leads to the formation of

decomposition products such as catalytically active metal oxide nanoparticles. In this case, elucidating the actual nature of the catalyst would be quite challenging.[36]

The WOCs can be evaluated by several criteria such as *Turn over number* (TON), *Turn over frequency* (TOF), *faradaic efficiency* (FE), and overpotential (η). The TON is defined as the number of produced dioxygen per molecule of catalyst before deactivation under given conditions and TOF is defined as the number of turnovers of the catalytic cycle with respect to the time. It is very important to stress that numerous experimental aspects can strongly affect the TON and TOF values. Therefore, caution must be taken when comparing different WOCs.[37] The *faradaic efficiency* describes the ratio of the measured and the theoretical amount of dioxygen during catalysis. The overpotential refers to the difference between the catalytic potential E_{cat} and thermodynamic water oxidation potential. The potential at the onset, at the maximum, or half of the maximum of a catalytic current in a cyclic voltammogram can be designated as E_{cat}. However, using several methods for the estimation of E_{cat} causes significant uncertainty concerning this parameter.

1.3.2 Mechanistic Considerations

The mechanism of water oxidation by molecular catalysts involves three main stages: I) generation of high-valent metal-oxo units, II) O-O bond formation, and III) O_2 evolution. In the first step, after binding a water molecule to the catalytic active site, a reactive high-valent metal-oxo species is formed through several steps of proton-coupled electron transfer (PCET).[34,38,39] PCET allows the catalysts reach high oxidation states with a low energy requirement and without accumulating extra charge at the metal center. One example can be described in $[L_xM^n–OH_2]$ type of complexes (eq. 1.4), where removing the electrons from the metal ion and protons from the aqua ligand leads to the generation of $[L_xM^{n+2}=O]$ species. However, the redox potential of the catalysts is a key aspect of this process and can be dictated by the metal center and its ability to access multiple oxidation states as well as the coordinating ligands.

$$[L_xM^n\text{-}OH_2] \underset{+e^-,+H^+}{\overset{-e^-,-H^+}{\rightleftharpoons}} [L_xM^{n+1}\text{-}OH] \underset{+e^-,+H^+}{\overset{-e^-,-H^+}{\rightleftharpoons}} [L_xM^{n+2}\text{=}O] \quad (1.4)$$
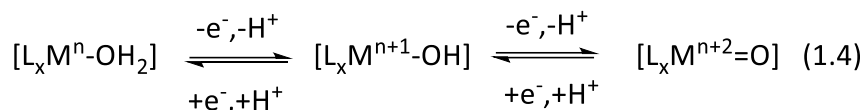
The formed M=O intermediates are the key components of the O-O bond formation step, therefore understanding their electronic features is critical for designing efficient WOCs. A simplified MO splitting diagram of a metal-oxo complex with a tetragonal ligand field is presented in Figure 1.2. In O_h environment, the substitution of one ligand of the octahedral sphere with a terminal oxo unit affords an M-O σ and two π bonds in a tetragonal field with C_{4v} symmetry due to the destabilization of the d_{z2}, d_{xz}, and d_{yz} orbitals.[40] Based on this electronic structure, the reactivity, and stability of the high valent M=O is dependent on the d electron counts.

The structure, properties, and reactivity of some transition metal complexes including Fe^{IV}, Mn^V, Ru^{IV}, and Ru^V have been intensively investigated due to their potential application in the design of artificial water oxidation catalysts.[41–44] As described by Winkler and Gray, the formation of metal-oxo multiple bonds is unlikely beyond group 8 elements in tetragonal coordination spheres. The hypothetical wall which lies between groups 8 and 9 in the periodic table is known as the "oxo-wall".[45,46] For transition metals with a higher d electron count, variation in geometry or reducing the coordination number is required. For example, a metal with d^4 configuration and in C_{4v} symmetry can easily form the double bond metal-oxo species, while the metal ions with five d-electrons or more cannot support the formation of the M=O bond due to the occupation of the π* orbitals (d_{xz}, d_{yz}) of the M-O bond. However, some exceptions from the oxo-wall principle were observed for several d^5 and d^6 complexes.[45]
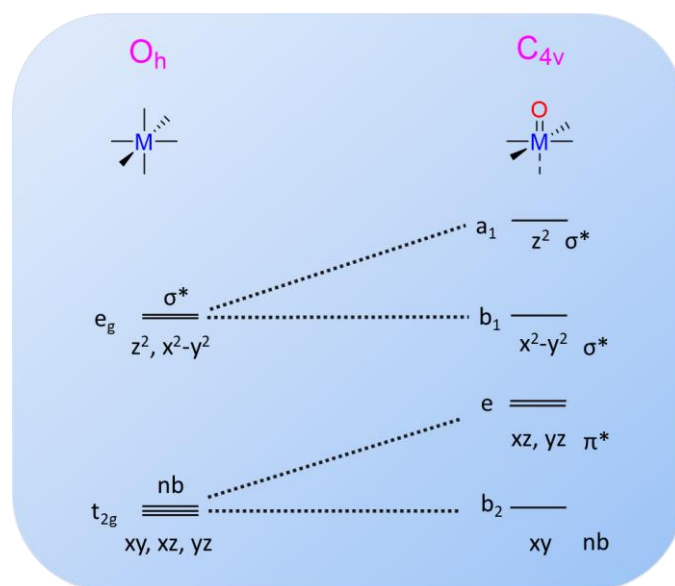
Figure 1.2. Qualitative frontier molecular orbital splitting diagram for a metal-oxo complex (d^4 system) in O_h and C_{4v} symmetry.[40]

Two major mechanistic pathways are proposed in the literature for the key O-O bond formation step in water oxidation catalysts: I) solvent water nucleophilic attack (WNA) and II) interaction of two metal-oxo units (I2M) (Scheme 1.3).[47–50] In the former one, a nucleophilic water or hydroxide group from the solvent attacks the electrophilic metal-oxo species, resulting in the formation of hydroperoxide intermediates. Subsequent oxidation of M-OOH leads to the cleavage of the M-O bond and the concomitant evolution of dioxygen. This mechanism is further supported by the isolation of a M^{IV} side-on peroxo intermediate (η^2-M^{IV}–OO) generated after the rate-determining O-O bond formation event.[51] The single-site O-O bond formation mostly occurs in mononuclear water oxidation catalysts, however, some dinuclear complexes have been reported to follow the WNA mechanism.[52–55] Usually, a higher potential is required to produce the electron-deficient high-valent metal-oxo species, which decreases the rate of O_2 generation via this scenario.

The second mechanism, I2M, proceeds via the interaction of two metal-oxo units bearing significant radical character, in an intra- or inter-molecular manner. In this pathway, the O-O bond formation takes place after further oxidation of [M-O-O-M] intermediate. Precise characterization of the M^n=O/M^{n-1}-O· species remains one of the challenges in the field of water oxidation catalysis due to the reactive nature of the oxyl radicals. Detailed insight into the key microscopic steps in the oxygen evolution cycle is provided recently by density

functional theory (DFT).[56–59] Generally, electron rich catalysts containing flexible ligand scaffolds prefer the I2M pathway.[48,60,61] However, minor changes in the coordination environment and electronic structure of the catalysts can switch the mechanism in another direction.[53,62]

Besides these two main pathways, a third possibility for O-O bond formation was reported in a mononuclear ruthenium pincer complex containing two hydroxo or oxo units in a *cis* arrangement.[63] The evolution of dioxygen, in this case, was attributed to the reductive elimination of the hydrogen peroxide upon irradiation. This was supported by isotopic labeling experiments confirming the formation of an intramolecular O-O bond.

Labeling experiments are one of the mechanistic techniques, which can elucidate the reaction path by interpretation of the generated dioxygen under ^{18}O water-enriched conditions.[52,53,64,65] This method requires different degrees of labeled solvent and catalyst, which are further analyzed by online mass spectrometry. Kinetic measurements mainly by UV/vis spectroscopy can also extract information, in case the O-O bond formation is one of the rate-determining steps.

Additionally, the foot-of-the-wave analysis (FOWA) is another valuable methodology for the determination of the reaction mechanism under electrocatalytic conditions. This method enables detailed investigation even when an S-shape response is not obtained using cyclic voltammetry. Moreover, FOWA is not influenced by side phenomena such as catalyst deactivation or substrate consumption at the electrode surface, because the data are recorded at the foot of the wave where the catalytic response is not perturbed by such processes. The FOWA mathematical equations were adopted for cases where the rate-determining step (RDS) is first order (eq. 1.5) or second order (eq. 1.6) with regard to the catalyst concentration, corresponding to a WNA or intermolecular I2M scenario. (i: CV current intensity, i_p: peak current of a redox process of the catalyst, E^0: potential of water oxidation catalysis and, C^0_{cat}: initial bulk concentration of catalyst).[66] However, it should be mentioned that this methodology does not differentiate between intramolecular I2M and WNA for dinuclear catalysts, as both pathways have first order dependency on the catalyst concentration.

$$\frac{i}{i_p} = \frac{4 \times 2.24 \sqrt{\frac{RT}{Fv} k_{WNA}}}{1 + e^{\frac{F(E^0 - E)}{RT}}} \quad (1.5)$$

$$\frac{i}{i_p} = \frac{4 \times 2.24 \sqrt{\frac{RT}{3Fv} C_{cat}^0 k_D}}{[1 + e^{\frac{F(E^0 - E)}{RT}}]^{3/2}} \quad (1.6)$$

As mentioned above, O_2 evolution and regeneration of the catalysts is the final step in the water oxidation pathway. This step is usually less demanding from an energy point of view compared to the O-O bond formation step.[47]
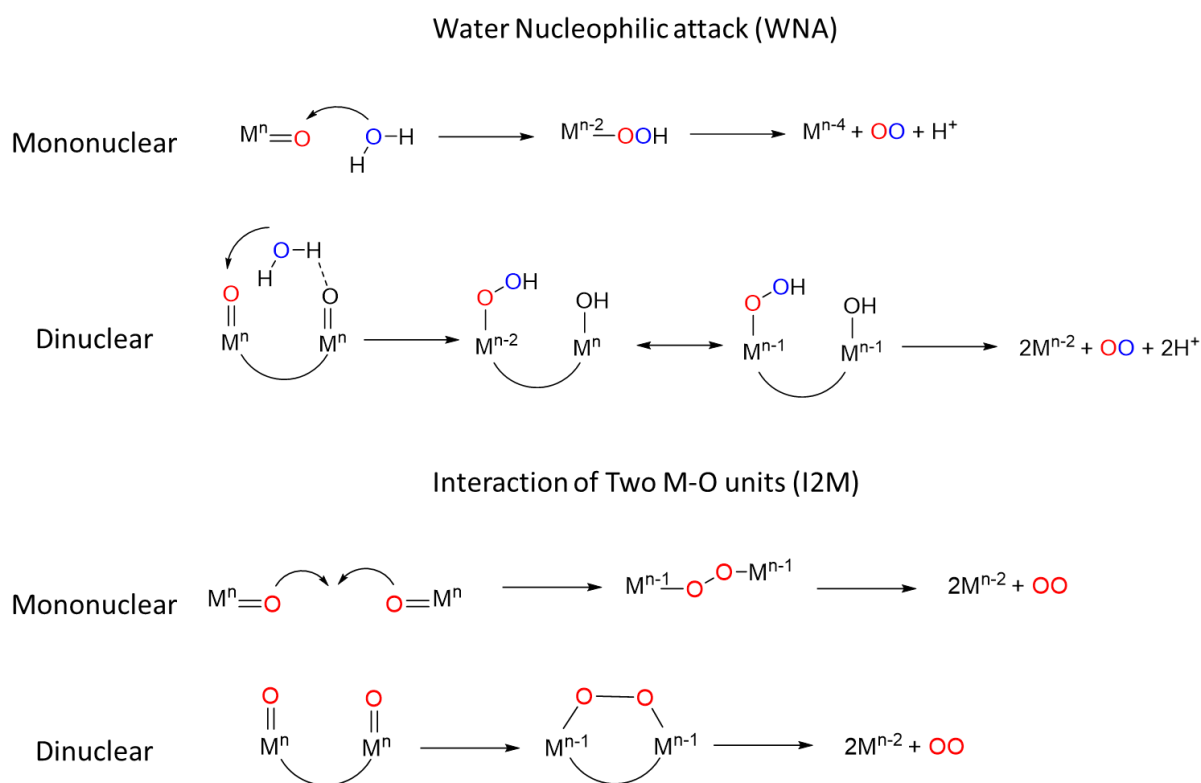
Scheme 1.3. Representation of the two mechanistic pathways for O-O bond formation in high-valent metal-oxo complexes: WNA and I2M for both mononuclear and dinuclear catalysts.[47]

1.4 Molecular Ru-Based Water Oxidation Catalysts

1.4.1 Principles for the Design of Efficient Molecular Water Oxidation Catalysts

Huge efforts have been made forwards to the development of molecular water oxidation catalysts based on different transition metals in the last decade. The field of MWOCs benefits from several advantages such as[25] I) **Well-defined structure**: the molecular catalysts can be

easily characterized by various spectroscopy and X-ray crystallography techniques. In addition, kinetic and computational studies can provide more insight into the catalytic mechanism of the water oxidation cycle II) **Tunability**: the efficiency of MWOCs can conveniently be adjusted based on rational ligand design, choice of transition metals, oxidation states, geometric arrangement of the active site, and addition of functionalities to modify the solubility as well as accomplish the anchoring of the catalysts onto the solid surfaces III) **Metal-atom economy**: regarding the final application in artificial photosynthesis, the most prominent advantage of molecular catalysts is the efficient utilization of metal atoms especially for catalysts based on rare transition metals. In contrast to material catalysts which are generated from the aggregation of hundreds to thousands of metal ions and only a small number of them at surfaces, edges, and corners serve as active sites, metal utilization for homogenous molecular catalysts can be optimized to 100%.

Among the transition metals (TMs), the largest group of synthetic molecular water oxidation catalysts are based on ruthenium and iridium. From a fundamental point of view, the impressive catalytic performance of 2nd and 3rd row TMs originates from their core-orbital structure. The ability to form strong coordination bonds (σ-interaction) with donor atoms using 4d or 5d orbitals leads to a higher ligand association constant and consequently, a decrease in the rate of the degradation pathways during the WOC.[67] Another advantage of these metals is their capability to accommodate several oxidation states with minimum geometrical changes[68] which enables a higher electron transfer rate during metal-centered redox processes. Notably, efficient molecular catalysts based on ruthenium provide extraordinary TON over 10^5 and TOF higher than 1000 s^{-1} with low overpotential, comparable to OEC in PSII.[37] In addition, the relatively high stability of their intermediates under catalytic conditions makes a detailed mechanistic investigation more likely.[69] The next two sections summarize several prominent mononuclear as well as dinuclear Ru-based MWOCs and highlight their advantages, catalytic reactivity and, mechanistic pathways.

1.4.2 Mononuclear Ru-Based Water Oxidation Catalysts

Inspired by the multimetallic Mn_4CaO_5 active site of the natural OEC, it was long presumed that the presence of at least two metal centers is necessary in the structure of MWOCs to enable the accumulation of four oxidizing equivalents responsible for catalytic water splitting. In 2005, Thummel and coworkers introduced the first series of mononuclear WOCs, revealing

that a single metal site is also sufficient for water oxidation catalysis.[70] The chemically driven oxidation reaction of the mononuclear complex $[Ru(npm)(pic)_2(H_2O)]^{2+}$ (npm = 4-t-butyl-2,6-di-(1',8'-naphthyrid-2'-yl)-pyridine, pic = 4-picoline) **I**, (Chart 1.1) by utilizing excess equiv. CAN as sacrificial oxidant exhibited a TON of 260 and TOF of 0.014 s^{-1}.[71] Recognition of this aspect of single-site WOCs provided more opportunities for the further development of MWOCs.

Inspired by the features of carboxylate groups in stabilizing the high valent Mn states at the OEC, the group of Sun presented a very efficient mononuclear WOC based on a negatively charged 2,2'-bipyridine-6,6'-dicarboxylate (bda^{2-}) ligand.[72,73] The water oxidation capability of this system was further evaluated by the occupation of the axial positions with different pyridine substituents. The $[Ru(bda)(pic)_2]$ complex, **II**, (Chart 1.1) containing axial 4-picoline demonstrated a significant performance toward O$_2$ evolution.[72] Isolation of the intermediate after catalytic activities revealed that the O-O bond formation proceeds via an intermolecular I2M mechanism.[57,59] In presence of CAN, two monomeric Ru^V=O units coupled together via a peroxo bridging unit to form a dimeric complex Ru^{IV}-OO-Ru^{IV}, which further oxidized to a superoxo species, followed by the release of the dioxygen.[73,74] The special proficiency of Ru-bda catalysts was also supported by the crystal structure of a Ru^{IV} dimer with a seven-coordinated bridging unit [HOHOH]$^-$.[72]

Significant improvement in TOF value was achieved by the exchange of the axial 4-picoline ligand with π-extended isoquinolines.[57] To further enhance the catalyst efficiency, the isoquinoline axial ligand was furnished with halogen groups. The resulting complex $[Ru(bda)(^Fisoq)_2]$, reached an extremely high activity with TOF of 1000 s^{-1}, comparable to the OEC reaction in photosystem II (100-400s^{-1}).[75] To disentangle the structural and electronic properties of the complex with regard to its catalytic reactivity, the analogous complexes were modified with different electron donating, electron withdrawing, and hydrophobic groups at the axial pyridyl ligand.[73,76,77] A remarkable increase in TOF was achieved for both electron withdrawing as well as hydrophobic ligands mainly due to improving the rate of the dimerization process. Electrostatic interactions can also accelerate the rate of oxygen evolution in intercatalyst coupling systems. This effect was studied by modification of the bda-based complexes with positively (N-methyl-4,4'-bipyridinium) and negatively (pyridine-4-sulfonate) charged ligands at the axial positions.[78] The higher observed catalytic activity, in

this case, was attributed to the dimeric intermediate formation rate enhancement via the electrostatic interactions.

In 2015, Llobet's group reported a new family of ruthenium complexes based on the pentadentate ligand [2,2':6',2''-terpyridine]-6,6''-dicarboxylic acid (tda^{2-}) and axial pyridines. [79] In oxidation state Ru^{II}, the ligand was bound to the metal center in κ-N^{3}O fashion with a dangling carboxylate. Chemical oxidation of [Ru^{II}(tda-κ-N^{3}O)(py)$_2$] by CAN, followed by the coordination of a hydroxyl group to the high-valent intermediate under basic conditions, led to the formation of a seven coordinated complex [Ru^{IV}(OH)(tda-κ-N$_3$O)(py)$_2$]$^+$, **III**, (Chart 1.1). The foot-of-the-wave analysis revealed an impressive turnover frequency of 8000 s^{-1} at pH = 7, with a TOF$_{max}$ of 50 000 s^{-1} under pH = 10. Based on DFT calculations, the O-O bond formation processes via a WNA pathway, in sharp contrast with the bda-derivatives. The high catalytic proficiency of **III** can be attributed to stabilization of the high Ru oxidation states of the intermediates by using an anionic ligand (tda^{2-}), in conjunction with the functionality of the carboxylate as a proton shuttle to facilitate the O-O formation via this mechanism.

The expansion of the coordination number from six to seven before the onset of catalysis is another interesting feature of the bda-Ru and tda-Ru complexes (**II** and **III**). Several factors govern the interesting reactivity of seven-coordinated complexes. First, the high-valent species are more stable and accessible in complexes with CN = 7 due to the capability of the metal ion to keep its 18-electrons structure. [80] Second, the variability of the seventh coordination in many cases facilitates the ligand substitution with water molecules. Finally, after O-O bond formation, the seven-coordinate species can directly release O$_2$ and regenerate the initial six-coordinate complex without requiring to take any compensatory ligand. [47]

Exchange of the carboxylate groups by phosphonate moiety resulted in the formation of the prominent MWOC [(N^{3}O-H$_3$tPa)Ru^{II}(py)$_2$]$^+$, **IV**, (Chart 1.1) comprised of the deprotonated ligand 2,2':6',2''- terpyridine-6,6''-diphosphononic acid and pyridines. [81] The active catalyst **IV** was generated via intramolecular oxygen insertion into a C-H bond of one of the pyridyl side-arms upon electrochemical treatment in phosphate buffer solution. A TOF$_{max}$ of 16000 was determined for this type of complex based on the foot of wave analysis (FOWA). Theoretical investigations proposed the WNA pathway where the Ru^{III} unit undergoes a two-electron

oxidation process followed by the coordination of the water substrate which was considered as the rate-determining step of this mechanism.

Another system based on polypyridyl ligands is [Ru(qpy)(pic)$_2$]$^{2+}$, **V**, (Chart 1.1), bearing the qpy (2,2':6',2'':6'',2'''-quaterpyridine) and two 4-picolines at the axial positions.[82] Several attempts were made to isolate the intermediates responsible for the critical O-O bond formation step. Chemical water oxidation treatment with CAN led to the formation of [Ru(ONNO)(pic)$_2$]$^{3+}$, in which the ONNO ligand originated from the oxidation of the qpy to qpy-N,N'''-dioxide during catalysis. The obtained complex was considered as the actual and active WOC. Kinetic studies supported by ^{18}O labeling experiment proposed that the O-O bond formation by **V** occurs through a WNA mechanism.[82]

I II III

IV V
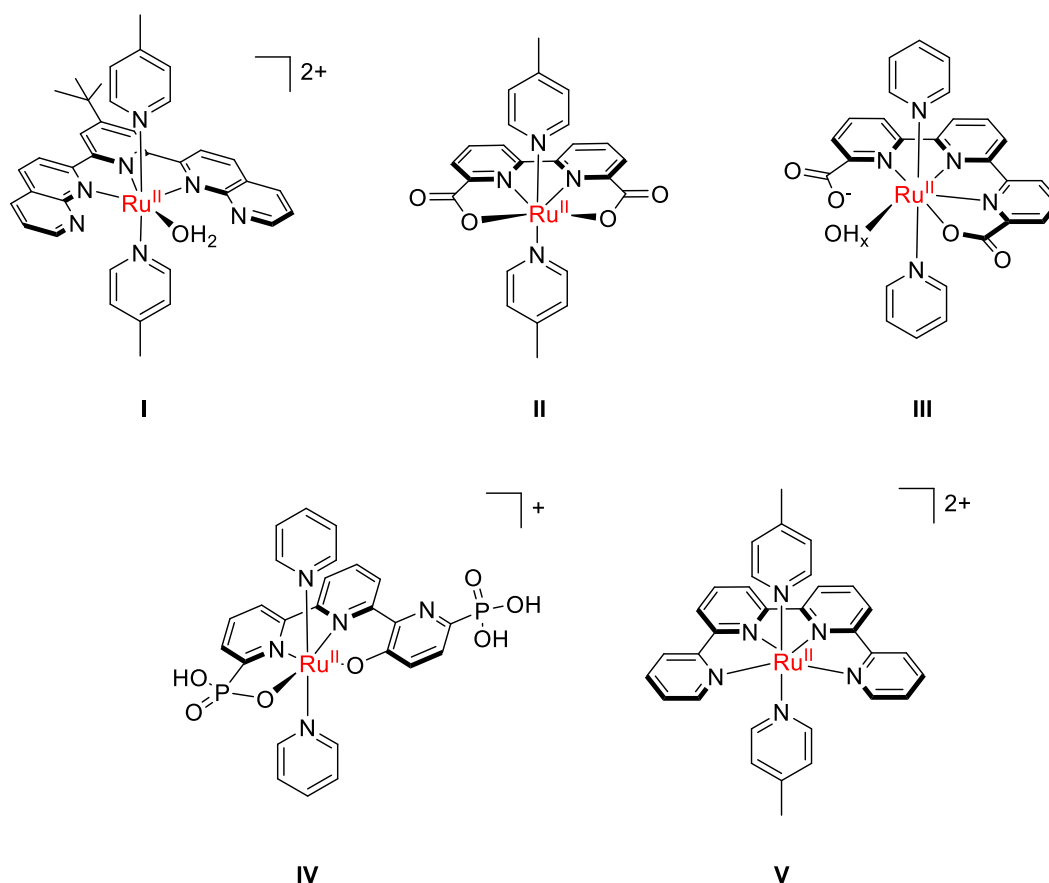
Chart 1.1. Selection of literature known mononuclear Ru-based water oxidation catalysts.[70–72,79,81,82]

1.4.3 Dinuclear Ru-Based Water Oxidation Catalysts

In 1982, T.J. Meyer and co-workers introduced the first well-characterized dinuclear ruthenium WOC *cis,cis*-[[Ru^{III}(bpy)$_2$(H$_2$O)]$_2$(μ-O)]$^{4+}$ (bpy = 2,2'-bipyridine), **VI**, which is known as the "blue dimer". The dimeric complex **VI**, is composed of two [Ru^{III}(bpy)$_2$(H$_2$O)] motifs

which are connected by a dianionic oxido bridge to support the strong electronic coupling between two metal centers (Chart 1.2).[83] The catalytic performance of the blue dimer was evaluated by a chemical water oxidation experiments using CAN under acidic conditions (pH = 1), with a TON of 13.2 and a TOF of $4.2 \cdot 10^{-3}$ s^{-1}.[84] However, **VI** was found to decompose by reductive cleavage of the bridging unit in oxidation states lower than III, III within the cyclic voltammetry time scale. This degradation pathway is associated with the breakdown of the active catalyst to mononuclear ruthenium units.[60,85,86] In addition, coordination of anions to the active site of the bimetallic complex instead of water molecules (anation), was considered as another factor that negatively affects the catalytic reactivity of **VI**.[83,86,87] Several experimental and theoretical methods were applied to unravel the mechanism of water oxidation by the blue dimer, however, some steps are still under debate.[54,88,89] By means of ^{18}O-labeling experiments, Hurst and co-workers proposed ligand participation in the O-O bond formation step.[88,90–92] This mechanism proceeds via attaching a hydroxyl fragment to bpy ligand resulting in the formation of an intermediary ligand cation which is then attacked by another water at the β-position. Finally, the interaction of two hydroxide groups at the bipyridine ligand yields the O_2 formation.[88]

The invention of the blue dimer with modest reactivity led to the development of more efficient MWOCs with synthetic flexibility. In 2004, the Llobet group presented a prominent dinuclear ruthenium WOC [{Ru(trpy)(H_2O)}$_2$(μ-[H]bpp)]$^{3+}$ (trpy = 2,2':6',2''-terpyridine), **VII**, (Chart 1.2), based on a polypyridyl dinucleating scaffold, capable of triggering the water splitting reaction without any oxo bridge. [93] Here, two ruthenium ions were located in close proximity using the compartmental 3,5-bis(2-pyridyl)pyrazolate ([H]bppH) ligand system. Thanks to this design, a significant cooperative effect was observed between the two ruthenium ions, leading to a lower pK_a value than for the mononuclear complex *out*-[H]bppRu(H_2O), due to the formation of the stable {$Ru_2O_2H_3$} unit.[94] Chemical water oxidation experiments under acidic conditions using CAN demonstrated a TON of 17.5 corresponding to an efficiency of 70% with respect to the amount of CAN.[56] The rate of O_2 evolution in **VII** was compared with the previously reported blue dimer. Substitution of the oxo bridge by a chelating ligand resulted in higher stability, by preventing the decomposition upon reductive cleavage.[84] In addition, introducing the negatively charged [H]bppH ligand made the rate of the anation process slower due to reducing the overall charge of the active intermediate. However, bimolecular catalyst-catalyst interactions, as well as bbp$^-$ ligand oxidation especially

at the pyrazolate C^4-position, were considered as the major deactivation pathways of **VII**.[56] ^{18}O labeling experiments along with kinetic studies suggested the intramolecular (I2M)[52] mechanism, which was the first example of this type of pathway at that time.[52] Besides that, the influence of the substituents at both trpy and ligand backbone on the catalytic activity was investigated thoroughly.[95]

Later, the group of Thummel reported a new family of dinuclear ruthenium complexes involving a rigid backbone ligand, in which pyridine-type axial ligands were introduced instead of another polypyridyl group.[70,96] The significant improvement in catalytic activity (TON up to 600) compared to the blue dimer and bpp-Ru_2 was attributed to the special steric configuration of **VIII** which provides open sites for binding of the substrate water to the equatorial position.

Based on the same design strategy, a series of rugged WOCs, the [{Ru(pySO$_3$)$_2$(H$_2$O)}$_2$(μ-^{Me}bbp)]$^-$, **IX**, (Chart 1.2), containing 3,5-bis{6-(2,2′-bipyridyl)}-4-methyl-pyrazolate (^{Me}bbp$^-$) and pyridine-3-sulfonato (pySO^{3-}) axial ligands were established by the group of F.Meyer.[53,62,97] The sulfonate groups at the axial pyridines improved the solubility of the complex in aqueous media and enabled mechanistic studies. The higher stability of these types of complexes compared to **VII** can be attributed to expanding the sidearm of the bbp$^-$ in equatorial position with an additional pyridyl unit.[93] The precatalyst was prepared with complexes with different bridging and nonbridging units such as DMSO, Cl$^-$, OAc$^-$, CO$_3$H$^-$ in the *in,in*-position of the binding pocket.[62] However, these have to be replaced by aqua ligands to generate the real active species.

Complex **IX** catalyzed water oxidation with a TON of 22.6 corresponding to an efficiency of 90% and with a TOF of 0.068 s^{-1} using CAN as a sacrificial oxidant at pH = 1. The contrast of reactivity between **IX** and **VII** (TON of 17.5) under identical conditions can be explained by the substitution of the hydrogen atom at the 4-position of the pyrazolate ligand with a methyl group in **IX**, which remarkably hampers oxidative decomposition of the backbone ligand.

Mechanistic investigations through ^{18}O labeling experiment revealed that the O-O bond formation occurs via WNA at one of the metal-oxo units,[53] which is in sharp contrast to the complexes bearing the bpp$^-$ ligand, **VII**, which proceed via I2M. This different observation can

possibly be attributed to subtle changes in the geometry of bbp⁻ based complexes, which considerably restricts the through-space interaction between the two Ru-OH$_x$ groups.[98]
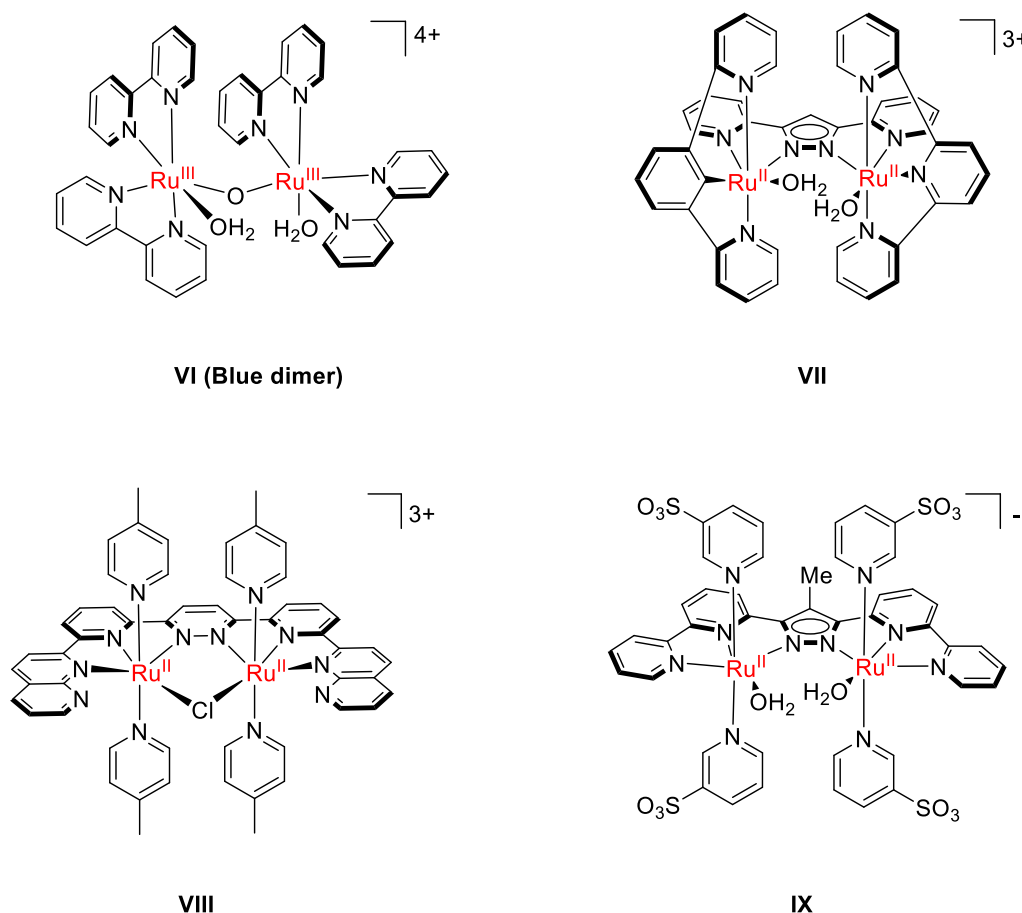
Chart 1.2. Selection of literature known dinuclear Ru-based water oxidation catalysts.[53,83,93,96]

1.5 Heterogenization of Molecular Water Oxidation Catalysts

For the construction of water oxidation anodes/photoanodes, the immobilization of the prominent MWOCs onto the conductive or semiconductive support is the next step. Understanding the fundamental aspects of the catalyst behavior on anodes is essential to design more efficient MWOCs for photoelectrochemical cells. Simple drop casting of the active homogenous catalyst on the electrode surfaces may not result in stable devices due to the uncontrollable aggregation of catalysts and leaching issues. Therefore, effective strategies are needed for the heterogenization of the molecular catalysts without restricting their intrinsic reactivity. Moreover, further optimization of the heterogeneous surface by addressing issues such as density of the active sites, hydrophobicity/hydrophilicity, surface area, and mass transfer limitation is necessary.

Several methods can be applied to immobilize a homogenous molecular catalyst onto a solid platform such as 1) physisorption, through Van der Waals forces, 2) electrostatic interaction, which arises from different charges between the WOC and the surface, 3) encapsulation, anchoring of the molecular catalyst inside a matrix, and 4) chemisorption, covalent attachment of the catalyst to the surface. Non-covalent immobilization on carbonaceous surfaces is another promising approach, which attracted extensive attention in recent years. This strategy will be illustrated in more detail in the following sections.

For linkage assembly, the molecular catalysts should be equipped with appropriate anchoring groups which possess suitable properties according to their application. The WO catalysts in water-splitting dye-sensitized photoelectrochemical cells (WS-DSPECs) necessitate the accumulation of four consecutive oxidizing equivalents to enable the oxidation of water to dioxygen. Hence, the catalyst should have a long-lived excited state to accomplish the accumulation process before the unfavorable electron-hole recombination.[99,100] In contrast, the anchors on dyes should create a strong electronic coupling to the metal oxide conduction bands to enhance the electron transfer dynamics in a dye-sensitized photoelectrochemical cell (DSSC).[101–103] Overall, the anchors for both catalysts and dyes must possess some common properties such as high stability under prolonged photoexcitation process, efficient surface bonding stability in an aqueous environment, optimized electron injection into the surface, and resistance under oxidizing conditions.[104]

1.5.1 Immobilization of Molecular Catalysts on Metal Oxide Surfaces

Several organic and inorganic substances can be used as a platform for complex immobilization. A suitable support should fulfill some criteria such as reasonable chemical and mechanical stability, resistance toward high temperature and under acidic or basic conditions, and providing the optimized surface coverage without suppressing the catalytic activity.

Metal oxide materials with the formula of MO_x (M= Ti, Fe, Al, Sn, Si) can be employed as appropriate supports for the covalent attachment of the molecular catalysts. The properties of the oxides can vary tremendously but most of them are thermodynamically stable, accessible, and can be supplied in numerous nanometer-sized structures. Some oxides especially indium tin oxide (ITO) are widely used as a photo-electrode in organic–semiconductor devices due to their high electrical conductivity and optical transparency.[105,106]

Additionally, the control of charge transfer from the electrodes to the molecular catalyst is more efficient in covalent linkages due to strong chemical bonding between the components. Therefore, this approach is the most widely used method for assembling hybrid photoelectrochemical systems

A proper choice of anchoring groups is necessary for achieving high binding stability between the surface and molecular adsorbent. The most common anchors for metal oxide electrodes are carboxylic acids and phosphonic acids, but they show limited stability in aqueous media.[101,107,108] In contrast, hydroxamic acids and silatranes, which have been recently presented, are more promising for the generation of hybrid assemblies. These functional groups are more resistant against hydrolysis and have more stability over an extended pH range.[102,109–111]
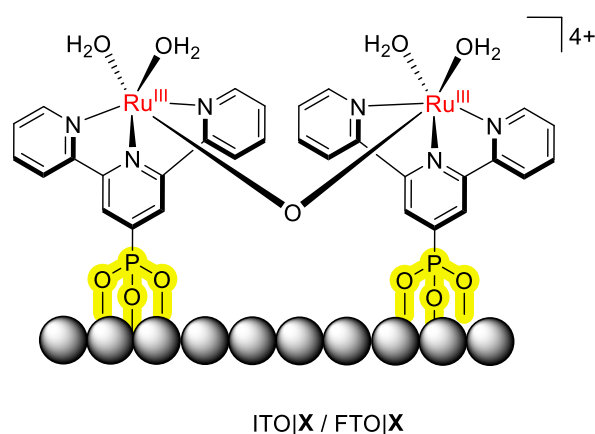
Initial efforts to anchor ruthenium water oxidation catalysts onto metal oxides were carried out in 2007. A μ-oxo bridged ruthenium-based complex, **X**, (Chart 1.3), containing phosphonate group at the terpyridine ligand, was prepared by the T. J. Meyer research group, and the activity toward water oxidation was investigated after immobilization on the ITO and FTO (fluorine-doped tin oxide) electrodes.[112] Calculation of the formed oxygen based on the surface coverage of the electrode revealed a TON of 1.8 for Ru^{VI}-O-Ru^{V} in aqueous HOTf (0.1 M, pH = 1) in the presence of CAN.
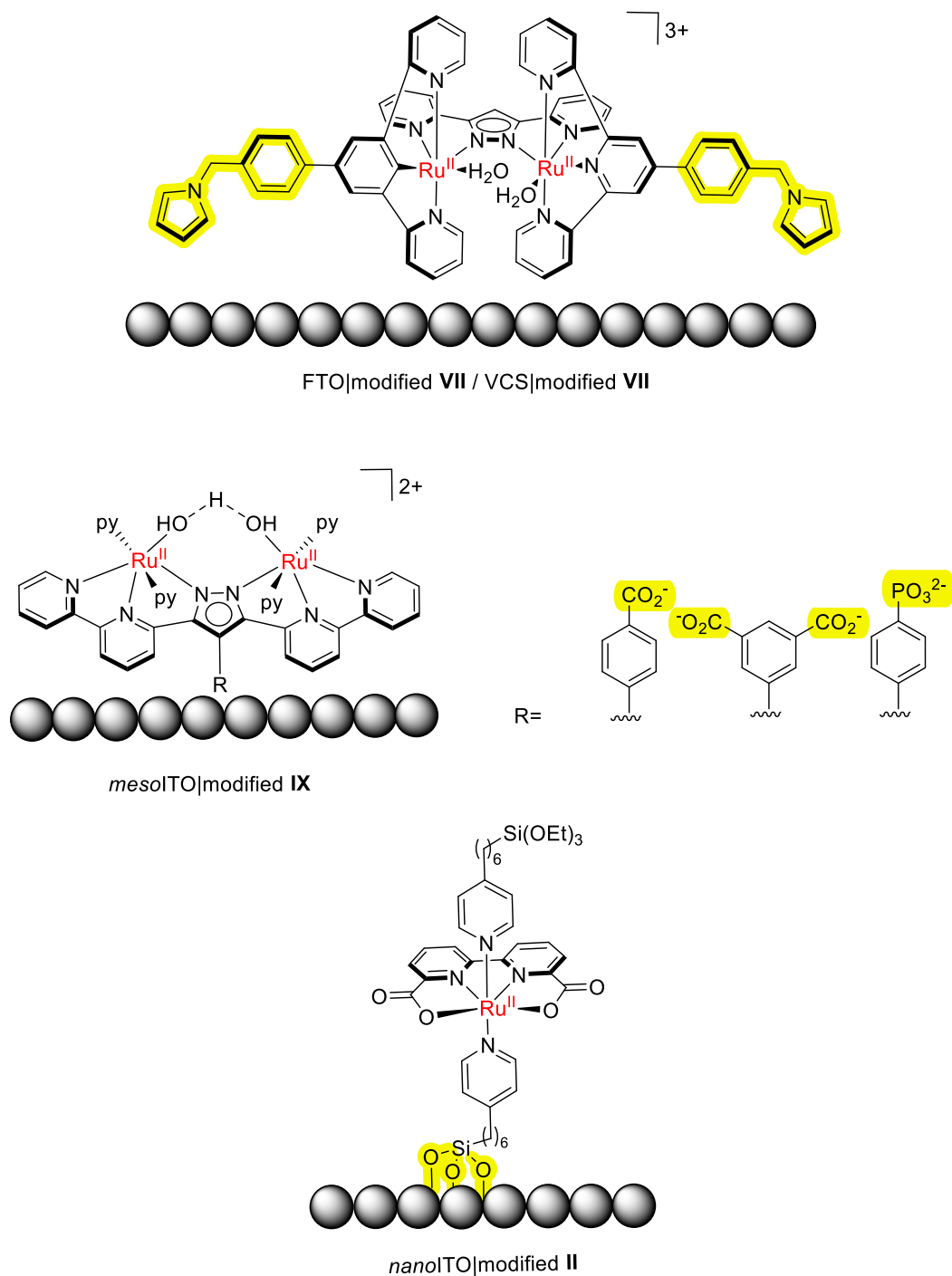
Following the heterogenization approach, the robust bpp-based ruthenium complex was furnished with N-substituted pyrroles to the axial terpyridine, (Chart 1.3), in order to assess the catalytic performance in heterogeneous phase.[113] Anchoring onto two solid supports, FTO and vitreous carbon sponges (VCS), via polymerization gave rise to a significant improvement in TON due to diminishing the decomposition pathway via the catalyst-catalyst interactions. The formed hybrid displayed a TON of 76 and a TOF of 0.005 s^{-1} at pH = 7, which is remarkably higher than **X** anchored via phosphonic acid moieties.

Later, the immobilization of bbp-Ru_2 complexes was achieved on electrically conductive mesoporous ITO electrodes by the introduction of different functional groups (carboxylate and phosphonate) at the pyrazolate core, (Chart 1.3), to provide suitable hybrid materials for electro-catalytical applications.[114,115] Rotating ring disk electrode (RRDE) techniques were adapted to evaluate the stability of the resulting hybrid electrode as well as to detect the

desorbed species in-situ under catalytic conditions. The complex anchored via carboxylate group, was found to gradually detach from the surface at low potentials below the oxygen evolution reaction onset.[114] To improve the binding stability to the solid support, the bbp⁻ ligand scaffold was modified with two carboxylate groups at the pyrazole ligand. However, introducing the second binding sites enhanced the solubility of the resulting complex in an aqueous environment, which led to faster desorption from the electrode surface. It turned out that the complex bearing the phosphonate anchor has higher chemical stability with similar catalytic performance under reactive conditions. The leaching of **IX** from the surface was only observed at high potentials, mainly due to the oxidative cleavage of the P−C(aryl) bond once the complex reaches the high-valent $Ru^{V}Ru^{IV}$ state.[114]

Based on the outstanding success of homogenous MWOCs established by bda-Ru systems, recently, the group of T. J. Meyer fabricated a stable hybrid consists of a bda-based complex modified with triethoxysilyl groups immobilized on a mesoporous nanostructured core/shell SnO_2/TiO_2 electrode (Chart 1.3). The water oxidation catalysis of the triethoxysilyl-derivatized complex was examined over a wide range of pH due to the strong binding stability of the anchor to the oxide surfaces.[116] A noticeable loss of the catalyst was observed upon prolonged electrochemical measurements which can be attributed to the exchange of the axial ligands with a water molecule and leaving the anchoring groups on the surface.

ITO|**X** / FTO|**X**

FTO|modified **VII** / VCS|modified **VII**

*meso*ITO|modified **IX**

R=

*nano*ITO|modified **II**

Chart 1.3. Selection of immobilized molecular ruthenium complexes on metal oxide surfaces.[112–114,116]

1.5.2 Immobilization of Molecular Catalysts on Carbonaceous Surfaces

As discussed in the previous section, covalent attachments of molecular catalysts on metal oxides are one of the common approaches for the construction of hybrid materials. However, a large drawback of this strategy is the limited stability of oxide anchoring groups in aqueous environments, especially where increasing the pH, leads to leaching from the surface and loss of reactivity.[114,115] Moreover, additional surface treatments of the oxide electrode may be

necessary to improve active sites before the anchoring step. Immobilization on carbonaceous surfaces such as graphite, graphene, and carbon nanotubes (single or multiwall) can be considered as an alternative strategy for hybrid construction. Several methods were established to maintain the catalytic proficiency of the homogenous catalysts after anchoring and even in some cases, improvement in reactivity was observed.[117–119]

Carbon nanotubes (CNT) can be employed as semiconductors, conductors, or insulators based on their structural features.[120] Conductive carbon nanostructures may also serve as an interlayer film between photoactive oxide materials and the molecular catalyst to enable electron transfer between the photoelectrode components and facilitate the anchoring process.[119,121] Multiwalled carbon nanotubes (MWCNTs) are good candidates for this purpose due to their specific properties such as providing a large electrochemical surface area, having high stability, and good conductivity.[122,123]

To produce single-walled nanotubes (SWNT), a single sheet of graphene is wrapped into a cylindrical form.[120] Carbon atoms are arranged in a hexagonal structure, forming covalent bonds (via sp^2 molecular orbitals) with three neighboring atoms each. A delocalized π-band is formed by hybridization of the valence electron in the p_z orbitals. In contrast, MWCNTs contain several SWNTs with different chiralities.[120]

There are two main approaches to immobilize the molecular catalyst on CNT surfaces (*i.e.* covalent and non-covalent). Electrografting is a powerful way to bind organic reagents such as amines, alcohols, carboxylate, diazoniums and, halides to conductive or semiconductive carbon substrates.[124] One example of covalent grafting is the functionalized bda-Ru with diazonium units on the axial pyridine, **IIa**, (Chart 1.4), that was attached to the graphite surface upon repetitive cycling voltammetric treatments.[125] The electrochemical results indicated low stability of the hybrid at high potentials because of decomposition of the complex into RuO_2 particles.[125] Immobilization on carbonaceous surfaces can also occur via non-covalent interactions. The molecular complex can be modified with polyaromatic groups with expanded π systems such as pyrene or long hydrophobic aliphatic chains like dodecyloxy groups. In 2014, the Sun group modified a well-defined mononuclear ruthenium WOC with a dodecyloxy tail to accomplish the surface anchoring on carbon supports.[126] It revealed that

the hydrophobic groups can improve the stability of the hybrid by overcoming the solubility issue in an aqueous solution.

Immobilization through π-π interactions has several advantages over covalent attachment on conductive metal oxide materials. The extended aromatic anchoring moieties usually display hydrophobic properties, hence they can prevent the catalyst from leaching into the aqueous solution. In addition, the sample preparation is quite straightforward via this method and π-stacking can easily take place between the WOC and the electrode surface without any additional treatment. Moreover, the stability of carbon-based anchoring groups is not dependent on pH, therefore the catalysis can be conducted in a wide range of pH. However, graphitic materials have a narrower electrochemical potential window compared to metal oxides and they are quite expensive for large-scale application.

To examine new approaches for stable anchoring, the group of Sun reported a hybrid anode consisting of the bda-Ru catalyst, **IIb**, immobilized on MWCNTs through π-π interactions of pyrene groups (Chart 1.4).[122] A decrease in catalytic current was observed after 10 h electrolysis, mainly due to desorption of the catalyst from the electrode surface. In addition, the lower TOF$_{max}$ value compared to the homogenous systems was attributed to the slow two-dimensional diffusion of the complex on the MWCNTs which restricts the critical O-O bond formation step, associated with an intermolecular pathway.[127]

Later, the tda-Ru catalyst was successfully immobilized on MWCNTs deposited on a glassy carbon electrode using two different pyrene moieties, **IIIa** and **IIIb**, (Chart 1.4).[117] **IIIa** revealed a TON of 670 000 and TOF$_{max}$ of 8076 s^{-1} after 2.5 h bulk electrolysis at pH = 7. However, a gradual decrease in current density was observed during the experiment, possibly due to oxidative degradation of the methylene groups of the linker. In contrast, **IIIb** exhibited extremely high stability, reaching a TON of 180 000 in a similar manner (2.5 h electrolysis, pH = 7), and for prolonged electrolysis, it showed a significant TON of 1.2 million. Most importantly, as the tda-derived complexes favor a WNA scenario, they retain their high catalytic performance under conditions of restricted mobility after immobilization on the surface.[127] This finding stressed the importance of the O-O bond formation mechanism in the construction of hybrid anodes for real applications in water splitting devices.[79,117]

Recently, LIobet and coworkers presented a new and convenient heterogenization strategy for the generation of robust hybrid anodes. A series of Ru-based oligomers {[Ru^{II}(tda-κ-N$_3$O)(4,4'-bpy)]$_n$(4,4'-bpy)} (4,4'-bpy = 4,4'-bipyridine, n = 1, 2, 4, 5, and 15), **XI**, (Chart 1.4) based on the tda^{2-} ligand was prepared and immobilized on graphitic surfaces through CH-π interactions, without further functionalization.[128] Electrochemical studies showed that increasing the length of the oligomer can significantly decrease the rate of desorption from the MWCNTs. The generated hybrid behaved as a rugged photoanode for water oxidation, displaying exceptional current densities at neutral pH.[128]

This new anchoring strategy on graphitic surfaces was then applied to other MWOCs. Firstly, a trinuclear supramolecular macrocyclic catalyst [{Ru(bda)(bpb)}$_3$], (bpb = 1,4-bis(pyrid-3-yl) benzene), **XII**, (Chart 1.4), in which three Ru(bda) subunits were linked through aromatic bridging (bpb) ligands was studied.[129] Immobilization of **XII** on CNTs through non-covalent π-π and CH-π interactions yielded a stable anode, achieving a TON of 1.8 million (99% efficiency) during the controlled potential electrolysis.[130] Furthermore, its exceedingly high stability was illustrated by X-ray absorption (XAS) spectroscopy, revealing the absence of any RuO$_2$ nanoparticles after the catalysis.[130]

Secondly, a robust molecular hybrid anode for OER including Ru-bda oligomer anchored on MWCNTs was reported very recently.[131] During the electrocatalytic process, the tetradentate bda ligand changes its coordination sphere from κ-N$_2$O$_2$ to κ-NO to liberate free binding sites for the coordination of water molecules. The impressive activity of the new hybrid was attributed to the remarkable binding stability of the oligomer to graphitic materials through multiple ligand-based CH-π interactions. This promising approach allows better control of molecular coverage on surfaces compared to other anchoring techniques, hence it can be used as an alternative for the generation of efficient water oxidation photoanodes.
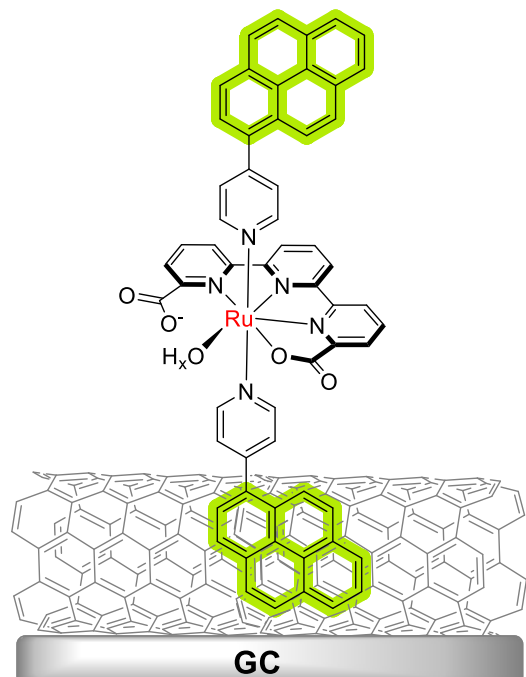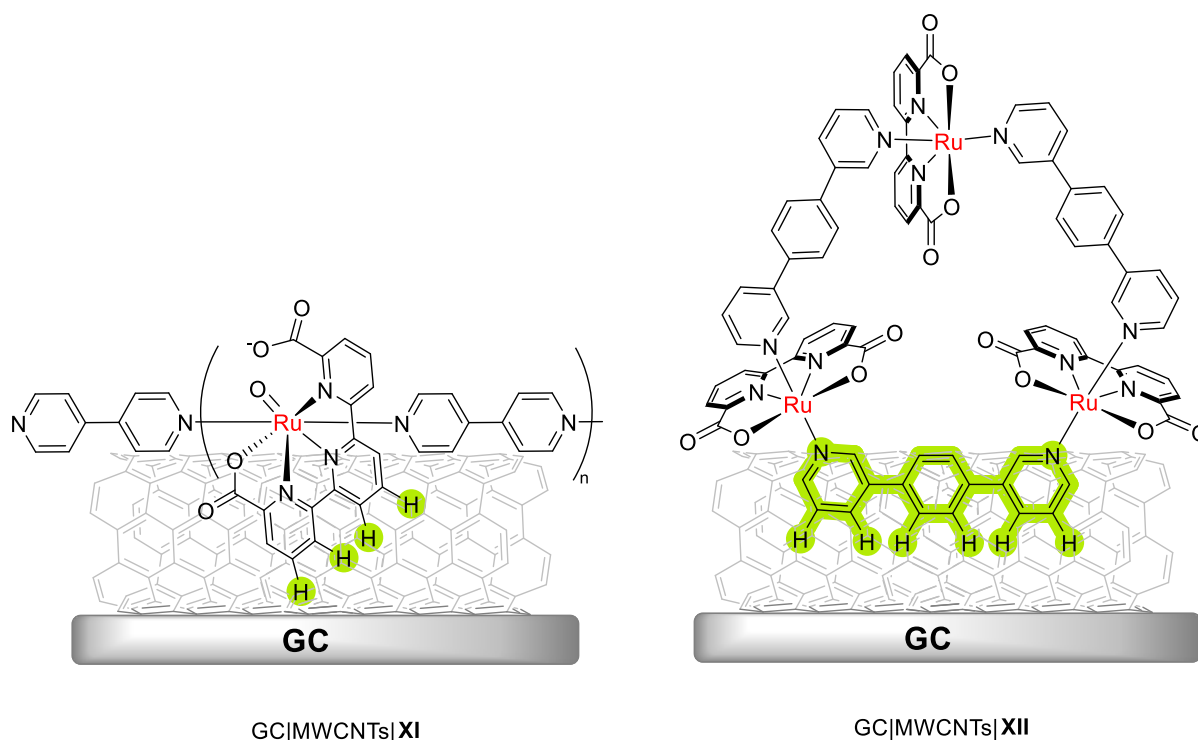
GC|**IIa**
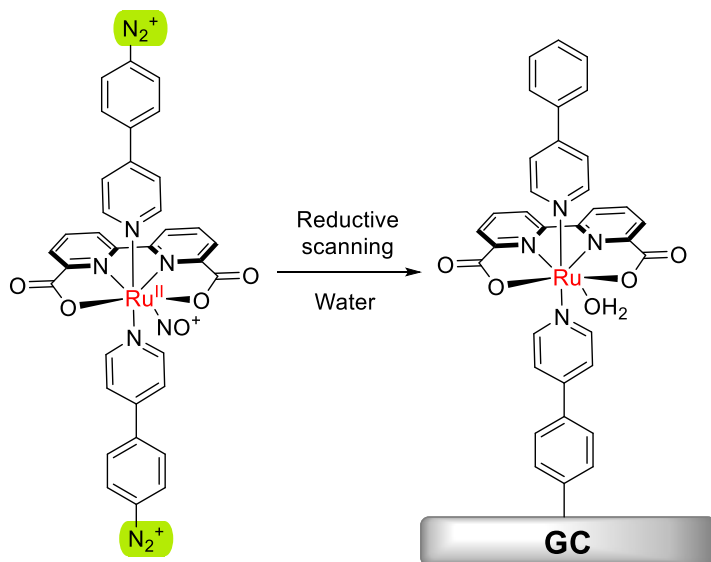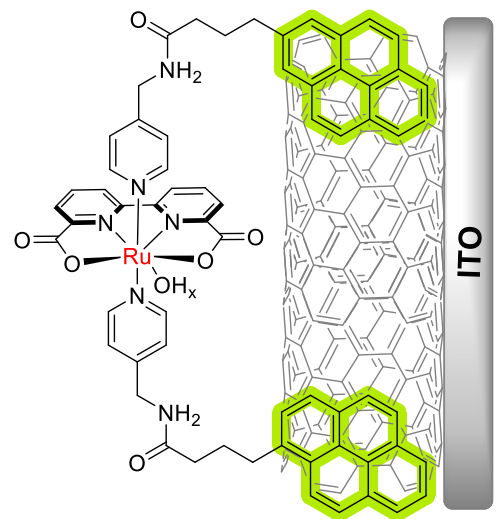
MWCNTs/ITO|**IIb**
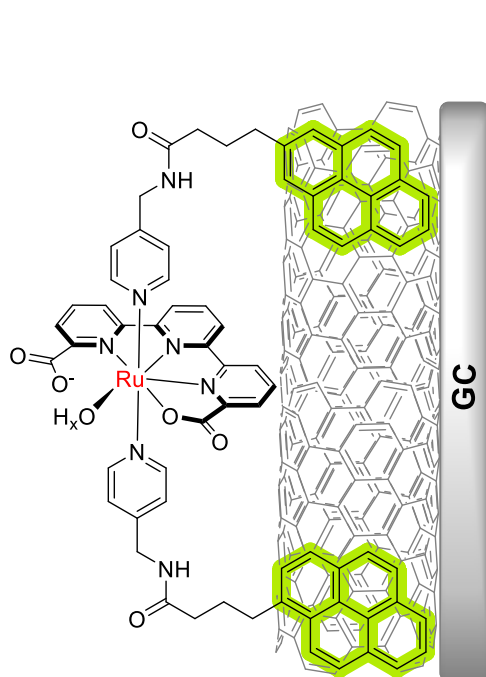
GC|MWCNTs|**IIIa**

GC|MWCNTs|**IIIb**

GC|MWCNTs| **XI**

GC|MWCNTs| **XII**

Chart 1.4. Representation of immobilized molecular ruthenium complexes on carbonaceous surfaces.[117,122,125,128,130]

1.6 Strategies for the Evaluation of Water Oxidation Catalysts

Various techniques have been exploited to assess the performance of WOCs in both homogenous and heterogeneous systems. The following sections will only describe the methods used in parts of this thesis.

1.6.1 Homogenous Catalysis

Chemical Water Oxidation

In this method, generation of the high-valent metal-oxo complexes which then gives O_2 via an I2M or WNA mechanism is achievable by the introduction of a sacrificial oxidant in bulk solution. The produced O_2 gas can subsequently be measured by oxygen sensor electrodes or in the gas phase by mass spectrometry as well as gas chromatography. CAN is one of the most powerful oxidants which is widely used to probe the WOCs behavior. CAN can act as a one-electron oxidant and has a redox potential of approximately +1.75 V *vs.* NHE in an aqueous perchlorate solution (pH = 0.9).[132] It is also commercially available and has high stability at a very low pH (eq. 1.7).[133] However, the latter property restricted its application for studying WOCs at neutral to alkaline pH, relevant to conditions of the artificial photosynthesis cells.

$$4Ce^{IV} + 2H_2O \xrightarrow{\text{WOCs}} 4Ce^{III} + O_2 + 4H^+ \quad (1.7)$$
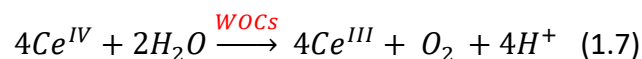
$[Ru^{III}(bpy)_3]^{3+}$ is an alternative one-electron oxidant with a reduction potential of 1.2 V *vs.* NHE at near-neutral conditions.[134] The drawback of this oxidant is its low thermodynamic potential, which is not sufficient to screen a majority of WOCs. Moreover, it easily decomposes to $[Ru^{II}(bpy)_3]^{2+}$ even in the solid-state. To overcome this issue, sodium peroxodisulfate can be used in combination with $[Ru^{II}(bpy)_3]^{2+}$ to regenerate the primary oxidant in situ.[135]

Potassium peroxymonosulfate (Oxone), sodium periodate ($NaIO_4$), and sodium hypochlorite (NaClO) are common two-electron oxidants, which are extensively applied to characterize WOCs under neutral or alkaline conditions.[133,136,137] The main disadvantage of these oxidants is their ability to behave as an oxo-transfer reagent (OAT). Hence, it would be challenging to distinguish if the oxygen atom in the liberated O_2 originated from the chemical oxidant or water.[133,138]

Electrochemical Water Oxidation

Electrochemical measurements are widely used for redox potential analysis to obtain kinetic and thermodynamic information of the electrocatalytic reactions. Interpretation of the catalytic peak current of an S-shaped voltammogram in homogenous H_2O oxidation catalysis may be used to determine the observed rate constant (k_{obs}) (eq. 1.8), where i_{cat} is the catalytic peak current, i_p is the current in absence of the catalyst, n is the number of electrons involved in the catalytic step, n' is the number of the transferred electrons in absence of the catalyst, *v* is the scan rate, R is the universal rate constant, T is temperature and F is the *Faraday* constant.[139]

$$\frac{i_{cat}}{i_p} = \frac{n}{0.4463n'}\sqrt{\frac{RTk_{obs}}{n'vF}} \quad (1.8)$$

1.6.2 Heterogenized Molecular Catalysis

Rotating Ring Disk Electrode Approach

Rotating ring disk electrode (RRDE) measurement is one of the most powerful electrochemical techniques which provides insight into the reaction mechanism and catalytic processes that occur on the surface. A RRDE setup comprises two working electrodes (disk and ring), one counter electrode, and one reference electrode (Scheme 1.4). The two WE are placed in close proximity to each other and are only separated by a thin Teflon spacer. A bipotentiostat is used to simultaneously measure the potentials at the disk and ring electrodes against the reference electrode. In this method, the product, formed at the disk electrode is transferred to the ring electrode, where it can be detected by applying an appropriate potential. This approach also allows deriving turnover frequency, *Faradaic efficiency*, and kinetic information of the immobilized catalysts.[140–142]

Disk: $2H_2O \rightarrow O_2 + 4H^+ + 4e^-$

Ring: $O_2 + 4e^- + 4H^+ \rightarrow 2H_2O$
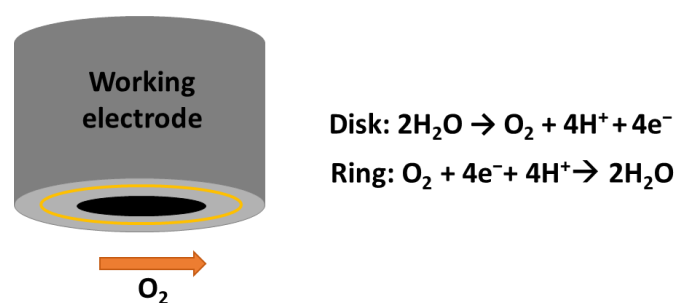
Scheme 1.4. Schematic representation of an RRDE cell containing a disk (black circle) and ring electrode (grey circle). During the experiment, the entire cell is rotated with a defined rotation speed (ω).

In heterogeneous systems, the current density which reflects the kinetic rate of the catalytic process is related to the overpotential according to the *Tafel* equation (1.9). (η: overpotential, i_0: exchange current density, i: current density, α: charge transfer coefficient, R: universal gas constant, T: temperature, n: number of involved electrons and, F: Faraday efficiency).[143,144] Equation 1.9 can be described in the simple form of Eq. 1.10, where a is the *Tafel* constant, and b is the *Tafel* slope. This equation allows the extraction of mechanistic insights and information regarding the rate-determining steps of the OER.

$$\eta = \frac{RT}{\alpha nF} \ln i_0 - \frac{RT}{\alpha nF} \ln i \quad (1.9)$$

$$\eta = a + b \log i \qquad (1.10)$$

Chemical Composition Investigation by X-ray Photoelectron Spectroscopy (XPS)

X-ray photoelectron spectroscopy is an established technique that gives insights into the structural integrity and chemical nature of the surface. The XPS spectra are obtained by irradiation of the analyte with a strong X-ray beam, while simultaneously measuring the kinetic energy of the photoelectrons that are released from the material being probed. The emitted electrons have characteristic energies specific to the respective elements in the analyzed sample. This method enables the quantification of the surface elements by interpretation of the binding energy and intensity of the photoelectron peaks. Qualitative information can also be achieved through a comparison of the energy position of the detected peak with a reference sample.

Imaging Techniques

Transition electron microscopy (TEM) and scanning electron microscopy (SEM) are valuable tools for characterizing the morphology and composition of a certain sample. In TEM, a beam of electrons is passed through the sample, leading to a well-defined image, while in SEM a fine beam of focused electrons is used to scan the surface. The scattered beam of electrons can be further analyzed by electron energy loss spectroscopy (EELS) to give more insight into the electronic and structural features of solid materials.

2 Thesis Outline

A series of prominent pyrazolate-based ruthenium complexes were established in the group of F. Meyer and investigated as water oxidation catalysts in both homogenous and heterogeneous systems.[53,97,114,115] For the construction of hybrid anodes suitable for photo- and electrocatalytic applications, their immobilization on various oxide surfaces (FTO, ITO, $(Pr,Ca)_2MnO_4$, $SrTiO_3$) was achieved using different anchoring groups such as phosphonate, carboxylate, and bis-carboxylate (described in section 1.5.1).

In this work, to pursue the aim of the C01 project in the SFB 1073 "Hybrid assemblies for fundamental studies of photo-induced multistep charge transfer catalysis", the anchoring strategies are extended by using pyrene anchoring groups that enable π-π interactions with carbonaceous surfaces. To that end, the bbp-based ruthenium complexes are equipped with peripheral pyrenes attached to multiple axial pyridine ligands or the C^4-position of the pyrazolate backbone (Chart 2.1). This allows for immobilization of the modified complexes on electronically conducting MWCNTs deposited on the glassy carbon electrodes. The main part of chapter 3 discusses the reactivity and stability of the resulting hybrids toward oxygen evolution reactions using several electrochemical and spectroscopic techniques.[145]
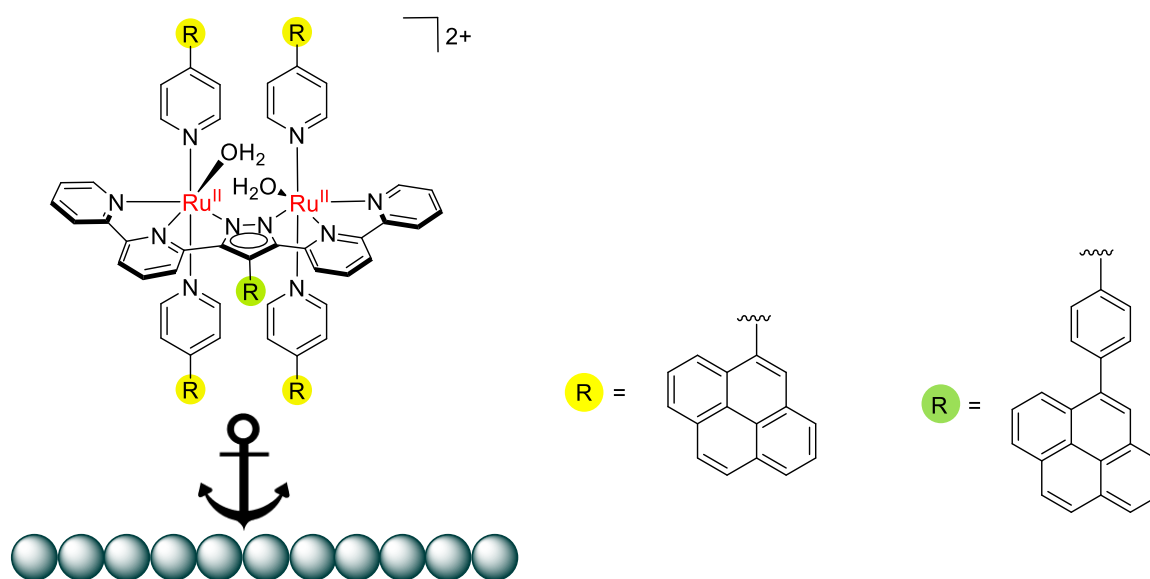
Chart 2.1. Overview of the bbp-based ruthenium complexes studied in this work. R represents the substituents at the axial pyridines or the pyrazolate backbone.

In pursuit of developing stable and active oxide-based hybrid materials, chapter 4 aims at the establishment of new mononuclear ruthenium complexes using dianionic N-donor scaffolds. The capability of two catalysts toward water oxidation is investigated either electrochemically or chemically (in presence of oxidants) in aqueous media. Further results regarding the immobilization of the complexes on oxide solid supports for the formation of the hybrid electrodes are shown at the end of the chapter.

$R = H, COOH, N(Me)_2$
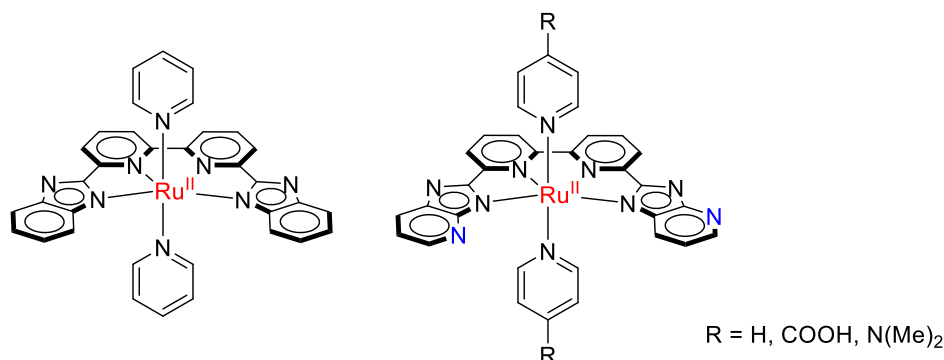
Chart 2.2. Targeted mononuclear ruthenium WOCs discussed in chapter 4.

The low binding stabilities of the molecular catalysts equipped with carboxylate and phosphonate to oxide supports are identified as the weak point in the design of hybrid devices[114] and hence, further improvement is required. Chapter 5 focuses on the synthesis and characterization of a triethoxysilyl-derivatized bbp-based complex and its immobilization on mesoporous ITO electrodes (Chart 2.1). Moreover, the integrity of the resulting hybrid electrode is explored in acidic environments in the course of this work.

The last chapter reports the synthesis and characterization of dinuclear ruthenium complexes based on an asymmetric pyrazolate ligand (Chart 2.3). The overall goal of this part is to investigate the influence of the new design on the mechanism of the O-O bond formation step compared to complexes bearing bpp and bbp ligand strands (see section 1.4.3) as well as their immobilization on solid supports for the construction of new hybrid materials.
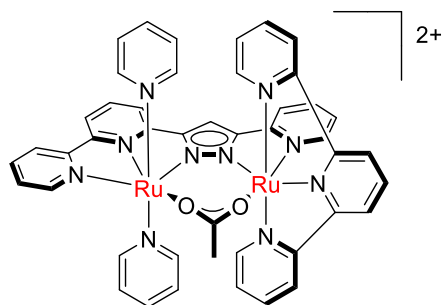
Chart 2.3. Targeted dinuclear ruthenium WOCs based on an asymmetric pyrazolate ligand.

3 Immobilization of the bbp-Ru$_2$ Catalysts on Carbonaceous Surfaces

3.1 Introduction

The synthesis of efficient molecular water oxidation catalysts and their stable anchoring on suitable solid supports are highly required for the development of hybrid materials. As mentioned in the introduction, a series of ruthenium catalysts based on the dinucleating bis(bipyridyl)pyrazolate ligand scaffold (bbp$^-$) was established in the group of F.Meyer and their immobilization on electrically conductive oxides was achieved via different functional groups at the ligand backbone, viz., a single carboxylate, two carboxylates, and a phosphonate anchor (see Chart 1.3).[114,115] The hybrids displayed high water oxidation activity in an acidic aqueous solution without decomposition of the catalyst into metal oxide nanoparticles (RuO$_2$). However, the binding between the anchoring groups and oxide surfaces was identified as the weak point and needs to be improved. To overcome this issue, herein, we investigate non-covalent immobilization on carbon nanotubes using pyrene groups attached to different sites of the molecular catalyst. Next to a thorough electrochemical and spectroscopic characterization of the new modified bbp-Ru$_2$ catalysts, the stability and catalytic activity of the resulting hybrid electrodes will be discussed in the following section. The results of this chapter have already been published and hence, some parts have been adapted from the published manuscript.[145]

3.2 Synthesis of the Modified bis(bipyridyl)pyrazolate Ligand

Preparation of the prolignad ^{pyr}**bbpH** involves multi-step synthetic procedures (Scheme 3.1).[146,147] First, 2,2´-bipyridine was oxidized in presence of hydrogen peroxide in trifluoroacetic acid (TFA) to form 2,2´-bipyridyl-*N*-oxide **(3-1)**. Treatment of **(3-1)** with TMSCN (excess) and benzoyl chloride in dry dichloromethane resulted in the formation of 6-cyano-2,2´bipyridine **(3-2)** which can be converted to 6-acetyl-2,2´-bipyridine **(3-3)** via the iminomethylether or 6-(2,2´-bipyridyl)methylcarboxylate **(3-4)** via a *Grignard* reaction. The diketone **(3-5)** was prepared through a pseudo-Claisen condensation of the ester **(3-3)** and ketone **(3-4)** using NaO^{t}Bu as a base. Finally, the closure of the pyrazole ring took place via the

reaction of the diketone with hydrazine monohydrate. To introduce the anchoring groups to the parent ligand ^{H}**bbpH**, the proton at the C^4-position of the pyrazole was exchanged with iodide after treatment with *N*-Iodosuccinimide in presence of *p*-toluenesulfonic acid in DMF.[148] Protection of the pyrazole with MOMCl in THF was performed to improve the selectivity and avoid the coordination of the palladium catalyst to the ligand scaffold during the cross-coupling reaction. The 4,4,5,5-tetramethyl-2-(4-(pyren-1-yl)-phenyl)-1,3,2-dioxaborolane **(3-6)** was synthesized according to the literature procedure[149] and reacted with ^{I}**bbp(MOM)** in a Suzuki-Miyaura cross-coupling to generate the ^{Pyr}**bbp(MOM)**. The MOM protecting group was finally removed after stirring in an HCl/EtOH solution overnight. The proligand ^{Pyr}**bbpH** was characterized by 1D and 2D NMR spectroscopy (^{1}H and ^{13}C). The number of signals in the ^{1}HNMR spectrum is corresponding to a compound with C$_s$ symmetry (Figure 3.1).
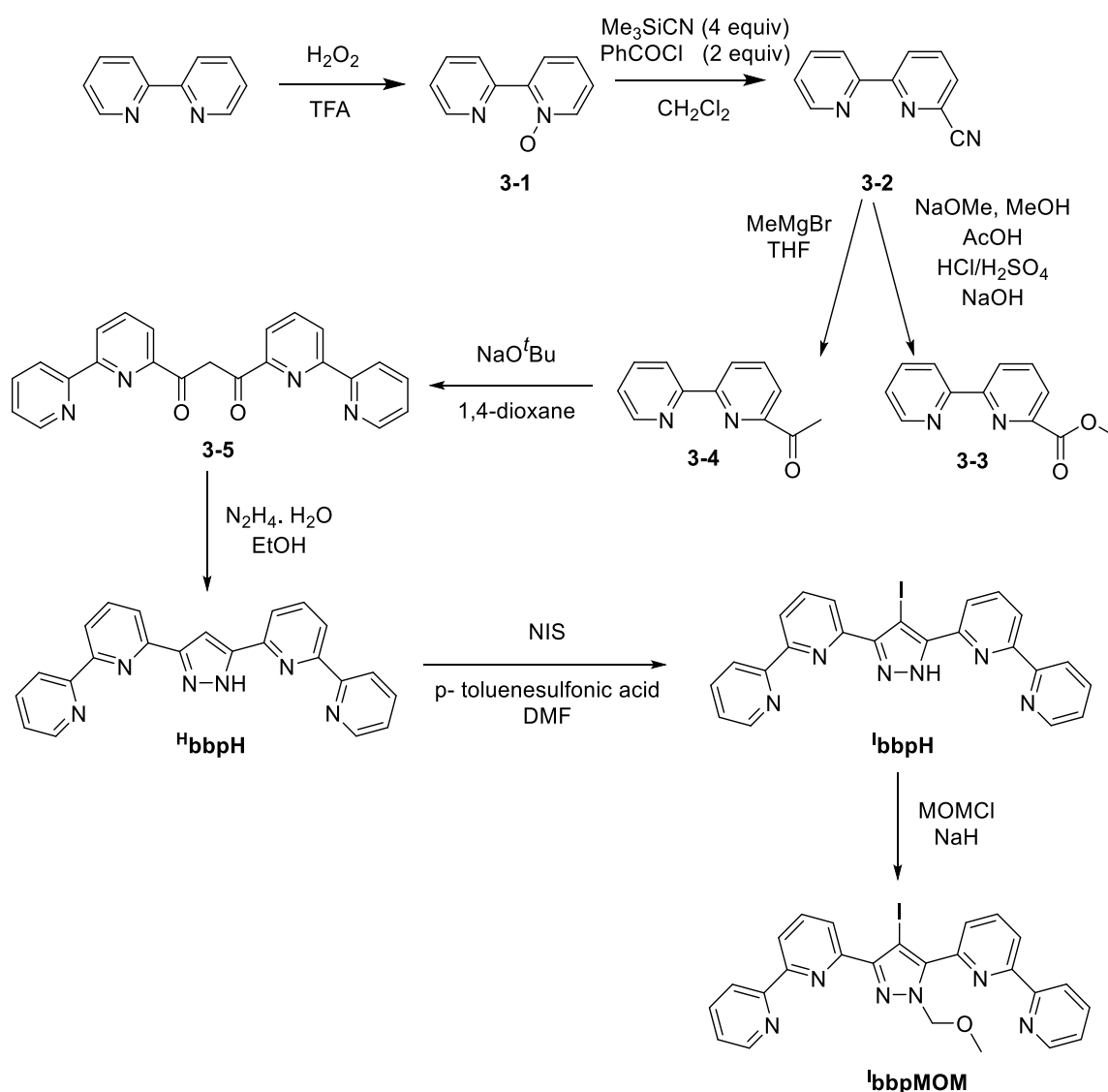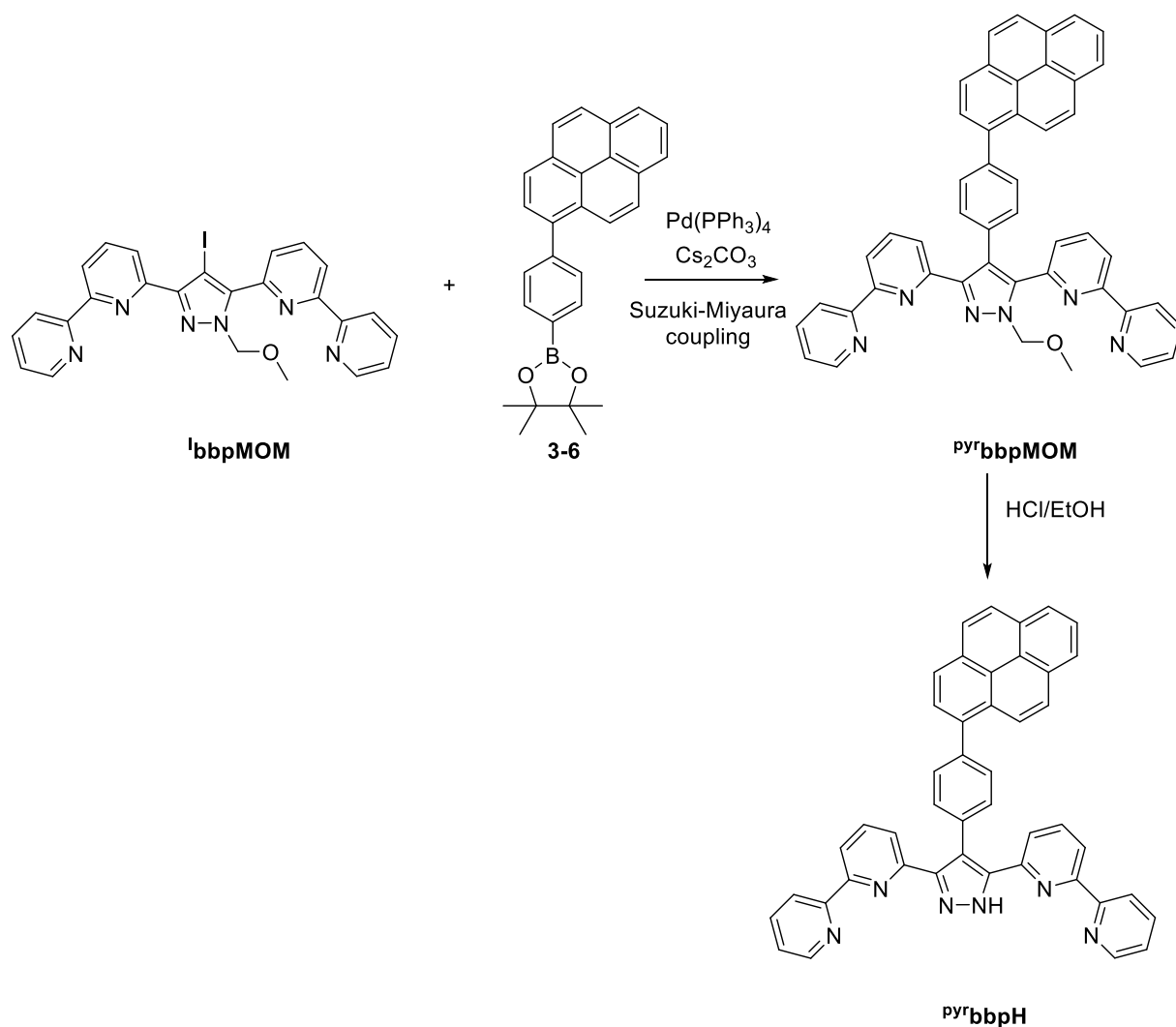
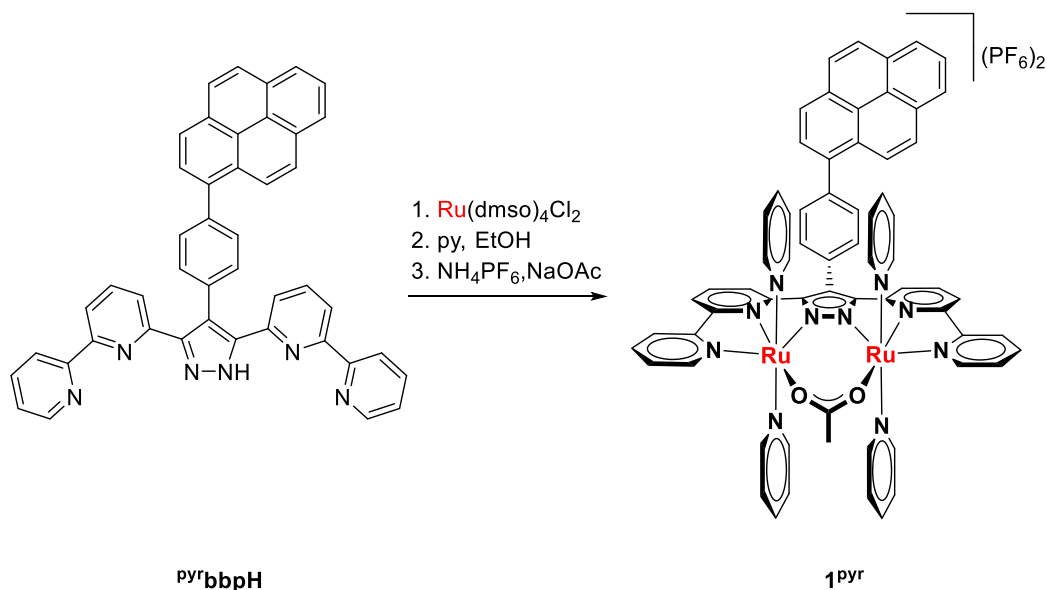**Scheme 3.1.** General synthetic scheme for the ligand ^{pyr}**bbpH**.
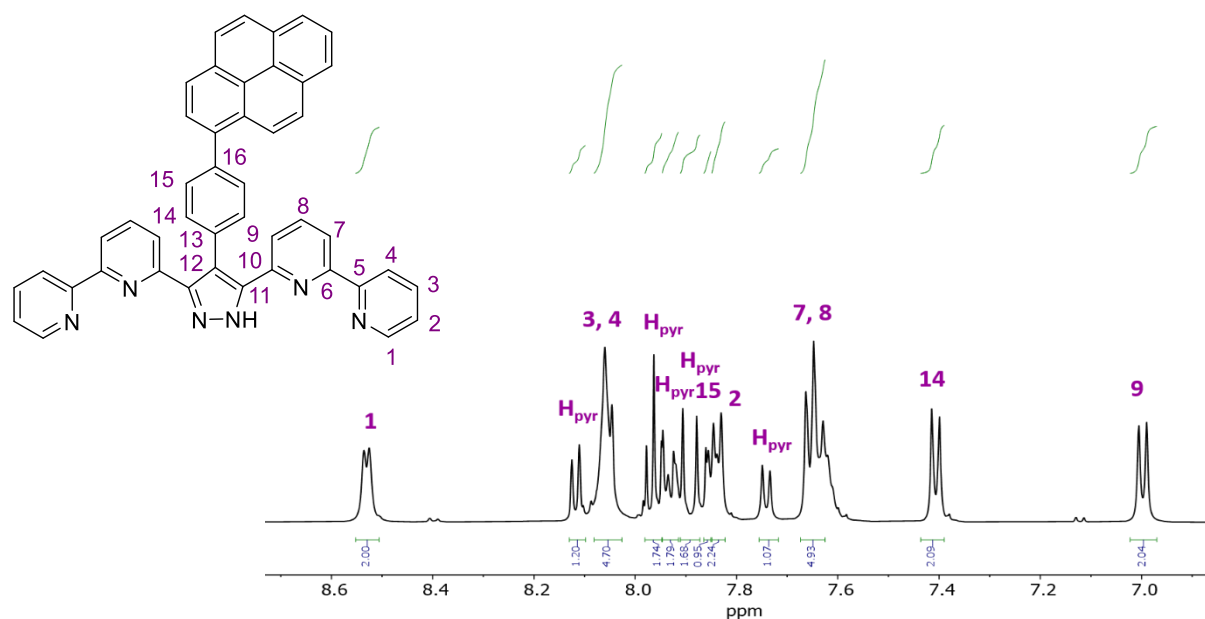
Figure 3.1. ^{1}H NMR spectrum of ^{pyr}**bbpH** measured in methanol-d_4; the aromatic section is shown.

3.3 Synthesis of the bbp-Ru₂ Complexes Equipped with Peripheral Pyrene Groups

The complex containing multiple pyrenes at the axial ligand position was first developed by Dr. Jann Odrobina[150] following multi-step procedures adapted from the literature.[53,62,97] A dilute solution of the **Me bbpH** ligand in EtOH was added slowly to a concentrated solution of RuCl₂(dmso)₄ and NEt₃ in degassed EtOH to yield the intermediate [(Me bbp)Ru₂Cl₃(dmso)₂(H₂O)].[62] Without further isolation, the complex was treated with five equiv. of the pyrene modified pyridine and NaOAc followed by anion exchange with NH₄PF₆ to produce the acetate bridged **1^4pyr**. No further modifications in the synthetic protocol were needed due to introducing the pyrene groups at a late stage of the synthesis. Complex **1^4pyr** was fully characterized by 1D and 2D NMR spectroscopy, ESI-MS, electrochemistry in solution and UV/vis spectroscopy. The structure of the complex was also confirmed by single crystal X-ray diffraction.[150] **1^pyr** was also synthesized via a general procedure established for **Me bbp-Ru₂(OAc)** (Scheme 3.2).[53,97]


1. RuCl₂(dmso)₄
   NEt₃, EtOH
2. py^pyrene, EtOH
3. NaOAc, acetone/water
   NH₄PF₆

Me bbpH
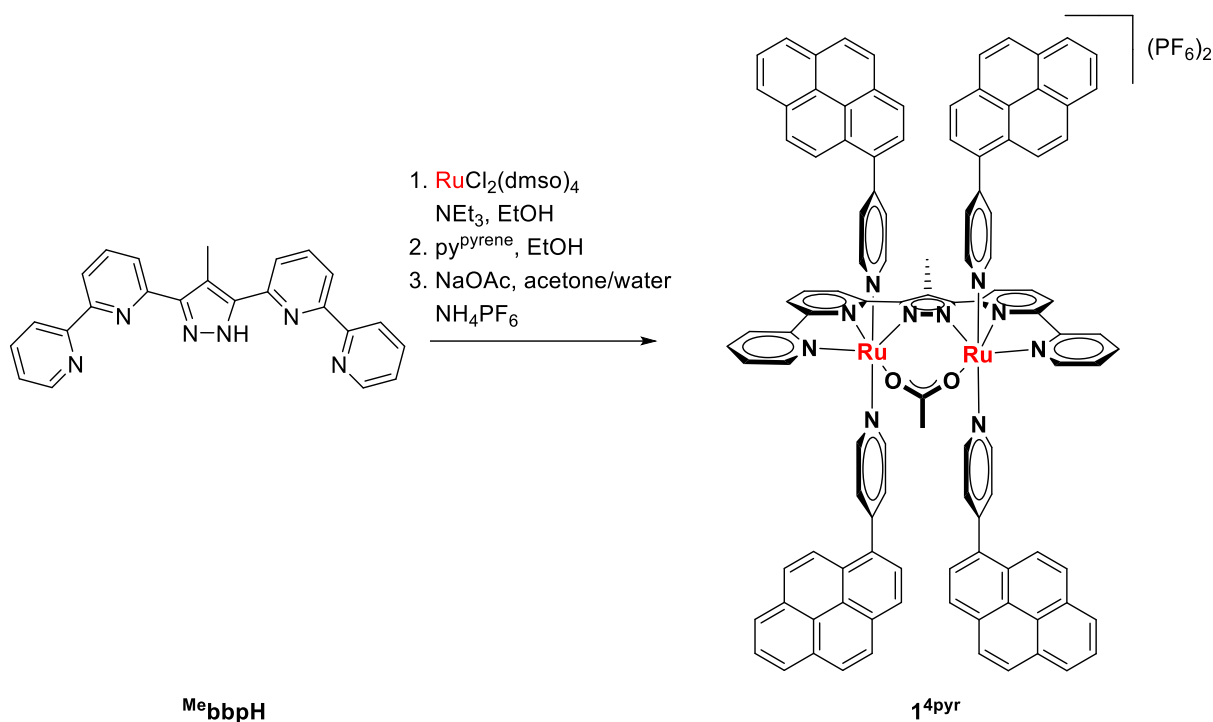
1^4pyr

Scheme 3.2. Synthetic route for the preparation of **1⁴ᵖʸʳ** and**1ᵖʸʳ**.[145,150]

1D and 2D NMR (^{1}H and ^{13}C), UV/vis spectroscopy as well as electrochemistry, and ESI mass spectrometry were conducted to characterize **1ᵖʸʳ**. The ESI(+)-MS of a methanol solution of **1ᵖʸʳ** shows a signal at m/z = 615.1 corresponding to the $[M-PF_6]^{2+}$ ion (Figure A73). All resonances of the bbp⁻ ligand backbone in the ^{1}H NMR spectrum are similar to the parent complex **ᴹᵉbbp-Ru₂(OAc)**.[62] The characteristic singlet at 3.04 ppm corresponds to the methyl group of the acetate bridge and the signal at very low field is assigned to H-1 with the help of ^{1}H–^{1}H-COSY. The symmetry of the complex is concluded from the number of signals in the aromatic region. The ratio of the integrals of the **ᵖʸʳbbp⁻** and axially coordinated pyridines portrays a C_{2v} symmetric complex on the NMR timescale (Figure 3.2).
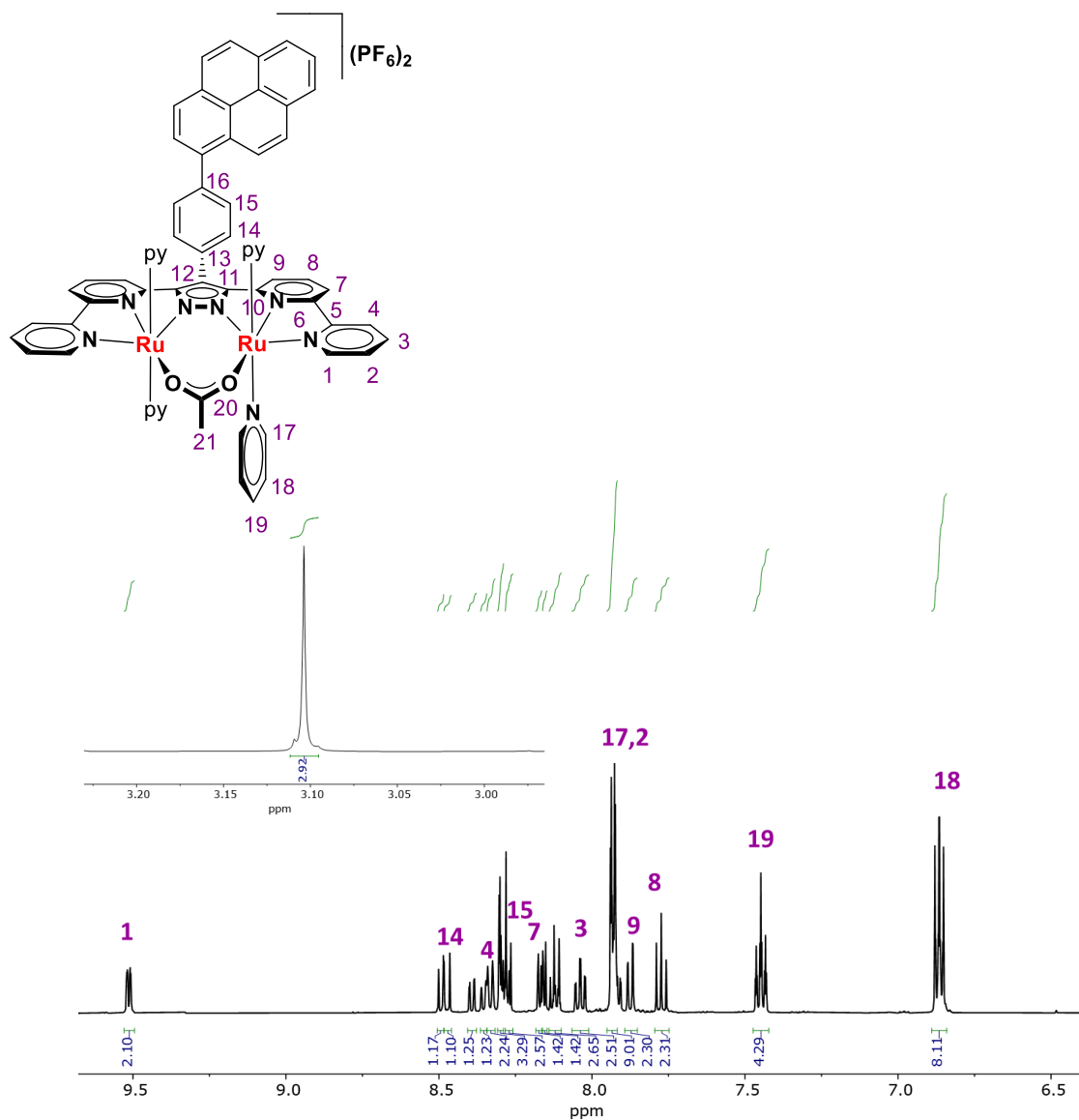
Figure 3.2. ^{1}H NMR spectrum of **1**[pyr] in acetone-d_6. The inset depicts the signal of the acetate bridge.

Single crystal suitable for X-ray diffraction analysis was obtained by slow diffusion of diethyl ether into a solution of the complex in acetone. Two molecules with similar metric parameters were observed in the asymmetric unit. Each ruthenium is coordinated to five nitrogen atoms and one oxygen atom arising from the two axial pyridines, tridentate pocket of the [pyr]**bbp**[-] and acetate bridge in an octahedral environment (Figure 3.3). The two ruthenium ions, acetate bridge, and the pyrazolato unit are almost located in one plane, which can be reflected in the small angle between the planes defined by the pyrazole ring and the acetate (3.55°/7.27°). The phenyl group coordinated to the pyrazolate-C⁴ forms an angle of 55.3°/58° with the pyrazole core. Selected bond lengths and distances are shown in Table A2 (see Appendix).
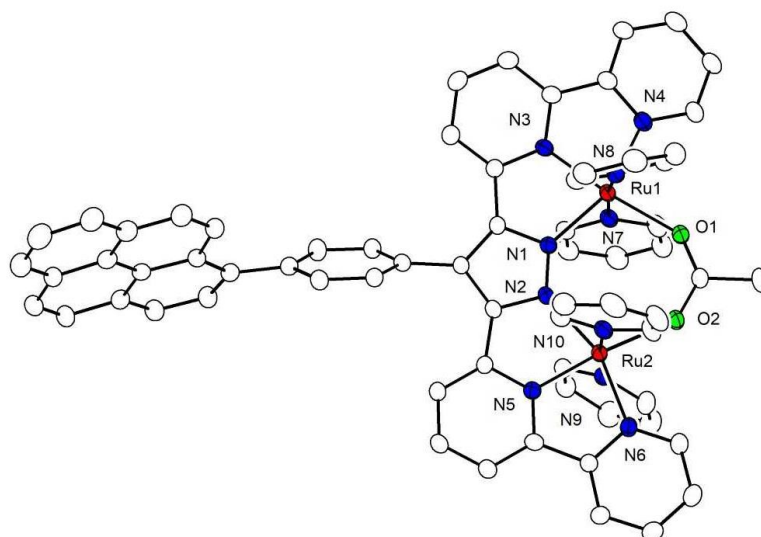
Figure 3.3. Molecular structure of the cation of **1^{pyr}** obtained by XRD. Hydrogen atoms, counterions, and solvent molecules have been omitted for clarity.

3.4 Electrochemical Investigations in Solution

The redox properties of **1^{pyr}** were investigated using cyclic voltammetry (CV) and square wave voltammetry (SWV) in propylene carbonate (0.1 M, NBu$_4$PF$_6$). Cyclic voltammetry of **1^{pyr}** exhibits two sequential reversible oxidative waves corresponding to the Ru^{II}Ru^{II}/Ru^{II}Ru^{III} and Ru^{II}Ru^{III}/Ru^{III}Ru^{III} couples. The presence of the redox processes was further confirmed by SWV (see inset Figure 3.4). Moreover, CV experiments were conducted at different scan rates (20, 50, 100, 200 mV/s) confirming the reversibility of the two redox events (Figure A81). The peak separation ($\Delta E_{1/2}$) is around 400 mV which is very similar to the values reported for the parent complex **^{Me}bbp-Ru$_2$(OAc)**.[53,97,114,115] Comparison of the half-wave potentials ($E_{1/2}$) of **1^{pyr}** with other bbp-based ruthenium complexes reveals that the pyrene anchoring groups do not drastically influence the electronic properties of the ruthenium ions. The redox potentials of **1^{pyr}** as well as other related complexes are tabulated in Table 3.1.
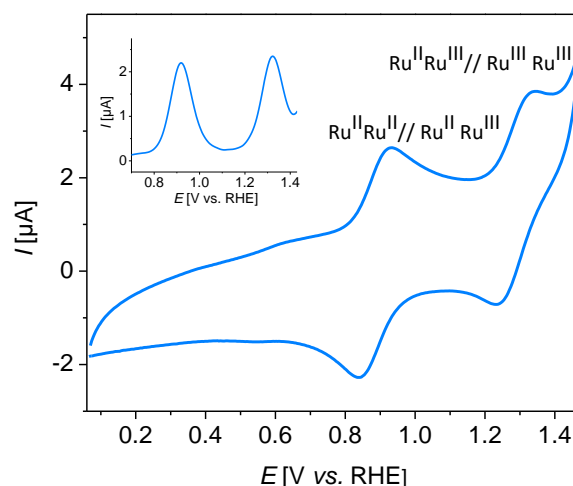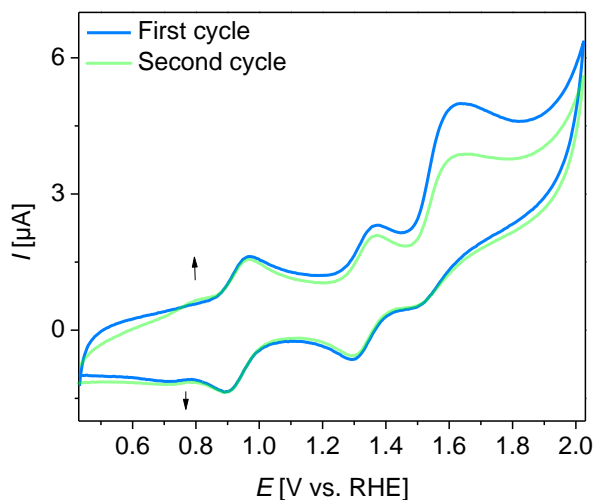
Figure 3.4. Cyclic voltammetry of **1^{pyr}** in PC with NBu₄PF₆ as conducting salt at a scan rate of 50 mV/s WE: GC, CE: Pt, Ref. Ag wire. Final potentials are converted to RHE scale. Inset depicts the square wave voltammetry between 0.7-1.4 V.

Table 3.1. Half wave potential ($E_{1/2}$) and peak separation ($\Delta E_{1/2}$) for bbp-based ruthenium complexes.

Complex	$E_{1/2}$ [V *vs.* RHE] (mV)		$\Delta E_{1/2}$ (mV)	Ref
	Ru^{II}Ru^{II}/Ru^{II}Ru^{III}	Ru^{II}Ru^{III}/Ru^{III}Ru^{III}		
^{H}bbp-Ru$_2$(OAc)	0.91	1.3	390	53,97
^{Me}bbp-Ru$_2$(OAc)	0.88	1.28	400	53,97
^{COOH}bbp-Ru$_2$(OAc)	0.90	1.3	400	115
^{POOOH}bbp-Ru$_2$(OAc)	0.89	1.25	360	114
1^{4pyr}	0.86	1.26	400	150
1^{pyr}	0.87	1.28	410	this work

A third oxidative wave appeared after scanning to higher potentials beyond 1.4 V vs.RHE with irreversible behavior (Figure 3.5). This redox process was also observed in the CV of **^{pyr}bbpH** and is assigned to the oxidation of the pyrene (Figure A82). Shao-Horn and co-workers proposed that the polymerization of pyrene derivatives can take place upon electrochemical oxidation.[151] The second cycle shows a very small peak at 0.8 V vs.RHE that is likely due to a species generated upon oxidation of the pyrene unit at high potential.

Figure 3.5. Cyclic voltammetry of **1^{pyr}** in PC (0.1 M NBu$_4$PF$_6$) at a scan rate of 50 mV/s in the range of 0.4-2 V *vs.* RHE.

UV/vis SEC experiments were conducted in propylene carbonate solution of **1^{4pyr}** and **1^{pyr}** to get more insight into the chemical reversibility of the first redox process (Ru^{II}Ru^{II}/Ru^{II}Ru^{III}). A UV/vis spectrum of the Ru^{II}Ru^{II} complex was recorded before applying the potential. Then, the potential was increased to 1.1 V for **1^{4pyr}** and 1.0 V for **1^{pyr}**, followed by re-reduction to the initial species at 0.7 V and 0.6 V for **1^{4pyr}** and **1^{pyr}**, subsequently.

For both complexes, the majority of the bands below 400 nm are ligand based and they remain unchanged upon oxidation. A broad band at 470 nm for **1^{4pyr}** and 400 nm for **1^{pyr}** disappears after oxidation to the Ru^{II}Ru^{III} species (Figure 3.6). The UV/vis spectrum before oxidation is fully superimposed with the spectrum after re-reduction confirming the chemical reversibility of the first redox process.
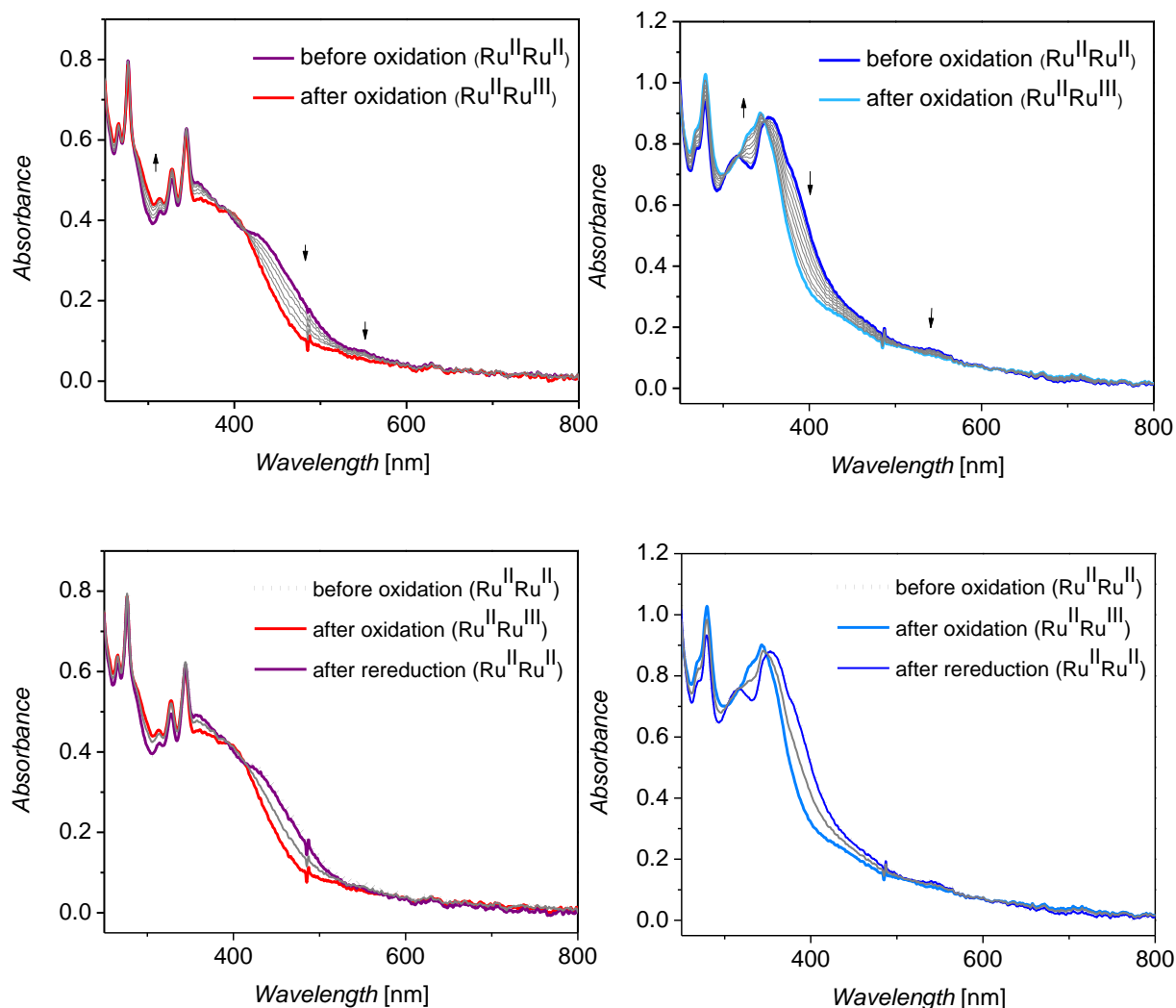
Figure 3.6. UV/vis spectroelectrochemistry (UV/vis SEC) in propylene carbonate (0.1 M NBu$_4$PF$_6$) . Electrochemical oxidation from Ru^{II}Ru^{II}→Ru^{II}Ru^{III} at 1.1 V for **1^{4pyr}** (top-left) and 1.0 V for **1^{pyr}** (top-right) followed by re-reduction from Ru^{II}Ru^{III}→Ru^{II}Ru^{II} at 0.7 V for **1^{4pyr}** (Bottom-Left) and at 0.6 V for **1^{pyr}** (Bottom-right). All potential are reported versus RHE. WE: platinum net, CE: Platinum wire and Ref: MSE.

3.5 Immobilization of the Modified bbp-Ru₂ Complexes on MWNCTs

### 3.5.1 Preparation and Characterization of the GC|MWCNT Electrodes Decorated with Complexes

Molecular complexes **1^{4pyr}** and **1^{pyr}** were immobilized on electronically conducting MWCNTs using pyrene anchoring groups. A suspension of MWCNTs in THF (1 mg in 1 ml) was drop-casted (2.5 µl × 10) on a clean glassy carbon electrode to get uniform coverage. To absorb the catalyst on the surface, the modified electrodes were dipped in a 1 mM solution containing

the respective complex in methanol for 24 h. Then, the electrodes were rinsed with water and methanol to remove the unanchored complexes from the surface. The obtained GC|MWCNT|$\mathbf{1^{4pyr}}$ and GC|MWCNT|$\mathbf{1^{pyr}}$ were considered as hybrid working electrodes and their electrochemical properties were investigated in an aqueous HOTf (0.1 M, pH = 1) using a three-electrodes-setup.

To prove that the complexes were successfully attached to the MWCNTs, the cyclic voltammetry measurements were conducted in aqueous HOTf (0.1 M, pH = 1) below the oxygen evolution onset (Figure 3.7). The first intense peak around $E_{1/2}$ = 0.57 V was also observed for the free-metal ligand (GC|MWCNT|$\mathbf{^{pyr}bbpH}$) under identical conditions (Figure 3.8), and therefore, it was assigned to the redox event of the pyrene anchor. Recent studies revealed that the pyrene anchored on MWCNT-modified gold electrodes forms highly active surface-bound quinone derivatives upon electrochemical oxidation.[152] Interestingly, the first cycle of GC|MWCNT|$\mathbf{1^{4pyr}}$ and GC|MWCNT|$\mathbf{1^{pyr}}$ shows no anodic peak at $E_{1/2}$ = 0.57 V. Instead, a huge current was detected above 1.2 V vs. RHE corresponding to the two-electron oxidation of the pyrene to redox-active pyrenequinone.[152] It also turned out that the oxidation of the pyrene occurs at a lower potential after immobilization on MWCNTs. This significant shift was attributed to the interactions of the pyrene groups with carbonaceous surfaces.
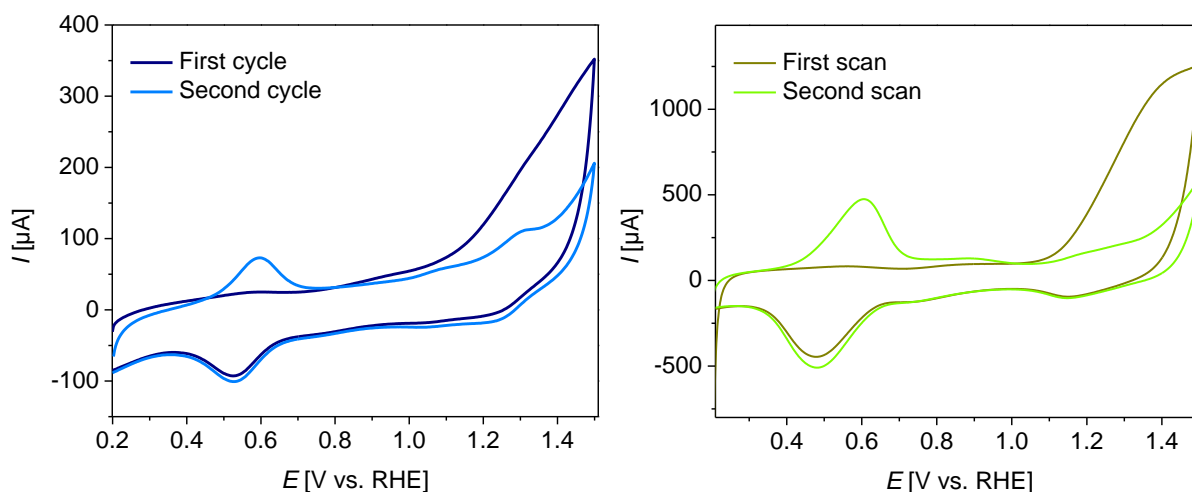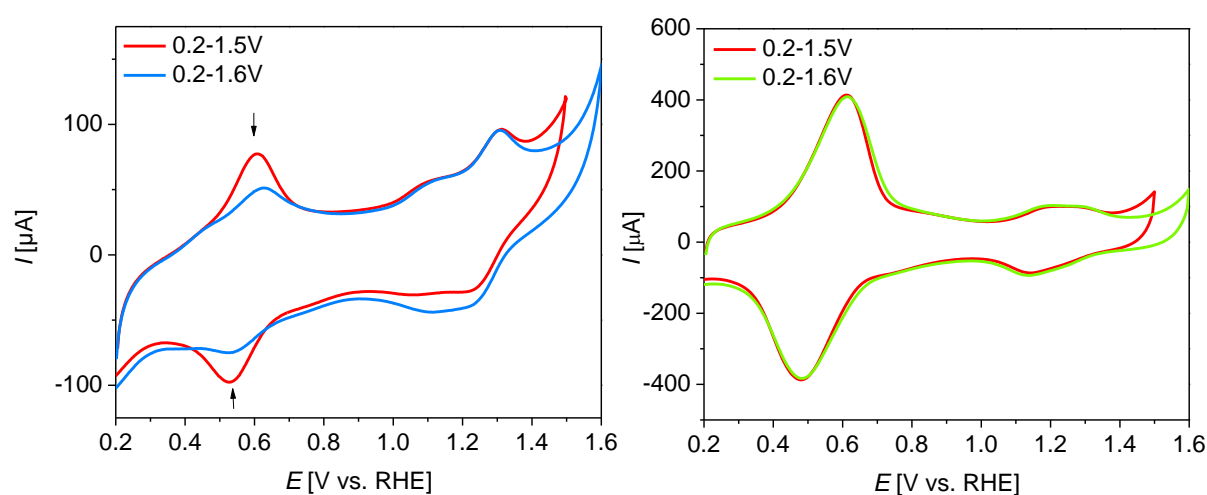

Figure 3.7. Cyclic voltammetry of GC|MWCNT|$\mathbf{1^{pyr}}$ (left) and GC|MWCNT|$\mathbf{1^{4pyr}}$ (right) hybrid electrode, depicting the first and second scan in an aqueous HOTf (0.1 M, pH = 1) at a scan rate of 50 mV/s. CE: Pt, Ref. MSE. All potentials are referenced versus RHE.
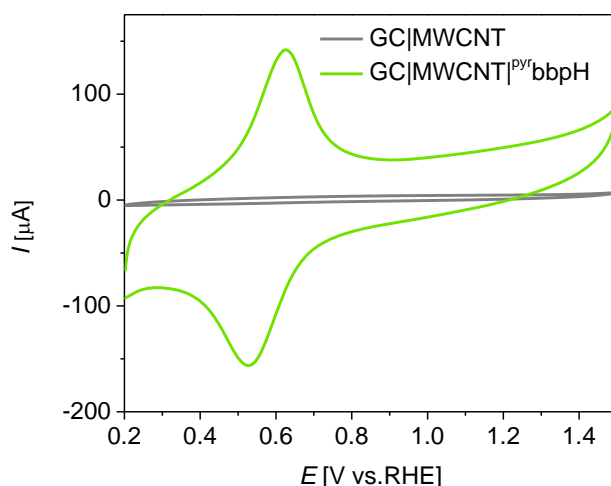
Figure 3.8. Cyclic voltammetry of the GC|MWCNT| ^{pyr}**bbpH** implemented as working electrode under similar conditions (green). GC|MWCNT background is shown in grey.

For GC|MWCNT|**1^{pyr}**, the intensity of the first wave was considerably reduced after scanning to the potential above 1.5 V, due to several side reactions which can have a negative effect on the reversibility of the redox process.[152,153] This phenomenon was not observed in the case of GC|MWCNT|**1^{4pyr}**, but the reason for this different behavior is not clear. Two further redox processes observed at $E_{1/2}$ = 1.13 and 1.27 V *vs.* RHE for GC|MWCNT|**1^{4pyr}** and $E_{1/2}$ = 1.06 and 1.26 V *vs.* RHE for GC|MWCNT|**1^{pyr}** are assigned to the sequential one-electron oxidation from Ru^{II}Ru^{II} to Ru^{II}Ru^{III} and Ru^{III}Ru^{III}, subsequently (Figure 3.9).

Figure 3.9. Cyclic voltammetry of GC|MWCNT|**1^{pyr}** (left) and GC|MWCNT|**1^{4pyr}** (right) for second scan (from 0.2 to 1.5, and 0.2 to 1.6 V) in aqueous HOTf (0.1 M, pH = 1). The measurement was recorded at a scan rate of 50 mV/s. CE: Pt, Ref. MSE. The potentials are referenced versus RHE.

3.5.2 Characterization of Hybrid Electrodes with HRTEM and EELS Spectroscopy

High-resolution transmission electron microscopy and electron energy loss spectroscopy measurements, as well as data analysis in the course of this project, were carried out by Gaurav Lole. High-resolution transmission and scanning electron microscopy (HRTEM and STEM) were applied to gain insights into the structural integrity of the MWCNTs after the immobilization process. A suspension of MWCNTs in THF (1 mg in 1 mL) was drop-casted on a TEM grid to obtain a uniform surface coverage. One grid was soaked in a methanol solution containing the complex (0.1 M) overnight to accomplish the absorption of the catalyst to the surface. HRTEM images of MWCNTs before and after complex immobilization are displayed in Figure 3.10. The average spacing between the two walls is 0.36 nm in the pristine sample and negligibly changes (0.37 nm) after attachment of 1^{pyr} to the surface. This result reflected the fact that immobilization via π-π interactions and non-covalent adsorption of the organic compounds on carbon surfaces does not influence the structural features of the MWCNTs.[154] TEM images exhibit a bunch of MWCNTs with lengths in the order of μm and diameters in the range of 20–30 nm (Figure 3.11). Inconsiderable crooked walls in some areas were also observed for the surface-bound 1^{pyr}. The inset in Figure 3.11 demonstrates the STEM images of the MWCNTs before and after loading the complex. MWCNTs|1^{pyr} shows a slightly higher and sharper contrast compared to the pristine sample.
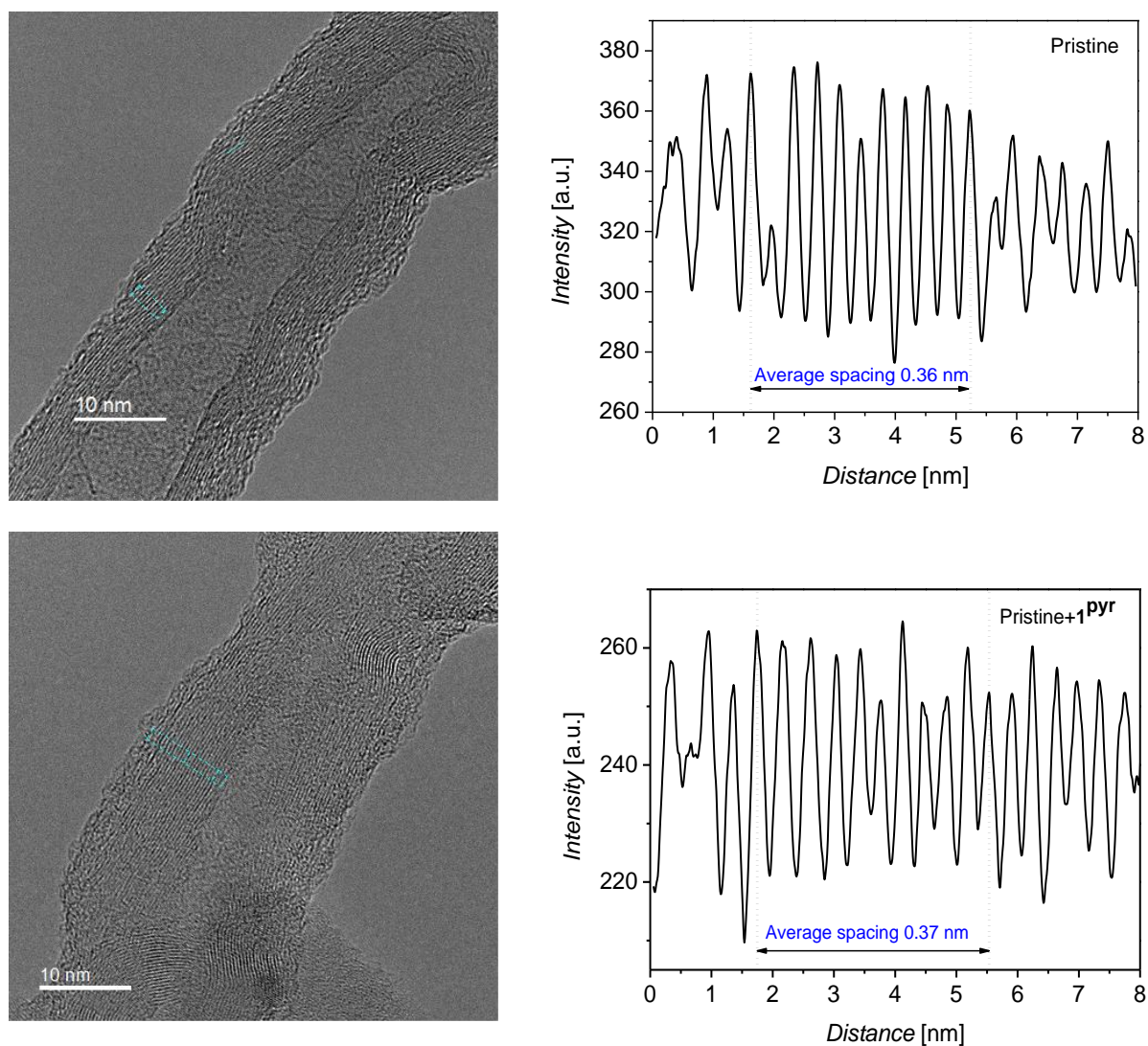
Figure 3.10. High-resolution transmission electron microscopy (HRTEM) of MWCNTs before (top) and after immobilization of complex **1^{pyr}** (bottom). The average spacing between walls was obtained in the designated area of the image. Both TEM grids are prepared under the same conditions.
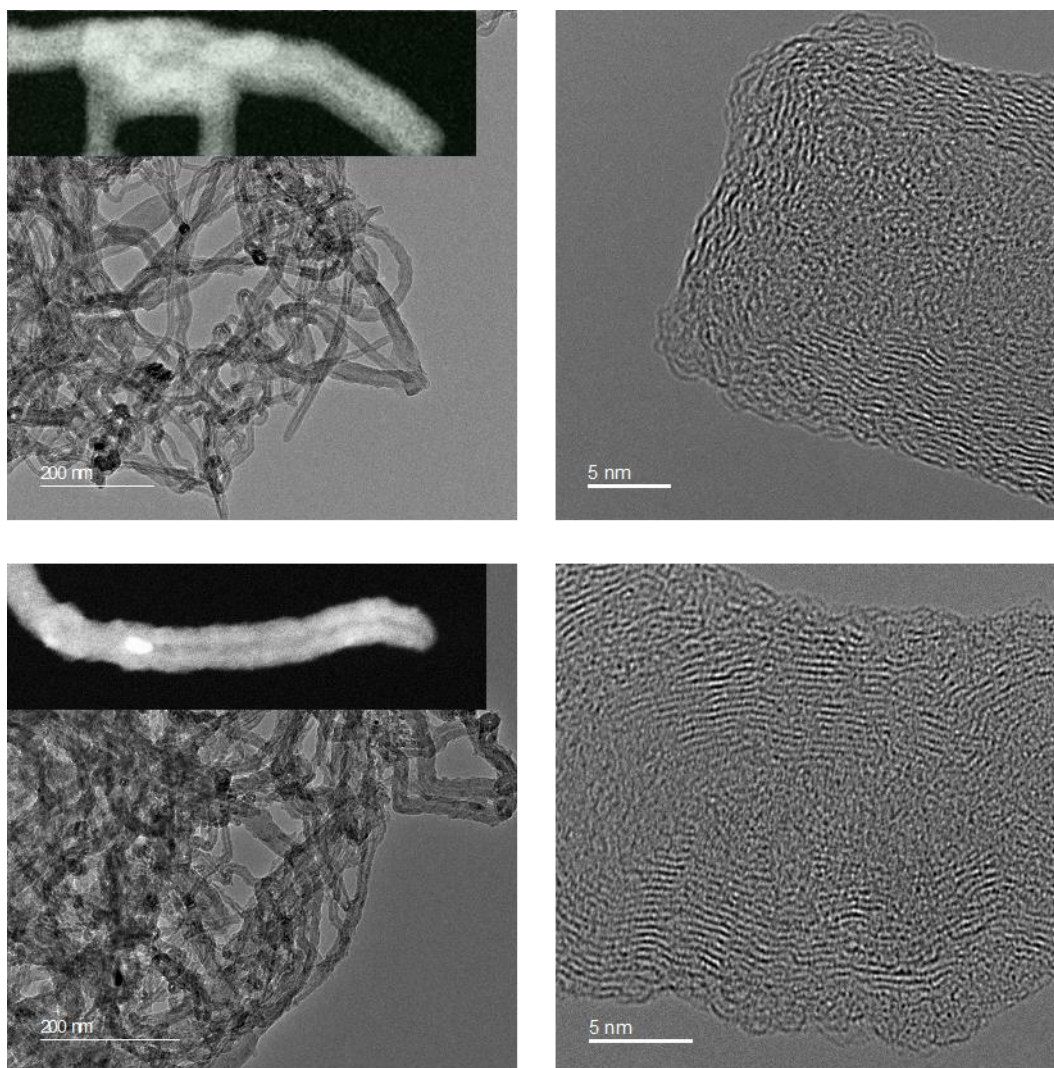
Figure 3.11. TEM images of MWCNTs before (top) and after immobilization of catalyst **1^pyr** (bottom). High angle annular dark field scanning electron microscopy (STEM) images for both samples are shown in the inset with slightly enhanced contrast and sharper surfaces for sample after immobilization.

Electron energy loss spectroscopy (EELS) was performed for the electronic characterization of the MWCNTs surface. The spectrum after loading **1^pyr** shows a Ru M edge peak at E = 483 eV above the noise level of ±3σ (σ is the standard deviation), and a weak O K edge at E = 530 eV (Figure 3.12). The latter one appeared only after complex immobilization indicating the presence of some O-containing species on the surface which can be formed due to using methanol as a solvent for the preparation of the electrode. The plain MWCNTs used in this work with I(π*)/I(300 eV) = 0.56 show an estimate of sp² bonding ratio of about 75%. The core loss spectra at the C K edge exhibit a characteristic signature for mixed sp²/sp³ hybridized carbon atoms. The presence of the sp² contribution can be further confirmed by the excitation into the antibonding state (π*) at an energy loss of 293 eV.[155–157] Upon immobilization of the

pyrbbpH and **1pyr** to the MWCNTs, the weight of π−π* transition was enhanced to 85%. The obtained value is in good agreement with the bending radius of the carbon nanotubes.[154] However, momentum transfer calculations are required for precise quantification, which is out of the scope of this project.
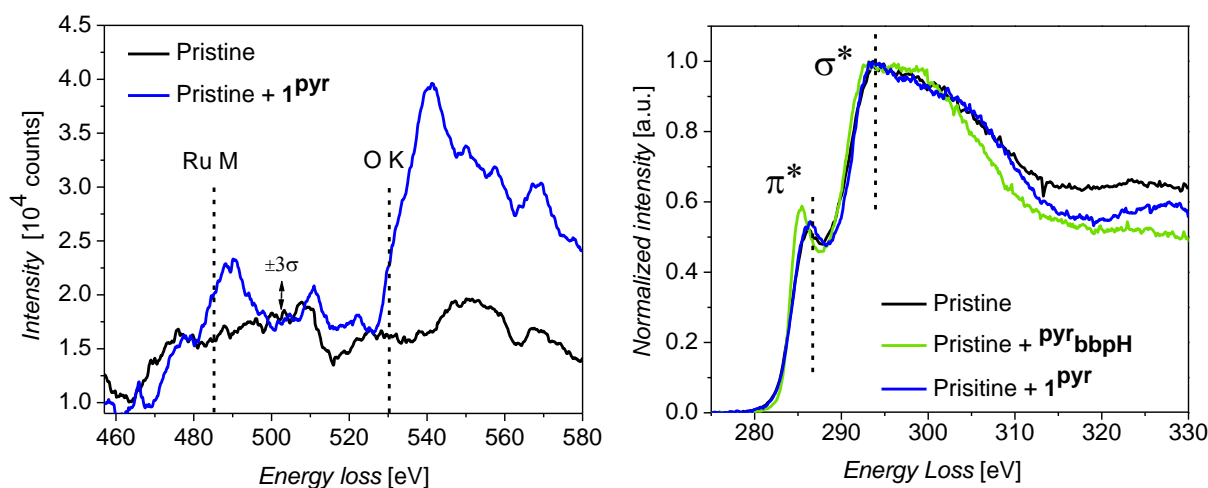
Figure 3.12. Electron energy loss spectra of plain MWCNTs, MWCNT|**pyrbbpH**, and MWCNT|**1pyr** exhibit a Ru M edge and a weak O K edge peak after immobilization of the complex (left). Core loss spectrum at the C K edge (right).

The presence of unoccupied π* states was verified by low loss electron spectroscopy. The spectrum depicts a π → π* transition band at energy loss around 6 eV and a typical valence plasmon band of carbon π and σ states at E = 24 eV (Figure 3.13). The band intensity at E = 6 eV was increased after immobilization of the **pyrbbpH** and subsequently **1pyr** to the surface, which is attributed to the π → π* excitations within the complex. It seems that the π and π* states are responsible for charge transfer between the anchored complex and MWCNTs due to their vicinity to the Fermi energy.[158] Moreover, the absence of any plasmon excitation at E =10 eV exclude the possibility of partial oxidation of the MWCNTs during the immobilization process.[159]
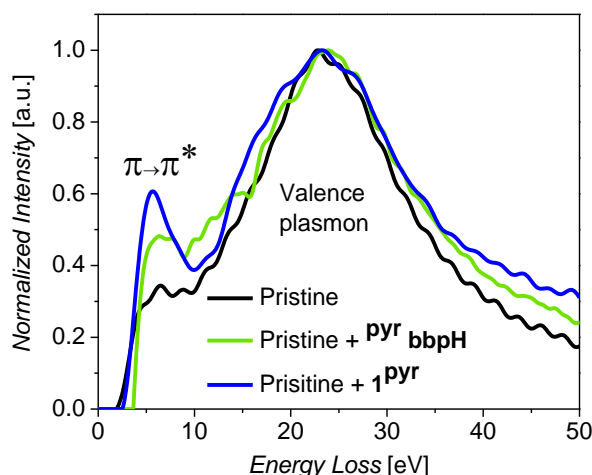
**Figure 3.13.** Low loss plasmon spectra showing the increased weight of π−π* transitions upon immobilization.

3.6 Investigation of the Stability and Catalytic Activity of the Hybrids with RRDE Experiments

To evaluate the stability and water oxidation capability of the resulting hybrids, rotating ring disk electrode measurements (RRDE) were conducted below and above the onset of OER. This method offers deeper insight into the correlation between the electrochemical behavior of the disk electrode and formed products probed at the ring electrode. During the experiment, the generated species are transferred to the ring by forced convection and reduced there under mass-limiting conditions. In addition, the current at the ring provides information about side reactions limiting the efficiency of the oxygen evolution reaction.[160] All RRDE experiments in course of this work were performed in close cooperation with Dr. Fatemeh Ebrahimi.

The working disk electrodes were prepared by drop-casting of MWCNTs on a glassy carbon surface following a similar procedure as described in section 3.5.1. Next, the electrodes were soaked in a methanol solution containing the respective complex to enable the absorption process. The measurements were carried out in an acidic electrolyte (0.1 M aqueous HOTf, pH = 1) and the entire cell was rotated with rotation rate ω to enforce the transportation. Applying an appropriate potential is necessary to drive the ORR at the ring electrode. To determine this potential, a sweep voltammetry measurement of the platinum ring was conducted first in argon saturated and then in oxygen saturated aqueous HOTf (0.1 M, pH = 1) at various rotation speeds (Figure 3.14). It turned out that a potential of 0.15 V *vs*. RHE should apply to the ring electrode to enable the O$_2$ detection under diffusion limited

conditions. All potentials are corrected after subtracting the electrolyte resistance and converted to RHE.
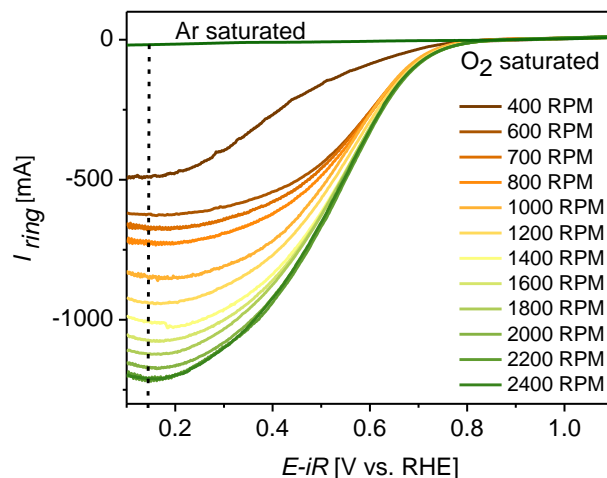
Figure 3.14. Sweep voltammetry measurement of platinum ring electrode under O_2 saturation in an aqueous HOTf (0.1 M, pH = 1) to determine the oxygen reduction potential.

An anodic scan of GC|MWCNTs|1^{pyr} and GC|MWCNTs|1^{4pyr} was recorded in aqueous HOTf (0.1 M, pH = 1) by scanning the disk electrode at 50 mV/s and ω = 1600 rpm. The background currents were obtained by measuring the GC|MWCNTs disk devoid of any catalysts under identical conditions. Before each experiment, the electrolyte was degassed with high purity argon gas for 30 min to deplete the oxygen. The CV of GC|MWCNTs|1^{pyr} exhibits a redox process at $E_{1/2}$ = 0.57 V corresponding to oxidation of the pyrene anchor followed by two sequential one-electron processes corresponding to the $Ru^{II}Ru^{II}/Ru^{II}Ru^{III}$ and $Ru^{II}Ru^{III}/Ru^{III}Ru^{III}$ couples (Figure 3.15). At the onset potential of OER (1.55 V *vs*. RHE), a significant ring current was observed in the case of GC|MWCNTs|1^{pyr}, which originated from the reduction of O_2 that has been produced via catalytic water oxidation by the immobilized complex at the disk electrode. The absence of this current for a background measurement above the onset potential cautions the ability of the anchored catalyst to mediate the water oxidation catalysis.

The inset in Figure 3.15 portrays the slope at the disk and the ring electrodes above the potential of 1.45 V *vs*. RHE. Comparison of these slopes at the catalytic region provides information about the *Faradaic* efficiency without calculating the collection efficiency.[160] Identical *Tafel* slopes between 1.68 and 1.75 V *vs.* RHE reflect the high proficiency of the catalyst at the disk and exclude the formation of other side products during the reactive conditions.
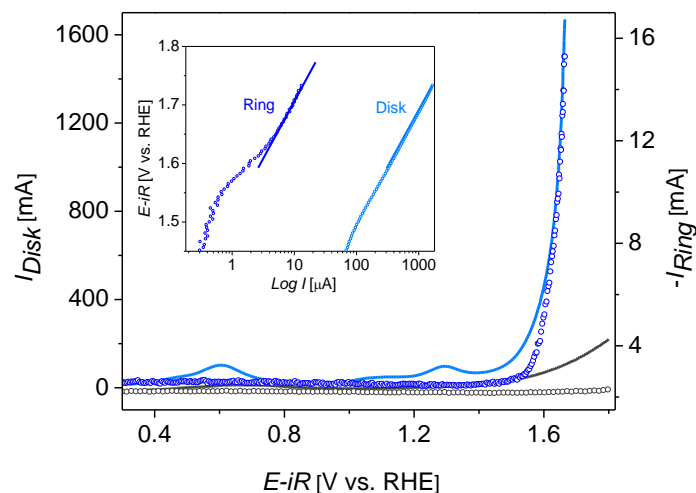
Figure 3.15. Anodic scan of RRDE cyclic voltammetry measurement of the GC|MWCNTs|**1**^{pyr} in an aqueous HOTf (0.1 M, pH = 1) at a scan rate of 50 mV/s and ω = 1600 rpm under inert conditions. The solid blue line corresponds to the disk current while the blue dots represent the platinum ring current for the ORR. The background measurement was performed under the same conditions but devoid of any catalysts. The grey solid line represents the GC|MWCNTs hybrid disk current and the grey dots display the observed current on the ring electrode. The inset depicts the *Tafel* slope of both disk and ring currents at E_{ring} = 0.15 V *vs.* RHE. A platinum wire was used as a counter electrode and MSE as a reference electrode which is later converted to RHE. The bias potentials were corrected after applying the uncompensated resistance (*iR*).

The RRDE-CV measurement of GC|MWCNTs|**1**^{4pyr} was conducted under identical conditions (pH = 1) to evaluate the activity and stability of the catalyst. Three redox waves were observed at $E_{1/2}$ = 0.57 V, $E_{1/2}$ = 1.15 and $E_{1/2}$ = 1.28 V vs. RHE, which were assigned to the oxidation of the pyrene and Ru^{II}Ru^{II}/Ru^{II}Ru^{III} and Ru^{II}Ru^{III}/Ru^{III}Ru^{III} couples, respectively (Figure 3.16). At an onset potential of 1.55 V vs. RHE, currents increased simultaneously at both electrodes, which is attributed to OER at the disk and ORR at the ring electrodes. The inset depicts the *Tafel* plots of both disk and ring currents within the same potential range as previously shown for GC|MWCNTs|**1**^{pyr} (from 1.68 to 1.75 V *vs.* RHE). Notably, the *Tafel* plot analysis displays that the ring current reaches 1 µA at 1.64 V for GC|MWCNTs|**1**^{4pyr} and at 1.57 V for GC|MWCNTs|**1**^{pyr}. Shifting to lower potentials suggests a higher catalytic activity for the complex anchored via the pyrazolate backbone in **1**^{pyr}.
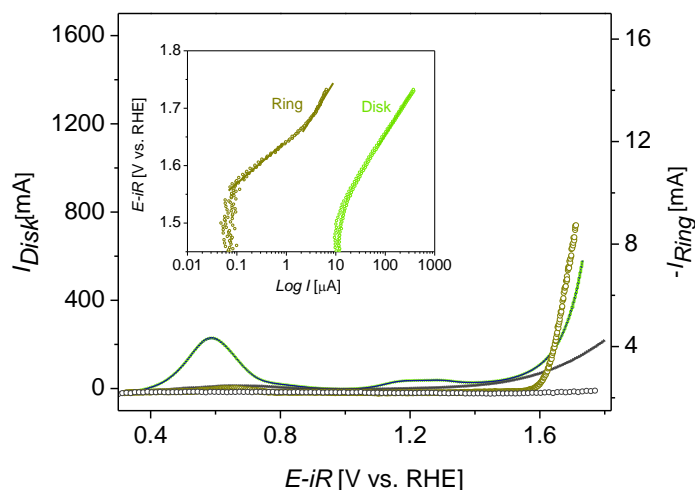
Figure 3.16. RRDE-CV measurement of hybrid GC|MWCNTs|**1^{4pyr}** (green solid line) and background (dark grey solid line). Dots show the current observed at the ring electrode (olive: containing molecular catalyst, grey: background). The analysis of disk and ring currents for the determination of the *Tafel* slopes at E_{ring} = 0.15 V vs. RHE is shown in the inset. The measurement was recorded in an aqueous HOTf (0.1 M, pH = 1) at a scan rate of 50 mV/s and ω = 1600 rpm under inert conditions. CE: Pt, Ref. MSE. The final potentials are referenced versus RHE.

For both hybrids, the number of adsorbed catalysts on MWCNTs can be approximately determined by integration of the Ru^{II}Ru^{II}/Ru^{II}Ru^{III} redox peak in the CV experiments. The RRDE-CV measurements normalized to the amount of catalyst are depicted in Figure 3.17. The GC|MWCNTs|**1^{pyr}** shows a higher anodic current compared to GC|MWCNTs|**1^{4pyr}** above the OER onset. This difference in reactivity may possibly originate from the more efficient exposure of the bimetallic cleft of the ruthenium core on the surface if the pyrene group is attached to the backside pyrazole C^4-position.
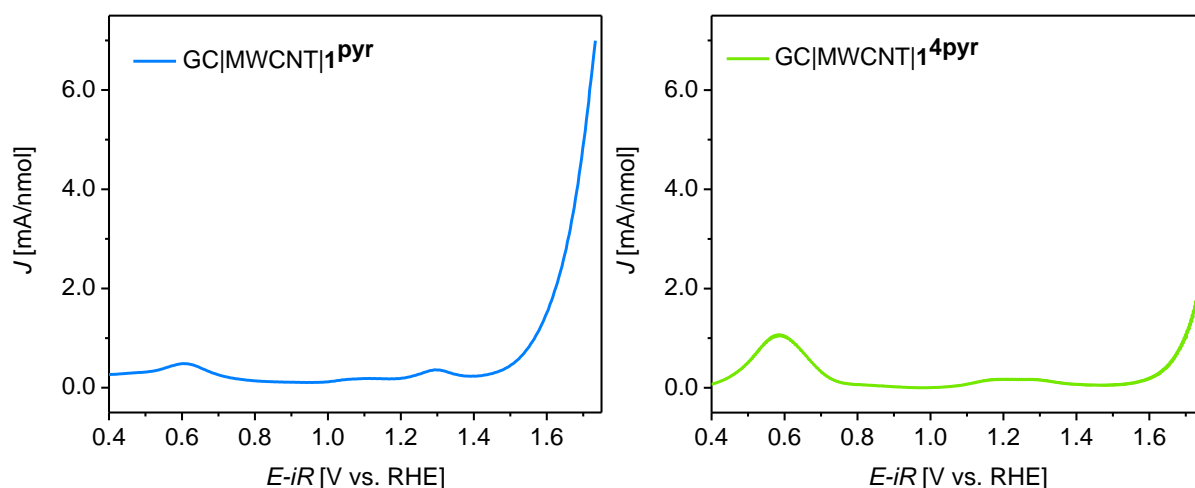
Figure 3.17. Normalized anodic scan of RRDE measurement of GC|MWCNTs|**1^{pyr}** (left) and GC|MWCNTs|**1^{4pyr}** WE (right). The currents are plotted after background subtraction. The measurements were carried out in an aqueous HOTf (0.1 M, pH = 1) at a scan rate of 50 mV/s and ω = 1600 rpm. CE: Pt, Ref. MSE.

To compare the stability and activity of the modified immobilized complexes, chronoamperometry of the hybrid electrodes in aqueous HOTf (0.1 M, pH = 1) was performed at different potentials starting from 1.5 V *vs*. RHE for 60 s. Then, the potential applied to the disk was enhanced by 50 mV until reaching the catalysis regime. Higher disk currents were obtained upon increasing the disk potential during every CA experiment, but with a different profile for each hybrid. For GC|MWCNTs|**1^{pyr}** both currents started decreasing even after 15s (dropped by 22% between 20-60 s) (Figure 3.18). This effect can be explained by gradual leaching of the catalyst from the disk electrode and loss of the surface coverage over the time scale of the experiment. GC|MWCNTs|**1^{4pyr}** revealed significant disk and ring currents at a potential above 1.75 V *vs.* RHE, which may be attributed to either a change in the O-O bond formation mechanism or enhanced mobility of the surface-bound catalyst that results in a better exposure of the active site of the ruthenium cores.[127] In addition, both currents remained stable at 600 μA during the 60 s CA experiment (Figure 3.19). It also can be observed that for both systems, the ring current followed the current at the disk, supporting the fact that disk current is dominated by OER and other side reactions do not provide any contributions at this potential (see Figure 3.18 and 3.19-right).
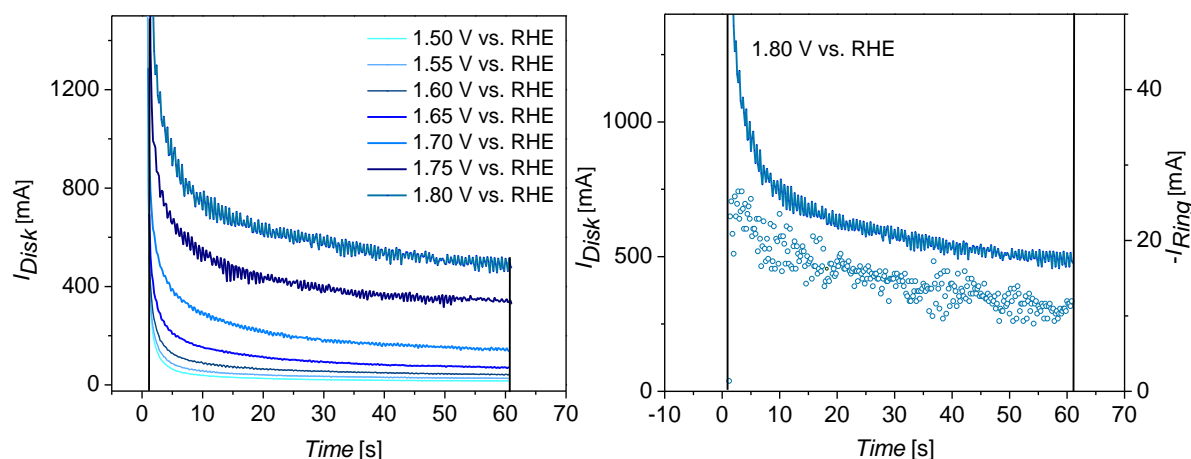
Figure 3.18. Chronoamperometry measurement of GC|MWCNTs|$\mathbf{1^{pyr}}$ at various potentials for 60 s in an aqueous HOTf (0.1 M, pH = 1) (left). The bipotential CA at E_{disk} = 1.8 V vs. RHE with corresponding ring current (blue dots) (right). ω = 1600 rpm. CE: Pt, Ref. MSE. The potentials are referenced versus RHE.
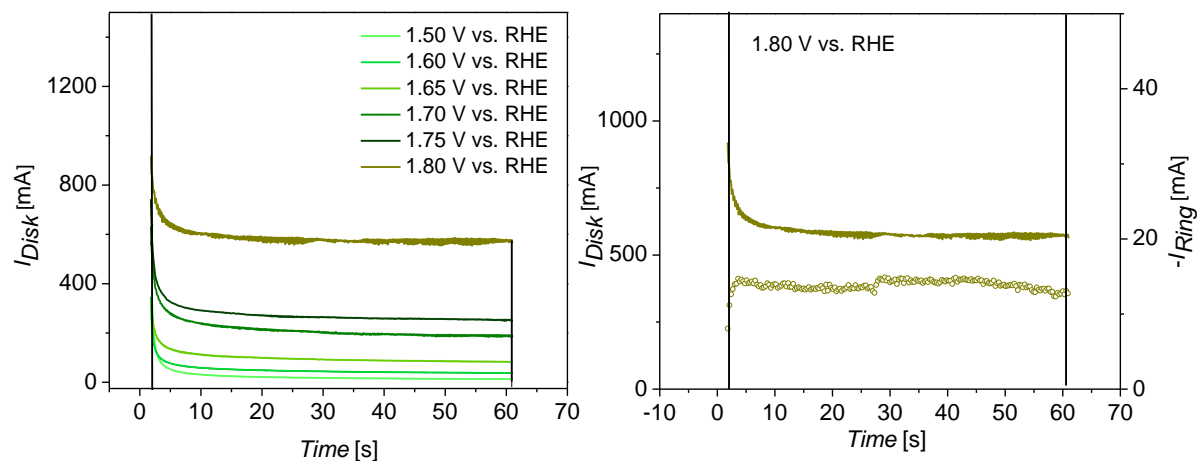

Figure 3.19. Multipotential chronoamperometry measurement of GC|MWCNTs|$\mathbf{1^{4pyr}}$ WE above the OER onset potential (left). CA measurement of GC|MWCNTs|$\mathbf{1^{4pyr}}$ at E_{disk} = 1.8 V vs. RHE depicting both disk (solid olive line) and ring currents (olive dots). The measurements were recorded in an aqueous HOTf (0.1 M, pH = 1) with ω = 1600 rpm for 60 seconds. CE: Pt, Ref. MSE. The potentials are referenced versus RHE.

In order to examine the long-term stability of both hybrid systems, chronoamperometry experiments were performed at E_{disk} = 1.8 V vs. RHE for 300 s under similar conditions (Figure 3.20). X-ray photoelectron spectroscopy (XPS) was also conducted after each CA to give more insight into the stability of the hybrid electrodes which will be discussed in more detail in section 3.7. Cyclic voltammetry measurements of the disk WE were recorded before and after each CA to determine the surface coverage. For both hybrids, the intensity of the first wave corresponding to the oxidation of the pyrene was drastically decreased after applying a

potential of 1.8 V for 300 s. In the case of GC|MWCNTs|1^{4pyr}, the concentration of two redox processes related to the oxidation from Ru^{II}Ru^{II} to Ru^{II}Ru^{III} and further to Ru^{III}Ru^{III} changed slightly after CA which is in agreement with other observations suggesting the higher stability of the 1^{4pyr} complex bearing four axial pyrene groups.

In addition, a repetitive CV measurement with 100 scans was conducted for both modified disk electrodes under identical conditions (Figure A83-84, top). A decrease in the intensity of the first redox wave took place faster for GC|MWCNTs|1^{pyr} due to the loss of the complex surface coverage over time. The changes of the disk current at $E_{1/2}$ = 0.57 V $vs.$ RHE are plotted as a function of scan number (Figure A83-84, bottom).
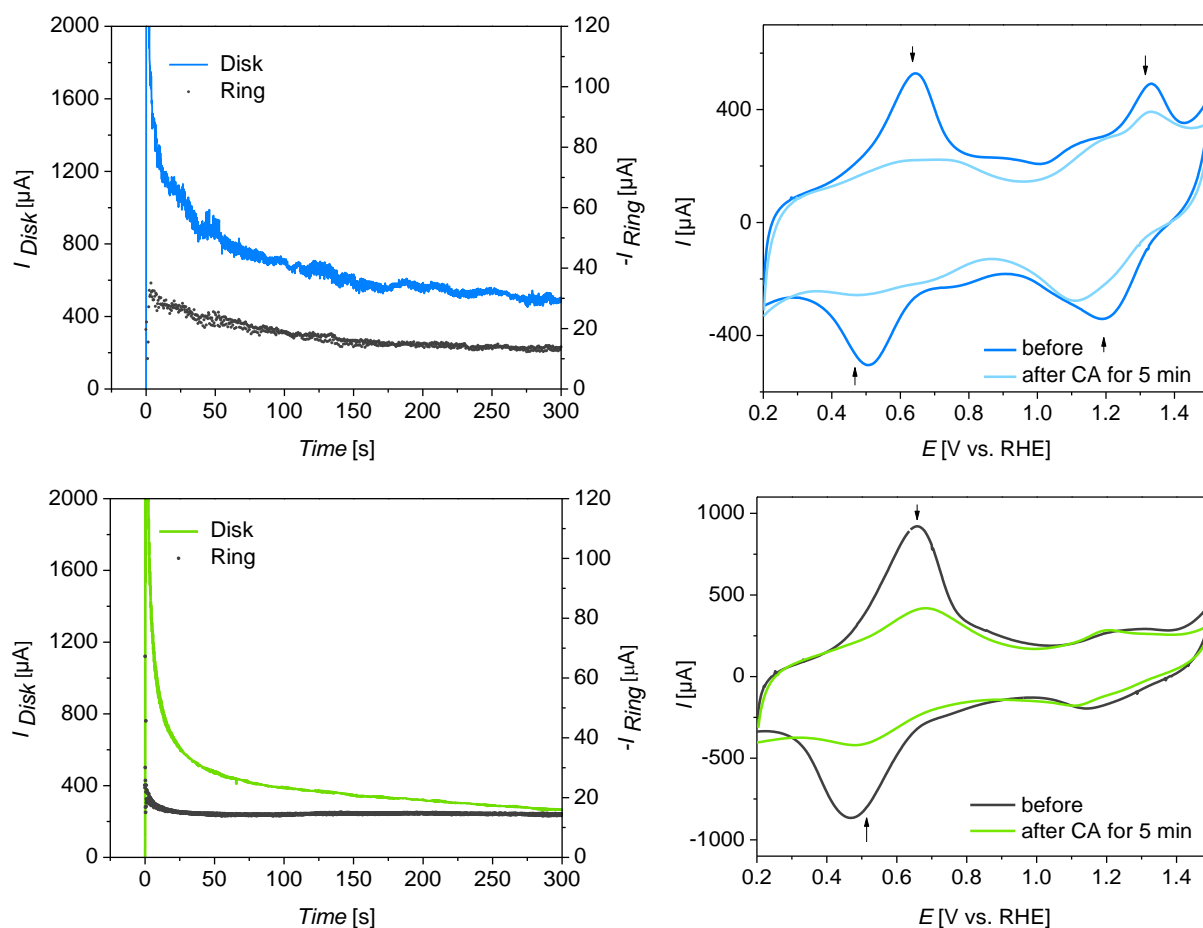
Figure 3.20. CA measurements of GC|MWCNTs|1^{pyr} WE (left-top) and GC|MWCNTs|1^{4pyr} (left-bottom) at 1.8 V $vs.$ RHE for 300 s showing both disk (blue and green solid line) and ring currents (grey continuous dot). CV measurement before and after CA for 300 s for GC|MWCNTs|1^{pyr} WE (right-top) and GC|MWCNTs|1^{4pyr} (right-bottom). All experiments are performed in an aqueous HOTf (0.1 M, pH = 1) with ω = 1600 rpm. CE: Pt, Ref. MSE. The measurements were recorded at a scan rate of 50 mV/s. All potentials are referenced versus RHE.

In order to determine if the MWCNT electrode is oxidized at high potentials, a CA of a bare electrode GC|MWCNTs was recorded at E_{disk} = 1.8 V vs. RHE for 300 s in aqueous HOTf. The produced gases in the headspace of the reaction cell were analyzed by GC-MS. (Figure 3. 21). The absence of any CO_2 signal after the CA experiment of the GC|MWCNTs excludes the possibility that the carbon nanotubes are oxidized at that potential range. The intense CO_2 peak around 18 s in the GC-MS trace is due to the control experiment where CO_2 was injected manually into the electrochemical cell under the same conditions.
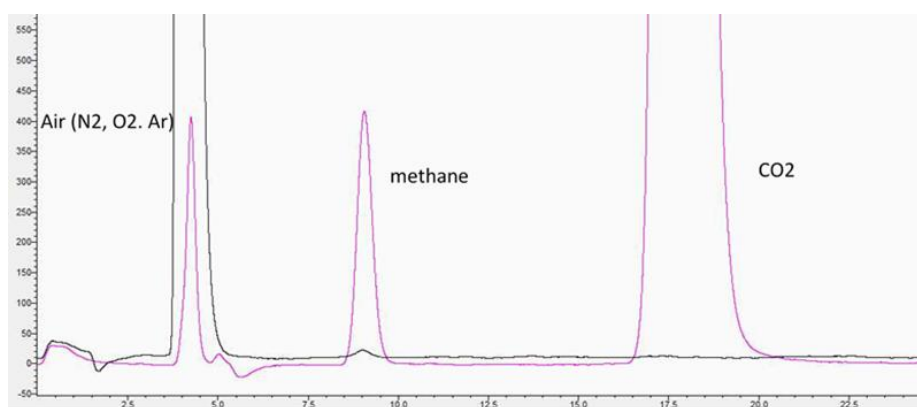
Figure 3.21. GC-MS analysis of the headspace of the electrochemical cell after 300 s CA of the GC|MWCNTs at the potential of 1.8 V vs. RHE (black line). The control experiment was performed by the addition of CO_2 to the reaction vial (pink color). Methane was also added for calibration purposes.

RRDE experiments also provide additional insight into other processes which take place during the catalysis such as leaching of the catalysts from the disk surface. The detached species from the disk WE can be detected at the ring by setting an appropriate applied potential. It should be pointed out that the reductive probing of the desorbed complexes is only achievable by careful and accurate designation of the ring potential. This procedure was adopted from the previous works reported in the literature.[114] To calculate the potential of the complex reduction reaction (CRR) at the ring electrode, a cathodic scan of the bare platinum ring was recorded in aqueous HOTf (0.1 M, pH = 1) saturated with oxygen at various rotation speeds (Figure 3.14). Then, a water soluble complex [(^{Me}bbp){Ru(OH₂)(4-SO₃-py)₂}₂]⁻ (derivative of **IX** bearing py-SO₃ instead of parent pyridines at axial positions) was dissolved in 0.1 M argon saturated aqueous HOTf (pH = 1) and the ring electrode was scanned in the diffusion limited region while a potential of 1.48 V was applied to the disk WE. A potential of 0.75 V *vs.* RHE was determined by comparison of ORR in the oxygen purged solution and CRR of [(^{Me}bbp){Ru(OH₂)(4-SO₃-py)₂}₂]⁻ under inert atmosphere. This approach is only applicable

when the CRR is distinguishable at the ring electrode from the ORR. The significant differences between these two processes enabled the observation of leaching processes under reactive conditions. Figure 3.22 shows RRDE measurements of GC|MWCNTs|$\mathbf{1^{pyr}}$ and GC|MWCNTs|$\mathbf{1^{4pyr}}$ in argon purged acidic solution (HOTf, pH = 1) at E_{CRR} = 0.75 V *vs*. RHE. Desorption of the complexes from the disk WE are unlikely in the non-catalytic area for both hybrid systems because no currents were observed at the ring. Above the onset potential, a tiny current appeared at the ring electrode which can be attributed to the catalyst degradation or desorption from the surface.
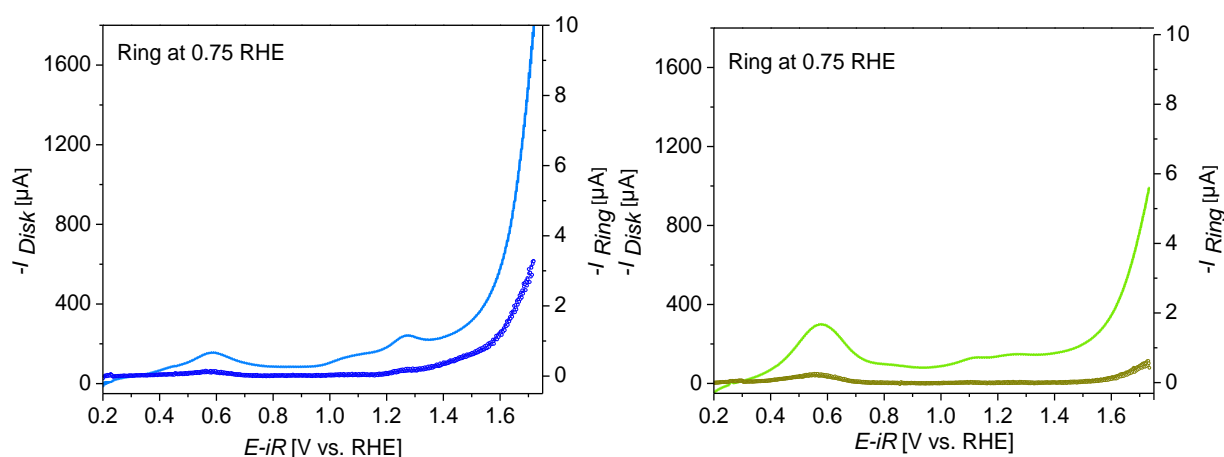
Figure 3.22. RRDE-CV experiment of GC|MWCNTs|$\mathbf{1^{pyr}}$ WE (blue line-left) and GC|MWCNTs|$\mathbf{1^{4pyr}}$ (light green line-right). A bipotential CV is recorded while a potential of 0.75 V was applied to the ring electrode which is suitable for complex reduction reaction (CRR). The currents observed at the ring are depicted as circles (blue circles for GC|MWCNTs|$\mathbf{1^{py}}$ and olive circles for GC|MWCNTs|$\mathbf{1^{4pyr}}$ WE). The measurement was carried out in aqueous HOTf (0.1 M,pH = 1) with ω = 1600 rpm and a scan rate of 50 mV/s. CE: Pt, Ref. MSE. All potentials are referenced versus RHE after uncompensated resistance correction.

TOF can be considered as a valuable parameter to assess the catalytic activity of various WOC catalysts. The TOF value at different applied potentials can be obtained by dividing the concentration of produced dioxygen during the OER by the number of anchored complexes on the surface (Equation 3.1). Integration of the reversible 1e$^-$ transfer process corresponding to the Ru^{II}Ru^{II}/Ru^{II}Ru^{III} couple after chronoamperometry measurements within the potential range of 1.5-1.8 V *vs.* RHE (Figure 3.23) delivers the number of absorbed species according to equation 3.2, where F is the *faraday* constant (96,485.33 C/mol). The surface concentration Γ of 1.75 ± 0.42 nmol/cm^2 and 1.98 ± 0.49 nmol/cm^2 were determined for hybrids

GC|MWCNTs|**1^{pyr}** and GC|MWCNTs|**1^{4py}**, respectively, after CA at 1.5 V *vs.*RHE (60 s). It is also possible to estimate the rate of formed dioxygen during the CA measurements if we assume all the anchored complexes are converted to electrocatalytically active species with a high faraday efficiency, using equation 3.3, where I_{disc} can be acquired from Figure 3.18 and 3.19 and t = 60 s.

$$TOF = \frac{n_{O_2}}{n_{Ru}} \qquad (3.1)$$

$$n_{Ru} = \frac{Q}{F} \qquad (3.2)$$

$$n_{O_2} = \frac{I_{disk}t}{4F} \qquad (3.3)$$
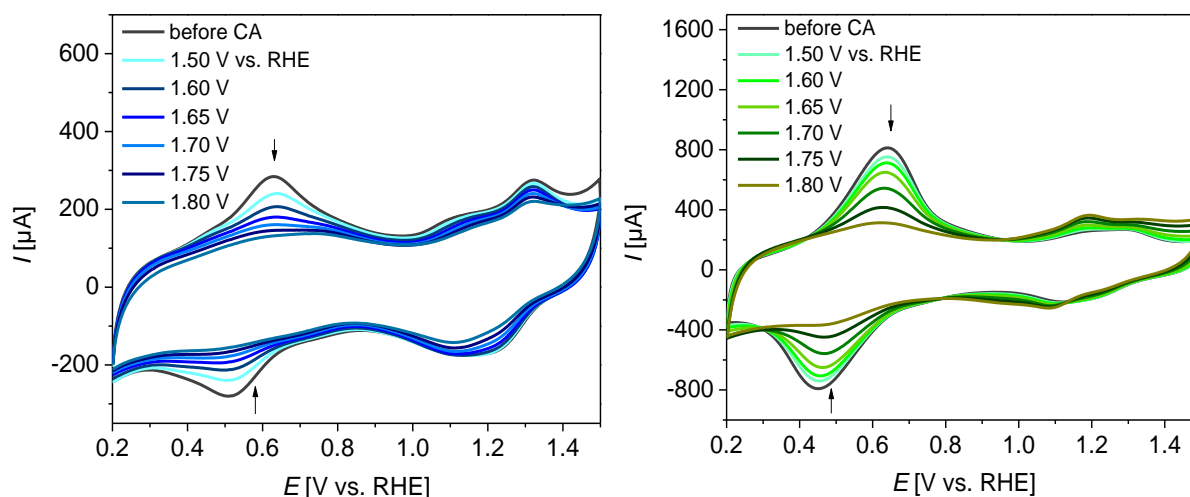
Figure 3.23. Cyclic voltammetry of GC|MWCNTs|**1^{pyr}** (left) and GC|MWCNTs|**1^{4pyr}** WE (right) after multi CA for 60 s. The measurements were conducted in aqueous HOTf (0.1 M, pH = 1). CE: Pt, Ref. MSE. All potentials are referenced versus RHE.

The calculated number of immobilized catalyst molecules is plotted as a function of applied potential as shown in Figure 3.24, which shows a drastic decrease in catalysts concentration for GC|MWCNTs|**1^{pyr}** by increasing the potential. This finding is in agreement with other observations revealing that the catalyst immobilized via the remote backbone anchor has lower stability in the timespan of electrochemical measurements. In addition, increasing the disk potential accelerated the rate of produced dioxygen in both systems as expected (Figure 3.25).
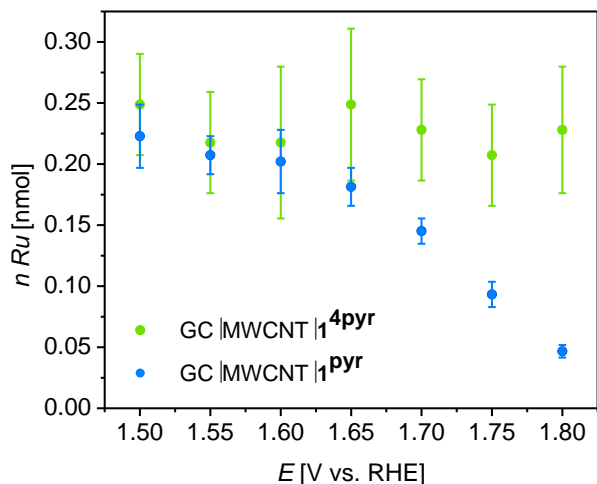
Figure 3.24. The amount of anchored catalyst on MWCNT surface at various potentials determined by the integration of the first redox process $Ru^{II}Ru^{II}/Ru^{II}Ru^{III}$ after CA for 60 s. The CA and CV experiments were recorded in aqueous HOTf (0.1 M, pH = 1). CE: Pt, Ref. MSE. All potentials are referenced versus RHE.
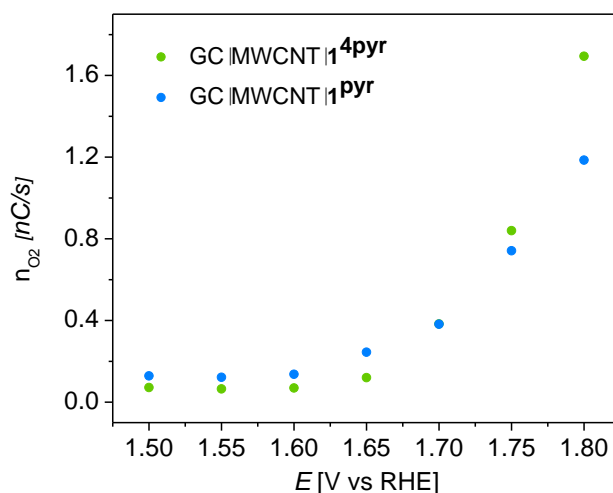
Figure 3.25. The amount of produced dioxygen at different potentials after correction of surface coverage for each CA step (60 s). CE: Pt, Ref. MSE. Measured in aqueous HOTf (0.1M, pH = 1).

A considerable increase in TOF was observed above the potential of 1.60 V vs. RHE as depicted in Figure 3.26. For GC|MWCNTs|1^{pyr}, the TOF increased from 0.59 s⁻¹ at 1.55 V to 25.41 s⁻¹ at 1.8 V. In the case of GC|MWCNTs|1^{4pyr}, it reached a maximum value of 7.43 s⁻¹ at 1.8 V corresponding to η = 0.63 V. At lower overpotentials, the values are in the range of related bbp-based ruthenium complexes immobilized on oxide surfaces (0.45 s⁻¹ at η = 0.52 V).[114,115] It should be mentioned that the TOF values of homogenous and heterogeneous systems are not comparable due to the fact that so many aspects can affect the outcome of the experiment. At higher potentials, the presented hybrids in this work exhibited significantly
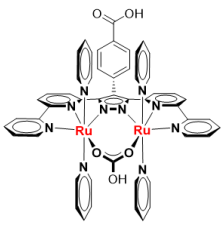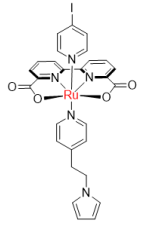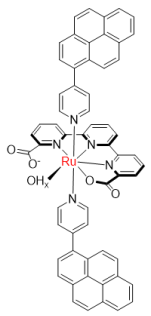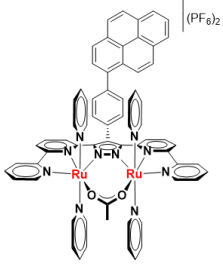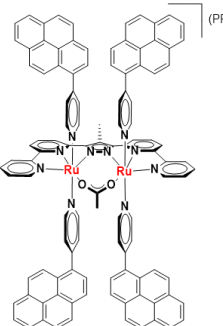
higher TOFs that are comparable with values reported for the water-soluble complex [(^{Me}bbp){Ru(OH$_2$)(4-SO$_3$-py)$_2$}$_2$]$^-$ (15.7 s^{-1} at η = 0.52 V and 50 s^{-1} at η = 0.77 V) in a homogenous system. However, the TOF was determined under different conditions using other techniques such as the FOWA. TOF$_{max}$ > 8000 s^{-1} was presented for a tda-based mononuclear ruthenium WOC immobilized on carbon surfaces.[117] However, the results were also obtained through the FOWA method and at pH = 7. Therefore, it would be problematic to evaluate the reactivity of various WOCs only based on their TOF. A comparison of the TOF values for literature known immobilized water oxidation catalysts is tabulated in Table 3.2.
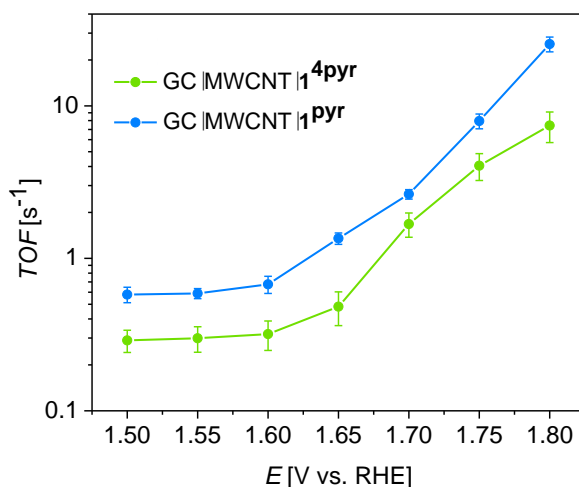
Figure 3.26. TOF calculation for both catalysts GC|MWCNTs|**1**^{pyr} WE (blue) and GC|MWCNTs|**1**^{4pyr} (green) resulting from multistep CA experiments in 0.1 M argon purged aqueous HOTf (pH = 1) at a rotation rate of 1600 rpm. Error bars stem from the accuracy of the catalyst concentration determination on the MWCNTs.

Table 3.2. Comparison of TOF values of several reported ruthenium water oxidation catalysts under different conditions. All the complexes were immobilized on solid supports such as oxide or carbonaceous surfaces, and the turnover frequency was calculated by RRDE experiments or by the FOWA method.[115,117,145,161]

Complex	TOF (s^{-1})	Overpotential (η) in V	Condition	Ref
	0.45 4.1	0.52 0.77	On *meso*ITO surface, pH = 1	115
	0.64 10.47	0.37 0.77	On graphite carbon surface, pH 7.2 buffer	161
	above 8000		On MWCNTs, pH = 7	117
	0.59 25.41	0.38 0.63	On MWCNTs, pH = 1	This work,145
	0.29 7.43	0.38 0.63	On MWCNTs, pH = 1	This work,145

A parameter that categorizes the efficiency of water oxidation catalysts is given by the *Faradaic* efficiency (ε). In RRDE experiments, the *Faradaic* efficiency can be calculated from the ratio of the disk and ring current with a good estimation of the number of transferred electrons following equation 3.4.

$$\varepsilon = \frac{I_{ring}/n_{ring}}{(I_{disk}/n_{disk})N} \quad (3.4)$$

To quantify the *Faradaic* efficiency, it is necessary to ascertain the number of transferred electrons at the ring working electrode (n_{ring}). Assuming complete oxidation of water into dioxygen, this number is considered to be four, however incomplete oxidation of water leads to the formation of other products such as hydrogen peroxide which decreases this number. In addition, diffusion limitation and kinetic effects can also influence the number of transferred electrons. n_{ring} can be calculated from the *Levich* equation which displays the relationship between the ring currents and rotation speeds (ω).

$$I_{ring,LC} = 0.62nF\pi(r_2^3 - r_1^3)^{2/3}D_0^{2/3}\omega^{1/2}v^{-1/6}C_{O_2} \quad (3.5)$$

Where *F* is the Faraday constant (C/mol), *n* is the number of electrons, r_1 is the inner diameter of the ring (2.5 mm) and r_2 is the outer diameter of the ring (3.5 mm). D_0 is the diffusion coefficient (9.67×10^{-6} cm^{2}s^{-1}), ω is the rotation speed, *v* is the kinematic viscosity (0.917×10^{-2} cm^{2}s^{-1}), and C_{O2} is the bulk concentration of dioxygen in saturated solution (0.63×10^{-6} molcm^{-3}) in 0.1 M aqueous HOTf (pH = 1).[162,163] Using equation 3.5 with the above parameters afforded a value of 2.6 corresponding to the number of transferred electrons (n_{ring}). The collection efficiency *N* defined by the number of produced products at the disk which was simultaneously detected at the ring electrode can be determined by equation 3.6.

$$N = \frac{-I_{ring}}{I_{disk}} \quad (3.6)$$

The *N* can be obtained via the ferrocyanide/ferricyanide half reaction[164] in an aqueous solution or via theoretical evaluations.[165] However, it was not possible to assign the *N* value from this reaction in our case due to the use of different electrolytes compared to the literature. A collection efficiency of 10% was determined for the same setup used for RRDE experiments using the platinum ring. A *Faradaic* efficiency of 10% and 30% was observed at

1.7 V *vs.* RHE for GC|MWCNTs|1^{pyr} and GC|MWCNTs|1^{4pyr}, respectively with ω = 1600 rpm and in 0.1 M aqueous HOTf (pH = 1) (Figure 3.27).
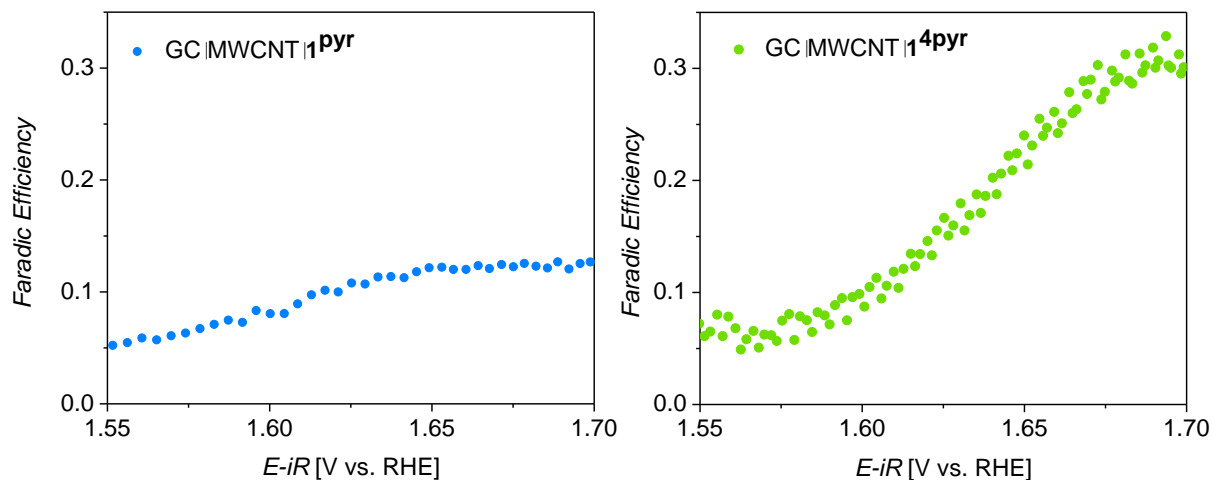

Figure 3.27. Faradaic efficiency of GC|MWCNTs|1^{pyr} WE (left) and GC|MWCNTs|1^{4pyr} (right) calculated by advanced RRDE experiments. All CV measurements were carried out in aqueous HOTf (0.1 M, pH = 1) with a three-electrode setup. CE: Pt, Ref. MSE. All the potentials were corrected for uncompensated resistance.

3.7 Surface Investigation with X-ray Photoelectron Spectroscopy (XPS)

X-ray photoelectron spectroscopy is an established technique that provides information about the structural properties and chemical composition of the surface. XPS experiments were conducted in this work to examine the chemical stability of the anchored complexes on MWCNTs during electrocatalytic conditions. The measurements were performed by Christian Höhn and Dr. Fatemeh Ebrahimi who also analyzed the data.

For the preparation of the specimen, a suspension of MWCNTs (1 mg, 1 ml) in THF was drop-casted on a glassy carbon surface to obtain a fine surface coverage. Soaking the electrodes in a methanolic solution containing the respective complex resulted in pristine samples (GC|MWCNTs|1^{pyr} and GC|MWCNTs|1^{4pyr}). The reference samples were prepared by drop-casting of the desired complex in methanol (1 mM) on a gold surface (Au|1^{pyr}, and Au|1^{4pyr}). To compare the XPS data, another reference sample of GC|MWCNTs was also provided. The XPS spectra of the full range of both pristine samples revealed the Ru, O, C, N, and F core levels as expected (Figure A88-89). The signals at 280.95 eV and 400.2 eV correspond to the binding

energy of the Ru(3d$_{3/2}$) and N(1s), respectively. Due to the overlapping of the Ru(3d$_{3/2}$) binding level with C(1s), the energy splitting of Ru(3d$_{3/2}$) and Ru(3d$_{5/2}$) was not resolved. The observation of the F core level is due to the presence of PF$_6^-$ counterions in both catalysts. The pristine samples were placed in a RRDE setup and a chronoamperometry measurement was recorded for 60 s at E_{disk} = 1.8 V *vs.*RHE in aqueous HOTf (0.1 M, pH = 1) to form the post mortem samples. High resolution scans of the N(1s) and Ru(3d) levels for both hybrids are displayed in Figure 3.28. XPS data of the pristine sample GC|MWCNTs|1^{pyr} exhibits the binding energy of the Ru(3d$_{5/2}$) at 280.90 eV. For the reference and post mortem sample, this band appears at 280.60 eV and 280.90 eV, respectively. In the case of GC|MWCNTs|1^{4pyr}, the Ru(3d$_{5/2}$) band was observed at 280.95 eV before electrochemical treatment (pristine), 280.65 eV for reference, and 280.85 eV after 60 s CA at a potential of 1.8 V *vs.* RHE. According to the spectral resolution of ΔE = ± 0.25 eV, no considerable shift of the Ru(3d$_{5/2}$) state was found for any of the measured samples. The N(1s) spectra show a significant band at 399.98 eV for all samples except the background GC|MWCNTs. This clearly indicates that the presence of the binding energy of N(1s) originates from the anchored complex on the surface. Within error, no shift in the binding energy was detected in this core level for samples either before or after the electrocatalytic measurements.
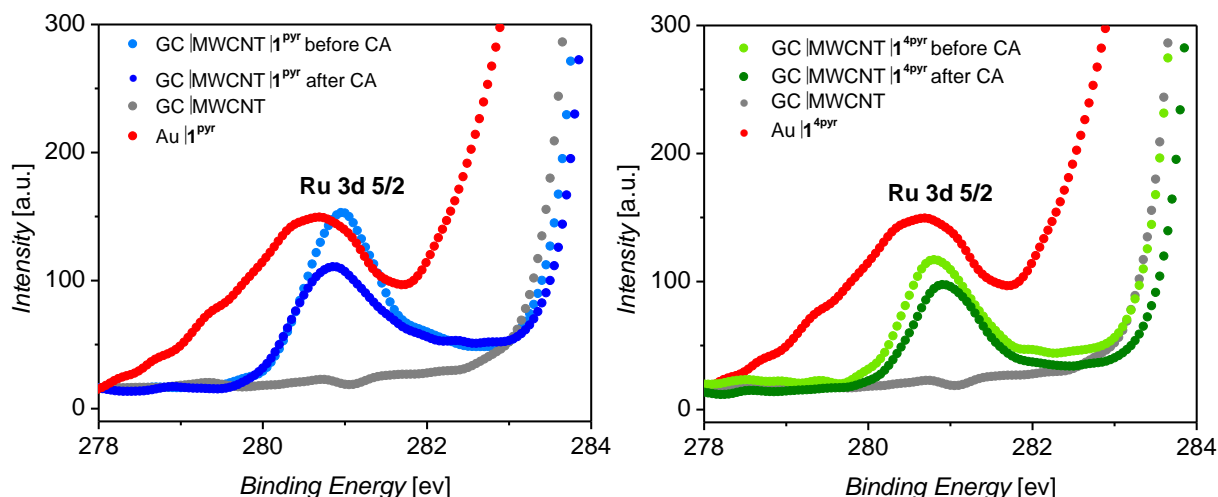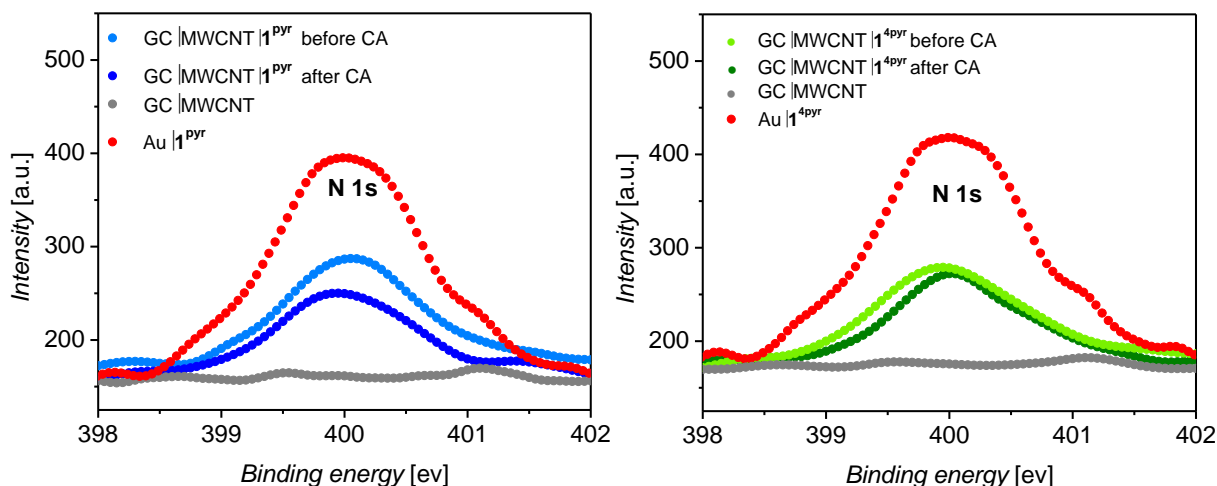
Figure 3.28. XPS spectra of Ru(3d$_{5/2}$) level (top) comparing the background, GC|MWCNTs|**1**^{pyr} before and after electrochemical treatment and reference sample (on gold) (top-left) and for GC|MWCNTs|**1**^{4pyr} (top-right). The scans of the N(1s) core are depicted for GC|MWCNTs|**1**^{pyr} in (bottom-left) and for GC|MWCNTs|**1**^{4pyr} (bottom-right). Post mortem samples were prepared by 60 s CA measurement at a potential of 1.8 V *vs*.RHE in a RRDE set-up using aqueous HOTf (0.1 M, pH =1) as the electrolyte.

Complex decomposition and formation of RuO₂ particles during harsh electrochemical conditions are reported in numerous systems for immobilized ruthenium water oxidation catalysts.[125] To ensure that the catalytic activity of the hybrids is due to the presence of the molecular catalysts on the surface and not to RuO₂ nanoparticles, the ratio of Ru to N was calculated for pristine and post mortem samples. For both catalysts, a significant decrease in the intensity of Ru and N core energy level peaks after 60 s CA was observed. However, the changes are more pronounced for the complex anchored via the pyrene linked to the pyrazolate backbone. In the case of GC|MWCNTs|**1**^{pyr}, the intensity of the Ru and N signals was reduced by 27% and 26% for the post mortem samples, respectively. GC|MWCNTs|**1**^{4pyr} shows higher stability during the electrochemical measurements consistent with data presented in this chapter. Analysis of the XPS spectra reveals a 19% decrease in the intensity of Ru and 15% in the N(1s) level. The N/Ru ratios for GC|MWCNTs|**1**^{pyr} and GC|MWCNTs|**1**^{4pyr} are shown in Figure 3.29. While, the percentage of Ru(3d$_{5/2}$) and N(1s), which reflects the number of complexes on the surface, dropped after the electrocatalysis, the ratio N/Ru stays almost constant within the error range (close to the 10:2 ratio for both hybrid materials based on the structural integrity of **1**^{pyr} and **1**^{4pyr}). All combined findings suggest that both complexes

are chemically robust during the electrochemical treatment and they do not convert into RuO_2 species via oxidative degradation pathways.
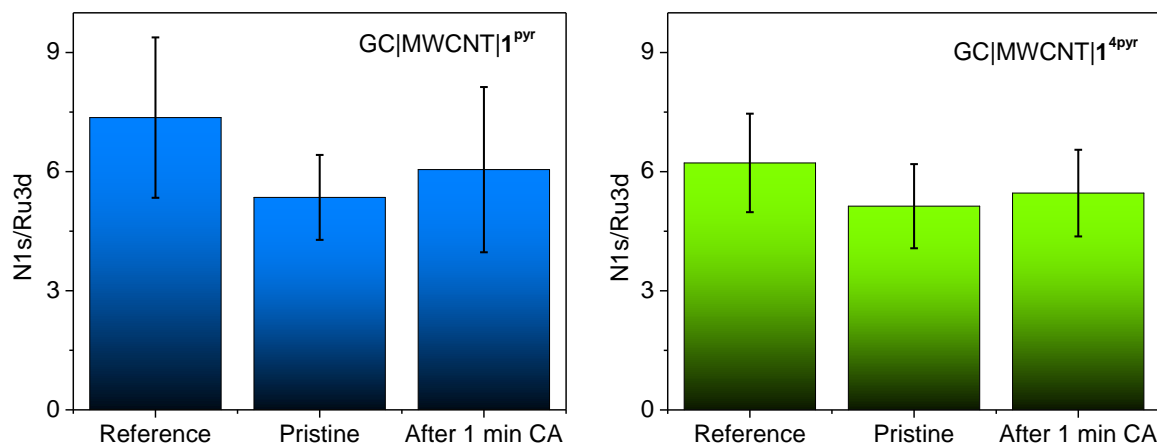
Figure 3.29. The ratio of N(1s) to Ru(3d) calculated from the XPS data for GC|MWCNT|**1**[pyr] (left) and GC|MWCNT|**1**[4pyr] (right) before and after electrocatalysis.

To support that the immobilization via the pyrene anchoring groups improved the stability of the hybrids, the simple complex **Mebbp-Ru₂(OAc)** was attached to the MWCNT electrode with the same procedure as described above. A 60 s chronoamperometry at a potential of 1.8 V *vs.*RHE was applied on the pristine sample and the structural integrity of the surface was analyzed by XPS. High resolution scans of the Ru(3d$_{5/2}$) level for pristine and post mortem samples reveal the significant loss of the catalyst under water oxidation conditions (Figure 3.30).
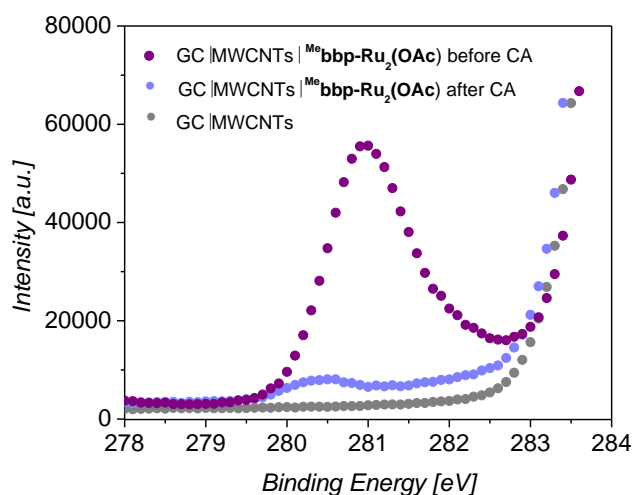
Figure 3.30. Survey scan of the Ru(3d$_{5/2}$) level of GC|MWCNT|**Mebbp-Ru₂(OAc)** before and after electrocatalysis. The CA measurement is performed in aqueous HOtf (0.1 M, pH = 1) at 1.8 V *vs.* RHE. CE:Pt, Ref: MSE.

3.8 Summary and Conclusion

Two dinuclear ruthenium water oxidation catalysts based on the anionic ligand system (bbp⁻) equipped with peripheral pyrene groups attached to either the axial pyridines or pyrazolate backbone were prepared. The complexes were fully characterized with various spectroscopic techniques, and their electrochemical properties in solution were studied by cyclic voltammetry and square wave voltammetry. The reduction potentials observed for $Ru^{II}Ru^{II}/Ru^{III}Ru^{II}$ and $Ru^{III}Ru^{II}/Ru^{III}Ru^{III}$ are similar to other related bbp-Ru₂ complexes indicating that the pyrene anchoring groups do not considerably influence the electronic properties of the diruthenium cores. **1**^{pyr} features an irreversible wave in the CV measurement corresponding to the oxidation of the pyrene moiety which was also observed for the metal free ligand ^{pyr}**bbpH**.

To assess the catalytic activity of hybrid electrodes, the modified complexes were immobilized successfully on conductive MWCNTs deposited on a glassy carbon electrode. TEM and EELS were used to monitor the MWCNTs surface before and after the immobilization process. Evidence of pyrene anchoring via π-π interactions was supported by an increase of spectral weight of π–π* transitions upon attachment of the ruthenium complexes or ^{pyr}**bbpH** to the surface.

The catalytic performance of GC|MWCNTs|**1**^{pyr} and GC|MWCNTs|**1**^{4pyr} hybrid anodes regarding WOC was investigated by RRDE experiments under acidic conditions. It turned out that the surface-bound pyrenes convert to redox-active pyrenequinones during the first scan of the cyclic voltammetry experiment. The intensity of this wave decreased after scanning to higher potentials especially in the case of GC|MWCNTs|**1**^{pyr}, which may be attributed to different charge transfers between the carbon surface and ruthenium units. Furthermore, it can be assumed that the orientation of the active sites will be changed after the immobilization of the complexes on the MWCNTs.

RRDE-CV measurements as well as chronoamperometry at various potentials above the OER onset revealed a higher catalytic activity for GC|MWCNTs|**1**^{pyr}. However, the complex started leaching from the surface gradually during the electrochemical measurement which was also confirmed by XPS analysis. On the other hand, the complex with four pyrene anchoring groups

demonstrated a strong attachment to the surface which may lead to an enhancement of the surface coverage and a decrease of the rate of the desorption process.

The turnover frequency of both complexes was determined using RRDE measurements in aqueous HOTf (0.1 M, pH = 1). The obtained values are comparable with the parent complex **^{Me}bbp-Ru₂(OAc)** which supported the idea that the catalytic activity of the complexes was not diminished after immobilization. Remarkably, the TOF value for GC|MWCNTs|**1^{pyr}** was higher than for GC|MWCNTs|**1^{4pyr}** at the same potential.

The *Faradic* efficiency of both hybrids was calculated based on the collection efficiency. Furthermore, the identical disk and ring *Tafel* slopes above the onset potential suggested that the disk current was dominated by the oxygen evolution reaction.

The chemical integrity of both modified complexes after immobilization on solid supports was investigated by XPS. No shift of the Ru(3d$_{5/2}$) and N(1s) levels was observed for the samples either before or after electrochemical treatment. In addition, the constant ratio of N(1s) to Ru(3d$_{5/2}$) indicated that both complexes are robust during catalysis and do not decompose to oxide nanoparticles or other species under reactive conditions. Hence, it can be concluded that the decrease in catalytic performance is due to the gradual leaching of the catalysts from the solid which is more pronounced for GC|MWCNTs|**1^{pyr}**.

As mentioned previously, in a related diruthenium complex equipped with a phosphonate anchoring group at the ligand backbone, oxidative P-C(aryl) bond cleavage was likely to happen once the complex reaches Ru^{V}Ru^{IV} level.[114] Additionally, the pyrazole-C^4 position possesses a radical character when the ruthenium cores reach higher oxidation states. All findings suggest that the pyrazolate backbone is not the best attachment position for anchoring groups, and further modification is needed to improve the stability of the hybrids under catalytic conditions.

4 Mononuclear Ruthenium Water Oxidation Catalysts

4-1 Introduction

To date, numerous mononuclear water oxidation catalysts based on transition metals have been reported, and among them, Ru-based catalysts gained special attention (See section 1.4.1). The development of rugged and efficient MWOCs with impressive performance can be achieved through careful ligand design and hence, both primary and secondary coordination spheres provided by the ligand have to be considered. The primary coordination sphere entails coordination number, the geometric configuration of the active site, robustness, net charge effect, σ/π-donating as well as π-accepting properties. The secondary coordination sphere includes substituents electronic effect, steric hindrance, hydrophilicity, and hydrogen bonding effect.[166] As discussed previously, the introduction of the carboxylate-containing ligand (bda^{2-}) led to the generation of the most prominent mononuclear WOC, which exhibited unprecedented proficiency in terms of reactivity and oxidative ruggedness.[72,166] The remarkable performance of bda-based complexes was attributed to their unique seven coordination feature and small hindrance of carboxylate moieties which enable the fast binding of the water molecule to the ruthenium center and further coupling of two high valent Ru=O intermediates. Therefore, to develop MWOCs capable of reaching coordination number seven, a constrained equatorial tetra-dentate ligand with a wide open site for extra coordination of the substrate water is required.

A change in coordination environment of the metal center to generate the seven coordinated intermediate was also observed in a single site Ru-based catalyst [Ru^{II}(npm)(pic)$_2$(H$_2$O)]$^{2+}$(npm = 4-t-butyl-2,6-di(1',8'-naphthyrid-2'-yl)pyridine, pic = 4-picoline), **I**, (Chart 4.1).[167] It was shown that, under water oxidizing conditions, oxygen atom transfer (OAT) from the high-valent Ru=O to noncoordinating nitrogen atoms of the npm ligand enables storing oxidizing equivalent in form of N-O bonds to trigger the critical O-O bond formation at lower overpotential.[167,168] Similarly, oxidation of the polypyridine backbone ligand to N-O groups was also reported in [Ru(qpy)(pic)$_2$]$^{2+}$, **V**, (see Section 1.4.2), in which the qpy was converted to qpy-N,N'''-dioxide during chemical water oxidation experiments. The formed [Ru(ONNO)(pic)$_2$]$^{3+}$ was considered as the real active catalyst (Chart 4.1).[82] Based on these

findings, a fundamental understanding of the effects and the potential modification of the ligand structure around the metal center under operating conditions is necessary for the design of new-generation WOCs.
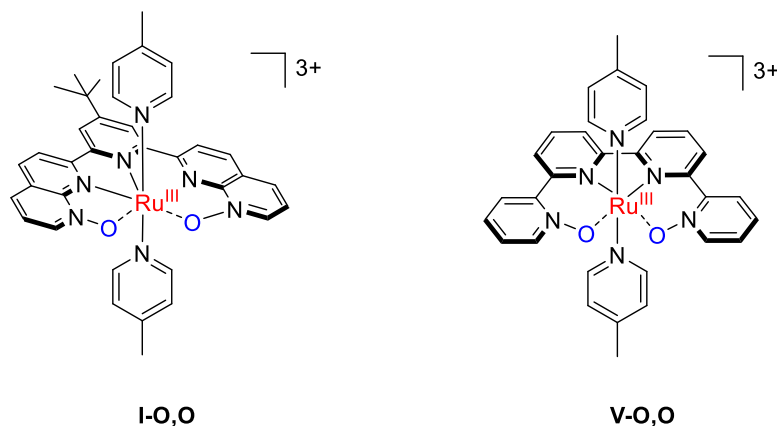

Chart 4.1. Activation of the catalyst via OAT to the ligand backbone.[82,167]

Since the highly active bda or tda ligand scaffold are not suitable for hybrid formation due to the potential binding of carboxylic acid functional groups to oxide surfaces, a series of new mononuclear ruthenium complexes based on a dianionic N-donor scaffold was developed in course of this work. However, it should be mentioned that, recently, the group of Llobet presented a new anchoring strategy to immobilize the bda and tda type of complexes on graphitic surfaces through aromatic CH-π interactions, without compromising the catalyst active sites (see Section 1.5.2).[128,131] To investigate the role of polypyridine N-O ligands on the performance of the designed catalyst, CH units of the phenyl groups at the ligand backbone were substituted with nitrogen atoms. The water oxidation ability of all catalysts along with their behavior after immobilization on surfaces will be discussed in this chapter.

4-2 Ligand and Complex Synthesis

H_2L^1 ligand was prepared via a reported procedure according to the literature[169] and H_2L^2 through a synthetic modification. 6,6'-dimethyl-2,2'-bipyridine (**4-1**) was oxidized with an excess amount of chromium trioxide under acidic conditions to yield the [2,2'-bipyridine]-6,6'-dicarboxylic acid (**4-2**). Subsequently, the reaction of 2,3-diaminopyridine and (**4-2**) in presence of phosphoric acid resulted in the formation of H_2L^2 (Scheme 4.1) which was characterized by NMR spectroscopy and ESI mass spectrometry (Figure A75).
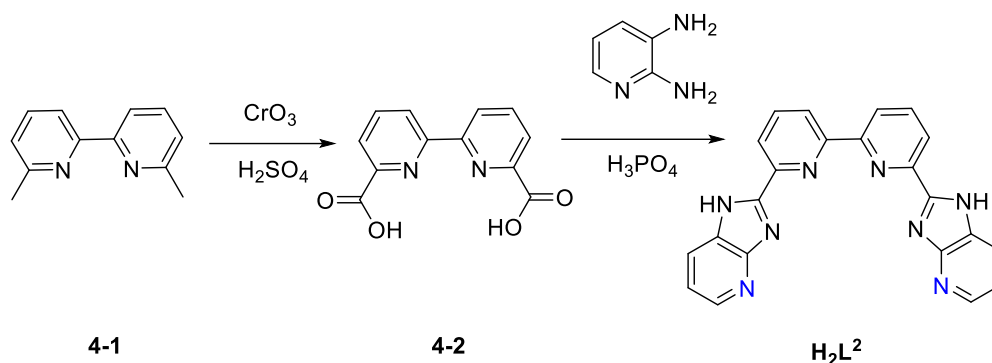
Scheme 4.1. Synthetic procedure for preparation of **H₂L²**.

The synthesis of mononuclear ruthenium complex **2** was initiated by the reaction of **H₂L¹** with [RuCl₂(C₆H₆)]₂ and triethylamine in degassed methanol followed by the addition of excess pyridine. Complexes **3**, **4**, and **5** were obtained via the same procedures but by treatment of **H₂L²** with RuCl₂(dmso)₄ as the ruthenium precursor (Scheme 4.2). Isonicotinic acid was introduced as an anchoring group for immobilization studies and 4-(dimethylamino)pyridine to improve the solubility of the complex and facilitate the crystallization process. Slow evaporation of complex **2** in chloroform afforded single crystals suitable for X-ray diffraction (Figure 4.1). The XRD analysis revealed that the ruthenium ion is surrounded by six nitrogen atoms of the ligand backbone and the axial pyridines in an {N6} coordination environment. The bond distances of the ruthenium atom to the inner pyridyl ring Ru1-N2 and Ru1-N1 are 1.963 and 1.967 Å, respectively which are much shorter than the Ru-N bonds involving the outer imidazole groups (Ru1-N3 2.133 Å, Ru1-N4 2.145 Å). In addition, the angle of N3-Ru1-N4 is widened by 32° compared to the ideal octahedral geometry. The deviation from an ideal octahedral configuration is imposed by the equatorial ligand.
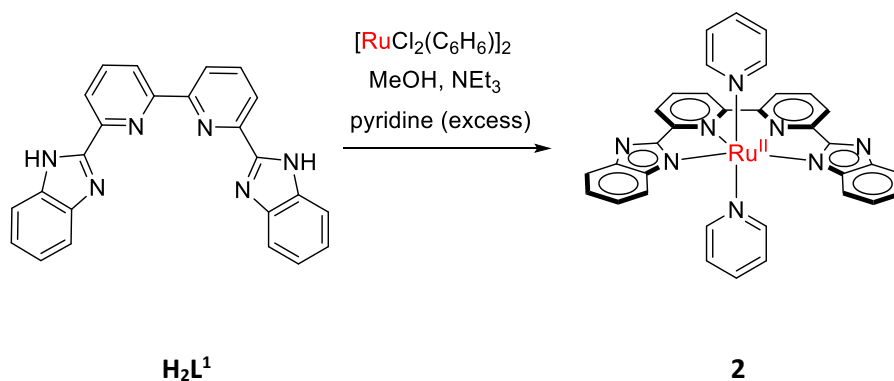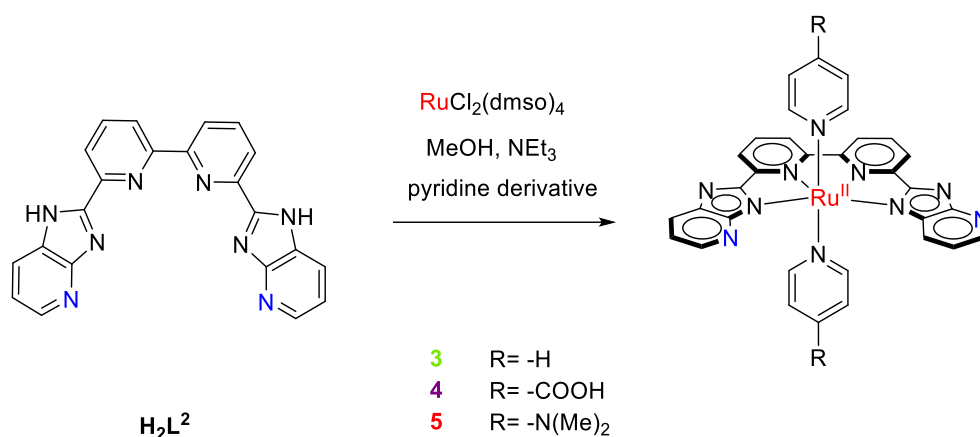
Scheme 4.2. Synthesis of the mononuclear ruthenium complexes **2**, **3**, **4**, and **5**. Variation of the axial ligands was performed in the case of complexes based on the **H₂L²** ligand.
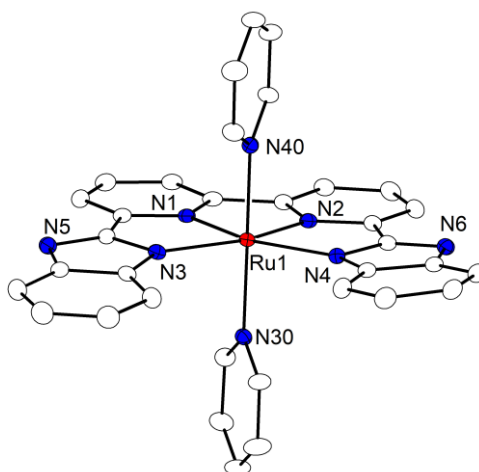
Figure 4.1. Molecular structure of **2**. Hydrogen atoms are omitted for clarity.

The integrity of the complexes was confirmed by 1D and 2D NMR spectroscopy and ESI-MS. A positive mode ESI mass spectrum of **2** showed a signal at m/z = 647.1 corresponding to the $[M+H]^+$ ion (Figure A76). The ^1H NMR spectrum of **2** in methanol-d_4 displays 10 distinct signals in the aromatic region corresponding to the equatorial ligand and two axial pyridines (Figure 4.2). From the integration and number of signals, it can be concluded that the complex has C_{2v} symmetry. The deshielded signal at 8.7 ppm is assigned to H-11 with the integration of two protons. The assignment of the remaining hydrogen and carbon atoms was possible by 2D NMR experiments (^1H-^1H COSY,^1H-^{13}C HMBC, and ^1H-^{13}C HSQC) (see Appendix). ESI-MS of **3** in methanol reveals a prominent peak at m/z = 649.2 corresponding to the $[M+H]^+$ ion (Figure A77). The ^1H NMR spectroscopy of **3** in methanol-d_4 shows 15 signals in the aromatic area. The number of signals and the ratio of the integrals represent a complex without C_2 symmetry. Three signals at 6.7, 7.9, and 8.5 ppm are attributed to the axial pyridines, suggesting a lower

symmetry of the complex (C$_s$). To get more insight into the structure of the complex in solution, the ^{1}H-^{1}H NOESY spectrum of **3** was recorded in methanol-d_4. The correlation between H-12 (positive, red) and H-8 which is highlighted as green boxes in Figure 4.3, indicates the formation of an *in, -out* isomer. Complexes **4** and **5** were also characterized with 1D and 2D NMR spectroscopy.
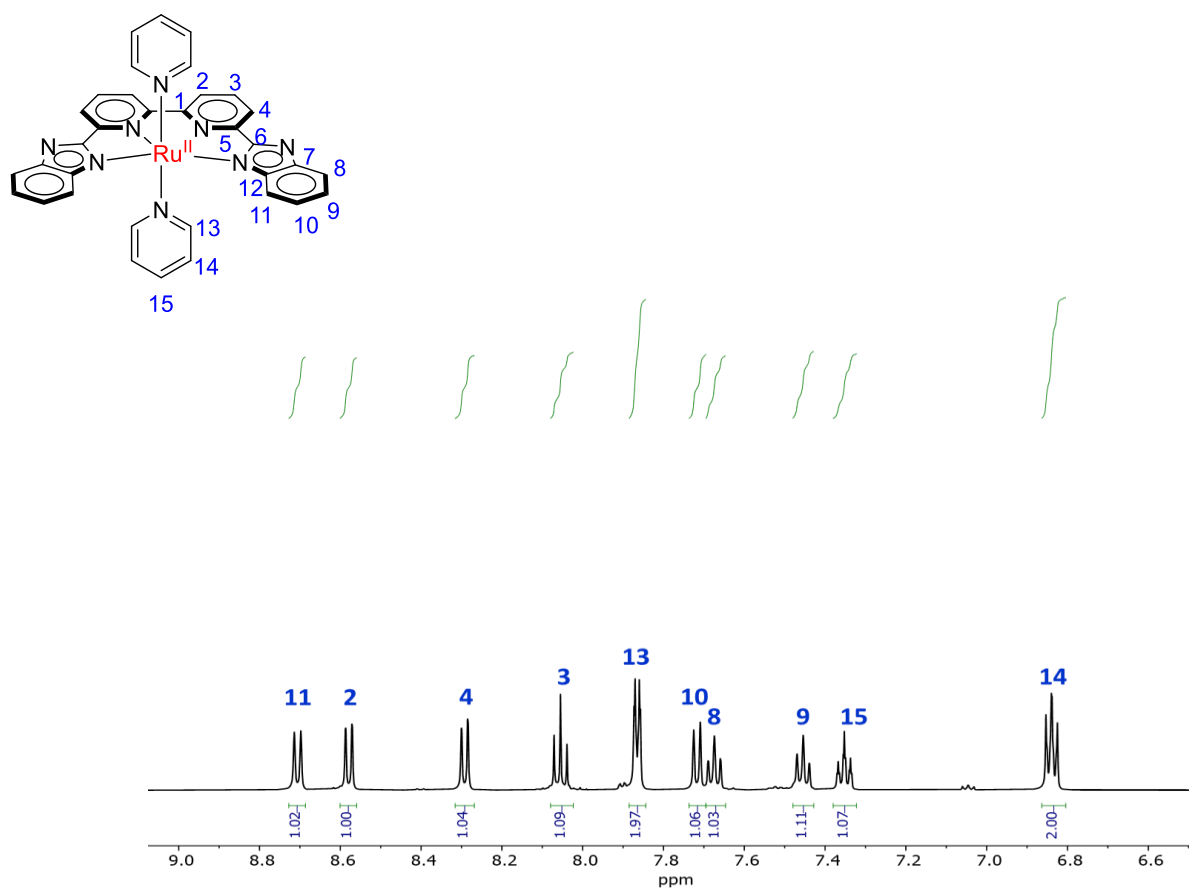
Figure 4.2. ^{1}HNMR spectrum of **2** recorded in methanol-d_4 affording ten signals in the aromatic region corresponding to the equatorial ligand backbone and axial pyridines. The signals were assigned with the help of 2D NMR spectroscopy.
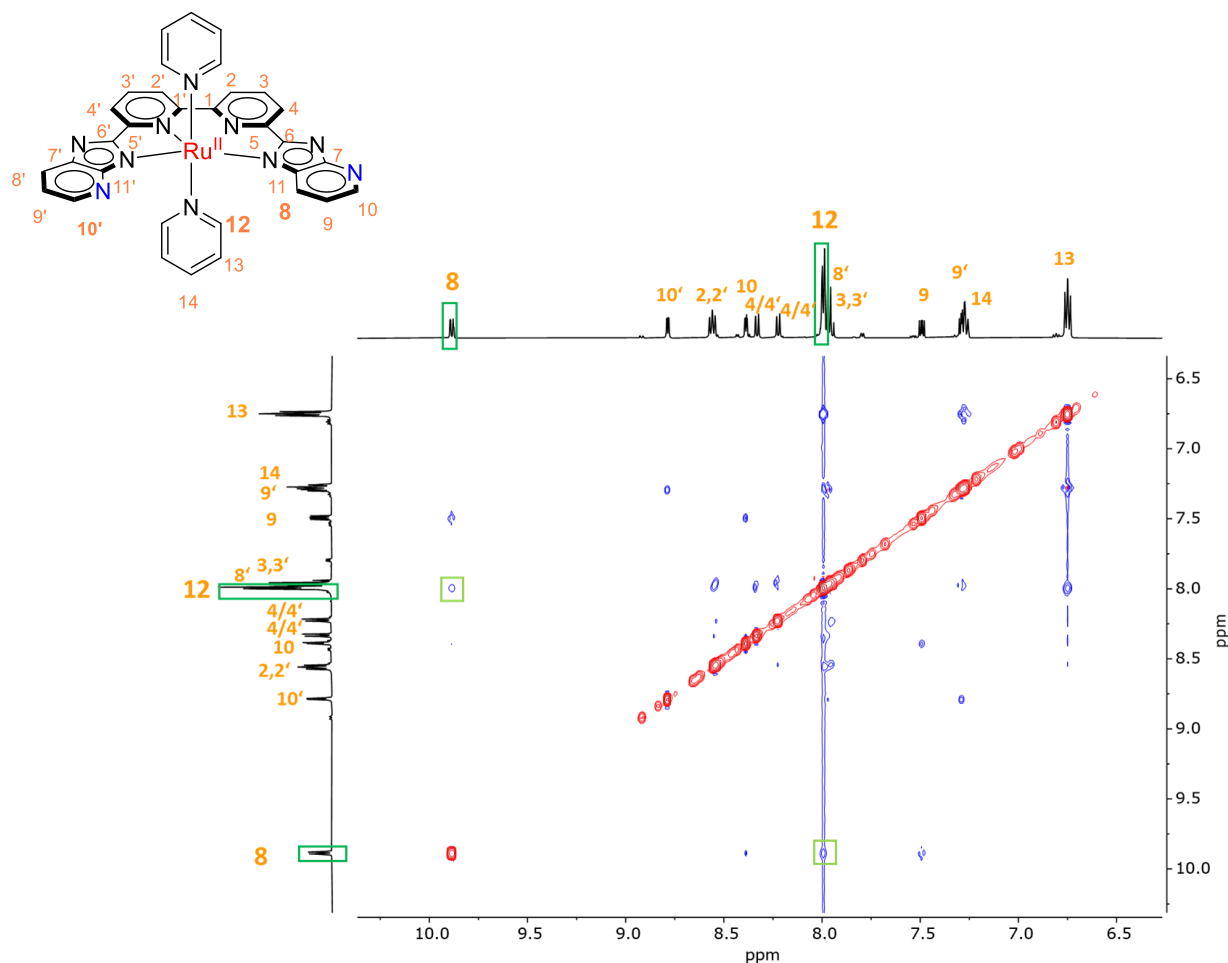
Figure 4.3. ^{1}H-^{1}H NOESY spectrum of **3** in methanol-d_4. The mentioned through-space interaction is depicted with small green boxes. The measurement was performed at room temperature.

To provide deeper insight into the integrity of complexes under acidic conditions, the protonated products were successfully synthesized by the addition of trifluoromethanesulfonic acid or hexafluorophosphoric acid to a solution of **2** or **3** in dichloromethane. Crystals of **[2H]PF₆** and **[2H₂](CF₃SO₃)₂**, in which either one side or both sides of the imidazole ring are protonated, were obtained by diffusion of diethyl ether into the solution of the product in methanol and further characterized by X-ray diffraction (Figure 4.4). The hydrogen atoms are disordered for N5 and N6 in **[2H]PF₆**. Analysis of bond distances between the ruthenium atom and inner pyridyls as well as ruthenium to outer imidazole groups reveals almost the same values as neutral complex **2**. Moreover, the angle of N3-Ru1-N4 in **[2H]PF₆** and N1-Ru1-N1' in **[2H₂](CF₃SO₃)₂** is widened by 33° similar to **2**, confirming the slight deviation from an ideal Octahedral environment.

The same procedure was followed for the crystallization of **[3H]CF₃SO₃** and **[3H₂](CF₃SO₃)₂,** however, the resulting crystals were not suitable for X-ray diffraction analysis.
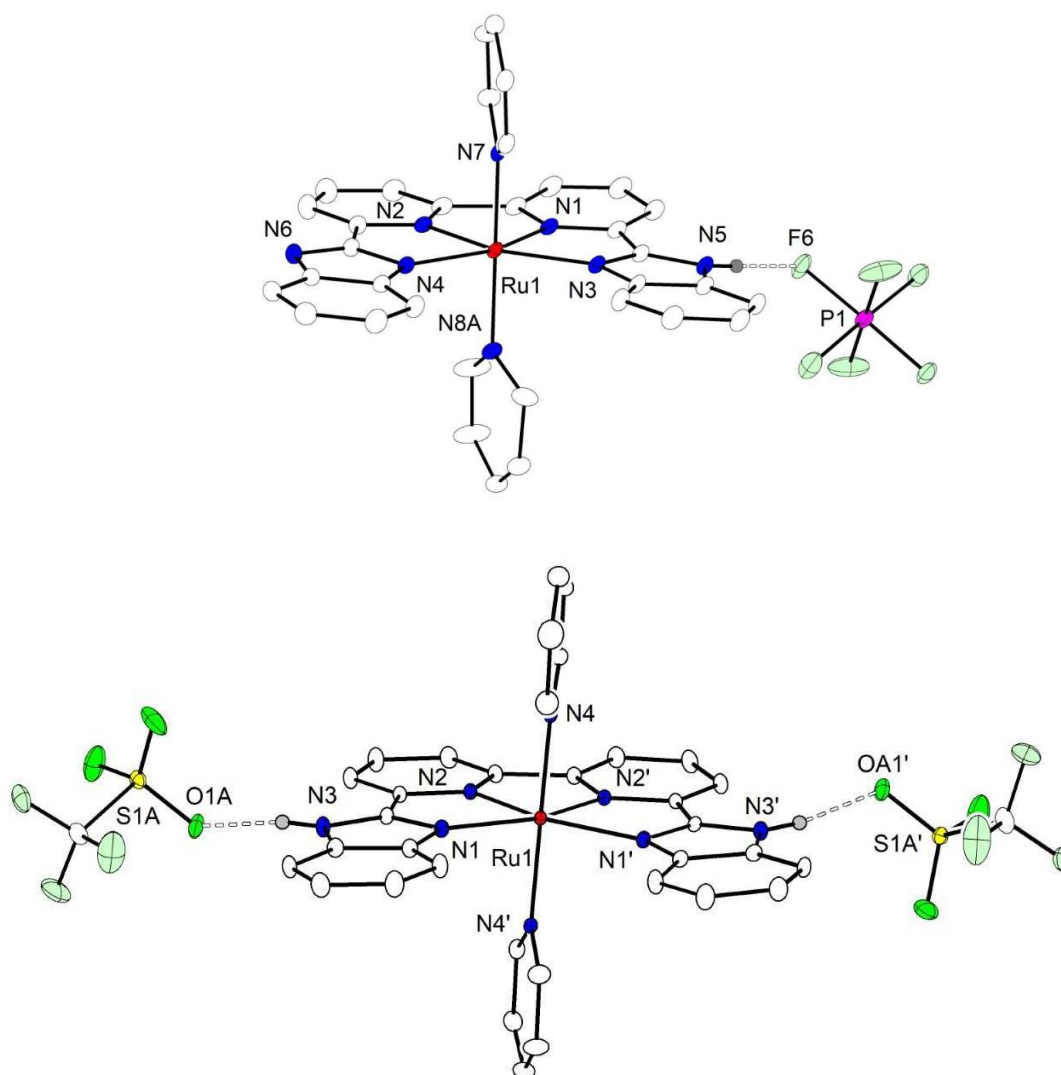
Figure 4.4. Molecular structures of **[2H]PF$_6$** (top) and **[2H$_2$](CF$_3$SO$_3$)$_2$** (bottom). Hydrogen atoms of the axial pyridines and backbone ligand except for the imidazole ring are omitted for clarity.

The in situ formation of the protonated products after the addition of one equiv. or excess amounts of HOTf to a solution of **2** or **3** in methanol was investigated by NMR spectroscopy. Increasing the charge of the complex from neutral to +1, resulted in a considerable deshielding of the protons (Figures 4.5 and 4.6). However, due to the fast exchange rate of protons on the NMR timescale, the spectrum still shows a symmetric structure, and only negligible changes in chemical shifts were observed upon the second protonation. All hydrogen and carbon resonances were assigned by means of 2D NMR spectroscopy (^{1}H-^{1}H-COSY, ^{1}H-^{13}C-HSQC, ^{1}H-^{13}C-HMBC)(see appendix).
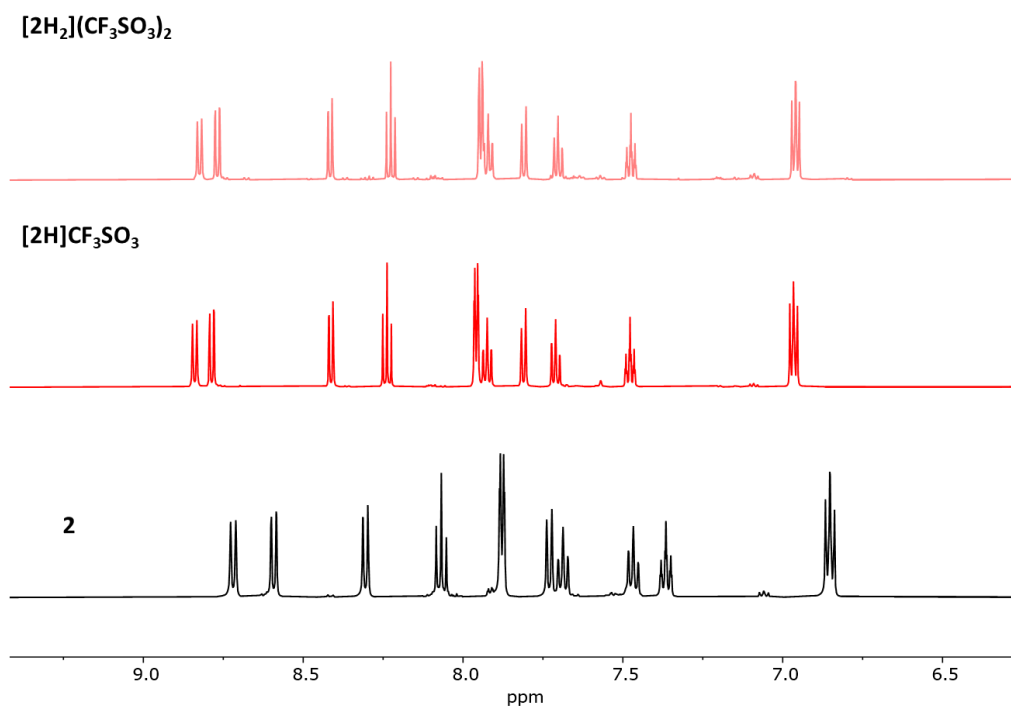
Figure 4.5. ^{1}H NMR spectroscopy of **2** before (bottom) and after the addition of 1 equiv. (middle) and 3 equiv. (top) of HOTf confirming the formation of protonated species. The spectra were recorded in methanol-d_4 at room temperature.
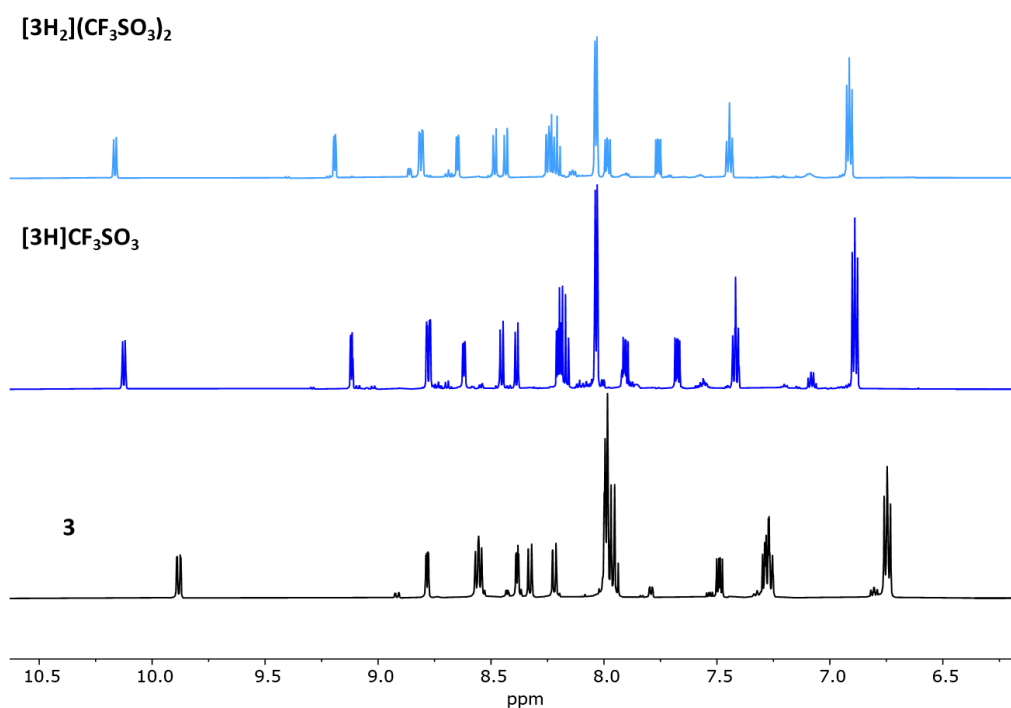
Figure 4.6. ^{1}H NMR spectroscopy of **3** before (bottom) and after the addition of 1 equiv. (middle) and 3 equiv. (top) of HOTf confirming the formation of protonated species. The spectra were recorded in methanol-d_4 at room temperature.

77

Additionally, the generation of protonated species was also confirmed by the addition of aqueous HOTf (0.1 M, pH = 1) to a solution of **2** or **3** in methanol, whilst monitoring the changes in UV/vis spectra. The spectrum of **2** shows absorption maxima at 331 and 384 nm along with broad bands at 490 and 556 nm (Figure 4.7-left). Addition of a stoichiometric amount of HOTf affords a slight shift in the band at 384 nm, while upon the addition of excess amounts of acid, the intensity of this shoulder (384 nm) decreases and a new band arises at 356 nm. To investigate the reversibility of this process, 2 equivalents of a strong base (1,5,7-Triazabicyclo[4.4.0]dec-5-en: TBD) were added to the mixture, which reversed the changes and gave a similar spectrum as **2**. The UV/vis spectrum of **3** displays two intense bands at 331 and 375 nm along with broad shoulders at 429, 495, and 560 nm (Figure 4.7-right). Upon addition of two equivalents of acid, the band at 331 slightly shifts the lower wavelengths and a new peak is observed at 355 nm. Reformation of the original species **3** was also achieved by the addition of base, TBD, (as mentioned above) to the solution at the end of the experiment.
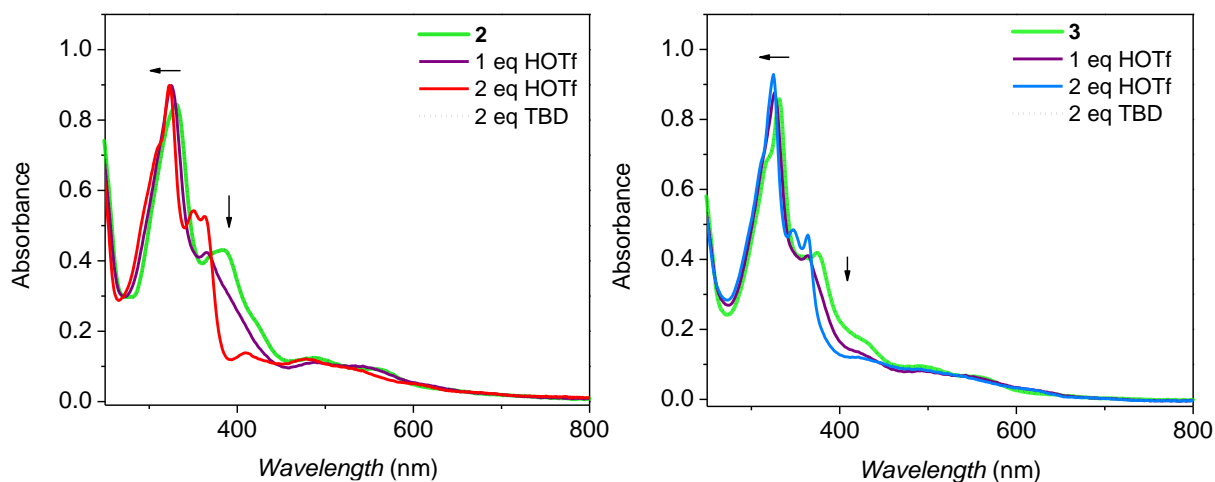
Figure 4.7. Spectral changes upon addition of HOTf and TBD into the solution of **2** (left) and **3** (right) in the UV-vis region (green: initial, dashed: after addition of base). The measurements were carried out in methanol at room temperature.

4-3 Electrochemical Investigation in Solution

The redox properties of complexes **2** and **3** were studied by cyclic voltammetry and square wave voltammetry in 1:1 mixture of aqueous HOTf (0.1 M, pH = 1) and 2,2,2-trifluoroethanol (TFE). The TFE was used in order to improve the solubility of complexes in aqueous media. The CV experiments exhibit a reversible redox wave at $E_{1/2}$ = 1.23 V (**2**) and $E_{1/2}$ = 1.16 V (**3**) vs. RHE corresponding to the one-electron process Ru^{II}/Ru^{III}, followed by a large electrocatalytic

current with onset potential above 1.4 V *vs.* RHE (Figure 4.8). The presence of this oxidation wave was supported by square wave voltammetry measurements which are depicted in the inset of Figure 4.8. The $E_{1/2}$ values of **2** and **3** are very similar to **I** and **V** (1.26 V and 1.18 V vs. RHE, respectively).[82] However, the measurements were carried out in different electrolytes in both cases (**I**: H_2O/CH_3CN (3:1 v/v), **V**: H_2O (pH = 6). The similarity of the redox potentials indicates the same electronic environment around the ruthenium metal center. The electrochemical stability of both complexes was explored by repetitive CV experiments within the potential region of 0.8-1.83 V *vs.* RHE at a scan rate of 50 mV/s. The peak current of the Ru^{II}/Ru^{III} redox wave gradually decreases in case of **2**, reflecting the decomposition of the complex, while **3** demonstrates relatively higher stability upon scanning within this potential range (Figure 4.9).
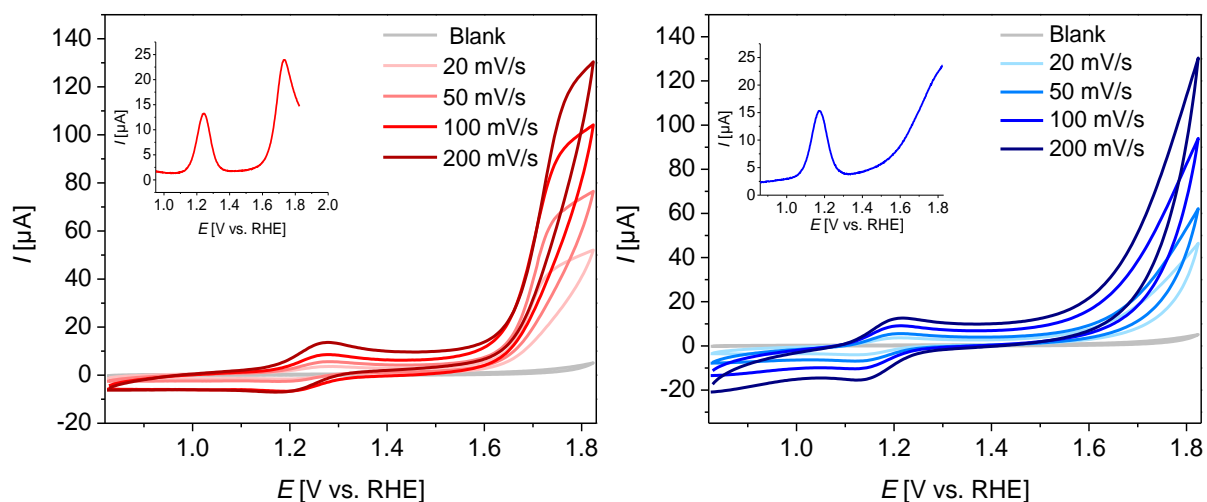
Figure 4.8. Cyclic voltammetry measurements of **2** (left) and **3** (right) at a concentration of 10^{-3} M in 1:1 mixture of aqueous HOTf (0.1 M, pH = 1) and TFE at different scan rates (20, 50, 100, 200 mV/s). The inset displays the square wave voltammograms. WE: glassy carbon, CE: platinum, and ref. SCE. All potentials are reported versus the RHE.
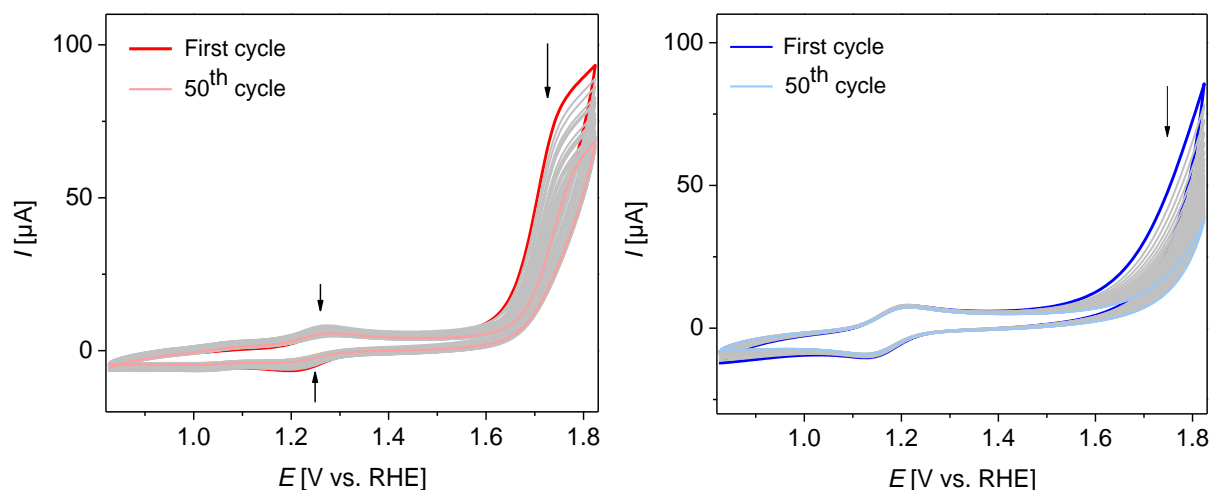
Figure 4.9. Repetitive CV measured of **2** (left) and **3** (right) in 1:1 mixture of aqueous HOTf (0.1 M, pH = 1) and TFE at a scan rate of 100 mV/s. WE: glassy carbon, CE: platinum, and ref. SCE. All potentials are reported versus the RHE. The decrease in catalytic current upon cycling is depicted as an arrow sign.

UV/vis-SEC measurements were performed to evaluate the reversibility of the first redox process (Ru^{II}/Ru^{III}) in 1:1 mixture of aqueous HOTf (0.1 M, pH = 1) and TFE. Upon oxidation of **2** at 1.35 V and **3** at 1.25 V vs. RHE, a slight decrease in band intensity at 320, 346, 362 nm is detected in the UV/vis spectrum (Figure 4.10). In addition, the broad band at 480 nm disappears after full oxidation to the Ru^{III} species. The final spectrum was obtained by electrochemical reduction of **2⁺** at 1.10 V and **3⁺** at 1.12 V vs. RHE. The identical spectroscopic features of the first (before oxidation) and the last UV/vis spectra (after re-reduction) indicate that this electrochemical oxidation is a reversible process.

To quantify the variation of the band intensity at 480 nm, a concentrated solution of **3** was prepared and subjected to chemical oxidation by the addition of 1.0 equiv. CAN. Sequential titrations with the oxidant led to a significant decrease in the intensity of this band after full conversion to the oxidized Ru^{III} species (Figure 4.11).
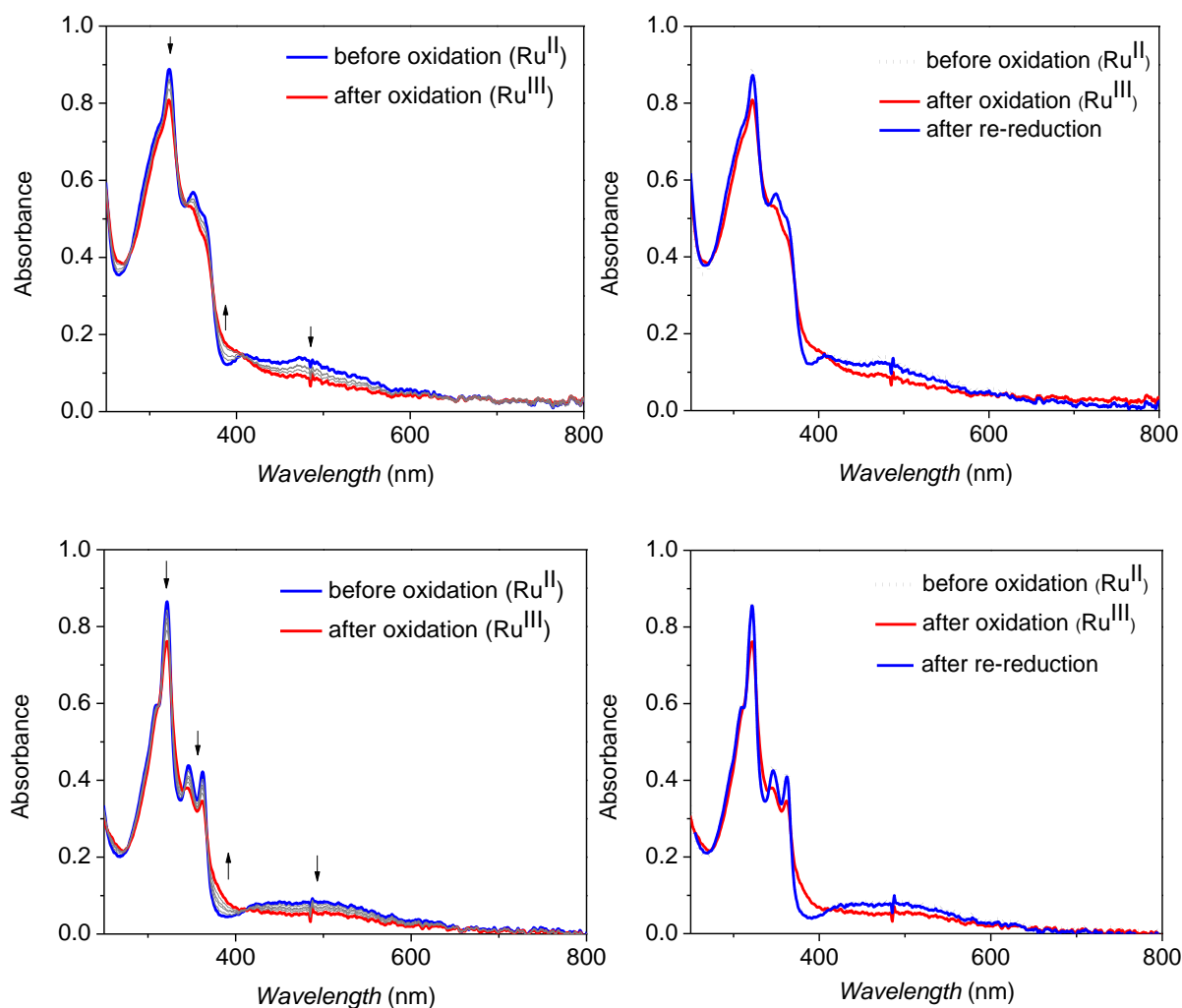
Figure 4.10. UV/vis SEC data for the electrochemical oxidation from Ru^{II} to Ru^{III} at an applied potential of 1.35 V for **2** (top-left) and 1.25 V vs. RHE for **3** (bottom-left). (Blue indicates before oxidation and red after oxidation process). UV/vis SEC spectra for re-reduction from Ru^{III} to Ru^{II} at 1.10 V for **2** (top-right) and 1.12 V vs. RHE for **3** (bottom-right). (Dashed lines: the initial spectra before applying potential). The measurements were conducted in 1:1 mixture of aqueous HOTf (0.1 M, pH = 1) and TFE. WE: platinum mesh, CE: platinum, and ref. SCE.
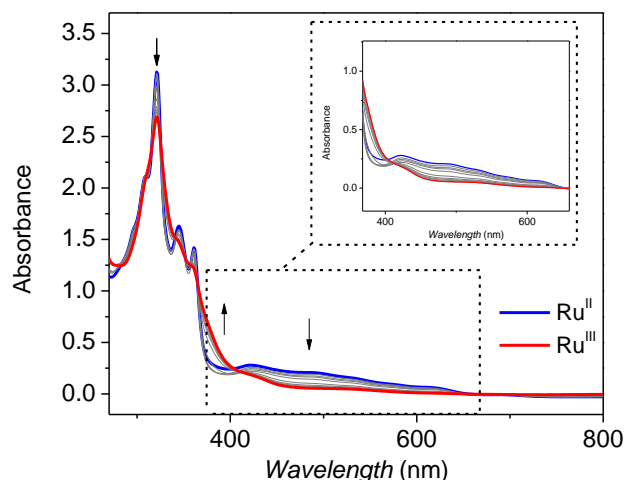
Figure 4.11. UV/vis spectra for the chemical oxidation of **3** from Ru^{II} (Blue) to Ru^{III} (Red) with 1 equiv. CAN in TFE. The oxidant was dissolved in aqueous HOTf (pH = 1, 0.1 M) and each spectrum was recorded after the addition of 0.1 equiv. CAN.

To get further insight into the redox properties of **4**, cyclic voltammetry and square wave voltammetry were recorded in an aqueous phosphate buffer (pH = 7), due to the higher solubility of the complex at this pH. The cyclic voltammogram shows a reversible redox wave at $E_{1/2}$ = 0.77 V *vs.* RHE corresponding to the Ru^{II}/Ru^{III} couple (Figure 4.12).
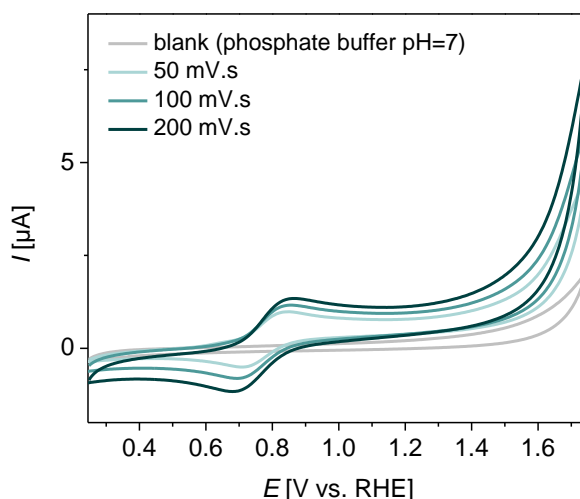
Figure 4.12. CV experiment of **4** in an aqueous phosphate buffer (pH = 7) at three different scan rates (50, 100, 200 mV/s). WE: GC, CE: Pt, ref. SCE. The potentials converted to RHE scale.

4.4 Chemical Water Oxidation Catalysis

To assess the catalytic performance of the complexes under homogenous conditions, a 1.0 mM solution of the complex was oxidized with a sacrificial oxidant in an acidic environment to fulfill the four-electron oxidation of water to molecular dioxygen. The oxidants should have

the reduction potential adequate for the chemically driven water oxidation experiment to mimic the conditions in artificial photosynthetic devices. CAN which serves as a 1e$^-$ oxidant, was used in course of this study due to its characteristic features such as high stability at low pH, commercial availability, and the possibility to investigate the WOCs with a high energy barrier.[133]

The catalytic proficiency of mononuclear complexes **2**, **3**, and **4** was investigated by the addition of 100 equiv. of CAN to the degassed aqueous HOTf (0.1 M, pH = 1) containing the complex (1.0 mM) at 25 °C. Under these conditions, the maximum TON (100 % efficiency) is 25. The gas produced during the experiment was monitored simultaneously by an oxygen sensor and an on-line manometry to confirm that the observed pressure is due to dioxygen production, not other gases such as CO_2 which can originate from the ligand degradation. The pressure differences between the reaction and a reference cell were converted to the number of dioxygen molecules via the general gas equation (*PV = nRT*). Then, the TON was determined by dividing the amount of the generated O_2 by the number of complexes.

All complexes exhibited low solubility in aqueous HOTf and were dissolved only after increasing the total charge of the complex via the addition of the oxidant. Complex **2** reveals a significant gap between the manometry (blue) and optical oxygen sensor (black) readings which indicates the formation of gases other than O_2 during the catalysis. In addition, some light yellow precipitates were detected over time after the addition of the oxidant (Figure 4.13). To check if degradation of the ligand causes this phenomenon or not, the formed gasses in the head space of the cell were analyzed by a GC-MS experiment which confirmed the presence of CO_2 gas (Figure A92). All these findings revealed the poor robustness of **H$_2$L^1,** which leads to a gradual degradation of the catalyst under catalytic conditions.
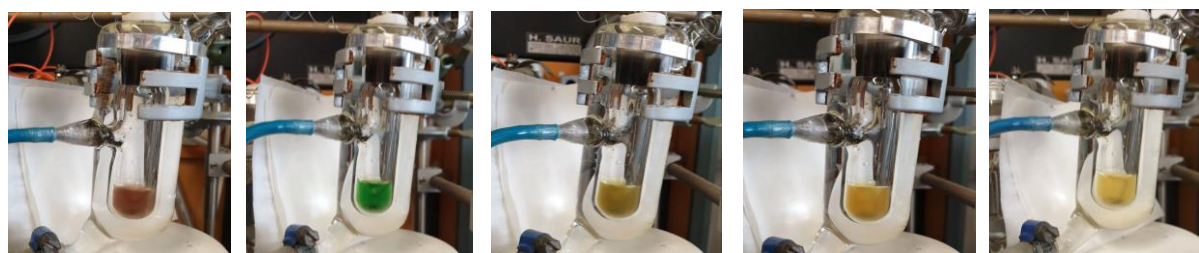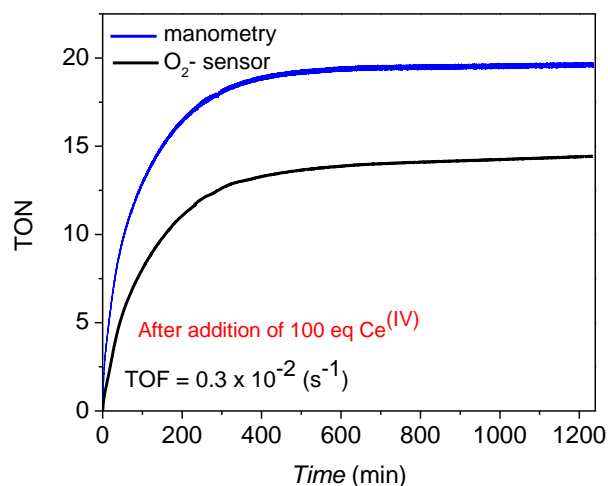
Time

Figure 4.13. Catalytic activity monitored by on-line manometry (blue) and O_2 sensor (black) of **2** in aqueous HOTf (pH = 1, 0.1 M) with the addition of 100 equiv. CAN resulting in TON_{max} of 25 (top). Pictures show a color change of the solution and the gradual formation of yellow solids after the addition of CAN (from left to right).

In contrast, complex **3** under identical conditions (in 0.1 M aqueous HOTf at 25 °C) reaches a turnover number of 20 after 20 minutes corresponding to an efficiency of 80%. The observed values for the manometry (blue solid) and the O_2 sensor (black solid) are in good agreement, indicating that dioxygen is the only formed gas during the catalysis (Figure 4.14). Slight delays were observed in the response of the oxygen sensor which is attributed to the slow diffusion of the produced oxygen from the solution to the gas phase and where the sensor is located. The afforded TOF value of **3** after the addition of 100 equiv. CAN is higher than the case of **2** and is similar to values reported for catalysts **I** (TOF = 0.025 s^{-1}) and **V** (TOF = 0.014 s^{-1}), but still is not comparable with catalysts based on bda and tda ligand scaffolds (TOF = 32 s^{-1}, 8000 s^{-1}, respectively). However, the latter values were obtained under different setups and conditions.[57,79,82,167] The efficiency of the system also increased from 50 to 80% from **2** to **3**.

These results demonstrate that the more robust chemically driven water oxidation catalyst can be achieved via modification of the ligand.
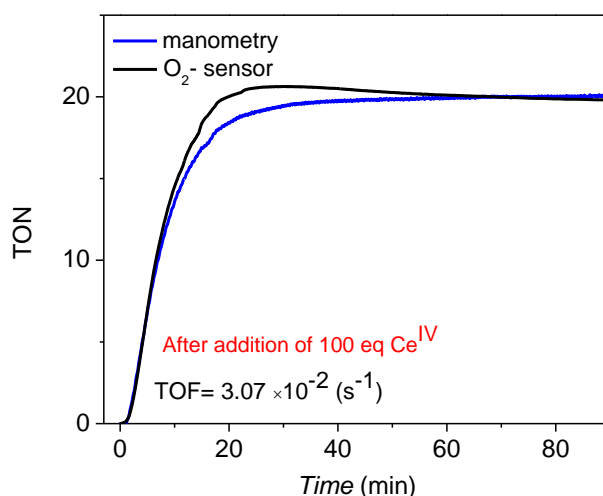
Figure 4.14. Chemical water oxidation catalysis with **3** upon the addition of 100 equiv. CAN into a solution of the complex in aqueous HOTf (0.1 M, pH = 1) at 25 °C. The oxygen evolution was monitored simultaneously by on-line manometry (blue) and optical oxygen sensor (black).

To detect any intermediates indicating the formation of N-O bonds similar to **I-O,O** and **V-O,O**,[82,167] the integrity of the catalyst species present in the solution after catalysis was investigated by mass spectrometry. The ESI-MS of the reaction mixture using **2** did not show any distinctive signals corresponding to the isotopic pattern of ruthenium, which indicates the oxidative decomposition of the catalyst during chemical water oxidation. In the case of **3**, any peak contributing to the mass of the complex plus additional oxygen atoms was not detected and the main signal at m/z = 490.1 is assigned to the complex without axial pyridines (Figure 4.15). In addition, complex **3** was reacted with trimethylamine N-oxide under reflux conditions to probe the capability of the ligand system for N-O formation. However, the characterization of the reaction products did not show any evidence of ligand oxidation and the complex remained intact. Therefore, triggering of the O-O bond formation via the OAT mechanism is unlikely here. The noticeable change in the catalytic activity of **3** compared to **2** can be explained by replacing the C-H units of outer phenyls with more electronegative nitrogen atoms, which decrease the electron density and make the oxidation more difficult.
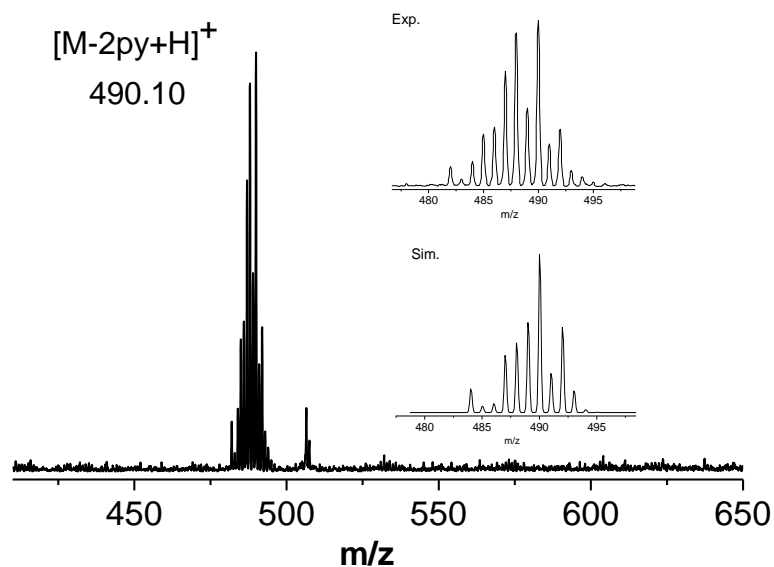
Figure 4.15. ESI-MS of **3** after chemical water oxidation experiment measured in methanol (positive mode). The inset exhibits the expansion of the [M-2py+H]$^+$ signal at 490.1 and the simulation.

To get insight into the nature of the chemical water oxidation mechanism, the amount of produced oxygen is plotted versus time for various catalyst concentrations ranging from 0.37-1.77 mM (Figure 4.16-left). The experiments were performed by the addition of 100 mM CAN to **3** in 0.1 M aqueous HOTf (pH = 1) while monitoring the gas pressure by on-line manometry. The initial rate of oxygen evolution obtained by the linear fit of the first 80 seconds is plotted versus the concentration of the catalyst after the addition of the oxidant (Figure 4.16-right). Based on the linear dependency on the concentration, it can be concluded that the chemically driven water oxidation mechanism is first-order with respect to the amount of **3** in acidic conditions.
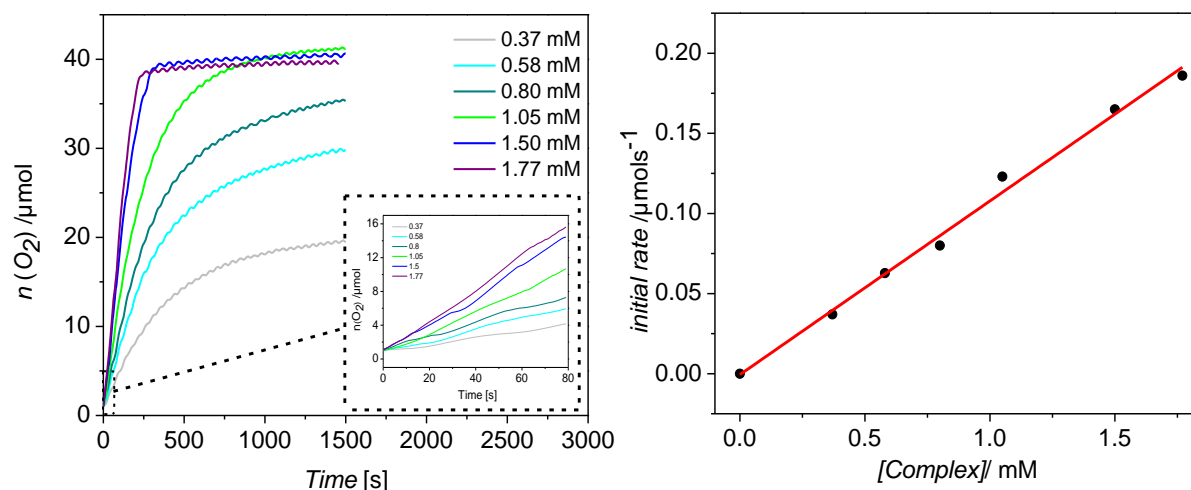
Figure 4.16. The oxygen evolution recorded by on-line manometry after the addition of CAN to the aqueous HOTf (0.1 M, pH = 1) containing **2** at various concentrations (0.37 grey, 0.58 aqua, 0.8 green, 1.05 lime, 1.5 blue, 1.77 mM purple). The inset depicts the first 80 s of oxygen generation (left). The initial rate of chemical water oxidation for the first 80 seconds versus catalyst concentration (right).

A significant decrease in catalytic activity was observed after the substitution of the axial pyridines with isonicotinic acid (Figure 4.17). The manometry experiment shows a TON of 4 corresponding to an efficiency of 16% after the addition of 100 equiv. CAN to an aqueous HOTf (0.1 M, pH = 1) containing complex **4** at 25 °C. Comparison of the manometry and the oxygen sensor indicates the formation of gases other than dioxygen during the chemical water oxidation catalysis. It should be mentioned that the experiment stopped before completing a full cycle of the water oxidation process due to the slow rate of oxygen generation. Several explanations can be proposed regarding the deactivation of **4** during the experiment. One might be attributed to the ligand degradation and transformation into other inactive species which were also observed for some reported ruthenium WOCs.[170] Anation side reactions using CAN as the sacrificial oxidant can also impact the rate of O-O bond formation.[62,171] Inhibition of the catalysis in the case of **4** is more likely due to the presence of the carboxylic acid substituents which can coordinate to the ruthenium active site of another complex via intermolecular interactions thus ceasing the reactivity. Based on these findings, it can be concluded that complex **4** is a poor catalyst for chemically driven water oxidation catalysis under homogenous conditions.
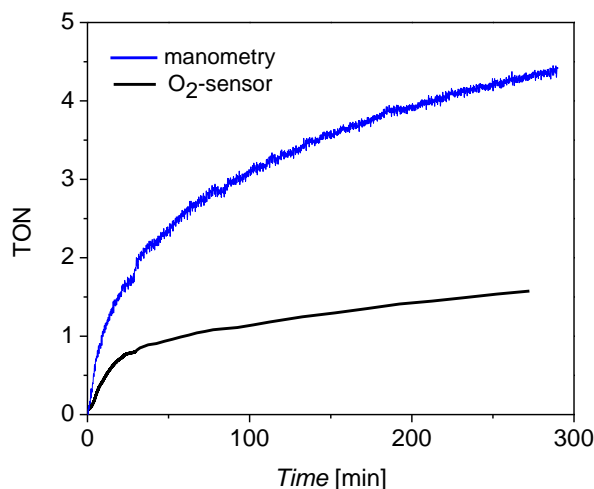
Figure 4.17. Catalytic performance of **4** monitored by manometry (blue) and optical oxygen sensor (black) in aqueous HOTf (0.1 M, pH = 1) using 100 mM CAN as sacrificial oxidant at 25 °C (TON_{max} = 25, 100% efficiency).

4.5 Immobilization of the Mononuclear Complex 4 on Mesoporous ITO

The mesoITO electrodes were prepared following the procedures described in the experimental chapter. After cleaning the ITO glasses, the coating of mesoITO on the slides was performed via the doctor blading method. After two annealing steps at 500 °C and 300 °C the slides were cut in the proper dimension, and the resulting sheds were soaked in a methanolic solution containing complex **4** (1 mM) for 24 h. To remove any free and non-immobilized complexes from the electrode surface, the slides were rinsed with methanol.

To investigate the electrochemical properties of the immobilized complex on the oxide surface, the prepared ITO|*meso*ITO|**4** was immersed in a three-electrode setup using aqueous HOTf (0.1 M, pH = 1) as the electrolyte. Detachment of the complex from the surface was observed as soon as the electrode was soaked in the electrolyte solution. To resolve the solubility issue, the measurement was conducted in an aqueous phosphate buffer (pH = 7) which displayed the same results as under acidic conditions. The high solubility of **4** in an aqueous solution prevented any further studies of the immobilized hybrid catalysts.

Figure 4.18. Representation of the ITO|*meso*ITO|**4** electrodes before, after immersion in aqueous HOTf (0.1 M, pH = 1), immersion in an aqueous phosphate buffer (pH = 7), and after rinsing with methanol to remove the nonimmobilized species (from left to right).

4.6 Conclusion and Summary

To alleviate the synthetic efforts which are required for the preparation of the dinuclear WOCs, a series of mononuclear ruthenium complexes based on two tetradentate N-donor ligands were synthesized and their catalytic performance was investigated in solution. The formed complexes were characterized by 1D, 2D NMR spectroscopy, ESI(+)-MS spectrometry, and the structure of **2** and its protonated species (**[2H]PF$_6$** and **[2H$_2$](CF$_3$SO$_3$)$_2$**) was confirmed by X-ray diffraction. The proton resonances in the ^{1}H NMR spectra of complexes based on **H$_2$L^2** indicated the formation of an *in,-out* isomer in the solution. In addition, the through-space interactions of the proton next to the nitrogen atom of the phenyl group and the axial pyridines were confirmed by ^{1}H-^{1}H NOESY measurement. Electrochemical analysis of **2** and **3** exhibited a reversible redox wave corresponding to Ru^{II}/Ru^{III} couple which was followed by a catalytic water oxidation current at higher potential. The chemical reversibility of the first wave was further investigated by UV/vis-SEC, which confirmed that the spectrum before oxidation is fully recovered after oxidation and subsequent reduction.

The chemical water oxidation properties of complexes **2** and **3** were investigated in acidic conditions using CAN as the sacrificial oxidant (with a maximum TON of 25 in case of 100% efficiency). It revealed that the complex based on **H$_2$L^1** undergoes rapid deactivation, likely via the degradation of the ligand, because CO$_2$ gas was detected upon chemical treatment with CAN. In contrast, a TON of 20 (efficiency of 80%) was observed for **3** after the addition of 100 equiv. CAN into the solution. The good agreement of the manometry and O$_2$ sensor data excluded the generation of any gases other than dioxygen during the catalysis. The initial rate of catalysis for various concentrations of **3** demonstrated a first-order dependency of water oxidation on the catalyst concentration.

Several attempts were made to characterize the active intermediates in the case of **3** which were not successful so far. However, the project is still ongoing and further experiments need to be conducted to fully rationalize the higher catalytic activity of **3**.

In order to construct the hybrid materials for catalysis with immobilized active species, complex **4** was synthesized after some modifications in the synthetic procedure and characterized by NMR spectroscopy, and electrochemically in phosphate buffer solution. Inspired by previous works on immobilization of Ru$_2$-WOCs based on the bbp$^-$ ligand scaffold on oxide surfaces,[114,115] **4** was successfully attached on an ITO|*meso*ITO electrode via the growing process. However, gradual leaching of the complex from the *meso*ITO surface was observed after immersion of the electrode into the electrolyte solution in both acidic and basic conditions, which prevented any electrochemical characterization. The bbp-based ruthenium WOC equipped with a carboxylate anchoring group at the pyrazole-C^4 position was also found to desorb from the electrode surface at low applied potentials below the oxygen evolution onset.[114]

5 Immobilization of a triethoxysilyl-Derivatized bbp-Ru$_2$ Complex on Oxide Surfaces

5.1 Introduction

As previously described in the introduction, a systematic investigation regarding the stability of the bbp-based diruthenium complexes immobilized on metal oxides via different functional groups such as carboxylate and phosphonate has been conducted in the group of F. Meyer.[114,115] The evaluation of the hybrid's integrity by RRDE experiments revealed the low stability of these anchors under catalytic conditions, which restricts their application in water splitting devices. Several factors need to be considered for the development of efficient anchoring groups. These include oxidative resistance under a variety of pH conditions, effective charge transfer from the catalyst via the support interface, and minimal leaching from the surface. Recently, several alternative anchoring groups were reported in the literature which display higher binding stability and electron injection efficiency in comparison with commonly used anchors (*e.g.* carboxylic acids and phosphonic acids). Hydroxamic acids, silatranes, and silanes show an outstanding affinity for the metal oxide surfaces and more stablity against hydrolysis. In 2018, T.J. Meyer's group presented a stable hybrid anode consisting of the bda-based complex immobilized on mesoporous ITO electrode using triethoxysilyl groups attached to the axial pyridines (see section 1.5.1). Inspired by this work and to overcome the leaching issue observed for the carboxylate and phosphonate cases, herein we equipped the bbp-Ru$_2$ complex with four 4-(4-(triethoxysilyl)butyl)pyridine axial ligands. The following chapter discusses the synthesis, characterization, and immobilization of the new modified complex on *meso*ITO electrodes. In addition, its electrocatalytic water oxidation proficiency in the heterogonous phase is assessed.

5.2 Synthesis of bbp-Ru$_2$ Complex Equipped with 4-(4-(triethoxysilyl)butyl)pyridine

The bis(bipyridyl)pyrazolate ligand and dinuclear ruthenium complex containing dmso, chloride, and water ligands were prepared according to procedures adapted from the literature.[97,172] The reaction was initiated via the slow addition of **^{H}bbpH** to a concentrated

solution of RuCl$_2$(dmso)$_4$ in EtOH and NEt$_3$ under reflux conditions. After cooling down the mixture to 0 °C, the brown precipitates were filtered off and treated with sodium acetate in a mixture of acetone and H$_2$O to introduce the acetate bridge. The addition of **5-3** in EtOH at a late stage of the synthesis resulted in the formation of the desired complex **1**$^{4Si(OEt)3}$ with four anchoring groups at the axial positions. The modified pyridine ligand was synthesized by the reaction of 4-picoline (**5-1**) with 3-bromoprop-1-ene leading to 4-(but-3-en-1-yl)pyridine (**5-2**) which was subsequently treated with triethoxysilane to form the terminal triethoxysilyl group (**5-3**) (Scheme 5.1).
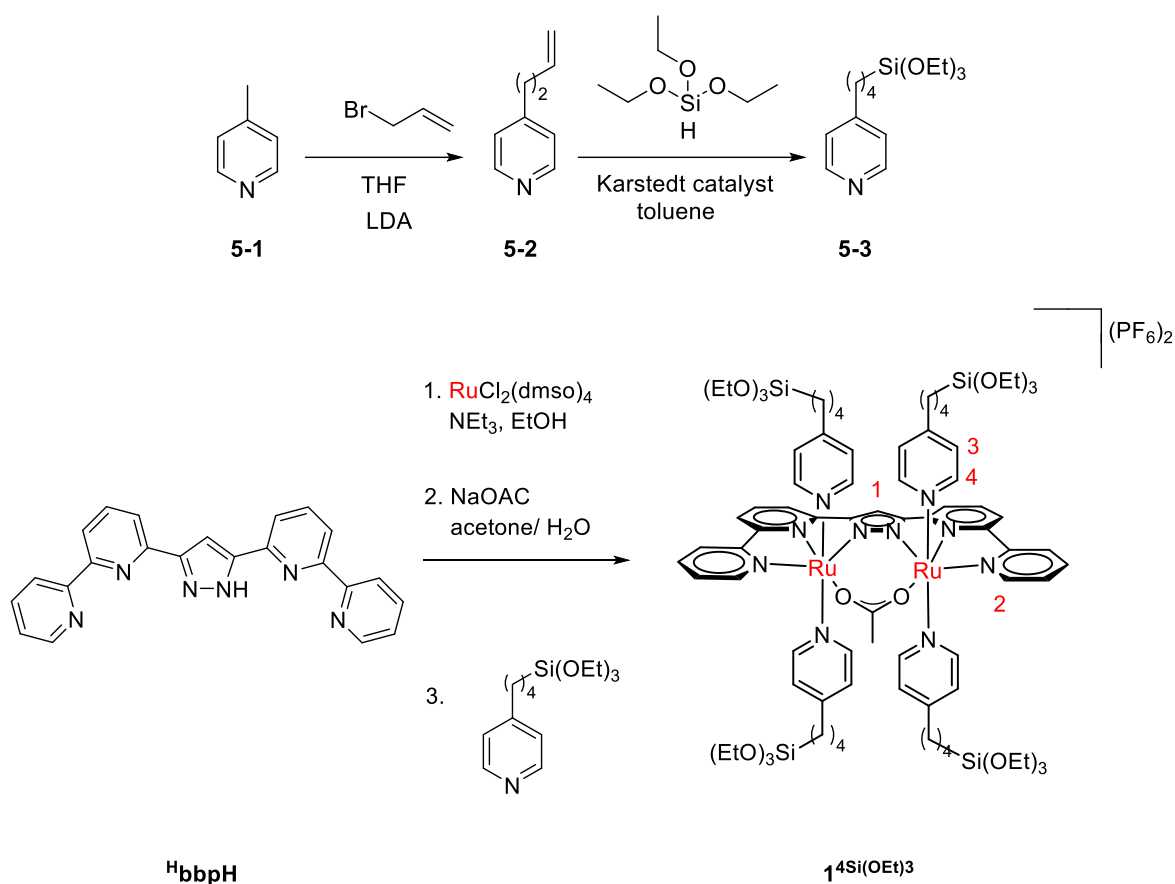
Scheme 5.1. Synthetic procedure for the modified pyridine (**5-3**) and complex **1**$^{4Si(OEt)3}$.

^{1}H NMR spectroscopy of **1**$^{4Si(OEt)3}$ in chloroform shows 17 distinct proton signals in both the aromatic and aliphatic regions corresponding to a C$_{2v}$ symmetric complex (Figure 5.1). The singlet resonance at 2.97 ppm is attributed to the methyl group of the acetate bridge. Comparing the chemical shift of this characteristic signal to the parent complex **^{Me}bbp-Ru$_2$(OAc)**[97]revealed that the electronic properties of the ruthenium centers are not influenced by the anchoring groups. The hydrogen and carbon signals are fully interpreted with the help of 2D NMR spectroscopy. The signals at 7.05 and 8.42 ppm can be assigned to the free **5-3**

which remained as an impurity in the final product. The high binding affinity of the triethoxysilyl groups to the alumina or silica gel prevented further purification by column chromatography. In addition, the triethoxysilyl groups can be easily hydrolyzed in presence of protic solvents such as methanol. The integrity of the complex in THF was examined by positive ion ESI-mass spectrometry which displays the target peak at m/z = 913.3 corresponding to the $[M-PF_6]^{2+}$ ion (Figure A78). Other signals at m/z = 749, 768.3, 814.6, 830.9, 851, 877.2, 897.3 are assigned to the partially hydrolyzed species.
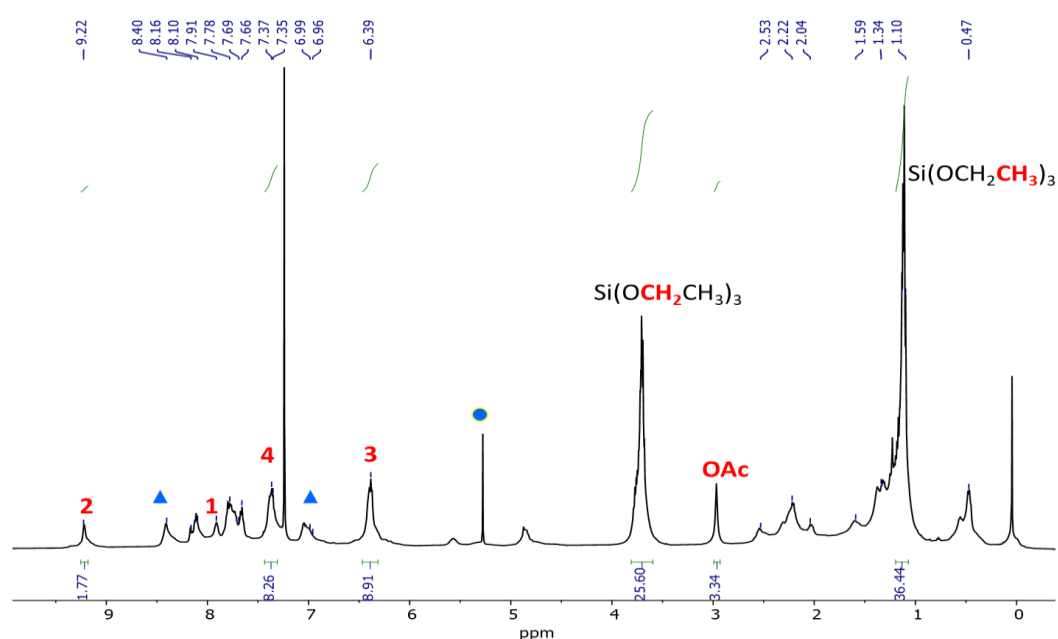
Figure 5.1. ^{1}H NMR spectroscopy of **1$^{4Si(OEt)3}$** in chloroform-*d* at room temperature. The blue dot is related to the residual solvent peak and the triangles to the excess **5-3**.

5.3 Electrochemical Characterization in Solution

The electrochemistry of **1$^{4Si(OEt)3}$** was investigated by cyclic voltammetry and square wave voltammetry in MeCN containing NBu₄PF₆ at room temperature. The spectrum portrays two sequential redox events which occurred at $E_{1/2}$ = 0.9 V and $E_{1/2}$ = 1.3 V *vs.* RHE. The first wave corresponds to the one-electron couple Ru^{II}Ru^{II}/ Ru^{II}Ru^{III} and the second one to the couple Ru^{II}Ru^{III}/ Ru^{III}Ru^{III} (Figure 5.2). The SWV was also conducted under identical conditions (MeCN, NBu₄PF₆) (inset-Figure 5.2). The redox processes are separated by $\Delta E_{1/2}$ = 0.4 V and their reduction potentials are in the same range of the parent complex **^{Me}bbp-Ru₂(OAc)** ($E_{1/2}$= 0.88 V and $E_{1/2}$= 1.28 V *vs.* RHE). This observation indicates that the triethoxysilyl substituents do not affect the electronic structure of the ruthenium cores. The linear dependence of the peak

current (i_p) on the square root of scan rates is exhibited in Figure 5.3, which displays a reversible behaviour. The peak-to-peak separation (ΔE_p) is around 160 mV and 100 mV for the first and second wave, respectively, which deviate from the reversible behavior based on the *Nernst* equation (59 mV for one-electron transfer).
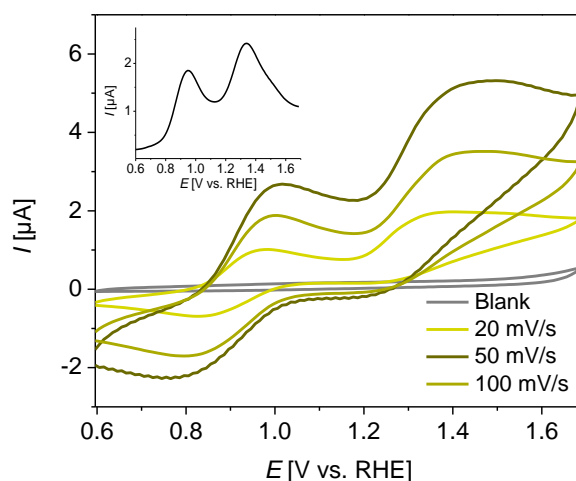
Figure 5.2. Cyclic voltammetry of **1**$^{4Si(OEt)3}$ in acetonitrile (NBu₄PF₆) at various scan rates. WE: GC, CE: Pt, Ref. Ag wire. The inset exhibits the SWV within the same potential range 0.6-1.7 V vs. RHE. All potentials are referenced versus RHE.
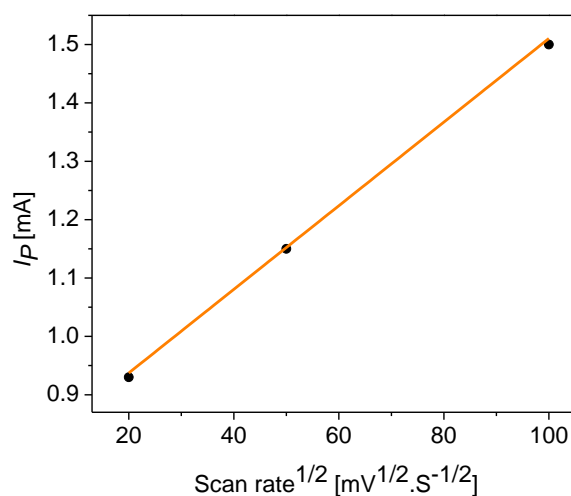
Figure 5.3. Dependency of the peak current on the scan rate (20, 50, 100 mV/s) for **1**$^{4Si(OEt)3}$.

An additional experiment that can provide more information about the nature of the redox events is UV/vis-SEC. Before applying any potential, the UV/vis spectrum of **1**$^{4Si(OEt)3}$ was recorded in propylene carbonate (NBu₄PF₆) representing some characteristic absorption bands at 382 nm and 546 nm which were also observed for the parent complex **^{Me}bbp-Ru₂(OAc)**. Then, a potential of 1.1 V *vs.* RHE corresponding to the first oxidation wave was applied and the variations in UV/vis band intensity were continuously monitored. Upon

oxidation to Ru^{II}Ru^{III}, the absorptions at 382 nm and 546 nm significantly decreased and a new band formed at 283 nm. Subsequently, the re-reduction spectrum for the Ru^{II}Ru^{II} species was obtained by decreasing the potential to 0.7 V *vs.* RHE. Surprisingly, it took 13 h to fully recover the original spectrum indicating a very slow electron transfer process that may possibly be imposed by the triethoxysilyl substituents. (Figure 5.4).
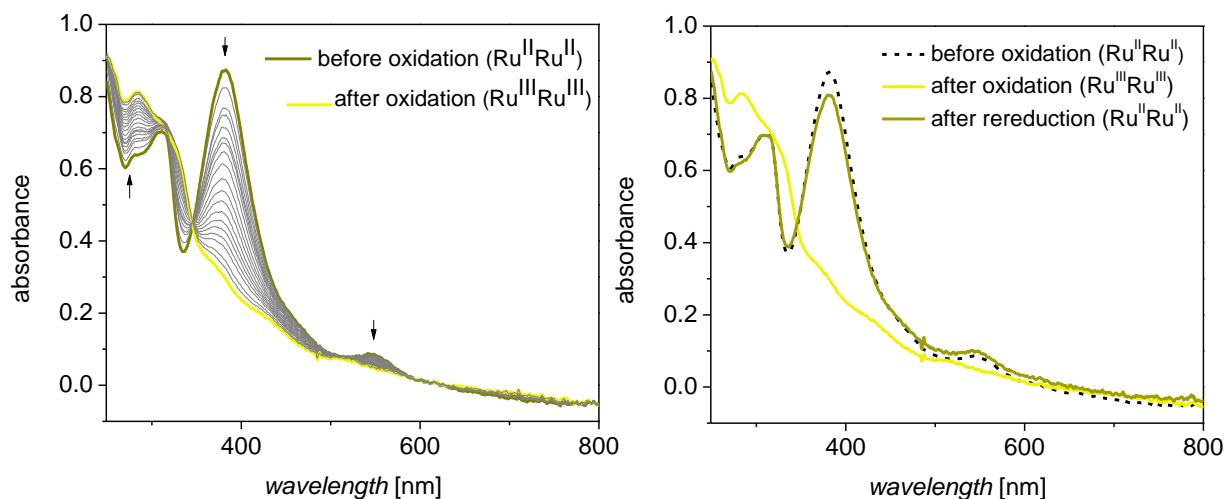
Figure 5.4. UV/vis spectroelectrochemistry experiment of **1$^{4Si(OEt)3}$** in propylene carbonate (NBu₄PF₆) by applying 1.1 V *vs.* RHE for oxidation from Ru^{II}Ru^{II}/Ru^{II}Ru^{III} (left) followed by the re-reduction to reproduce the initial spectrum at 0.7 V *vs.* RHE (right). WE: platinum net, CE: platinum wire, Ref. MSE.

5.4 Immobilization of 1$^{4Si(OEt)3}$ on Mesoporous ITO Electrode

The *meso*ITO slides were prepared by the doctor blade technique which was described in chapter 4. The absorption of the complex on the surface was carried out via the soaking of the ITO|*meso*ITO electrode in a 1.0 mM solution of **1$^{4Si(OEt)3}$** in EtOH overnight. Subsequently, the electrode was rinsed with methanol and water to remove the unattached complexes.

The electrochemical features of ITO|*meso*ITO|**1$^{4Si(OEt)3}$** as the working electrode were investigated by cyclic voltammetry in an aqueous solution using 0.1 M aqueous HOTf (pH = 1) as electrolyte. As expected, two redox waves were observed at $E_{1/2}$ = 0.8 and $E_{1/2}$ = 1.2 V vs. RHE corresponding to the sequential one-electron couples Ru^{II}Ru^{II}/Ru^{II}Ru^{III} and Ru^{II}Ru^{III}/Ru^{III}Ru^{III} which are very similar to the redox potentials under homogenous conditions (Figure 5.5). As shown in Figure 5.6, the peak current linearly increased with the scan rate based on the *Randles–Sevcik* equation (5.1), indicating electrochemical reversibility of the first redox event.

$$i_p = \frac{n^2 F^2}{4RT} v A \Gamma \quad (5.1)$$

Where i_p is the peak current, n is the number of transferred electrons in the redox process, R is the ideal rate constant, T is temperature, F is *faraday* coefficient, v is scan rate, A is the surface of the electrode, and Γ is the surface coverage of the attached complex which can be determined by integration of the peak area of the redox wave.
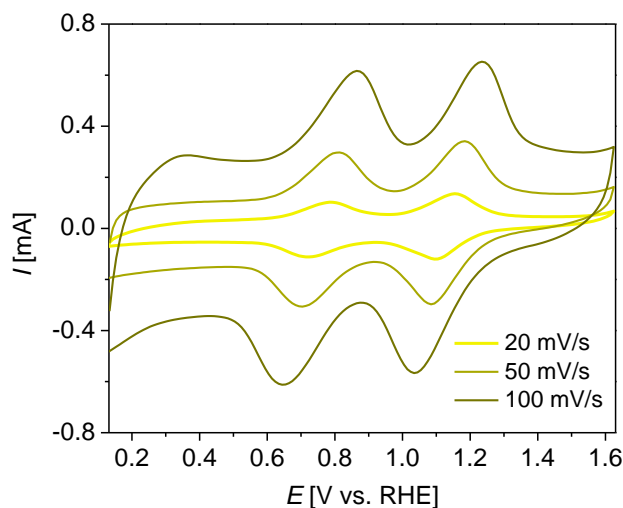
Figure 5.5. CV measurement of ITO|*meso*ITO|**1**$^{4Si(OEt)3}$ implemented as working electrode at various scan rates (20, 50, 100 mV/s) in 0.1M aqueous HOTf (0.1 M, pH = 1). CE: Pt, Ref. MSE. All potentials are referenced versus RHE.
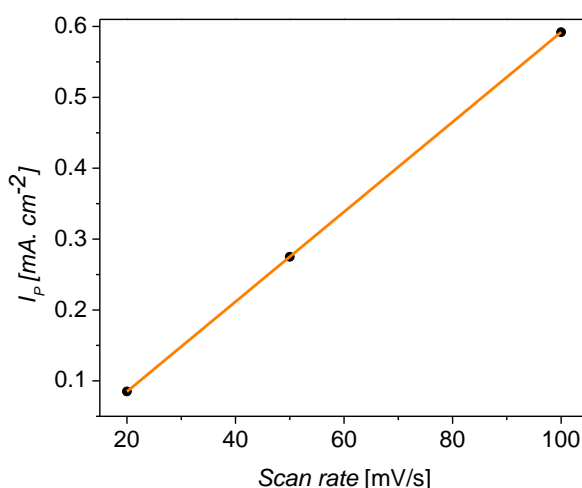
Figure 5.6. The plot of peak current versus scan rate for ITO|*meso*ITO|**1**$^{4Si(OEt)3}$ WE.

In order to evaluate the catalytic activity of the hybrid, the CV of ITO|*meso*ITO|**1**$^{4Si(OEt)3}$ was recorded in the potential range of 0.4-1.8 V *vs.*RHE. Surprisingly, no current from water oxidation catalysis was achieved within this potential range and further potential increases

did not improve the reactivity of the complex (Figure A86). The low reactivity of the catalyst may be originated from the slow acetate exchange by water molecules or hydrophobic features of anchoring groups which may block the active site for water coordination. The amount of anchored complex on the surface can be estimated based on the peak current of each redox process. Twenty CV cycles were performed under identical conditions (pH = 1, at room temperature) to assess the stability of the adsorbed species. A gradual decrease of current was observed for the first oxidation wave, suggesting the detachment of the catalyst from the electrode surface (Figure 5.7).
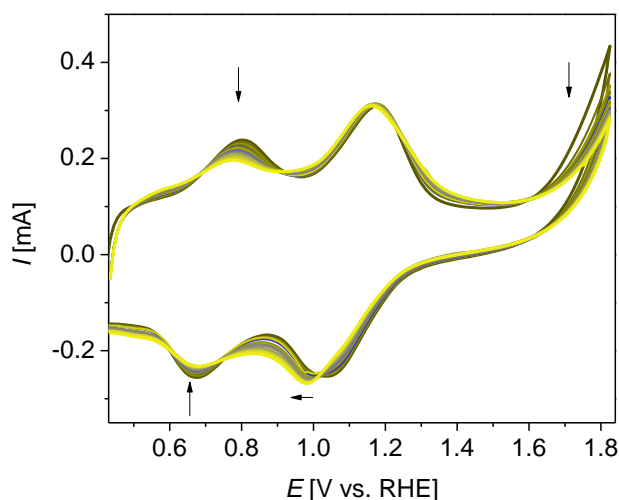
Figure 5.7. Repetitive cyclic voltammetry of ITO|*meso*ITO|**1**$^{4Si(OEt)3}$ WE in aqueous HOTf (0.1 M, pH = 1) at a scan rate of 50 mV/s. WE: GC, CE: Pt, Ref. MSE. All potentials are referenced versus RHE.

5.5 Conclusion and Summary

In summary, an acetate-bridged diruthenium complex based on the rugged bbp$^-$ ligand scaffold bearing axial pyridines with appended triethoxysilyl groups was synthesized and characterized by NMR spectroscopy and ESI-MS. Easy hydrolysis of the triethoxysilyl groups in protic solvents hampered the formation of single crystals suitable for X-ray diffraction. To investigate the effect of the anchors on the electronic properties of the complex, cyclic voltammetry and square wave voltammetry were conducted in solution (MeCN containing NBu$_4$PF$_6$). Observing the same reduction potentials as for the related complex with parent pyridine as an axial ligand (**^{Me}bbp-Ru$_2$(OAc)**) reflects the fact that the peripheral anchoring groups do not influence the electrochemical properties of the ruthenium ions. The electrochemical reversibility of the first redox wave was assessed by UV/vis SEC indicating a very slow electron transfer. Complex **1**$^{4Si(OEt)3}$ was successfully anchored on a *meso*ITO

electrode, and the electrochemical properties were investigated in both noncatalytic and catalytic regimes. Unfortunately, no catalytic current was observed upon scanning above the OER onset potential suggesting that the modified complex is not an active water oxidation catalyst. The low performance of the resulting electrode may be attributed to the hydrophobic properties of the triethoxysilyl anchors which may block the ruthenium active site, or slow exchange of the robust acetate bridge by water molecules after immobilization on the surface. No further analysis was pursued in the course of this project due to the inactivity of the hybrid.

6 Complexes Based on the 3-{6-(2,2'-bipyridyl)}5-(2-pyridyl)pyrazol Ligand Scaffold

6.1 Introduction

The asymmetric Ligand **HL³** was used in the group of F. Meyer since 2012 for the development of homonuclear and heterometallic [2 x 2] grid structures such as $[Fe(HL^3)_2]_2^{4+}$, $[Cu^{II}_4L^3_4]$, $[Fe_2Cu_2L^3_4]^{2+}$ and $[FeCu_3L^3_4]^{3+}$.[173] As described in the introduction, mechanistic studies suggested that the I2M mechanism is operative for the bpp-based complexes where O-O bond formation occurs via the interactions of two ruthenium-oxo motifs. In contrast, the catalysts based on the bbp⁻ ligand were found to follow the WNA pathway for O_2 generation. To elucidate the structural and electronic determinants for these disparate mechanisms, it was of interest to study a new generation of WOC based on the asymmetric **HL³** ligand.

6.2 Ligand Synthesis

The treatment of **3-3** and 2-acetylpyridine with sodium *t*-butoxide in 1,4-dioxane afforded the diketone (**6-1**), which was used without further purification in reaction with hydrazine monohydrate in EtOH to give **HL³** as yellow solid (Scheme 6.1).
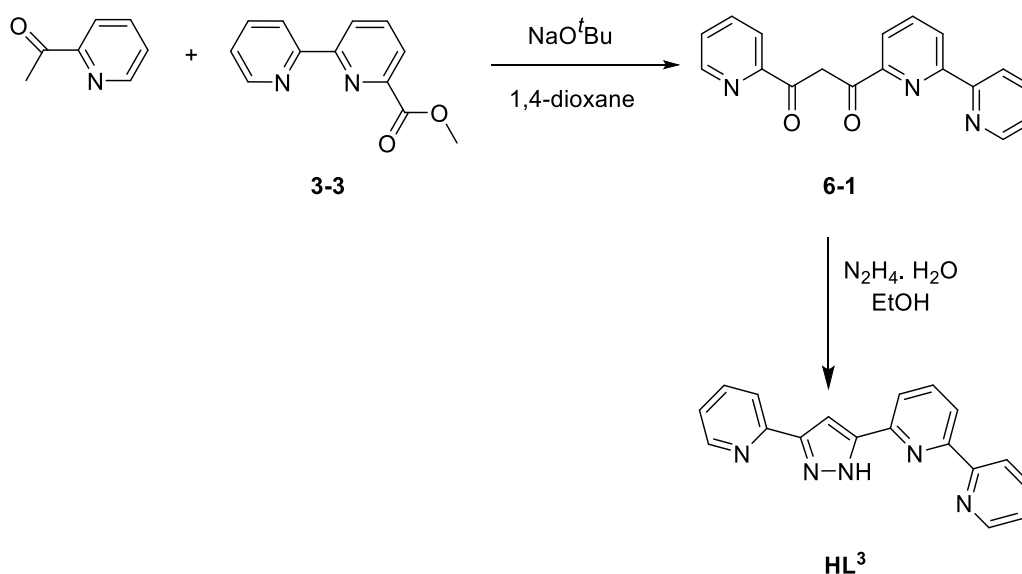
Scheme 6.1. Synthetic route for the synthesis of **HL³**.[173]

6.3 Complex Synthesis

Synthesis of [(L^3)Ru$_2$(OAc)(py)$_2$(trpy)](PF$_6$)$_2$, **8** (see Scheme 6.4) is the goal of this project. However, following the same strategy that was reported for the synthesis of the bbp-Ru$_2$ complexes with the general formula of [(^{Me}bbp)Ru$_2$(OAc)(py)$_4$](PF$_6$)$_2$, led to the formation of complex **6** and **7**. To obtain complex **8**, the synthetic procedure was modified by changing the addition order of the reagents. The spectroscopic features of complexes **6**, **7**, and **8** as well as their electrochemical and chemical water oxidation properties will be discussed in this section.

6.3.1 Synthesis of [(L^3)Ru$_2$(dmso)(py)$_4$Cl](PF$_6$)$_2$ (6)

For the preparation of the dinuclear ruthenium complex, a solution of proligand **HL^3** in EtOH was slowly added to a mixture of RuCl$_2$(dmso)$_4$ and NEt$_3$ under reflux conditions. After stirring for 20 hours, the resulting intermediate was filtered off and subsequently reacted with an excess of pyridine at 80 °C in EtOH for 6 hours. Then, 1.2 equiv. of 2,2':6',2''-terpyridine (trpy) was added and the reaction mixture was stirred at 80 °C for 2 days. Sodium acetate was also added at a late stage of the synthesis to form an acetate-bridged complex (Scheme 6.2).
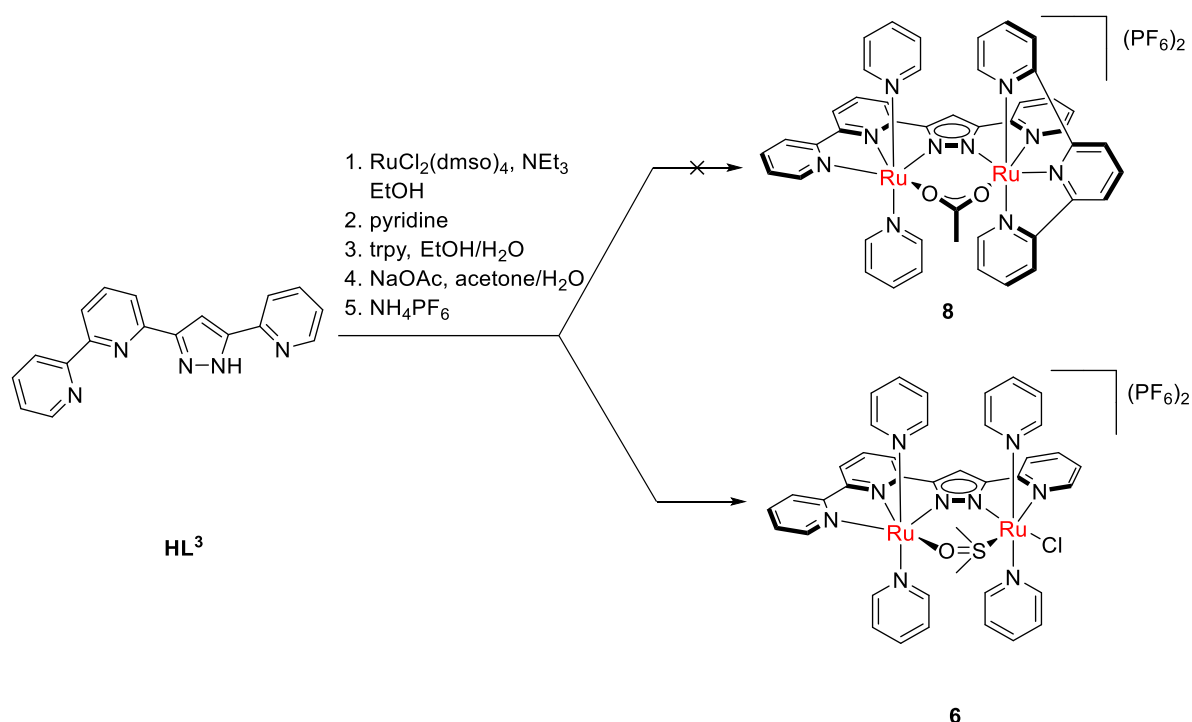
Scheme 6.2. Synthetic procedure for preparation of **6**.

Without further purification, the electrochemical fingerprint of the product was studied by cyclic voltammetry and square wave voltammetry in propylene carbonate (NBu$_4$PF$_6$). The CV

experiment shows four distinct redox processes indicating the presence of two different species in the solution (Figure 6.1), which was subsequently supported by ^{1}HNMR spectroscopy.
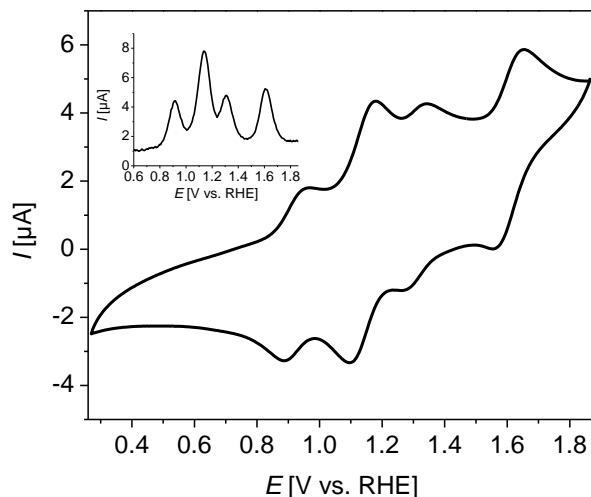
Figure 6.1. Cyclic voltammetry of the crude product before purification recorded in propylene carbonate at a scan rate of 50 mV/s. it shows four redox events at $E_{1/2}$= 0.9, 1.1, 1.3, and 1.5 V vs. RHE. WE: GC, CE: Pt, Ref. Ag wire.

To remove the side-product, column chromatography was applied using silica gel and DCM/MeOH as eluent. The ^{1}H NMR spectrum of the isolated product **6** shows 19 signals in both aliphatic and aromatic regions suggesting a C_s symmetric complex (Figure 6.2). Based on the integration, the singlet at 3.34 ppm is assigned to the S,O-bridging dmso ligand. In addition, the absence of a proton signal characteristic for an acetate group suggested the unsuccessful exchange reaction.
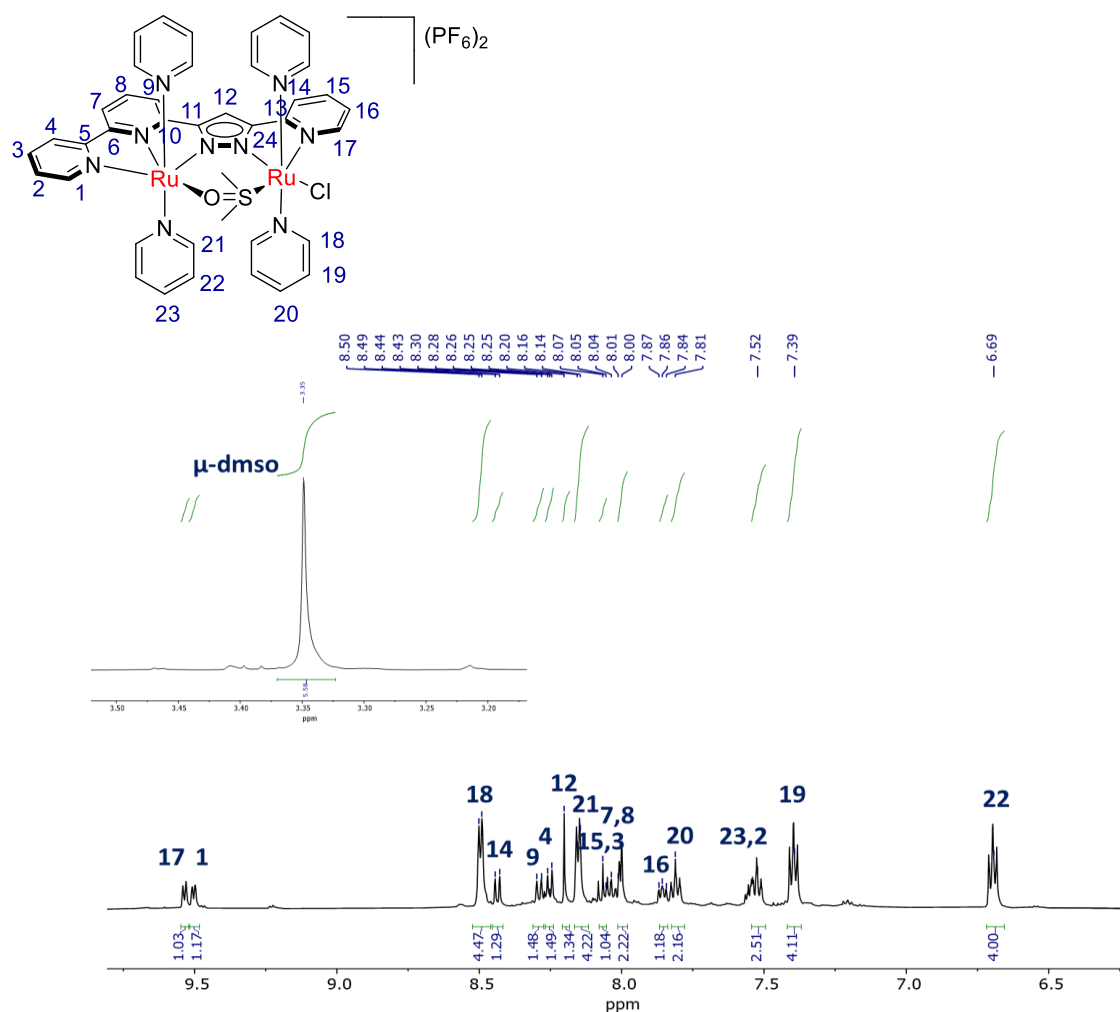
Figure 6.2. ^{1}H NMR spectrum of **6** in acetone-d_6 at room temperature. The inset shows the proton resonance of the dmso moiety at 3.34 ppm.

Crystals for X-ray diffraction analysis were obtained via slow diffusion of diethyl ether into the solution of the complex in acetone. The molecular structure (Figure 6.3) showed the formation of a dinuclear complex composed of the four axial pyridines, a dmso bridging unit, and chloride in the free binding pocket of the equatorial ligand.

Additionally, the redox properties of **6** were investigated by cyclic voltammetry under identical conditions (propylene carbonate with NBu$_4$PF$_6$ as the conducting salt) (Figure 6.4). The two redox waves at $E_{1/2}$ = 1.1 V and $E_{1/2}$ = 1.6 V vs. RHE correspond to the sequential one-electron couples Ru^{II}Ru^{II}/Ru^{II}Ru^{III} and Ru^{II}Ru^{III}/Ru^{III}Ru^{III}. Comparing the CV spectra before and after the purification process shows that complex **6** is the main formed species via this procedure.
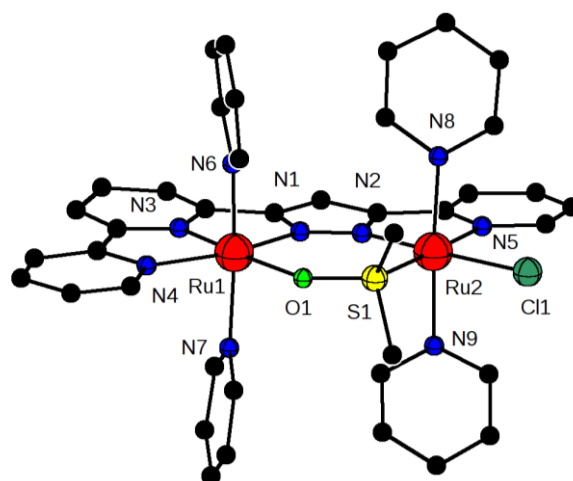
Figure 6.3. Picture of **6** confirmed by X-ray diffraction analysis. All hydrogen atoms are omitted for clarity.
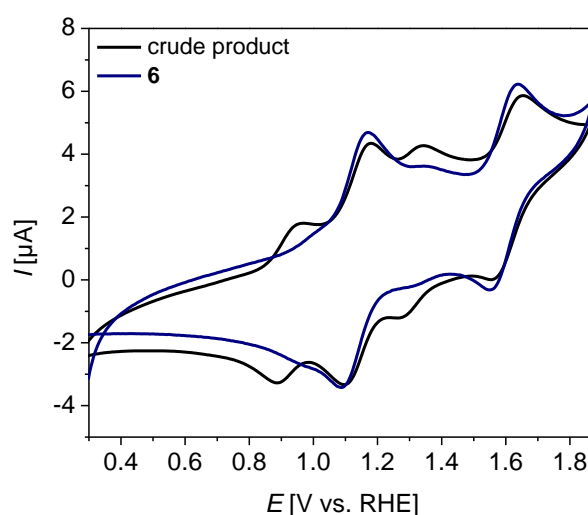
Figure 6.4. Overlay of the CV curves of **6** (navy) and the mixture before purification (black) in propylene carbonate (NBu$_4$PF$_6$) at a scan rate of 50 mV/s. WE: GC, CE: Pt, Ref. Ag wire. Final potentials are referenced versus RHE.

To enhance the driving force for the substitution of trpy with axial pyridine, an excess amount of trpy was used and the mixture was heated for a longer time. The changes in the reaction were monitored by ^{1}H NMR spectroscopy. As depicted in Figure 6.5, no significant shift was observed in the pattern of the aromatic signals even after five days of heating. However, two new proton resonances appeared at 8.5 and 8.7 ppm which are assigned to the free trpy.
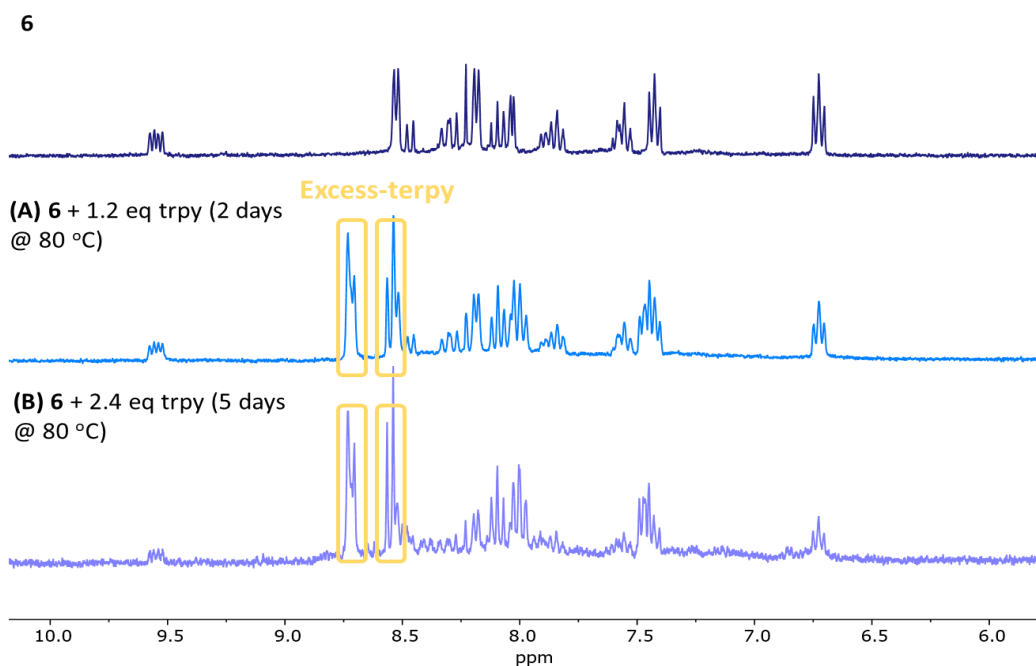
Figure 6.5. ^{1}H NMR spectra of **6** (top), after reaction with 1.2 equiv. trpy for 2 days **(A)** and with 2.4 equiv. trpy for 5 days **(B)**. The experiment was recorded in acetone-d_6 at room temperature.

6.3.2 Synthesis of [(L^3)Ru$_2$(OAc)(py)$_5$](PF$_6$)$_2$ (7)

Another procedure was pursued in order to prepare the target complex **8**. The synthesis commenced by reaction of proligand **HL^3** with RuCl$_2$(dmso)$_4$ in EtOH. The mixture was heated under reflux for one day and the resulting precipitate, without characterization in detail, was treated with sodium acetate and heated at 80 °C overnight. Subsequently, 10 equiv. pyridine was added and the mixture refluxed for another day. The brown crude was first purified by column chromatography to remove the free pyridine and then was reacted with one equiv. of trpy. Complex **7** was obtained after removing the solvent and anion exchange by NH$_4$PF$_6$ (Scheme 6.3). **7** was also characterized by various spectroscopic techniques.
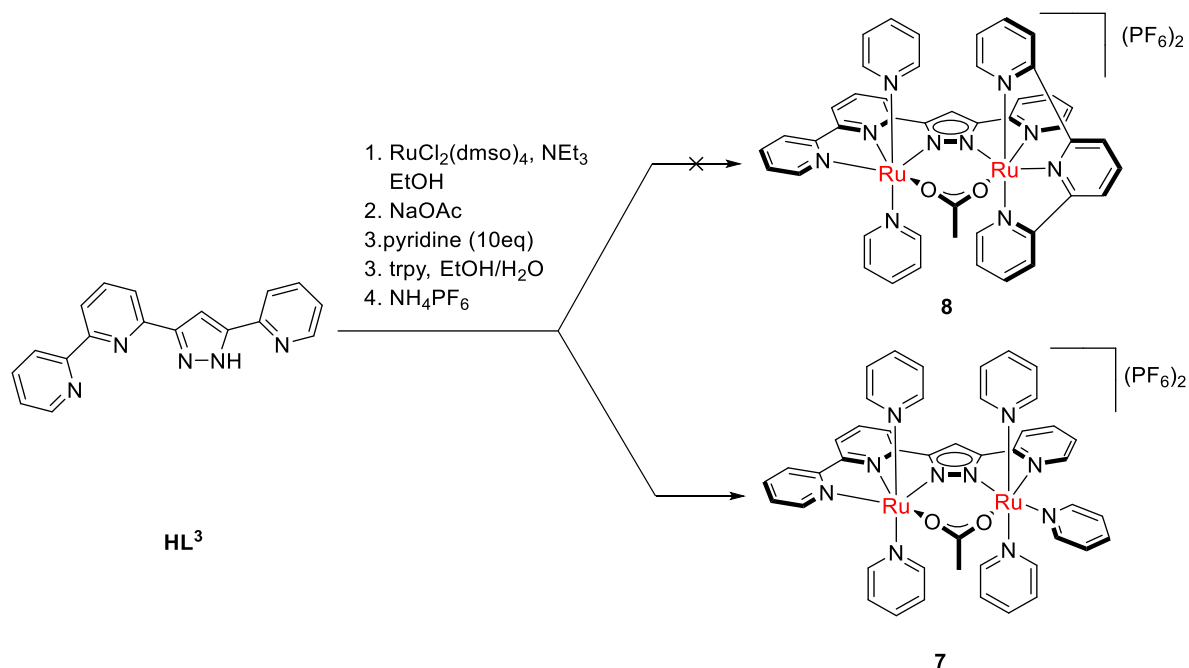
Scheme 6.3. Synthetic route for the synthesis for **7**.

Surprisingly, X-ray diffraction analysis revealed the formation of another product, with four pyridines at all axial positions and one at the free binding pocket of the ligand (Figure 6.6). The Ru…Ru distance in **7** (4.26 A°) is identical to the well-established complexes ^{Me}**bbp-Ru₂(OAc)** (4.25 A°) and ^{H}**bbp-Ru₂(OAc)** (4.30 A°). The torsion angles Ru1-O1…O2-Ru2 and Ru1-N1-N2-Ru2 for **7** (11.3, 4.2°) are similar to ^{H}**bbp-Ru₂(OAc)** (11.2, 5.7°) but considerably smaller than ^{H}**bpp-Ru₂(OAc)** (71.6, 25.4 °).[93,97] This finding reflects the fact that the acetate bridge is more tilted in complexes based on the bpp ligand.

The distortion from an octahedral structure was determined for both ruthenium ions in **7** by continuous symmetry measures (CSM).[174–176] The geometrical variation from the perfect octahedron (O_h) to the trigonal prism (D_{3h}) leads to an increase of S(O_h). For low spin ruthenium complexes in an octahedral environment, this number usually lies between 1-1.5. The obtained values of 1.17-0.64 for both Ru1 and Ru2 respectively, display only minor deviations, especially for Ru2.
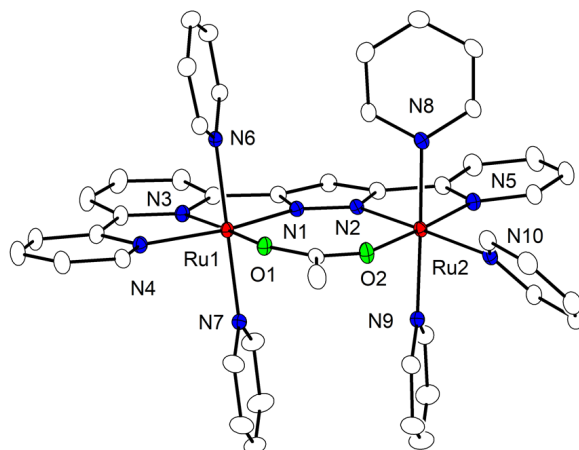
Figure 6.6. Molecular structure of the cation of **7**. Hydrogen atoms and counterions were omitted for clarity.

1D and 2D NMR spectroscopy were performed, allowing the full characterization of all protons and carbon resonances. 21 proton signals were observed in the aromatic region corresponding to the backbone ligand and the pyridine ligands (Figure 6.7). By using ^{1}H-^{1}H-COSY, ^{1}H-^{13}C-HSQC, and ^{1}H-^{13}C-HMBC techniques, the signal at very low field is assigned to H-1. The coordination of four axial pyridine ligands is confirmed by the presence of four sets of signals with the integration of 4 and two sets with the integration of 2. The proton resonance at 2.6 ppm is a characteristic signature of the acetate bridged complexes. Based on the simplicity of the ^{1}H NMR spectrum and integration of the peaks, it can be concluded that complex **7** has C_s symmetry. The integrity of **7** was also confirmed by positive ion mode ESI-MS (Figure A79). The detected peaks at *m/z* = 477.5 and 438.5 are assigned to the $[M-2PF_6]^{2+}$ and $[M-py-2PF_6]^{2+}$ ions, respectively.
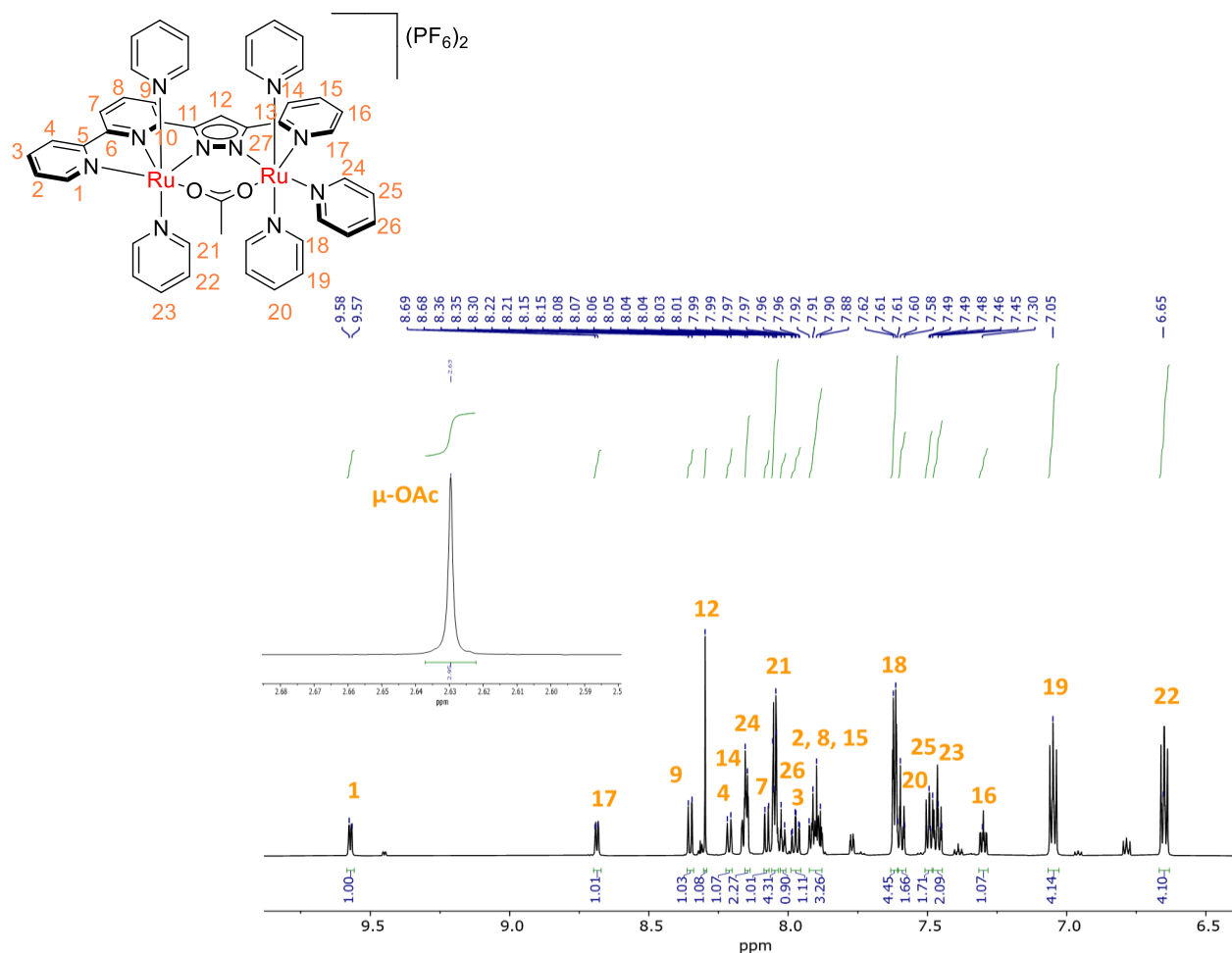
Figure 6.7. ^{1}H NMR of **7** in acetone-d_6 at room temperature. The inset shows the signal for the acetate bridge at 2.7 ppm.

Cyclic voltammetry of **7** was recorded in propylene carbonate with NBu$_4$PF$_6$ as the electrolyte. Two reversible redox processes are observed at $E_{1/2}$ = 0.9 and $E_{1/2}$ = 1.3 V vs. RHE corresponding to the oxidation from Ru[II]Ru[II] to Ru[II]Ru[III] and further to Ru[III]Ru[III]. Surprisingly, comparing the CV spectra of **7** and the mixture before purification, supporting the formation of **7** as a side product from the previous synthetic pathway (Figure 6.8). After several unsuccessful attempts, the question arises why the chelating effect of the trpy cannot lead the reaction in the right direction and what would be the energetic barrier of this conversion. However, another approach was followed in the next part to overcome the discussed issue.
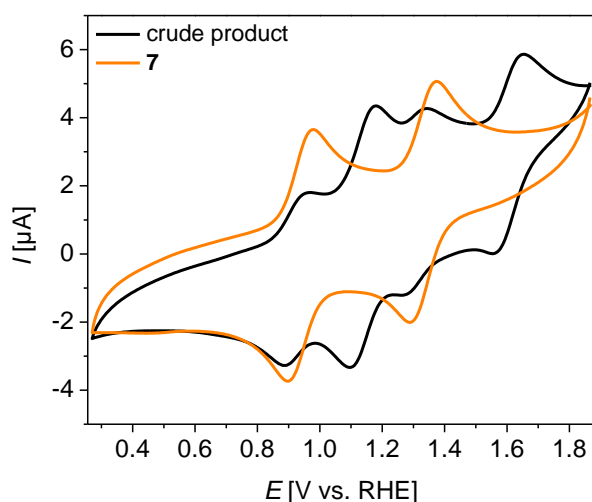
Figure 6.8. Cyclic voltammetry of the crude reaction mixture obtained according to Scheme 6.2 (black) and **7** (orange) at a scan rate of 50 mV/s in propylene carbonate (NBu_4PF_6). WE: GC, CE: Pt, Ref. Ag wire. Final potentials are referenced versus RHE.

6.3.3 Synthesis of [(L³)Ru₂(OAc)(py)₂(trpy)](PF₆)₂ (8)

The multistep synthesis is initiated with the reaction of **HL³** with $RuCl_2(dmso)_4$ in EtOH. The reaction was heated at reflux overnight followed by the addition of an excess of sodium acetate to form the acetate bridged complex. Subsequently, 1.2 equiv. of trpy was added and the reaction mixture was heated at 80 °C one day. Introduction of the pyridine at a late stage of the synthesis followed by anion exchange produced complex **8**, which was further purified by column chromatography (Scheme 6.4).
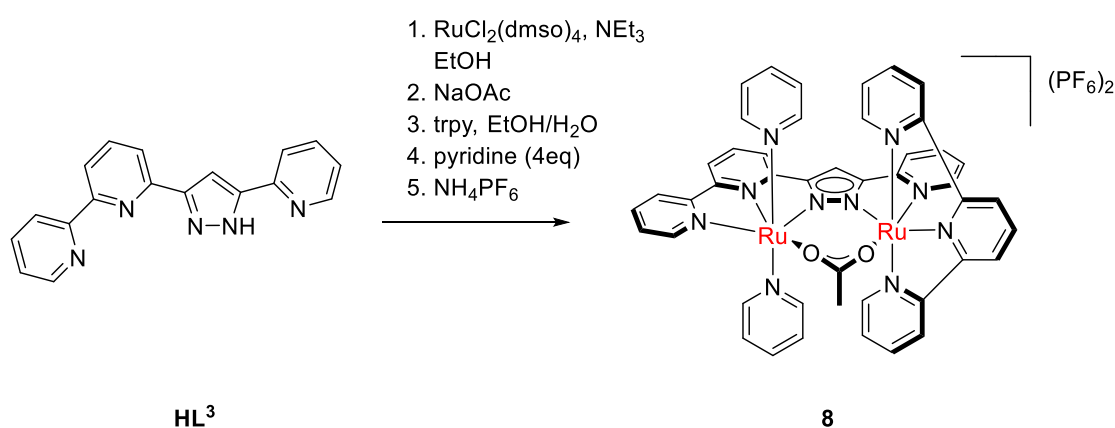
Scheme 6.4. Synthetic route for the synthesis of **8**.

Single crystals suitable for X-ray diffraction analysis were obtained by slow diffusion of diethyl ether into the methanol solution containing **8**. The metal-metal distance (d_{Ru-Ru} = 4.3 A°) is identical to other established WOCs based on the bpp⁻ and bbp⁻ ligand systems. The deviation from an octahedral coordination environment is reflected by the large torsion angles including the oxygen atoms of the acetate bridge and the nitrogen atoms of the pyrazolate motif. The torsion angles Ru1-O1…O2-Ru2 and Ru1-N1-N2-Ru2 for **8** are slightly larger (28.8, 5.81°) than the corresponding angles in **7** (11.3, 4.2°) and **ᴴbbp-Ru₂(OAc)**, (R= H, 11.2, 5.7°, R=Me, 4.2, 3°) but still smaller in comparison with the angles in **ᴴbpp-Ru₂(OAc)**. Some important geometrical parameters of the literature known complexes are listed in Table 6.1.

The distortion from an ideal polyhedral system was further described by CSM, where a large $S(O_h)$ value corresponds to a high deviation from a perfect octahedron. The determined $S(O_h)$ for Ru1 (1.170) is very similar to the values found for **7** (1.177) and ᴿbbp-based complexes (R=H, 1.18, R=Me, 1.21), reflecting only minor distortion from the octahedral geometry. In contrast, the larger value for Ru2 (1.53) in comparison to **ᴴbpp-Ru₂(OAc)** (1.38) and **ᴴbbp-Ru₂(OAc)** (1.13) indicates a twisted structure around the ruthenium center.
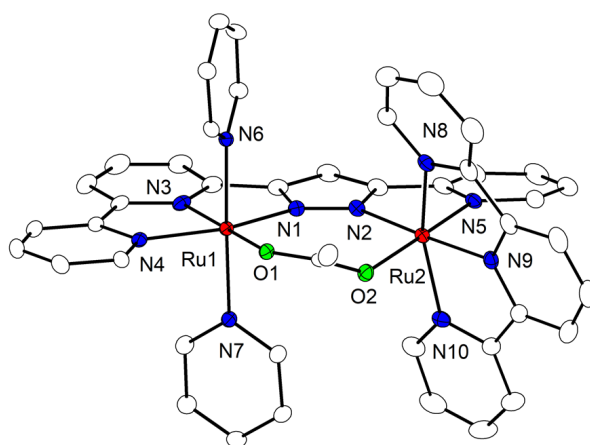
Figure 6.9. Molecular structure of the cation os **8**. PF₆ counterions and hydrogen atoms were omitted for clarity.

Table 6.1. Structural details of **7**, **8**, and the literature known complexes discussed in this chapter (**Hbpp-Ru₂(OAc)**, **Rbbp-Ru₂(OAc)**, R= H, Me).

Complex	d_{Ru-Ru} [A⁰]	$\theta_{Ru-O1…O2-Ru}$ [⁰]	$\theta_{Ru-N1…N2-Ru}$ [⁰]	CSM (Ru1)	CSM (Ru2)	Ref
ᴴbpp-Ru₂(OAc)	4.3	71.6	25.4	1.46	1.38	93
ᴴbbp-Ru₂(OAc)	4.25	11.2	5.7	1.18	1.13	97
ᴹᵉbbp-Ru₂(OAc)	4.25	4.2	3	1.21	1.13	97
7	4.26	11.3	4.2	1.17	0.64	This work
8	4.31	28.8	5.8	1.17	1.53	this work

For a better comparison, overlays of the molecular structures of **8** and **Hbpp-Ru₂(OAc)** are shown in Figure 6.10. For **8**, the ruthenium ions, the pyrazolate ligand, and acetate motif are almost in one plane, while in bpp-based complexes the acetate is oriented towards out of the plane.

Facile exchange of the acetate bridge with water molecules in **Hbpp-Ru₂(OAc)** under acidic conditions can be explained by the large torsion angles Ru1-O1…O2-Ru2 (71.6⁰), Ru1-N1-N2-Ru2 (25.4⁰) which led to a significant distortion from ideal octahedral geometry. In the case of **8** and bbp-based complexes, the acetate bridge and two ruthenium ions are located almost in one plane hence, there are stronger interactions between the acetate group and d-orbitals of the metals.
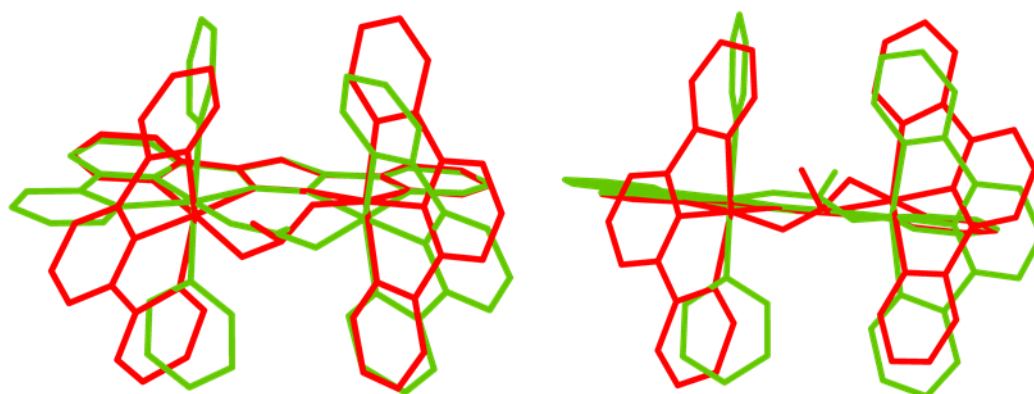
Figure 6.10. Overlay of **8** and **Hbpp-Ru₂(OAc)** from the two nitrogen atoms and C⁴ carbon atom of the pyrazolate ring. The hydrogen atoms and the counterions were omitted due to the clarity issue. Two different views of the molecular structures are shown0.

An ESI-MS experiment of a methanol solution containing **8** showed a dominant signal at m/z = 476.1 corresponding to the molecular ion peak $[M-2PF_6]^{2+}$ (Figure A80). The ^{1}H NMR of **8** in acetone-d_6 reveals 21 resonances in the aromatic region originating from the pyridines, trpy and pyrazolate backbone ligand (Figure 6.11). The distinctive signal at 9.33 ppm can be assigned to H-1, which was shifted (around 0.3 ppm) towards higher field compared to **7**. Signals at 7.16, 7.69, 8.20, and 8.42 ppm correspond to the axial pyridines (H-18, H-19, H-20) and the pyrazolate ring, respectively. The presence of the acetate bridge was confirmed by a characteristic proton resonance at 1.71 ppm, which exhibits a significant high field shift in comparison to **7** and bbp-based complexes. This variation in chemical shifts can be attributed to the presence of the trpy ligand which may provide a stronger shielding effect around the acetate methyl group. The remaining resonances were fully assigned by using 2D NMR spectroscopy. In addition, the number and integration of the signals suggest a complex with a low symmetry (C_s).
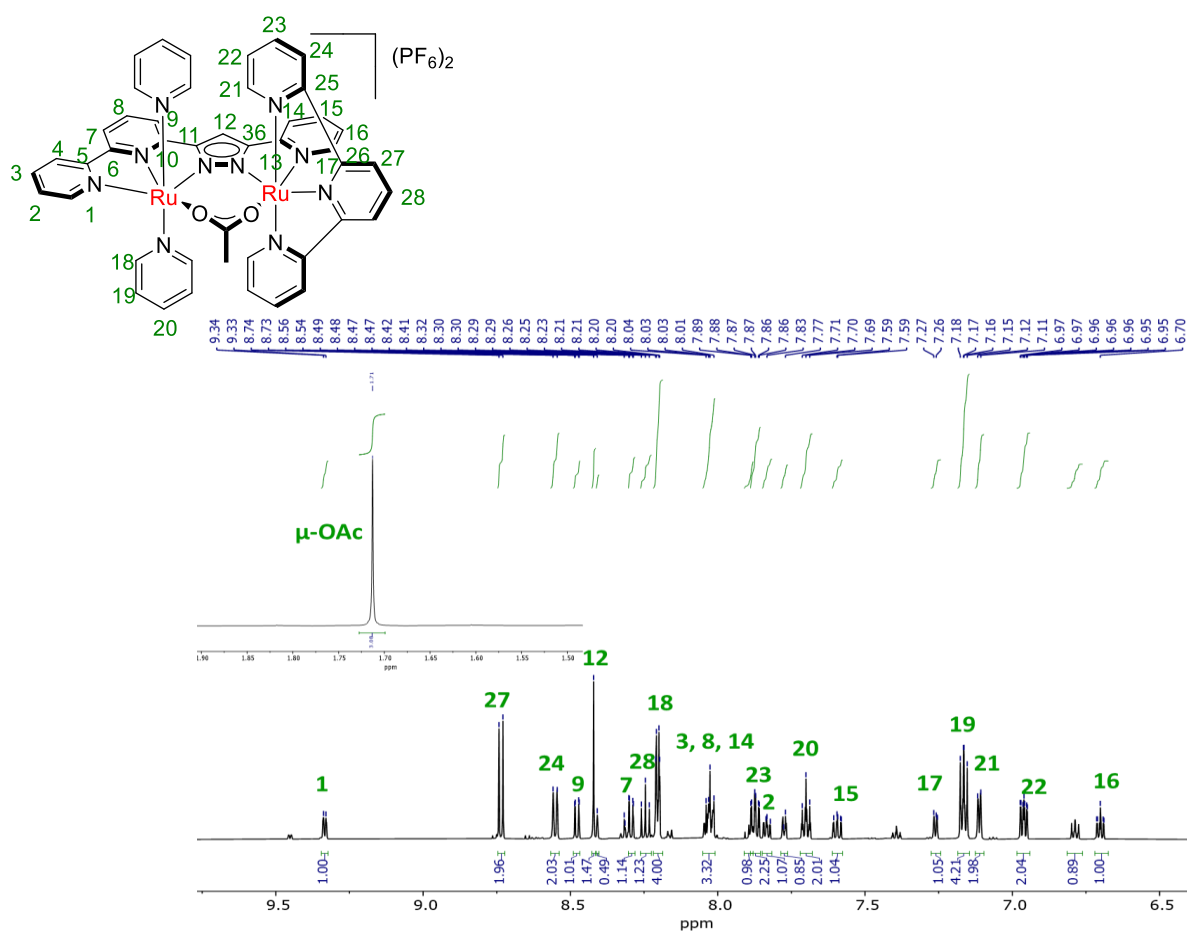
Figure 6.11. ^{1}H NMR spectrum of **8** in acetone-d_6 at room temperature. The inset shows the characteristic signal of the acetate bridge.

The electrochemical properties of **8** were investigated by means of cyclic voltammetry and square wave voltammetry in propylene carbonate (NBu_4PF_6). Two distinct redox waves are observed at $E_{1/2}$ = 0.9 and $E_{1/2}$ = 1.3 V *vs.* RHE corresponding to the sequential one-electron couples $Ru^{II}Ru^{II}$/ $Ru^{II}Ru^{III}$ and $Ru^{II}Ru^{III}$ /$Ru^{III}Ru^{III}$, which are separated by 376 mV ($\Delta E_{1/2}$). SWV of **8** was also conducted under identical conditions (rt, in propylene carbonate) to confirm the presence of the oxidation waves (inset, Figure 6.12). The ΔE_p of 64 and 61 mV are obtained for the first and second waves, respectively which indicates the reversibility of the two redox processes. Additionally, CVs were recorded at various scan rates (20, 50, 100, 200 mV/s) (Figure A87). The plot of the anodic peak current versus square root of the scan rates is depicted for both oxidation waves in Figure 6.13, confirming the reversibility of these two processes.
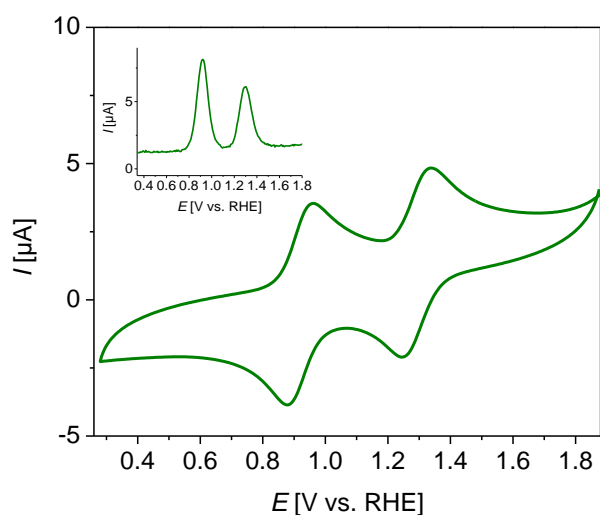
Figure 6.12. Cyclic voltammetry of **8** in propylene carbonate at a scan rate of 50 mV/s. The inset depicts the SWV. WE: GC, CE: Pt, Ref. Ag wire. Final potentials are reported versus RHE.
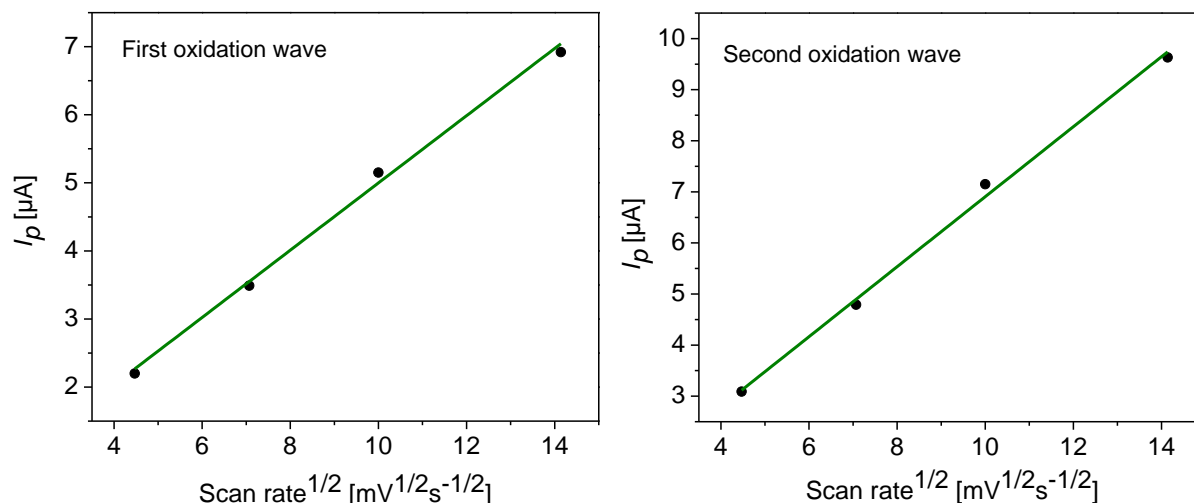
Figure 6.13. The dependency of the peak current to the square root of scan rate for the first (left) and the second oxidation waves (right), suggesting the reversibility of the two redox events.

UV/vis SEC was conducted to observe the changes in spectroscopic features of the oxidized species ($Ru^{II}Ru^{III}$ and $Ru^{II}Ru^{III}$), as well as investigate the electrochemical reversibility of the two redox processes. For the experiment, the complex was dissolved in propylene carbonate (NBu_4PF_6) and a potential of 1.1 V *vs.* RHE was applied to the cell, which is enough to drive the first oxidation process ($Ru^{II}Ru^{III}$). UV/vis spectroscopy was employed to monitor the variations in band intensities after conversion to oxidized species. The spectrum before oxidation reveals several absorptions maxima at 274, 315, 376, and 532 nm. Upon oxidation, the bands at 376 and 532 gradually disappear while the bands at 257 and 288 nm gain more intensity. To recover the first species ($Ru^{II}Ru^{II}$), a potential of 0.6 V *vs.* RHE was applied, while recording the UV/vis spectra. As shown in Figure 6.14, the original spectrum of **8** was almost recovered after oxidation and subsequent reduction, suggesting the chemical reversibility of the first redox event. For the second wave, the potential was first increased to 1.6 V *vs.* RHE, followed by the re-reduction to 1.1 V. Comparison of the first spectrum (before oxidation) and the last one (after re-reduction) indicates that the second electrochemical process is almost reversible. However, the band at 377 nm is not fully recovered, which may be attributed to some decomposition of the complex at that high potential.
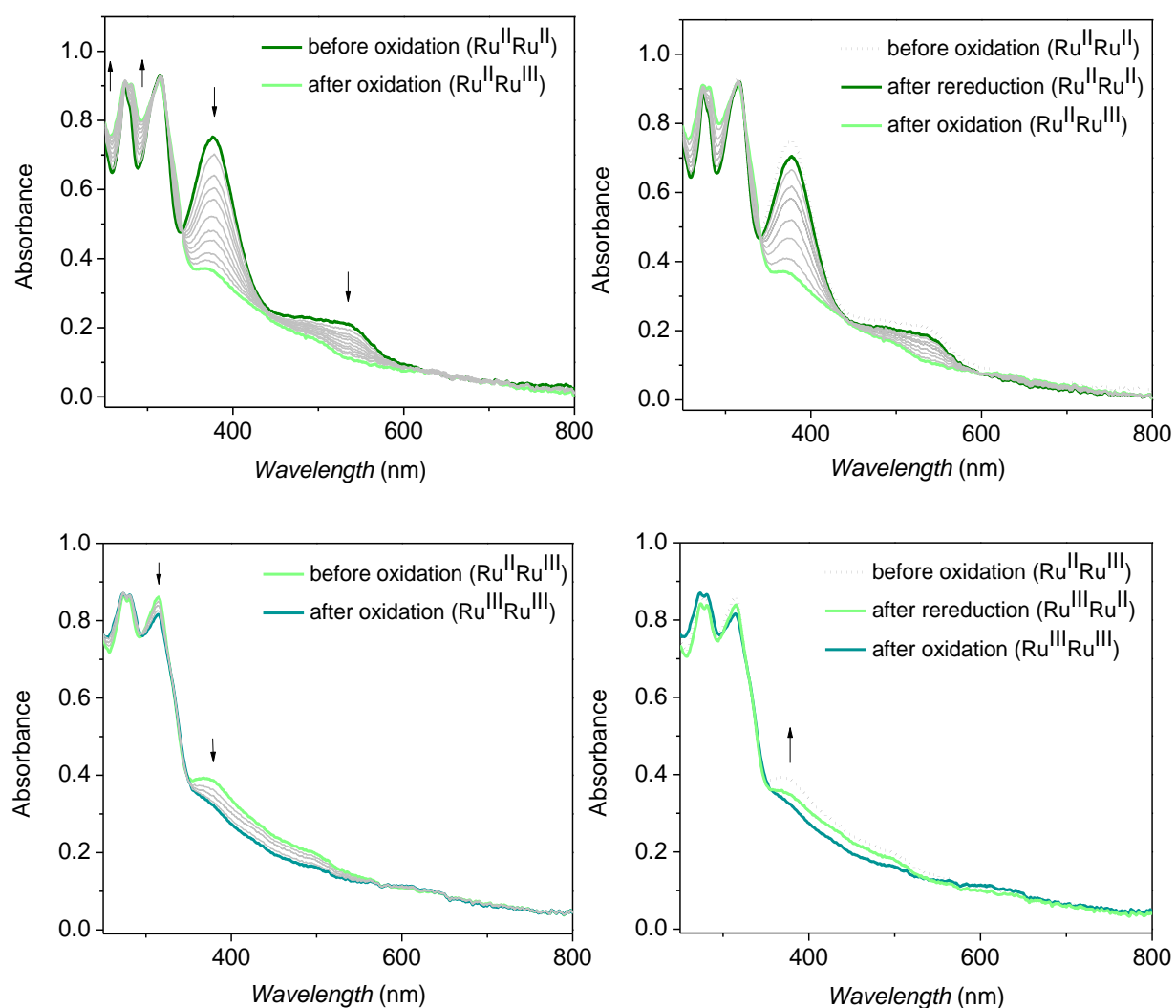
Figure 6.14. UV/vis spectroelectrochemistry (SEC) measurement of **8** in propylene carbonate. UV/vis spectrum for electrochemical oxidation from $Ru^{II}Ru^{II}$ to $Ru^{II}Ru^{III}$ at 1.1 V vs. RHE⁺ (top-left) and from $Ru^{II}Ru^{III}$ to $Ru^{III}Ru^{III}$ at 1.6 V vs. RHE (bottom-left). The overlay spectra before and after oxidation for both redox waves are demonstrated in the top-right and bottom-right. WE: platinum net, CE: Pt wire, Ref. Ag wire.

6.4 Chemical Water Oxidation Catalysis with CAN as an Artificial Oxidant

The catalytic activity of **8** was evaluated in 0.1 M aqueous HOTf (pH = 1) using excess amounts CAN as a sacrificial oxidant. After the addition of the oxidant, the produced gas in the reaction cell was simultaneously monitored by online manometry and an optical oxygen sensor. To exclude the formation of other gases than dioxygen during the catalysis, the obtained TON by these two measurements should be identical. Observation of a gap between manometry and oxygen sensor outcomes indicates the formation of other gases such as CO_2, which may originate from the degradation of the ligand during the harsh reactive condition.

The first addition of CAN to degassed aqueous HOTf (0.1 M, pH = 1) containing **8** led to a TON of 23.5 corresponding to an efficiency of 94% (Figure 6.15). The observed values for both manometry and oxygen sensor are in good agreement, confirming the presence of only dioxygen in the reaction cell. The response in the oxygen sensor is usually slower than manometry which can be attributed to the slow diffusion rate of O_2 from the aqueous phase into the gas phase and finally to the optical electrode tip. The catalytic performance of **8** is comparable with the well-known reported WOCs based on the bpp$^-$ and bbp$^-$ ligand scaffolds. Chemical water oxidation under the same condition (pH = 1, at 25°C) gave a TON of 17.5 corresponding to an efficiency of 70% for both bpp-Ru$_2$ and bbp Ru$_2$ with H substituent at the C^4-position of the pyrazolate backbone ligand.[93,97] This suggested identical deactivation mechanisms for both systems. However, the chemically driven water oxidation was relatively faster for **^{H}bbp-Ru$_2$(OAc)** (TOF = 3.8 × 10^{-2}) compared to the **^{H}bpp-Ru$_2$(OAc)** (TOF = 1.4 × 10^{-2}). A significant improvement in TON value was achieved by substitution of the hydrogen atom with a methyl group at the C^4 pyrazolate position.[53] **^{Me}bbp-Ru$_2$(OAc)** showed a TON of 22.4 (efficiency of 90 %) with very similar TOF (1.9 × 10^{-2}) to **^{H}bpp-Ru$_2$(OAc)**.[53]

In order to evaluate the robustness and stability of **8** under catalytic conditions, the experiment was continued by the addition of another 100 equiv. CAN to the mixture after the end of the first run (Figure 6.15). The treatment of **8** with more oxidant(100 equiv.) resulted in the same TON (23.4), while a considerable decrease was observed in the TOF value (first run: 0.054 s^{-1}, second run: 0.029 s^{-1}). The variation in TOF by sequential addition of oxidants can be caused by several factors such as I) drop of pH due to the release of four protons via the water oxidation reaction II) deactivation of the active catalyst by anation of nitrates

originating from the oxidant (CAN = $(NH_4)_2Ce(NO_3)_6$) and III) interaction with the Ce^{III} ions present in the solution.

Interestingly, complex **8** displays higher activity and stability than the related symmetric pyrazolate based complexes containing an acetate bridge,[93,97] which makes it a promising candidate for further catalytic and mechanistic investigations. The catalytic parameters (TON, TOF, efficiency) of the WOCs discussed in this chapter are tabulated in Table 6.2.
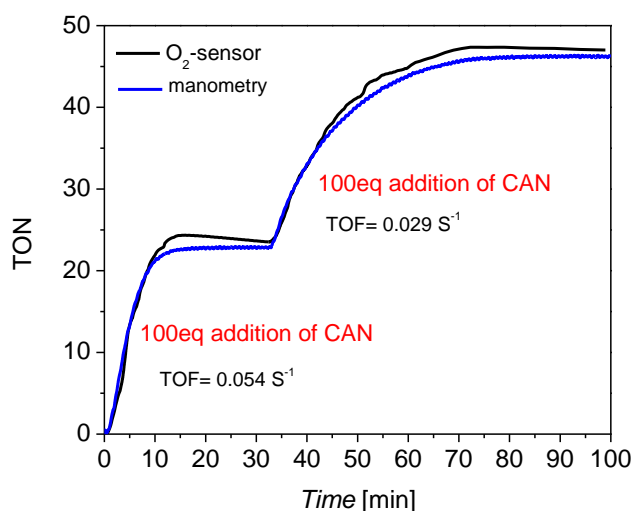

Figure 6.15. Chemically water oxidation catalysis of **8** in 0.1 M aqueous HOTf (0.1 M, pH = 1) upon sequential addition of CAN as artificial oxidant. The gas evolution was simultaneously monitored by manometry (blue) and oxygen sensor (black).

Table 6.2. Comparison of the catalytic performance of the ruthenium WOCs based on pyrazolate ligands. All the experiments were performed in aqueous HOTf (0.1 M, pH = 1) using CAN as the oxidant at 25 °C. The maximum turnover number which can result from this condition is 25. The asterisk refers to the complex with 3-pyridinesulfonic acid (py-SO$_3$) at the axial positions. All the reported TOF values correspond to the first addition of CAN.

Complex	TON	Efficiency (%)	TOF (s^{-1})	Ref
^{H}bpp-Ru$_2$(OAc)	17.5	70	0.014	93
^{H}bbp-Ru$_2$(OAc)	17.5	70	0.038	97
^{Me}bbp-Ru$_2$(OAc)	22.6	90.4	0.019	53.97
^{Me}bbp-Ru$_2$(H$_2$O)*	22.6	90.4	0.068	53
8	23.4	94	0.054	this work

6.5 Characterization of the Higher Oxidation States Species by Vis/NIR Spectroscopy

UV/vis-NIR spectroscopy was employed to get more insights into the electronic properties of **8** in higher oxidation states. An IVCT band is expected to be observed in the case of mixed-valent species (Ru^{II}Ru^{III}). The redox titration of **8** was carried out in 2,2,2-trifluorethanol (TFE) by sequential additions of CAN as oxidant while detecting the spectral changes in the Vis-NIR region. The experiment was conducted in a small cuvette with d = 0.1 cm to minimize the absorption of the solvent. The initial spectrum (Ru^{II}Ru^{II}) did not show any absorption within the wavelength range of 900-1700 nm. Upon titration with one equiv. of CAN, a broad IVCT band appeared at 1600 nm, supporting the formation of the Ru^{II}Ru^{III}. Further addition of the oxidant leads to a decrease of the intensity of this band, while another broad band forms at below 1000 nm (Figure 6.16). The same spectroscopic features were also observed for the similar complex **^{Me}bbp-Ru$_2$(OAc)**.[62] However, for **^{Me}bbp-Ru$_2$(OAc)** the titration was performed in propylene carbonate.
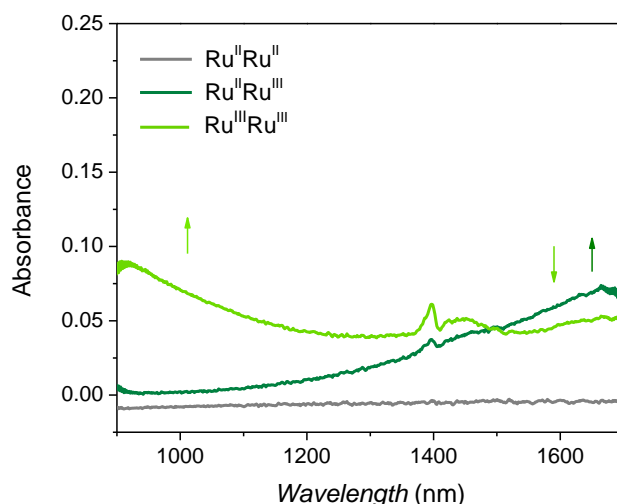
Figure 6.16. Redox titration of **8** with CAN in the Vis-NIR region. The oxidized species were formed by the addition of 1 equiv. (dark green) and subsequently 2 equiv. of CAN (light green) to the $Ru^{II}Ru^{II}$ (grey). CAN was dissolved in 0.1 M aqueous HOTf (pH = 1) for solubility reasons. Complex concentration: 8×10^{-3} M.

In the case of asymmetric **8**, it would be interesting to observe which metal center will be oxidized first after treatment with only one equiv. oxidant. Based on DFT calculations (see appendix), a clear assignment of Ru^{II}/Ru^{III} is not possible and the spin density is almost equally delocalized over both ruthenium ions (Figure 6.17). Several crystallization efforts have been performed to characterize the mixed-valent species but, unfortunately, the obtained crystals were not suitable for X-ray diffraction.
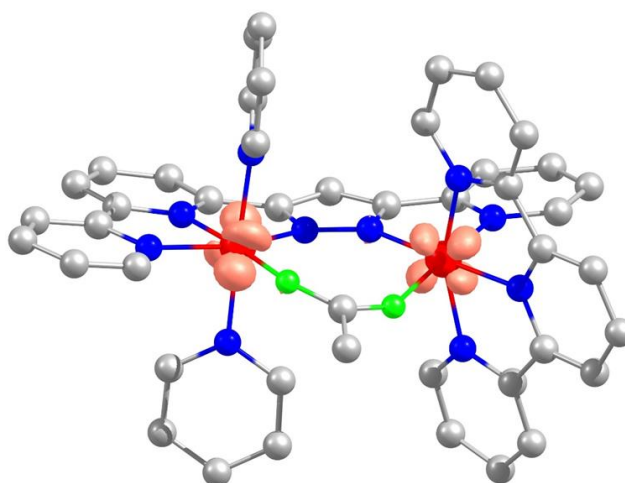
Figure 6.17. DFT calculation of the spin density on the metal centers. Mulliken spin populations of $Ru(1)(py)_2$ (left) and $Ru(2)(trpy)$ (right) are 0.54 and 0.43, respectively.

6.6 Conclusion and Summary

This chapter presented several dinuclear ruthenium complexes based on an asymmetric pyrazolate ligand. The goal of the project was to prepare complex **8** composed of 3-{6-(2,2'-bipyridyl)}5-(2-pyridyl)pyrazol ligand (**HL³**), meridional trpy, and two pyridines. However, following the same synthetic procedures which were reported for the related symmetric bpp-Ru₂ complexes led to the formation of complexes **6** and **7**. All products were purified and fully characterized by X-ray diffraction, 1D and 2D NMR spectroscopy, and ESI-MS. Cyclic voltammetry and square wave voltammetry of **6**, **7,** and **8** were conducted in propylene carbonate displaying two redox events corresponding to the sequential one-electron Ru^{II}Ru^{II}/Ru^{II}Ru^{III} and Ru^{II}Ru^{III}/Ru^{III}Ru^{III} couples. For **8**, the chemical reversibility of both redox processes was investigated through UV/vis-SEC measurements. To explore the catalytic activity of **8**, a chemical water oxidation experiment was performed in aqueous HOTf (0.1 M, pH = 1) using CAN as a sacrificial oxidant. A TON of 23.4 corresponding to an efficiency of 94% was achieved for **8**, which is one of the best among the rugged WOCs based on the bpp⁻ and bbp⁻ ligand systems. The stability of the active catalyst during the chemical-driven catalysis was further evidenced by a second addition of CAN to the mixture. Observing the same TON as in the first run indicates the robustness of the catalyst.

Due to the asymmetric structure of **8**, it would be interesting to detect which ruthenium ion will be oxidized first after treatment with one equiv. of the oxidant. The chemical oxidation of **8** was conducted in several organic solvents such as acetonitrile, propylene carbonate, acetone, and 2,2,2-trifluorethanol using CAN. Efforts were made to obtain single crystals for XRD analysis. However, the quality of the crystals was not suitable for further characterization.

UV/vis-NIR spectroscopy was used to get more insights into the electronic features of **8** in higher oxidation states. The observation of a broad IVCT band after the formation of the Ru^{II}Ru^{III} species indicated some degree of delocalization, and DFT calculations suggested that the spin density is almost equally distributed between the two ruthenium ions.

Providing a water-soluble version of complex **8** is highly required to determine the mechanism of O-O band formation via an ¹⁸O-labeling experiment. Substitution of the axial pyridines with pyridine-3-sulfonato (py-SO₃⁻) was considered as a solution to overcome the solubility

issue.[62,171] The low yielding preparation of complex **8** as well as the purification challenges prevented isolation of the pure complex bearing py-SO$_3^-$ at the axial positions.

Further efforts towards the synthesis of the water-soluble complexes and characterization of the mixed-valent Ru^{II}Ru^{III} are currently being pursued. In addition, equipment of **8** with anchoring groups either at the trpy or pyrazolate backbone for construction of hybrid electrodes is also being followed.

7 Summary and Perspective

The first part of this work presented two highly active diruthenium WOCs based on the bbp⁻ ligand scaffold which were modified with pyrene anchoring groups attached to either the pyrazolate backbone or to multiple axial ligand positions. This allowed for successful immobilization on MWCNTs. Various spectroscopic and electrochemical techniques were employed to characterize the new hybrid materials. HRTEM and EELS supported pyrene anchoring via noncovalent π-π interactions by revealing an increase of spectral weight of $\pi-\pi^*$ transitions upon immobilization. The water oxidation performance of hybrids was examined by RRDE measurements in aqueous HOTf (0.1 M, pH = 1). The complex anchored via four pyrene groups revealed higher stability under oxidizing conditions while the complex with one anchor at the ligand backbone showed higher catalytic activity. XPS was applied to investigate the chemical structure of immobilized catalysts after catalysis. Interpretation of the N/Ru ratio before and after electrochemical treatments confirmed the robustness of the hybrid and exclude the formation of degradation products. The TOF values of both systems were comparable with related bbp-based complex [(^{Me}bbp){Ru(OH$_2$)(4-SO$_3$-py)$_2$}$_2$]⁻, reflecting the fact that TOFs of anchored catalysts are not influenced by restricted diffusional mobility at the carbon surfaces.

To simplify the synthetic efforts required for dinuclear ruthenium complexes, a series of new mononuclear Ru catalysts bearing dianionic N-donor scaffolds **H$_2$L^1** and **H$_2$L^2** was prepared (Chapter 4). It was found that the complex based on **H$_2$L^1** gradually decomposes under catalytic conditions, while modification of the ligand by substitution of the vulnerable CH units of the phenyl ring by nitrogen atoms makes it a more robust WOC. Several attempts were conducted to confirm the role of N-O formation in promoting the activity. However, it could not be fully clarified at this stage and need further experiments. To generate hybrid materials for heterogeneous studies, the mononuclear catalyst was equipped with carboxylate anchors at the axial pyridine that enables immobilization ITO electrode. However, the high solubility of resulting hybrids in aqueous media prevented further characterization.

Previous results reported that the pyrazolate-C^4 position is not the most promising site for appending the anchor in pyrazolate-bridged diruthenium WOCs. Therefore, the complex based on bbp⁻ ligand was synthetically furnished with triethoxysilyl groups attached to axial

pyridine, and their immobilization was successfully achieved on ITO electrodes (Chapter 5). The ability of generated hybrid to drive the oxygen evolution reaction was evaluated through cyclic voltammetry experiments. However, no significant current was yielded in the catalytic regime, indicating that the modified complex is not an active catalyst. Hence, further optimization of the ligand framework using other stable anchors may be pursued.

The last chapter focuses on the synthesis and characterization of new complexes composed of an asymmetric ligand **HL^3**. The water oxidation proficiency of complex **8** was thoroughly investigated electrochemically using cyclic voltammetry and chemically in presence of CAN. The obtained TON and TOF values further compared favorably to similar pyrazolate-based catalysts **Hbpp-Ru$_2$(OAc)** and **Hbbp-Ru$_2$(OAc)**, indicating high stability of **8** under catalytic conditions. Moreover, preliminary attempts were made to synthesis mixed-valent species to get more insight into the electronic structure of the complex in higher oxidation states. The perspective work regarding this project involves anchoring of **8** onto solid supports for the generation of hybrid anodes as well as explore the effect of the new design on the water oxidation mechanism. Based on previous studies, in dinuclear WOCs which follow the WNA pathway for the O-O bond formation, the role of each metal center can be different. Hence, optimization of each ruthenium center individually (one more electrophilic and the other more basic) may allow us to direct the catalytic process toward the desired mechanism.

Overall, this thesis focused on the design of several ruthenium-based water oxidation catalysts and their immobilization on either carbon platforms or metal oxides. It also has been shown that a significant improvement in the stability of hybrids can be achieved via modification of the attachment position as well as changing the number of anchoring groups. Further works will aim at the development of efficient and stable molecular catalysts based on polaron absorbers along with a detailed understanding of charge transfer processes between absorbers, anchor groups, and catalyst complex.

8 Experimental Part

8.1 General Remarks and collaboration

Chapter 3 has been published in a scientific journal and the parts adapted from the published manuscript are marked with asterisks.

* S. Rajabi, F. Ebrahimi, G. Lole, J. Odrobina, S. Dechert, C. Jooss, F. Meyer, *ACS Catalysis* **2020**, 10, 10614-10626.[145]

The XPS measurements have been recorded by Christian Höhn and Dr. Fatemeh Ebrahimi.

The RRDE measurements were carried out in close collaboration with Dr. Fatemeh Ebrahimi.

High-resolution transmission electron microscopy (HRTEM) and electron energy loss spectroscopy (EELS) have been performed by Gaurav Lole, who also did the data analysis.

8.2 Materials and Methods

8.2.1 Materials

$RuCl_2(dmso)_4$,[177] 6,6´-bis-(1H-benzoimidazol-2-yl)-2,20-bipyridine (bpybzimH$_2$),[169] and 3-{6-(2,2'-bipyridyl)}5-(2-pyridyl)pyrazol[173] were prepared following literature procedures. Chemicals and reagents were purchased from commercial suppliers (Sigma Aldrich, TCI, ChemPur, ABCR, and ACROS) and were used without further purification. The synthesis of complexes was carried out under N_2 atmosphere using schlenk techniques. The solvents were HPLC or p.a. grade and were dried following standard procedures when it was necessary. High purity deionized water was prepared using an Aquatron A4000D water still (Bibby Scientific). CAN for chemical water oxidation experiment was ordered from ABCR and trifluoromethanesulfonic acid (99 % ACS grade) for preparation of aqueous HOTf (0.1 M, pH = 1) from STREAM/CYMIT. Multi-walled carbon nanotubes with O.D. × L 6-13 nm × 2.5-20, the ITO glass slides with surface resistivity of 8-15 Ω and ITO powder with ‹50 nm particle size were purchased from Aldrich.

8.2.2 Preparation of GC|MWCNT electrodes

The glassy carbon working electrodes were polished first with alumina paste, washed with deionized water, and dried. The modified electrodes were obtained by drop-casting a suspension of the MWCNTs in THF (1 mg in 1 mL) on a clean glassy carbon (GC) electrode to have a uniform surface coverage.

8.2.3 Preparation of ITO|*meso*ITO electrodes

The ITO slides were sonicated first in a solution of 2 % Hellmanex ®III in water for 20 minutes, then in deionized water for another 20 minutes, and finally in 2-propanol for additional 20 minutes and dried in the oven at 100 °C for 1 h. 100 mg of *meso*ITO powder was suspended in acetic acid (0.1 mL) and ethanol (0.34 mL) and was sonicated in an ultrasonic bath for 30 minutes. The dispersion (10 µL) was coated on ITO glass slides with doctor blading technique. The edges of the slides were covered by TESA tape to maintain a constant surface area. After drying the slides in air, the tape was removed and the slides were heated at 100 °C for 1 h. Then, they were annealed in a 500 °C oven within 2 h and cooled back to room temperature. To remove the oxygen, the slides were heated up to 300 °C in a 3 % H_2/N_2 atmosphere for 2 h and cooled back. Finally, the slides were cut into small pieces (7 x 5 mm) with a diamond knife.

8.2.4 NMR Spectroscopy*

All ^1H and ^{13}C NMR spectra were recorded on a Bruker Avance III 300, Bruker Avance III HD 400 and Bruker Avance III HD 500 spectrometer in $CDCl_3$ (δ = 7.26 ppm), acetone-d_6 (δ = 2.05 ppm), methanol-d_4 (δ = 3.31 ppm) with residual solvent signals as internal references. All signals were numbered for convenient assignments and the multiplicity was abbreviated as (s) for singlet, (d) duplet, (t) triplet, (q) quartet, and (m) as multiplet. The chemical shifts (δ) are given in ppm and coupling constants in Hz. Analysis of the spectra was carried out with MestReNova version 14.1.1-24571.

8.2.5 Mass Spectrometry*

Electrospray ionization (ESI) mass spectra were recorded with a Finnigan MAT LCQ or Bruker 7 Tesla Fourier Transform Ion Cyclotron Resonance (FTICR) mass spectrometer.

8.2.6 Electrochemistry*

Cyclic voltammetry and Square Wave Voltammetry were conducted with a Gamry interface (1010E) instrument. For homogeneous systems, the measurements were carried out in propylene carbonate and MeCN with $[^nBu_4N]PF_6$ (0.1 M) as conduction salt or in 1:1 mixture of aqueous HOTf (0.1 M, pH = 1) and TFE. The glassy carbon electrode first was polished with an alumina paste, washed with water, dried, and used as the working electrode (WE). A platinum electrode was used as the counter electrode and MSE (Mercury-mercurous sulfate electrode), SCE (calomel electrode), and Ag wire as the reference electrode. The final potentials were reported against RHE (SCE = 0.24 mV, Fc^+/Fc = 0.624, MSE = 0.64 mV (However, a different MSE electrode was used for RRDE measurements in chapter 3 and the potentials were converted to RHE scale by adding 0.7 mV). For the hybrids, the working electrode was substituted by the GC|MWCNT or ITO|*meso*ITO glass slides and measurements were carried out in 0.1 M aqueous HOTf (0.1 M, pH = 1). The electrochemical analysis was carried out with Gamry EChem Analyst software.

8.2.7 RRDE measurements*

Rotation ring disk measurements were performed with two interface1000E Gamry potentiostats. First, the cell was filled with 30 mL aqueous HOTf (0.1 M, pH = 1) as an electrolyte and purged with argon gas for 30 min to remove any dioxygen. The modified GC|MWCNT disks and a Pt ring were used as working electrodes. A Pt coil and MSE were used as counter and reference electrodes, respectively. All the measurements were carried out under argon gas flow with a rotation speed of 1600 rpm. The ring electrode was polished before each experiment with alumina paste for 10 min.

8.2.8 XPS measurements*

A SPECS PHOIBOS 100 Hemispherical XPS analyzer with a monochromatic X-ray source (SPECS FOCUS 500 monochromator, Al Kα radiation, 1486.74 eV) was applied to determine the elemental composition of the hybrids (GC|MWCNT|complex). The pass energy was set to 30 eV with a step size of 0.5 eV for the survey and 10 eV with a step size of 0.05 eV for fine spectra. Casa XPS was used to calculate atomic percentages of core levels.

8.2.9 Spectroelectrochemistry

UV/vis Spectroelectrochemistry experiments were conducted in a quartz cell with Pt mesh as working, Pt wire as counter and MSE (Hg/Hg$_2$SO$_4$), SCE (calomel electrode), or Ag wire as the reference electrode. A Metrohm Autolab PGSTAT101 was used as a potentiostat and UV/vis spectra were recorded with an Avantes AvaSpec-ULS2048L-StarLine spectrometer and an Avantes AvaLight-DH-S-BAL light source. The data were analyzed with NovaSoft and AvaSoft 7.7.

8.2.10 Chemical Water Oxidation

Chemical water oxidation experiments were performed in homemade cells with a volume of 16.5 mL and the temperature was kept constant (25°C) during the catalysis. Two cells were tightly closed with a septum. The evolution of the gas was monitored simultaneously with online manometry with a differential pressure manometer (Testo 521-1) which was connected to a reference cell with nearly the same size and a gas phase oxygen sensor (OXF900PT) which was purged through the septum of the reaction cell. The calibration before each experiment was performed with a two-point calibration in air and an N$_2$-atmosphere. For the experiment, the cell containing the complex was degassed with N$_2$ for some minutes and then 1.85 mL of 0.1 M degassed aqueous HOTf (pH = 1) was added to both cells. After reaching the equilibrium between the measurement and reference cell, 150 µl of aqueous HOTf (0.1 M, pH = 1) was added to the reference cell, while 150 µl degassed solution of CAN in aqueous HOTf (0.1 M, pH = 1) with the concentration of 10^{-3} M to the measurement cell.
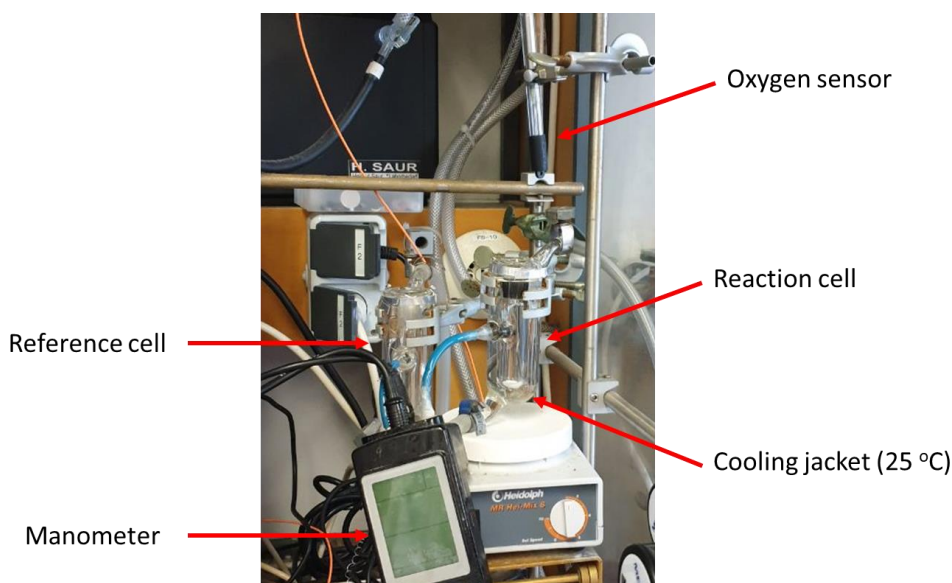
8.2.11 UV/vis-NIR spectroscopy

Spectra were recorded on TE Cooled InGaAs Array spectrometer (Sol^{TM} 1.7) using quartz cell (d= 0.1 cm) to diminish the saturation for solvents with high absorption in NIR region. The spectroscopic data were analyzed with BWSpec software.

8.2.12 X-Ray Crystallography

X-ray data were collected on an STOE IPDS II or a BRUKER D8-QUEST diffractometer (graphite monochromated Mo-Kα radiation, λ = 0.71073 Å) by use of w scans at low temperature. The structures were solved with SHELXT and refined on F^2 using all reflections with SHELXL.[178,179] Non-hydrogen atoms were refined anisotropically. Hydrogen atoms were placed in calculated positions and assigned to an isotropic displacement parameter of 1.5/1.2 U_{eq}(C) for complex **1^{pyr}** and 1.2 U_{eq}(C) for complexes **2**, **7** and **8**. PF$_6^-$ counterions (occupancy factors: 0.783(4) /0.217(4); 0.830(8) / 0.170(8); 0.552(4) / 0.448(4); 0.589(3) / 0.411(3)) and a diethyl ether solvent molecule (occupancy factors: 0.61(2) / 0.39(2)) in complex **1^{pyr}** were found to be disordered. SADI (d_{P-F}, $d_{F\cdots F}$), BUMP, RIGU, DELU, ISOR and DFIX restraints (d_{C-O} = 1.43 Å, d_{C-C} = 1.51 Å) and EADP constraints were used to model the disordered parts. All unit cells contain highly disordered solvent molecules for which no satisfactory model for a disorder could be found. The solvent contribution to the structure factors was calculated with PLATON SQUEEZE[180] and the resulting .fab file was processed with SHELXL using the ABIN instruction. The empirical formula and derived values are in accordance with the calculated cell content. In the case of **7** a PF$_6^-$ counterion was found to be disordered (occupancy factors: 0.426(7) / 0.574(7). Furthermore, diethyl ether (occupancy factors: 0.534(3) / 0.466(3)) and acetone solvent molecules were found to be disordered. The latter solvent was disordered about a center of inversion and was refined at ½ occupancy using SADI, FLAT and RIGU restraints. The disordered diethyl ether solvent molecule was refined using DFIX ($d_{CH2-CH3}$ = 1.51 Å; d_{CH2-O} = 1.43 Å) and RIGU restraints. SAME and RIGU restraints were used to model the disordered parts. Face-indexed absorption corrections were performed numerically with the program X-RED[181] for **1^{pyr}** and **2**, and by the multi-scan method with SADABS[182] for **7** and **8**.

8.2.13 High-resolution transmission and scanning electron microscopy (HRTEM and STEM)

HRTEM

HRTEM analysis of the MWCNT samples was carried out using an FEI Titan ETEM G2 80–300 equipped with a Cs-corrector of the image forming lens for enhanced HRTEM analysis operated at 300 kV. The microscope was used in the high vacuum (HV) mode with a cold trap to achieve better vacuum conditions.

EELS

EELS was performed using a Gatan Quantum 965ER post-column energy filter in the same FEI Titan ETEM G2 80–300 system. Spectra of the low loss, C K, Ru M, and O K edges were acquired. EELS data were analyzed using Gatan DM software with inbuilt EELS analysis functions. The power-law function was used to subtract the background from the high loss region. The low loss spectra were analyzed using the Fourier-log deconvolution function. The zero-loss peak is used to correct the energy calibration.

8.3 Ligand Synthesis

8.3.1 Synthesis of ^{pyr}bbp(MOM)*
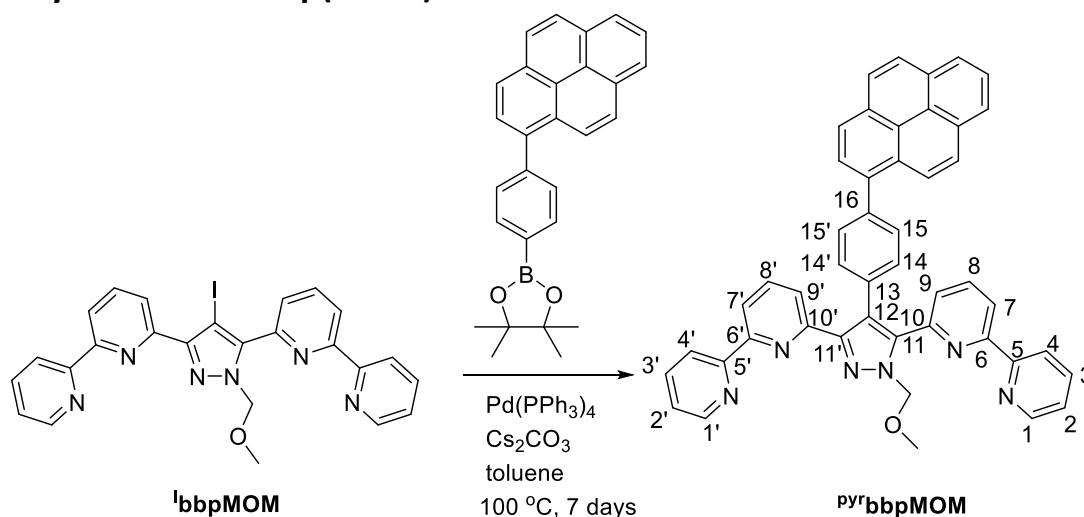
4,4,5,5-Tetramethyl-2-(4-(pyren-1-yl)phenyl)-1,3,2-dioxaborolane (315 mg, 0.78 mmol), **^{I}bbp(MOM)** (428 mg, 0.78 mmol), Pd(PPh$_3$)$_4$ (90.67 mg, 0.078 mmol) and Cs$_2$CO$_3$ (1.27 g, 3.89 mmol) were dissolved in dry and degassed toluene and was heated for 7 days at 100 °C. DCM (10 mL) and water (10 mL) were added to the suspension, the organic phase was separated and the aqueous phase was extracted with DCM (3 x 50 mL). The combined DCM phases were evaporated to dryness under reduced pressure and the crude product was purified by column

chromatography (basic Alox, hexanes/ethyl acetate 5:1). The product (300 mg, 0.43 mmol, 55%) was obtained as a yellow solid.

¹H-NMR (500 MHz, CDCl₃): δ (ppm) = 3.54 (s, 3 H, 18-H), 5.95 (s, 2 H, 17-H), 7.09-7.13 (m, 1H, H$_{pyr}$), 7.29-7.33 (m, 1H, H$_{pyr}$), 7.39 (dd, J = 7.8, 0.7 Hz, 1H, H$_{pyr}$), 7.40-7.44 (m, 1H, 2-H), 7.52 (M, 2H, 15-H, 15´-H), 7.61 (m, 3H, 2'-H, 4'-H, 7'-H), 7.79 (m, 1H, 3´-H), 7.81 (t, J =7.9 Hz, 8-H), 7.88 (d, J = 8.6 Hz,1H, H$_{pyr}$), 7.92 (t, J = 7.6 Hz, 1H, 3-H), 7.96-8 (m, 2H, 14-H, 14´-H),8.14 (m, 2H, H$_{pyr}$), 8.17-8.21 (m, 1H, 8-H), 8.21-8.28 (m, 2H, H$_{pyr}$), 8.38-8.42 (m, 2H, 4-H, 7´-H), 8.47 (dd, J = 7.5, 1.1 Hz, 1H, 9´-H), 8.62 (ddd, J = 4.8, 1.8, 1.0 Hz, 1H, 1´-H), 8.73 (ddd, J = 4.9, 1.7, 0.8 Hz, 1H, 1-H).

¹³C-NMR (75 MHz, CDCl₃): δ [ppm] = 57.3 (18-C), 80.7 (17-C), 119.6, 120.2 (9'-C), 121.3 (4-C, 7'-C), 121.4 (4'-C), 122.3 (9-C), 123.5, 124.6 (2-C), 124.8, 124.9, 125.0, 125.1, 125.2, 125.4, 126.0, 127.3, 127.4, 127.5, 127. 6, 128.2, 130.4 (14-C, 14'-C), 130.9, 130.5 (15-C, 15'-C), 133.4, 137.1, 137.3 (8-C), 137.3, 137.4, 137.5, 139.2, 141. 4, 148.2 (1'-C), ,148.3, 148.6, 149.0 (1-C), 151.9, 155.6, 155. 7, 155.9.

MS (ESI+): m/z (%) = 697.3 (100) [M+H]⁺, 719.3 (8) [M+Na]⁺.

7.3.2 Synthesis of ᴾʸʳbbpH*

ᴾʸʳbbpMOM   ᴾʸʳbbpH
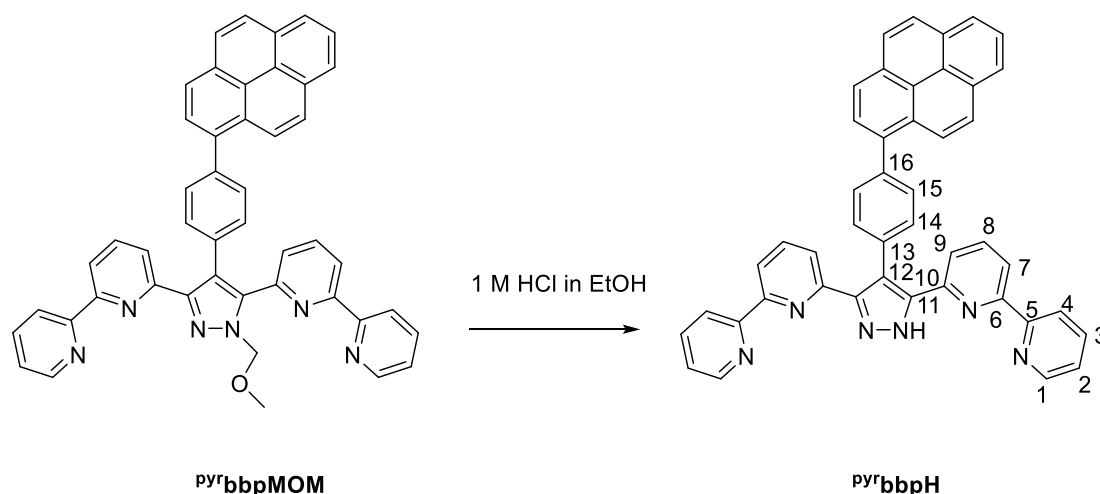
A 1 M solution of HCl in ethanol (10 mL) was added to ᴾʸʳ**bbp(MOM)** (225 mg, 0.32 mmol) at room temperature and the mixture was stirred overnight. The resulting precipitate was collected by filtration and washed with cold ethanol (2 x 1 mL). ᴾʸʳ**bbpH** was obtained as a yellow powder after drying under vacuum (180 mg, 0.27 mmol, 79%).

¹H-NMR (500 MHz, methanol-d_4): δ (ppm) = 8.53 (d, J = 5.2 Hz, 2H, 1-H), 8.12 (d, J = 7.1 Hz, 1H, H_{pyr}), 8.06 (m, 4H, 4-H, 3-H), 7.96 (t, J = 6.0 Hz, 2H, H_{pyr}), 7.91-7.95 (m, 2H, H_{pyr}), 7.87-7.91(m, 2H, H_{pyr}), 7.85 (dd, J = 7.6, 1.8 Hz, 2H, 15-H), 7.84 (d, J = 7.4, 2H, 2-H), 7.74 (d, J = 7.6 Hz, 1H, H_{pyr}), 7.65 (t, J = 7.3 Hz, 4H, 8-H, 7-H), 7.40 (d, J = 7.7, 2H, 14-H), 7.01 (d, J = 7.7 Hz, 2H, 9-H).

¹³C-NMR (75 MHz, methanol-d_4): δ [ppm] = 150.6 (2C, 10-C), 147.9 (2C, 5-C), 147.5 (2C, 3-C), 146.8 (2C, 6-C), 142.6 (2C, 1-C), 142.5 (2C, 8-C), 140.1 (1C, 16-C), 137.0 (1C, C_{pyr}), 133.2 (1C, C_{pyr}), 132.9 (1C, 14-C), 132.5 (2C, 11-C), 131.8 (1C, 12-C), 131.7 (2C, 15-C), 131.6 (1C, C_{pyr}), 129.1 (1C, C_{pyr}), 129.0 (1C, C_{pyr}), 128.8 (1C, C_{pyr}), 128.6 (1C, C_{pyr}), 128.5 (2C, 2-C), 127.9 (1C, C_{pyr}), 127.6 (1C, C_{pyr}), 126.7 (1C, C_{pyr}), 126.3 (1C, C_{pyr}), 126.0 (1C, C_{pyr}), 125.3 (1C, C_{pyr}), 124.9 (2C, 4-C), 124.6 (2 C, 9-C), 122.5 (2 C, 7-C), 121.4 (1 C, 13-C).

MS (ESI+): m/z (%) = 653.2 (100) [M+H]$^+$, 675.23 (5) [M+Na]$^+$.

UV/vis (CH$_3$OH): λ [nm] (ε [L M^{-1} cm^{-1}]) = 241 (4.4 ×10^4), 277 (3.8×10^4), 346 (1.9×10^4).

7.3.3 Synthesis of 4-(4-(triethoxysilyl)butyl)pyridine

4-(4-(triethoxysilyl)butyl)pyridine
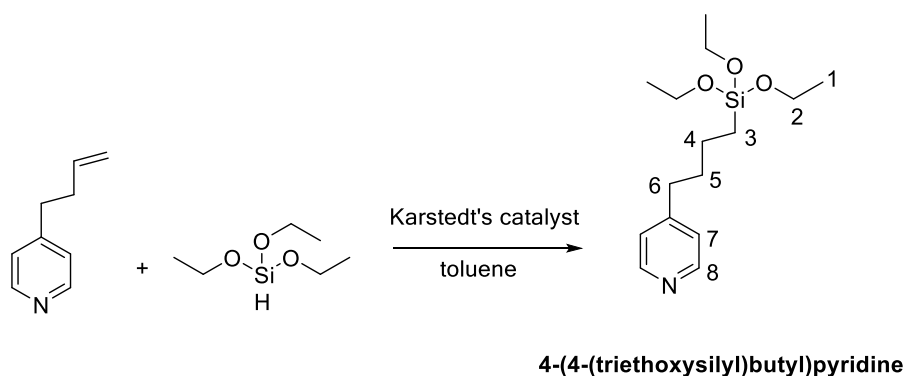
To a solution of 4-(but-3-en-1-yl)pyridine (500 mg, 3.75 mmol) and triethoxylsilane (0.75 mL, 4.1 mmol) in 20 mL toluene, Karstedt's catalyst in xylene (60 µL) was added sequentially within 1 h and the mixture was heated at 80 °C overnight. After cooling to room temperature, the solvent was removed under reduced pressure, which resulted in the product as a yellow oil. (800 mg, 2.69 mmol, yield: 80%) (It contains around 20% starting material as impurity).

¹H-NMR (300 MHz, CDCl₃): δ [ppm] = 8.47 (dd, J = 6, 1.7 Hz, 2H, 8-H), 7.98 (d, J = 6.1 Hz, 2H, 7-H), 3.87 (q, J = 6.8 Hz, 6H, 2-H), 1.68 (m, 2H, 6-H), 1.46 (m, 2H, 5-H), 1.21 (t, J = 7.1 Hz, 9H), 0.66 (m, 2H, 3-H).

MS (ESI+): m/z (%) = 298.1 (100) [M+H]$^+$, 320.1 (5) [M+Na]$^+$.

7.3.4 Synthesis of 6,6'-bis(1H-imidazo[4,5-b]pyridin-2-yl)-2,2'-bipyridine, (H₂L²)
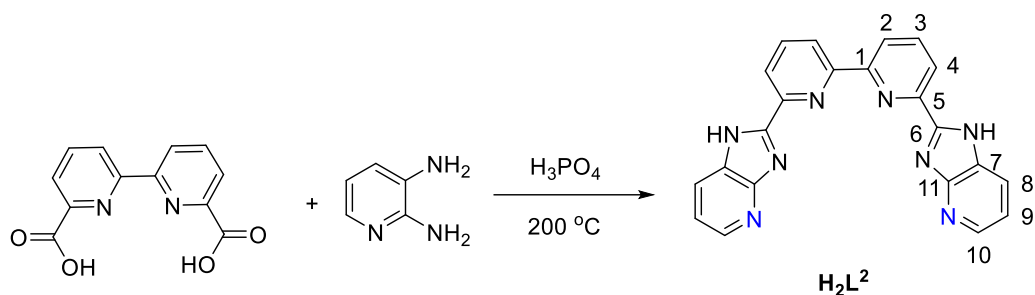
A mixture of 2,3-diaminopyridine (1.2 g, 10.56 mmol) and 2,2´-bipyridine-6,6´-dicarboxylic acid (1.19 g, 4.8 mmol) in phosphoric acid syrup (8 mL) was refluxed at 200 °C overnight. After cooling to room temperature, the solution was poured into ice and the precipitate was filtered off. The precipitate was suspended in water and neutralized with 25% aqueous ammonia to basic pH. The product was obtained after filtration and washing several times with water as a purple solid. (Yield: 1.1 g, 2.8 mmol, yield: 65%)

¹H-NMR (500 MHz, methanol-d_4): δ [ppm] = 8.43 (dd, J = 7.8, 0.8 Hz, 2H, 10-H), 8.19 (td, J = 7.1, 1.58 Hz, 4H, 3-H, 4-H), 8.03 (td, J = 7.5, 1.0 Hz, 4H, 8-H, 9-H), 7.04 (m, 2H, 2-H).

¹³C-NMR (125.8 MHz, methanol-d_4): δ [ppm] = 163.7 (11-C), 160.9 (6-C), 155.8 (5-C), 155.4 (7-C), 141.8 (8-C), 140.5 (2-C), 139.4 (10-C), 125.6 (4-C), 122.9 (1-C), 121.3 (9-C), 116.3 (3-C).

MS (ESI+): m/z (%) = 391.5 (100) [M+H]⁺, 413.1 (95) [M+Na]⁺.

7.4 Complex Synthesis

7.4.1 Synthesis of [ᵖʸʳbbpRu₂(μ-OAc)(py)₄](PF₆)₂ (1ᵖʸʳ)*
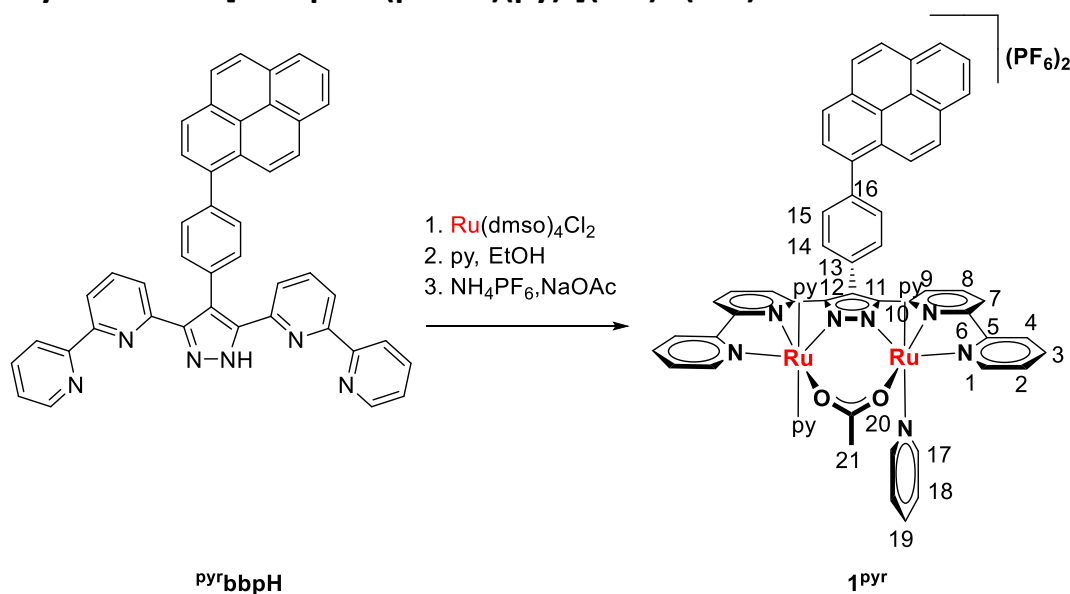
A solution of **^{pyr}bbpH** (175 mg, 0.27 mmol) in degassed EtOH (100 mL) was added dropwise to a solution of Ru(dmso)$_4$Cl$_2$ (386 mg, 0.79 mmol) and triethylamine (5.00 mL, 27.1 mmol) in degassed EtOH (20 mL) under reflux conditions. After the addition, the reaction was heated overnight at 80 °C. After cooling to -30 °C, the brown precipitate was separated by filtration and washed with a small amount of EtOH. The intermediate was then dissolved in EtOH (30 mL), pyridine (3 mL) was added, and the resulting solution was stirred under reflux overnight. After cooling to rt the solvent was evaporated and the residue was dissolved in acetone/water (50 mL, 1:1). NH$_4$PF$_6$ (250 mg, 1.53 mmol) was added and acetone was removed under reduced pressure. The precipitate was separated by filtration and washed with water (2 x 50 mL). The brown solid was purified by recrystallization from acetone/Et$_2$O. A mixture of the complex and NaOAc (300 mg, 3.65 mmol) in acetone/water mixture (20 mL, 1:1) was heated to reflux overnight. After cooling to rt the acetone was removed under reduced pressure and the formed precipitate was separated by filtration and washed with water (2 x 10 mL). The final product was obtained as a brown solid. (130 mg, 0.14 mmol, 51%).

^{1}H-NMR (500 MHz, acetone-d$_6$): δ (ppm) = 9.47 (d, J = 5.0 Hz, 2H, 1-H), 8.44 (m, J = 8.0 Hz, 2H, 14-H), 8.37-8.31 (m, 2H, H$_{pyr}$), 8.30-8.27 (m, 3H, H$_{pyr}$), 8.26 (m, 3H, H$_{pyr}$), 8.23 (dt, J = 5.7, 1.5 Hz, 2H, 4-H), 8.12 (dd, J = 7.6, 1.7 Hz, 2H, 15-H), 8.7 (d, J = 7.5, 2H, 7-H), 7.99 (dt, J = 7.8, 0.5 Hz, 2H, 3-H), 7.94 (d, J = 5.2 Hz, 8H, 17-H), 7.93 (m, J = 7.8 Hz, 2H, 2-H), 7.89 (dd, 8.1, 0.9 Hz, 2H, 9-H), 7.73 (t, J = 7.9 Hz, 2H, 8-H), 7.40 (t, J = 7.5 Hz, 4H, 19-H), 6.89 (d, J = 7.4 Hz, 8H, 18-H), 3.04 (s, 3H, 21-H).

^{13}C-NMR (75 MHz, acetone-d$_6$): δ [ppm] = 210.0 (1C, C$_{pyr}$), 186.5 (1C, 20-C), 162.0 (2C, 6-C), 160.1 (2C, 5-C), 159.3 (2C, 10-C), 152.5 (8C, 17-C), 151.1 (2C, 1-C), 149.6 (2C, 11-C), 142.7 (1C, C$_{pyr}$), 138.0 (2C, 3-C), 137.9 (1C, 13-C), 137.4 (4C, 19-C), 134.0 (2C, 8-C), 132.6 (1C, 16-C), 132.4 (2C, 14-C), 132.0 (2C, 15-C), 131.3 (1C, C$_{pyr}$), 129.4 (1C, C$_{pyr}$), 129.2 (2C, 2-C), 128.9 (1C, C$_{pyr}$), 128.8 (1C, C$_{pyr}$), 128.8 (1C, C$_{pyr}$), 128.5 (1C, C$_{pyr}$), 127.8 (1C, C$_{pyr}$), 127.5 (1C, C$_{pyr}$), 126.6 (1C, 12-C), 126.1 (1C, C$_{pyr}$), 126.0 (1C, C$_{pyr}$), 125.8 (8C, 18-C), 123.9 (2C, 4-C), 120.1 (2C, 9-C), 119.7 (2C, 7-C), 30.4 (1C, 21-C).

MS (ESI+): m/z (%)= 615.1 (100) [M-2PF$_6$]$^{2+}$, 1375.2 (9) [M-PF$_6$]$^+$.

UV/vis (CH$_3$OH): λ [nm] (ε [M^{-1} cm^{-1}]) = 241 (7.5×10^4), 277 (5×10^4), 315 (3.9×10^4), 346 (4.3×10^4), 540 (0.9×10^4).

7.4.2 Synthesis of [bbpRu₂(OAc)(py-SiO₃(Et)₃)₄](PF₆)₂ (1⁴ˢⁱ⁽ᴼᴱᵗ⁾³)

^H**bbpH**   **1**^{4Si(OEt)3}
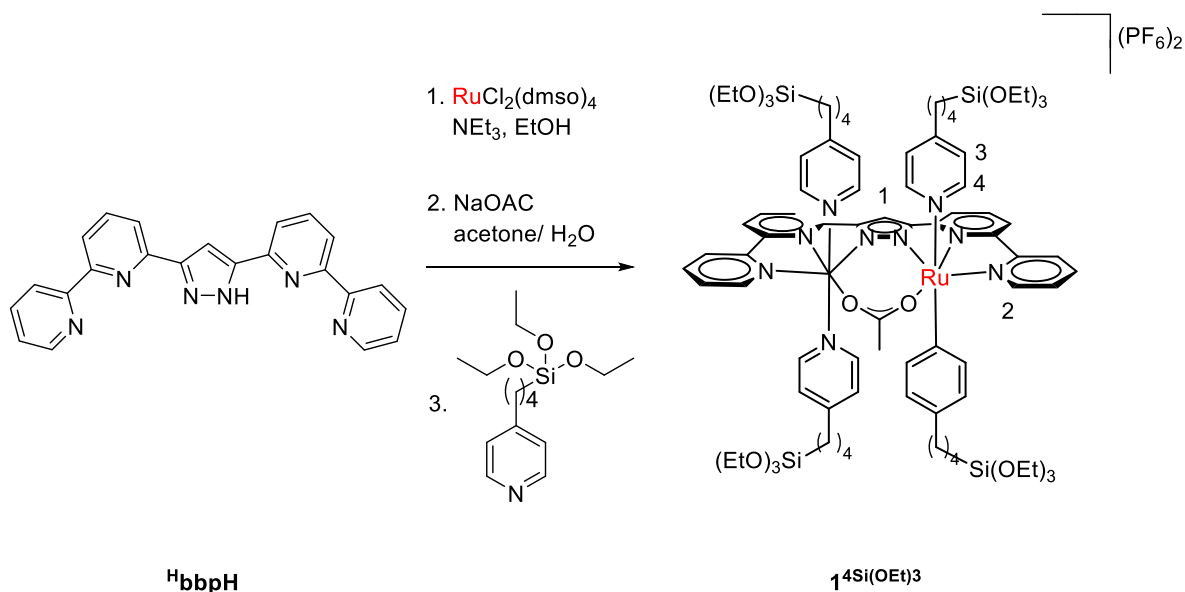
A dilute solution of ^Hbbp (200 mg, 0.515 mmol) in 20 mL EtOH and 1 mL NEt₃ was added very slowly over 4h to a solution of RuCl₂(dmso)₄ (1.10 g, 10.8 mmol) in 20 mL ethanol and triethylamine (2 mL) under reflux condition. The mixture was heated at 90 °C overnight. After cooling to -30 °C, the brown precipitate was filtered off and washed with EtOH (5mL) and then reacted with NaOAc (511 mg, 7.59 mmol) in acetone/H₂O mixture (50 mL, 1:1) was heated at 70 °C overnight. After removing the acetone, the formed precipitate was separated by filtration and washed with water (20 mL). Then, the brown solid (100 mg, 0.118 mmol) and 4-(4-(triethoxysilyl)butyl)pyridine (200 mg,0.67 mmol), were dissolved in 30 mL EtOH and the solution was heated to reflux for 2 days. Later, the solvent was removed under reduced pressure and the residue was dissolved in dry dichloromethane and stirred with KPF₆ for 2h. After separation of the salts by filtration, the solvent was removed to yield the product. (It contains some free 4-(4-(triethoxysilyl)butyl)pyridine as impurities). (100 mg, 0.05 mmol, yield: 40%).

¹H-NMR (500 MHz, CDCl₃): δ (ppm) = 9.22 (m, 2H, 2-H), 8.4 (m, 2H), 8.16 (s, 1H, 1-H), 8.11 (m, 2H), 7.9 (2H), 7.7 (2H), 7.6 (2H), 7.37 (m, 8H, 4-H), 7.03 (2H), 6.39 (m, 8H, 3-H), 3.69 (q, 23H), 2.95 (s, 3H, 5-H), 2.5, 2.2, 2.02, 1.10 (t, 36H), 0.47.

¹³C-NMR (75 MHz, CDCl₃): δ [ppm] = 185.8, 160.0, 158.8, 158.3, 151.6, 151.3, 150.6 (8C, 4-C), 150. 5, 149.5, 136.3, 136.1, 132.9, 128.2, 124.3 (8C, 3-C), 123.8, 122.2, 119.2, 117.7, 116.0, 108.0, 58.3, 34.3, 33, 29.5, 22.3, 18.2, 10.1.

7.4.3 Synthesis of [L^{1}Ru(py)$_2$] (2)
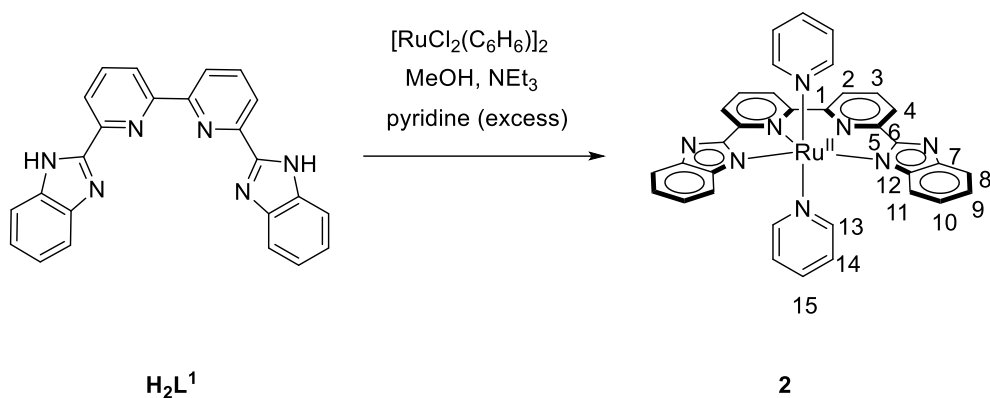
A solution containing 6,6´-bis-(1H-benzoimidazol-2-yl)-2,2´-bipyridine (**H$_2$L^1**) (300 mg, 0.77 mmol), [RuCl$_2$(C$_6$H$_6$)]$_2$ (197 mg, 0.4 mmol) and 1 mL NEt$_3$ in degassed methanol was heated to reflux under nitrogen for one day. Then, 1.4 mL pyridine (excess) was added to the reaction mixture and heated for another day. After cooling to room temperature, the brown solution was filtered and the solvent was removed. The resulting crude material was purified by column chromatography to give the product **2** as a brown solid (DCM/MeOH = 100:2). (150 mg, 0.23mmol, yield: 30%)

^{1}H-NMR (500 MHz, methanol-d_4): δ [ppm] = 8.7 (d, J = 7.7 Hz, 2H, 11-H), 8.57 (d, J = 7.8 Hz, 2H, 2-H), 8.29 (d, J = 7.9 Hz, 2H, 4-H), 8.05 (t, J = 7.8 Hz, 2H, 3-H), 7.86 (dd, J = 6.5, 1.5 Hz, 4H, 13-H), 7.71 (d, J = 7.2 Hz, 2H, 10-H), 7.67 (t, J = 7.6 Hz, 8-H), 7.45 (t, J = 7.4 Hz, 2H, 9-H), 7.35 (m, 2H, 15-H), 6.83 (t, J = 7.1 Hz, 4H, 14-H).

^{13}C-NMR (125.8 MHz, methanol-d_4): δ [ppm] = 161.2 (6-C), 158.9 (5-C), 156.3 (1-C), 153.4 (13-C), 143.4 (12-C), 142.5 (7-C), 137.9 (15-C), 135.5 (3-C), 125.9 (14-C), 125.3 (8-C), 124.8 (9-C), 123.6 (2-C), 122.7 (4-C), 117.6 (10-C), 116.8 (11-C).

MS (ESI+): m/z (%) = 647.1 (100) [M+H]$^+$.

UV/vis (MeOH): λ [nm] (ε [M^{-1} cm^{-1}]) = 329 (3.3 × 10^4), 382 (1.6 × 10^4), 490 (b, 0.4 ×10^4), 561 (0.4× 10^4).

7.4.4 Synthesis of [L^1-H$_2$Ru(py)$_2$] ([2H$_2$](CF$_3$SO$_3$)$_2$)
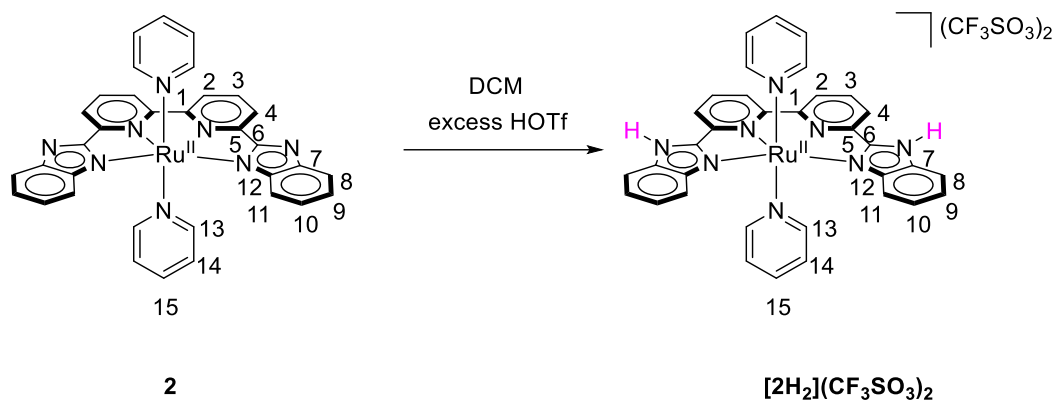
A solution of **2** (5 mg, 0.007 mmol) in DCM (2 mL) was stirred in presence of trifluoromethanesulfonic acid (HOTf) (0.66 M, 45 μL, 0.031 mmol) for 1 h. Then, the solvent was removed and the product was dried under vacuum.

^{1}H-NMR (500 MHz, methanol-d_4): δ [ppm] = 8.83 (d, J = 7.8 Hz, 2H, 11-H), 8.78 (dd, J = 8.1, 0.9 Hz, 2H, 2-H), 8.4 (dd, J = 7.8, 0.8 Hz, 2H, 4-H), 8.2 (t, J = 7.8 Hz, 2H, 3-H), 7.95 (m, 4H, 13-H), 7.92 (m, 2H, 10-H), 7.8 (d, J = 8.2 Hz, 8-H), 7.7 (m, 2H, 9-H), 7.47 (tt, 7.5, 1.6 Hz, 2H, 15-H), 6.96 (m, 4H, 14-H).

^{13}C-NMR (125.8 MHz, methanol-d_4): δ [ppm] = 161.6 (6-C), 153.5 (5-C), 153.3 (13-C), 141.4 (7-C), 138.8 (15-C), 137.0 (3-C), 135.9 (12-C), 127.7 (9-C), 127.4 (10-C), 126.6 (14-C), 125.7 (2-C), 124.2 (4-C), 122.8, 118.0 (11-C), 115 (8-C).

UV/vis (MeOH): λ [nm] (ε [M^{-1} cm^{-1}]) = 320 (3.5 × 10^4), 356 (2.1 × 10^4), 408 (0.5 x 10^4), 480 (b, 0.4 ×10^4).

7.4.5 Synthesis of [L²Ru(py)₂] (3)
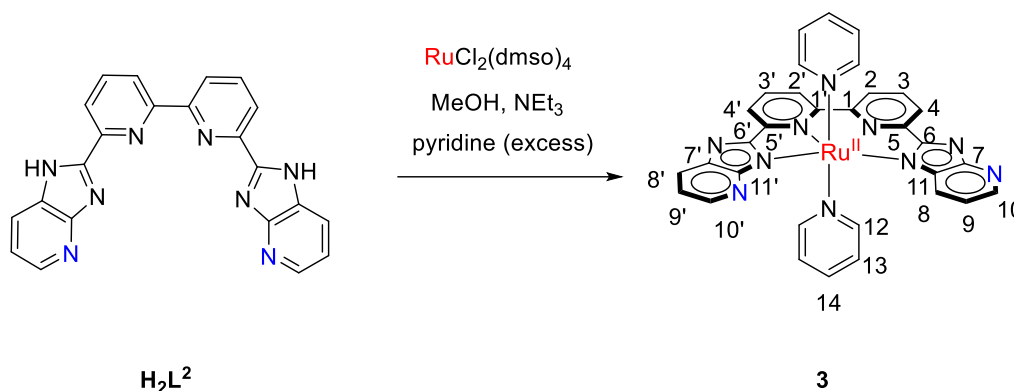
A suspension of 6,6'-bis(1H-imidazo[4,5-b]pyridin-2-yl)-2,2'-bipyridine (**H₂L²**) (300 mg, 0.76 mmol), RuCl₂(dmso)₄ (300 mg, 0.61 mmol) and triethylamine (0.5mL) in degassed EtOH (50 mL) was heated to reflux for 7 hours. Pyridine (0.6 mL, 7.45 mmol) was added and the reaction mixture was heated at 80 °C overnight. The precipitate was filtered off and the solvent evaporated. The crude material was dissolved again in ethanol (50 mL) and pyridine (0.3 mL, 0.37 mmol) was added and then the solution was refluxed for another day. After evaporation of the solvent, the product was purified by column chromatography (DCM/MeOH = 100:1). (70 mg, 0.10 mmol, yield: 10%).

¹H-NMR (500 MHz, methanol-d_4): δ [ppm] = 9.8 (dd, J = 8.1, 1.7 Hz, 1H, 8-H), 8.77 (dd, J = 4.6, 1.4 Hz, 1H, 10'-H), 8.54 (dt, J = 7.1, 0.7 Hz, 2H, 2,2'-H), 8.37 (dd, J = 4.7, 1.7 Hz, 1H, 10-H), 8.31 (dd, J =7.7, 0.6 Hz, 1H, 4/4'-H), 8.21 (dd, J =7.8, 0.6 Hz, 1H, 4/4'-H), 7.98 (m, 4H, 12-H), 7.96 (m, 1H, 8'-H), 7.93 (m, 2H, 3,3'-H), 7.48 (m, 2H, 9-H), 7.28 (m, 1H, 9'-H), 7.26 (m, 2H, 14-H), 6.7 (t, J = 7 Hz, 4H, 13-H).

¹³C-NMR (125.8 MHz, methanol-d_4): δ [ppm] = 180.2, 164.9, 164.3, 161.3, 159.2, 158.3, 158.1, 157.8, 153.4 (4C, 12-C), 146.7 (1C, 10'-C), 144.0 (1C, 10-C), 139.6, 138.0, 137.3 (2C, 14-C), 134.4 (1C, 3,3'-C), 126.4 (1C, 8'-C), 126.2 (1C, 8-C), 125.4 (4C, 13-C), 123.3 (2C, 2,2'-C), 123.2, 122,5 (1C, 4/4'-C), 121.7 (1C, 4/4'-C), 119.2 (1C, 9-C), 118.2 (1C, 9'C).

MS (ESI+): m/z (%) = 649.2 (100) [M+H]⁺.

UV/vis (MeOH): λ [nm] (ε [M⁻¹ cm⁻¹]) = 331 (3.4 × 10⁴), 374 (1.7 × 10⁴), 430 (0.6 × 10⁴), 497 (br, 0.3× 10⁴), 561 (br, 0.2× 10⁴).

7.4.6 Synthesis of [L^2-H$_2$Ru(py)$_2$] ([3H$_2$](CF$_3$SO$_3$)$_2$)

3   **[3H$_2$](CF$_3$SO$_3$)$_2$**
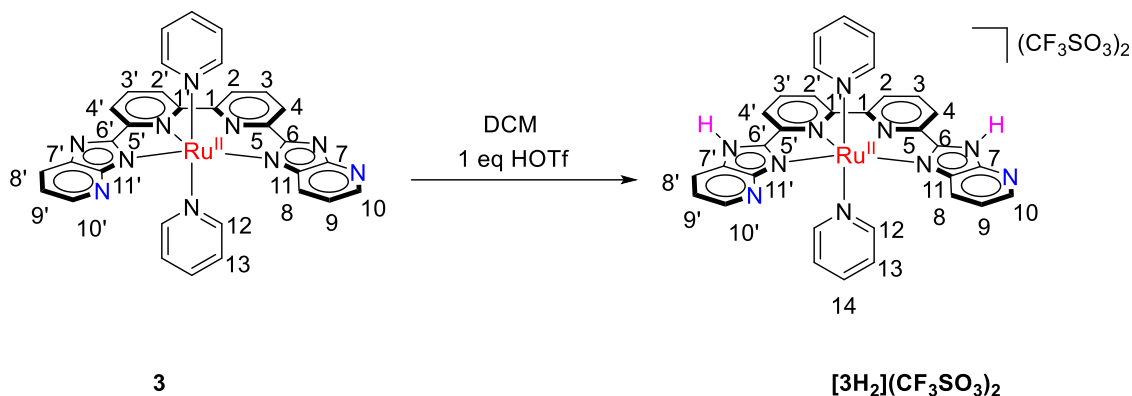
(45 μL, 0.031 mmol, 0.66 M) trifluoromethanesulfonic acid was added to a solution of **3** (4.5 mg, 0.007 mmol) in 2 mL DCM and the reaction mixture was stirred for 1 hour. The protonated product was obtained after the removal of the solvent.

^{1}H-NMR (500 MHz, methanol-d_4): δ [ppm] **=** 10.1 (dd, J = 7.9, 1.2 Hz, 1H, 8-H), 9.1 (dd, J = 4.8, 1.5 Hz, 1H, 10'-H), 8.8 (ddd, J = 8.1, 2.2, 0.8 Hz, 2H, 2, 2'-H), 8.6 (dd, J = 5.2, 1.4 Hz, 1H, 10-H), 8.48 (dd, J =7.7, 0.7 Hz, 1H, 4/4'-H), 8.43 (dd, J =7.8, 0.7 Hz, 1H, 4/4'-H), 8.2 (dd, J = 8.1, 1.3 Hz, 1H, 8'-H), 8.18 (m, 2H, 3,3'-H), 8.0 (m, 4H, 12-H), 7.9 (m, 1H, 9-H), 7.7 (m, 1H, 9'-H), 7.4 (tt, J = 7.6, 1.5 Hz, 2H, 14-H), 6.9 (m, 4H, 13-H).

^{13}C-NMR (125.8 MHz, methanol-d_4): δ [ppm] = 162.8, 162.0, 161.6, 156.2, 154.9, 154.1, 153.2 (12-C), 150.3 (10'-C), 141.7 (10-C), 138.8 (14-C), 138.5, 136.8 (8'-C), 136.3, 130.9, 128.9, 128.8, 126.4 (13-C), 126.4(2/2'-C), 126.3 (2/2'-C),125.0 (4/4'-C), 124.7 (4/4'-C), 123.9 (3/3'-C), 123,0 (9'-C), 122.9, 121.1 (9-C).

UV/vis (MeOH): λ [nm] (ε [M^{-1} cm^{-1}]) = 325 (3.6 × 10^4), 356 (1.7 × 10^4), 487 (br, 0.3× 10^4).

7.4.7 Synthesis of [L²Ru(py-COOH)₂] (4)
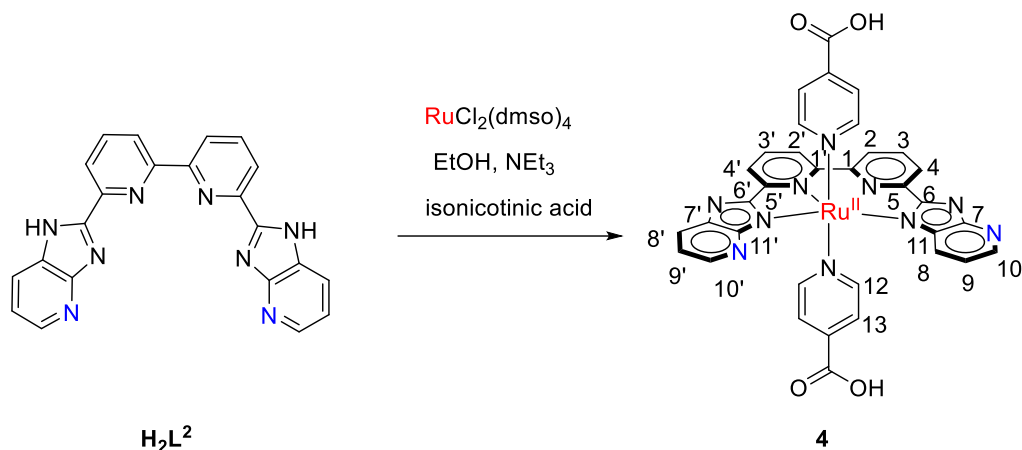
A suspension of **H₂L²** (300 mg, 0.77 mmol, 1.2 equiv.) and RuCl₂(dmso)₄ (300 mg, 0.62 mmol, 1 equiv.) in EtOH (50 mL) with NEt₃ (0.6 mL) was refluxed overnight. Then, isonicotinic acid (61 mg, 0.5 mmol, 1 equiv.) was added and the reaction mixture was stirred at 80 °C for another day. The mixture was then filtered and the solvent was evaporated. Without further purification, the intermediate complex was dissolved in EtOH/H₂O (5/1) and treated with another 1.5 equiv. of isonicotinic acid (92 mg, 0.75 mmol, 1.5 equiv.) under reflux conditions. After evaporation of the solvent, the crude material was purified via silica column and TLC plate chromatography using methanol and DCM. (20 mg, 0.03 mmol, yield: 4%).

¹H-NMR (500 MHz, methanol-d_4): δ [ppm] = 10.01 (dd, J = 8.1, 1.3 Hz, 1H, 8-H), 8.91 (dd, J = 4.8, 1.4 Hz, 1H, 10'-H), 8.64 (m, 2H, 2,2'-H), 8.49 (dd, J = 4.9, 1.3 Hz, 1H, 10-H), 8.37 (d, J =8.0 Hz, 1H, 4/4'-H), 8.26 (d, J =7.8 Hz, 1H, 4/4'-H), 8.07 (t, J =8.0 Hz, 1H, 3/3'-H), 8.04 (m, 4H, 12-H), 8.03 (m, 2H, 3/3'-H, 8'-H), 7.68 (m, 1H, 9-H), 7.42 (m, 1H, 9'-H), 7.13 (m, 4H, 13-H).

¹³C-NMR (125.8 MHz, methanol-d_4): δ [ppm] = 170.4, 161.4, 161.3, 156.6, 156.5, 156.4, 153.7, 153.5 (4C, 12-C), 153.3, 147.8 (1C, 10'-C), 146.6, 137.7, 135.3 (1C, 3/3'/8'-C), 135.2 (1C, 3/3'-C), 127.8 (1C, 8-C), 125.8 (1C, 3/3'/ 8'-C), 125.1, 124.8, 124.8, 124.7 (4C, 13-C), 124.4 (1C, 2,2'-C), 124.4 (1C, 2,2'-C), 123.6 (1C, 4/4'-C), 122.7 (1C, 4/4'-C), 120.3 (1C, 9-C), 119.7 (1C, 9'-C).

7.4.8 Synthesis of [L²Ru(DMAP)₂] (5)
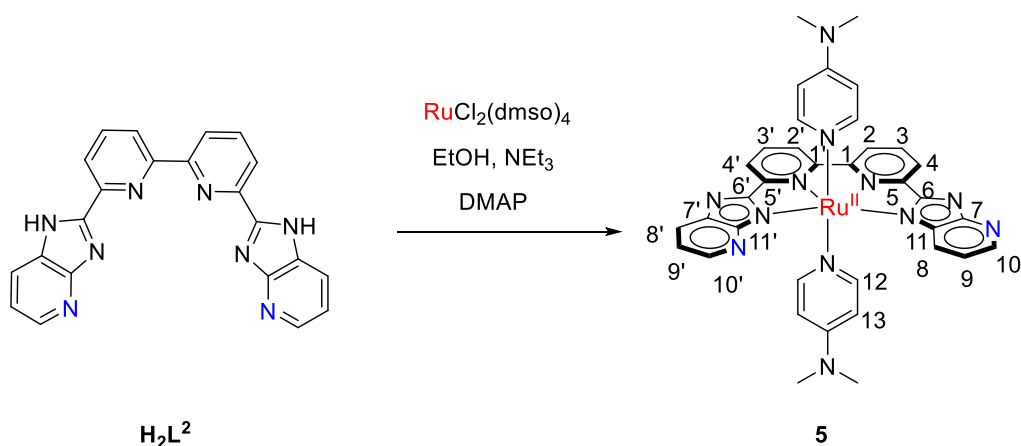
H₂L² (300 mg, 0.768 mmol, 1.2 equiv.), RuCl₂(dmso)₄ (300 mg, 0.62 mmol, 1 equiv.) and NEt₃ (0.6 mL) were suspended in EtOH (50 mL) and heated at reflux overnight. Then, 4-dimethylamino pyridine (DMAP) (75 mg, 0.57 mmol, 1 equiv.) was added and the mixture refluxed again for one day. Subsequently, the solvent was removed under reduced pressure and the crude material was reacted with DMAP (50 mg, 0.6 equiv.) in EtOH for one day at 80 °C. After cooling down to room temperature, the precipitate was filtered off and the solvent evaporated. The crude product was then purified via silica gel column with dichloromethane: MeOH (3:1). (30 mg, 0.04 mmol, yield: 5%).

¹H-NMR (500 MHz, methanol-d_4): δ [ppm] = 9.79 (dd, J = 8.1, 1.2 Hz, 1H, 8-H), 8.99 (dd, J = 4.6, 1.4 Hz, 1H, 10'-H), 8.62 (m, 1H, 2/2'-H), 8.59 (dd, J =5.4, 1.1Hz, 1H, 2/2'-H), 8.49 (d, J = 8.4 Hz, 4/4'-H), 8.41 (d, J = 7.7 Hz, 4/4'-H), 8.28 (m, 2H, 3,3'-H), 8.20 (dd, J =8.29, 1.2 Hz, 8'-H), 8.07 (m, 4H, 12-H), 7.82 (m , 1H, 9-H), 7.60 (m ,1H, 9'-H), 6.9 (d, J = 7.6 Hz, 13-H), 2.65 (s, 12H, H$_{DMAP}$).

¹³C-NMR (125.8 MHz, methanol-d_4): δ [ppm] = 165.7, 162.5, 160.7, 160.51, 159.1, 155.7, 149.9 (1C, 10'-C), 141.9, 139.8 (4C, 12-C), 138.8 (1C, 3/3'-C), 138.6 (1C, 3/3'-C), 130.8, 130.7 (1C, 8-C), 125.4 (1C, 2/2'-C), 125.4 (1C, 2/2'-C), 125.2 (1C, 4/4'-C), 125.0 (1C, 8'-C), 124.6 (1C, 4/4'-C), 121.8 (1C, 9'-C), 120.7 (1C,9-C), 108.2 (4C, 13-C), 40.4 (4C, C$_{DMAP}$)

7.4.9 Synthesis of [L³Ru₂(μ-dmso)(py)₄Cl](PF₆)₂, (6)
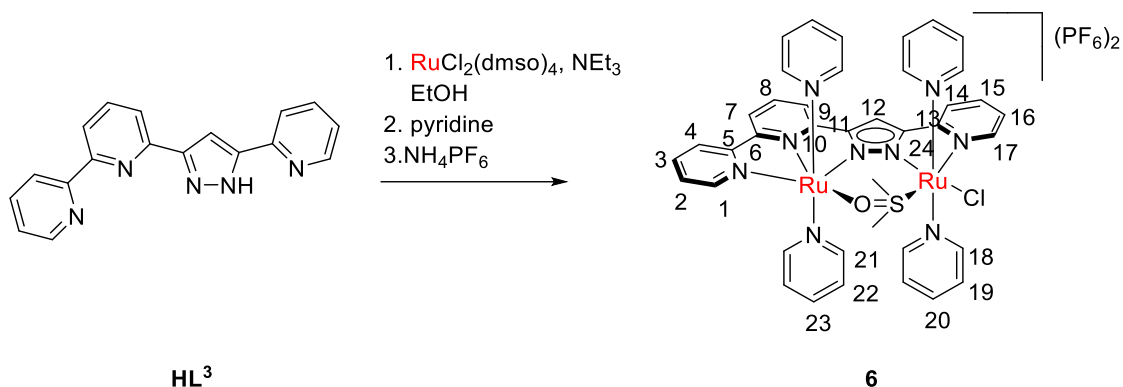
HL³   **6**

To a solution of RuCl₂(dmso)₄ (2 g, 4.13 mmol) and NEt₃ (5 mL) in degassed ethanol, a degassed solution of 3-{6-(2,2'-bipyridyl)}5-(2-pyridyl)pyrazol (**HL³**)[173] (537 mg, 1.79 mmol) and NEt₃ (5 mL) in degassed EtOH was added dropwise over 7 h under reflux condition and then the mixture was heated at 80 °C overnight. After cooling to 0 °C, the precipitate was filtered off and washed with diethyl ether.

The intermediate complex (268 mg, 0.32 mmol) was dissolved in a degassed EtOH/H₂O mixture (3:1) an excess amount of pyridine (0.5 mL) was added and the solution was stirred under reflux overnight. Afterwards, the solvent was removed under reduced pressure. The brown was solid dissolved in an acetone/H₂O mixture (1:1, 30 mL) and one spatula of NH₄PF₆ was added and acetone was removed under reduced pressure. The formed precipitate was filtered and washed with water to remove the excess NH₄PF₆ salt. The product was purified by column chromatography (silica gel, MeOH/DCM 1:9) (100 mg, 0.11 mmol, yield: 34%).

¹H-NMR (500 MHz, acetone-d_6): δ [ppm] = 9.53 (d, J = 5.8 Hz, 1H, 17-H), 9.5 (d, J = 5.1 Hz, 1H, 1-H), 8.49 (dd, J = 5.8 Hz, 4H, 18-H), 8.43 (dd, J = 5, 0.9 Hz, 1H, 14-H), 8.28 (d, J = 8.0 Hz, 1H, 9-H), 8.25 (d, J = 7.6 Hz, 1H, 4-H), 8.20 (s, 1H, 12-H), 8.15 (dd, 7.0 Hz, 4H, 21-H), 8.06 (t, J =8.0 Hz, 1H, 15-H), 8.02 (dd, J = 7.8, 1.5 Hz, 1H, 3-H), 8.00 (m, 2H, 7-H, 8-H), 7.86 (m, 1H, 16-H), 7.81 (m, 2H, 20-H), 7.55 (m, 1H, 2-H), 7.53 (m, 2H, 23-H), 7.40 (td, J = 6.9, 1.5 Hz, 4H, 19-H), 6.70 (td, J = 7.3, 1.5 Hz, 4H, 22-H), 3.34 (s, 6H, H$_{dmso}$).

¹³C-NMR (125.8 MHz, acetone-d_6): δ [ppm] = 161.6, 159.4, 157.8, 155.1, 154.8 (4C, 21-C), 153.1 (4C, 18-C), 152.9 (1C, 1-C), 152.9, 152.8, 151.4 (1C, 17-C), 140.2 (1C, 7-C), 139.1 (1C, 3-C), 138.6 (2C, 20-C), 138.3 (2C, 23-C), 135.3 (1C, 15-C), 129.5 (1C, 16-C), 126.9 (4C, 19-C), 125.5

(4C, 22-C), 124.7 (1C, 2-C), 123.7 (1C, 9-C), 121.2 (1C, 14-C), 120.3 (1C, 4-C), 107.9 (1C, 12-C), 42.2 (2C, C_{dmso}).

7.4.10 Synthesis of [L^3Ru_2(μ-OAc)(py)$_4$py](PF$_6$)$_2$, (7)
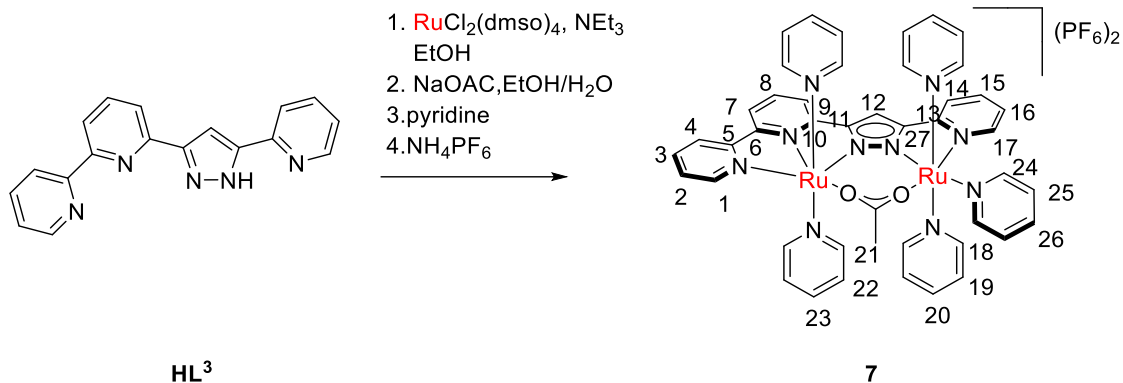
To a solution of RuCl$_2$(dmso)$_4$ (2 g, 4.13 mmol) and NEt$_3$ (5 mL) in degassed ethanol, a degassed solution of 3-{6-(2,2'-bipyridyl)}5-(2-pyridyl)pyrazol (**HL^3**)[173] (537 mg, 1.79 mmol) and NEt$_3$ (5 mL) in degassed EtOH was added dropwise over 7 h and then the mixture was heated at 80 °C overnight. After cooling to 0 °C, the precipitate was filtered off and washed with diethyl ether. The intermediate complex (268 mg, 0.32 mmol) was dissolved in a degassed EtOH/H$_2$O mixture (3:1) and (30 mg, 0.37 mmol) NaOAc was added and the reaction mixture was heated at reflux overnight. Afterwards, (0.1 mL, 1.20 mmol) pyridine was added and the mixture was stirred under reflux another day. Then, the solvent was removed under reduced pressure and the crude material was dissolved again in an acetone/H$_2$O mixture (1:1, 10 mL). After the addition of NH$_4$PF$_6$, acetone was removed and the resulting precipitate was filtered off and washed with H$_2$O. The product was purified by column chromatography on silica gel (MeOH/DCM 2:100). (15 mg, 0.015 mmol, yield: 25%).

^{1}H-NMR (500 MHz, acetone-d_6): δ [ppm] = 9.57 (dd, J = 5.6, 0.8 Hz, 1H, 1-H), 8.68 (d, J =5.2 Hz, 1H, 17-H), 8.35 (dd, J =7.3, 0.9 Hz, 1H, 9-H), 8.29 (s, 1H, 12-H), 8.21 (d, J = 7.5 Hz, 1H, 4-H), 8.16 (m, 1H, 14-H), 8.14 (m, 2H, 24-H), 8.07 (dd, J =7.9 Hz, 1H, 7-H), 8.04 (dd, J = 6.9, 1.2 Hz, 4H, 21-H), 8.02 (d, J =7.5 Hz, 1H, 26-H) 7.97 (td, J = 7.5, 1.9 Hz, 1H, 3-H), 7.91 (m, 1H, 2-H), 7.90 (m, 1H, 8-H), 7.87 (m, 1H, 15H), 7.62 (dd, J = 6.6, 1.5 Hz, 4H, 18-H), 7.59 (m, 2H, 20-H), 7.50 (m, 2H, 25-H), 7.45 (m, 2H, 23-H), 7.3 (m, 1H, 16-H), 7.04 (td, 7.0, 1.1 Hz, 4H, 19-H), 6.64 (td, J =6.3, 0.8 Hz, 4H, 22-H), 2.62 (s, 3H, H$_{OAc}$).

^{13}C-NMR (125.8 MHz, acetone-d_6): δ [ppm] = 186.8, 161.3 (1C, 6-C), 160.0 (1C, 5-C), 158.9 (1C, 13-C), 158.5 (1C, 10-C), 156.9 (2C, 24-C), 155.44 (4C, 21-C), 155.2 (1C, 17-C), 154.22 (4C, 18-C), 154.0 (1C, 11-C), 152.7 (1C, 27-C), 151.2 (1C, 1-C), 137.8 (1C, 3-C), 137.6 (1C, 26-C), 137.1 (2C, 23-C), 136.6 (1C, 15-C), 134.3 (1C, 8-C), 129.1 (1C, 2-C), 126.1 (2C, 20-C), 126.0 (2C, 25-C), 125.98 (4C, 19-C), 125.45 (4C, 22-C), 123.5 (1C, 16-C), 123.4 (1C, 4-C), 120.6 (1C, 14-C), 120.3 (1C, 9-C), 119.2 (1C, 7-C), 107.13 (1C,12-C).

MS (ESI+): *m/z* (%) = 438.5 (100) [M-py-2PF$_6$]$^{2+}$, 477.5 (35) [M-2PF$_6$]$^{2+}$.

7.4.11 Synthesis of [L^{3}Ru$_2$(μ-OAc)(py)$_2$trpy](PF$_6$)$_2$ (8)
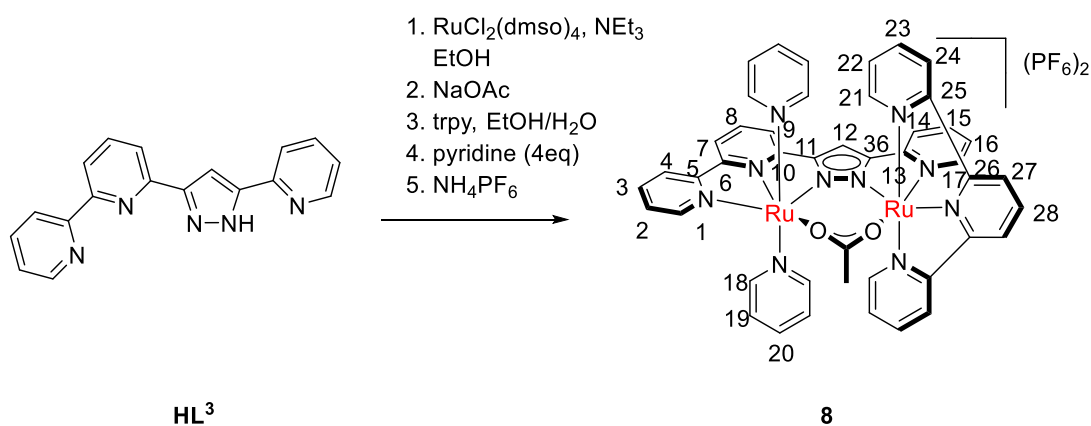
A degassed solution of 3-{6-(2,2'-bipyridyl)}5-(2-pyridyl)pyrazol (**HL^3**)[173] (537 mg, 1.79 mmol) in EtOH (30 mL) and 5 mL NEt$_3$, was added dropwise to the solution of RuCl$_2$(dmso)$_4$ (2 g, 4.13 mmol) and 5 mL NEt$_3$ over 6 h and the mixture was heated to 80 °C overnight. Next, the reaction mixture was cooled down to 0 °C and the formed precipitate was separated by filtration and washed with 10 mL EtOH. Then, (500 mg, 0.61 mmol) of the precipitate was suspended in 50 mL EtOH/H$_2$O mixture (3:1) and 250 mg NaOAc (250 mg, 3.06 mmol) was added and the reaction mixture was heated to reflux overnight. Next, trpy (170 mg, 0.73 mmol) was added to the mixture, and the reaction was left to stir at 90 °C for one day. Then, pyridine (0.2 mL, 1.46 mmol) was added and the solution was refluxed for another day. Finally, the solvent was removed under reduced pressure and one spatula of NH$_4$PF$_6$ was added to the crude and the mixture was purified by column chromatography on silica gel (MeOH/DCM 1:100). (50 mg, 0.04 mmol, yield: 10%).

^{1}H-NMR (500 MHz, acetone-d_6): δ [ppm] = 9.33 (ddd, *J* = 5.5, 1.5, 0.7 Hz, 1H, 1-H), 8.73 (d, *J* =8.7 Hz, 2H, 27-H), 8.55 (dt, *J* = 7.9, 1.0 Hz, 2H, 24-H), 8.47 (dd, *J* =7.6, 0.9 Hz, 1H, 9-H), 8.42 (s,

1H, 12-H), 8.41 (m, 1H, 4-H), 8.29 (m, 1H, 7-H), 8.24 (t, *J* =8.1 Hz, 1H, 28-H), 8.20 (dd, *J* =7.2, 1.4 Hz, 4H, 18-H), 8.02 (m, 3H, 3-H, 8-H, 14-H), 7.87 (td, *J* = 7.8, 1.5 Hz, 1H, 23-H), 7.83 (m, 1H, 2-H), 7.69 (tt, *J* =7.5, 1.5 Hz, 2H, H-20), 7.59 (td, *J* =7.8, 1.4 Hz, 1H, 15-H), 7.26 (m, 1H, 17-H), 7.16 (td, *J* = 7.2, 1.4 Hz, 4H, 19-H), 7.11 (m, 2H, 21-H), 6.96 (m, 2H, 22-H), 6.7 (m, 1H, 16-H), 1.7 (s, 3H, H_{OAc}).

^{13}C-NMR (125.8 MHz, acetone-d_6): δ [ppm] = 187.1, 161.7 (1C, 6-C), 160.6 (2C, 26-C), 160.4 (2C, 25-C), 160.3 (1C, 5-C), 159.1 (1C, 10-C), 157.4 (1C, 13-C), 154.2 (1C, 11-C), 153.1 (4C, 18-C), 151.3 (1C, 1-C), 150.9 (1C, 36-C), 137.9 (2C, 23-C), 137.7 (1C, 3-C), 137.5 (2C, 20-C), 136.6 (1C, 15-C), 135.2 (1C, 28-C), 134.2 (1C, 8-C), 128.9 (1C, 2-C), 127.9 (2C, 22-C), 125.8 (4C, 19-C), 124.4 (2C, 24-C), 123.9 (2C, 4-C), 123.5 (2C, 27-C), 122.8 (1C, 16-C), 120.3 (1C, 9-C), 120.1 (14-C), 119.7 (1C, 7-C), 27.8 (1C, C_{OAc}).

MS (ESI+): m/z (%) = 476 (100) $[M-2PF_6]^{2+}$, 501 (28).

Appendix

NMR Spectroscopy
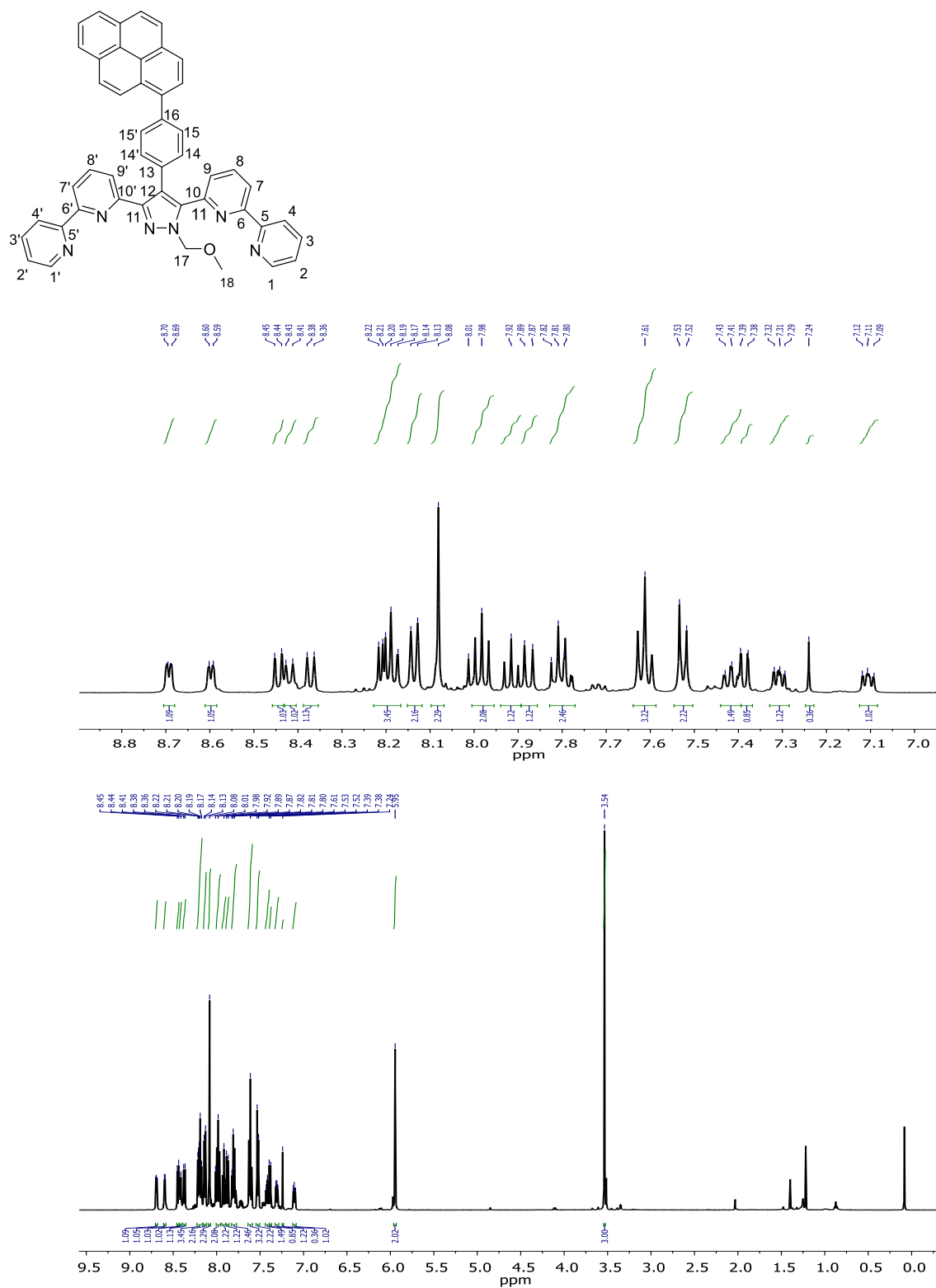
Figure A1. ^{1}H-NMR spectrum of ^{pyr}**bbp(MOM)** in CDCl₃.
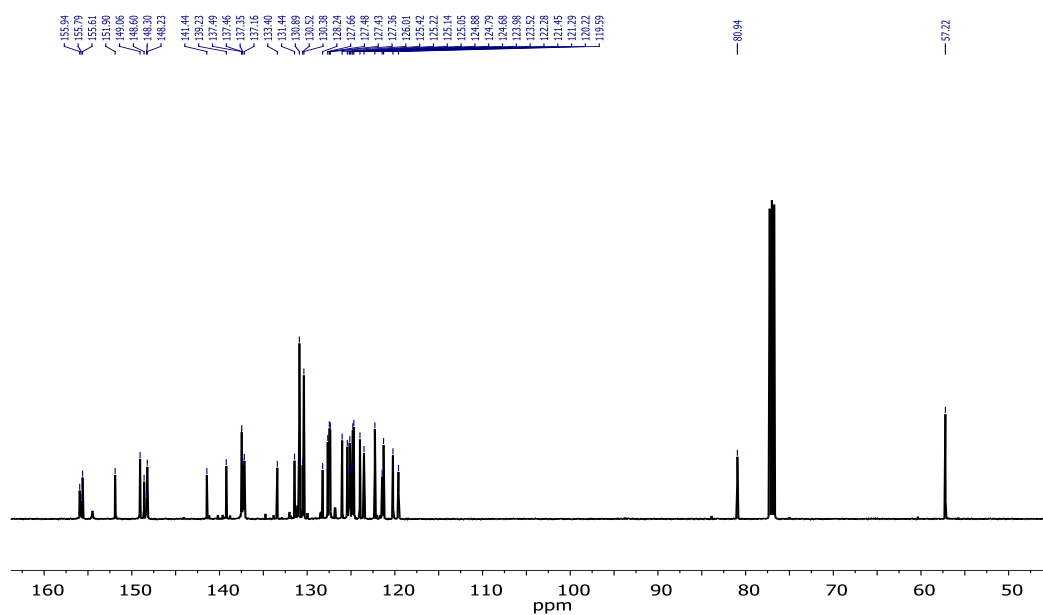
Figure A2. ^{13}C-NMR spectrum of ^{pyr}**bbp(MOM)** in CDCl$_3$.
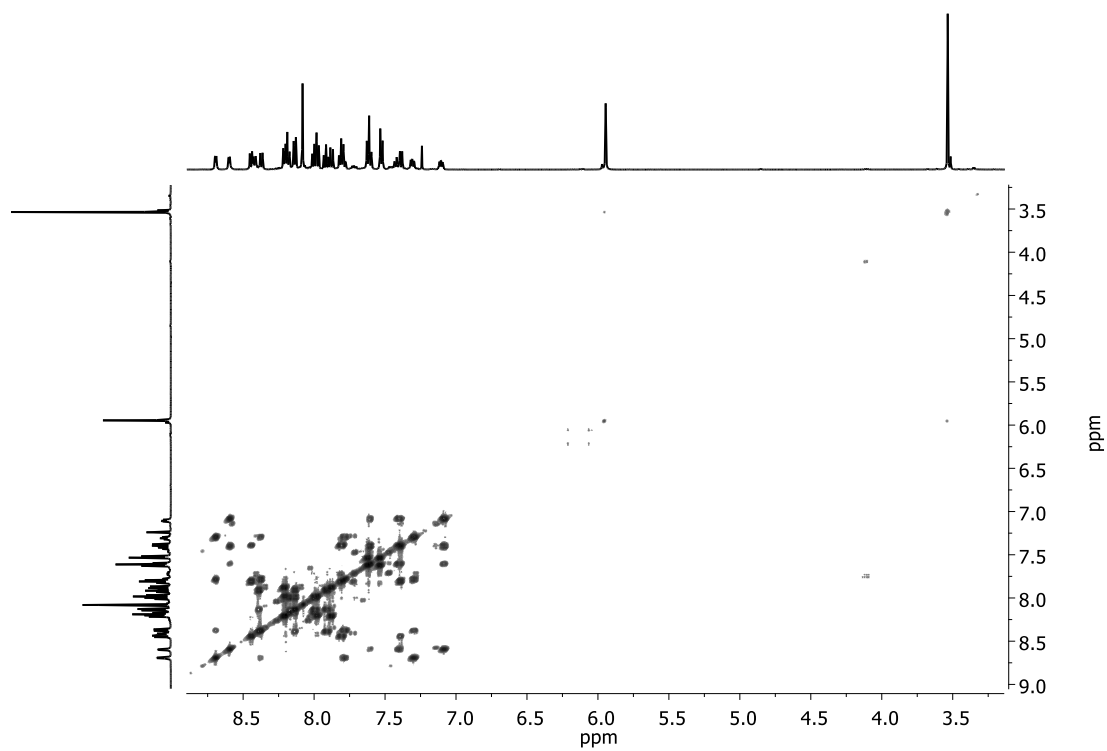
Figure A3. ^{1}H,^{1}H-COSY NMR spectrum of ^{pyr}**bbp(MOM)** in CDCl$_3$.
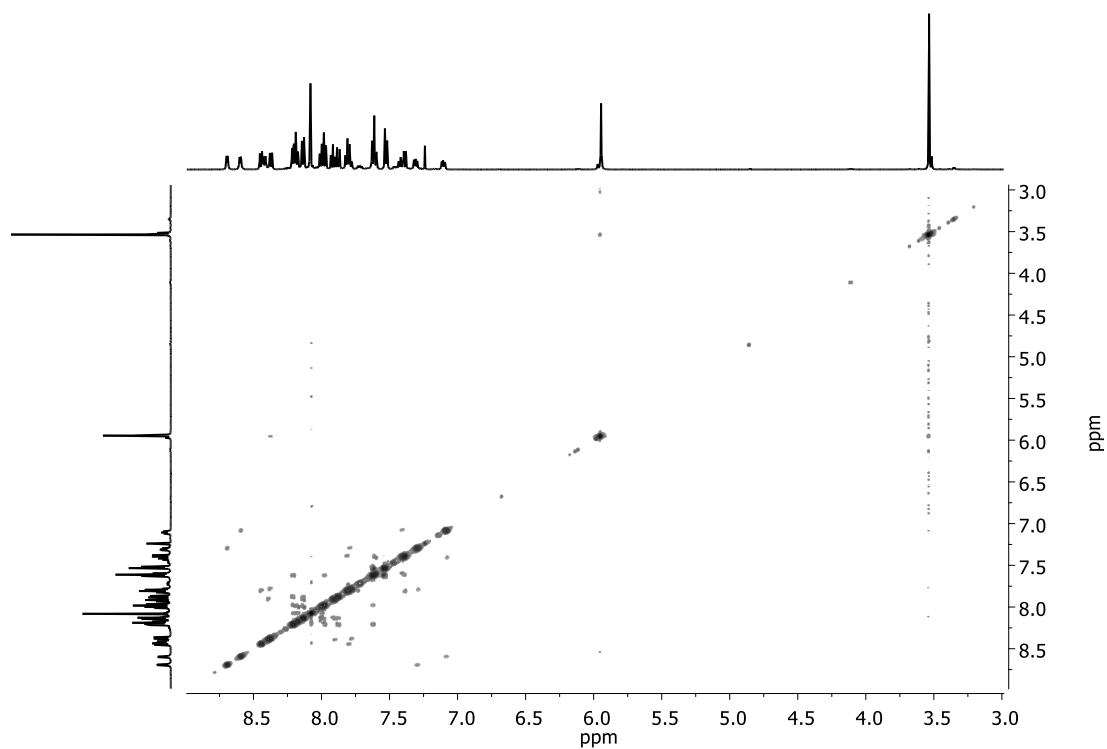
Figure A4. ^{1}H,^{1}H-NOESY NMR spectrum of ^{pyr}**bbp(MOM)** in CDCl$_3$.
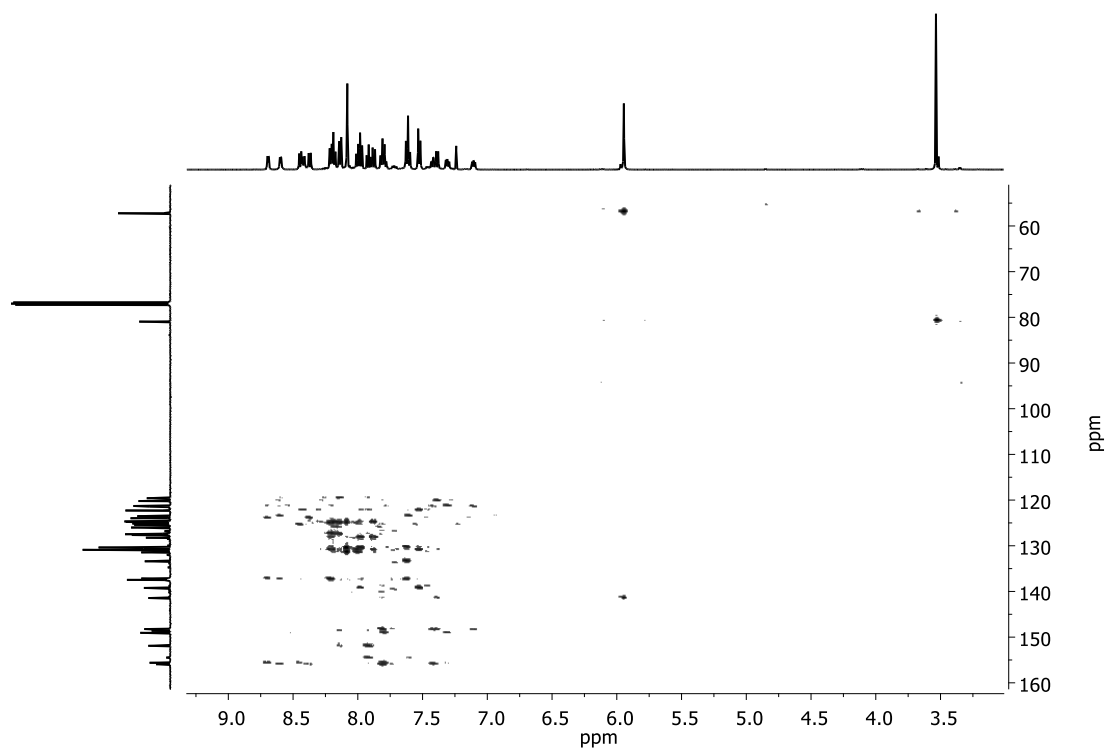
Figure A5. ^{1}H,^{13}C-HMBC NMR spectrum of ^{pyr}**bbp(MOM)** in CDCl$_3$.
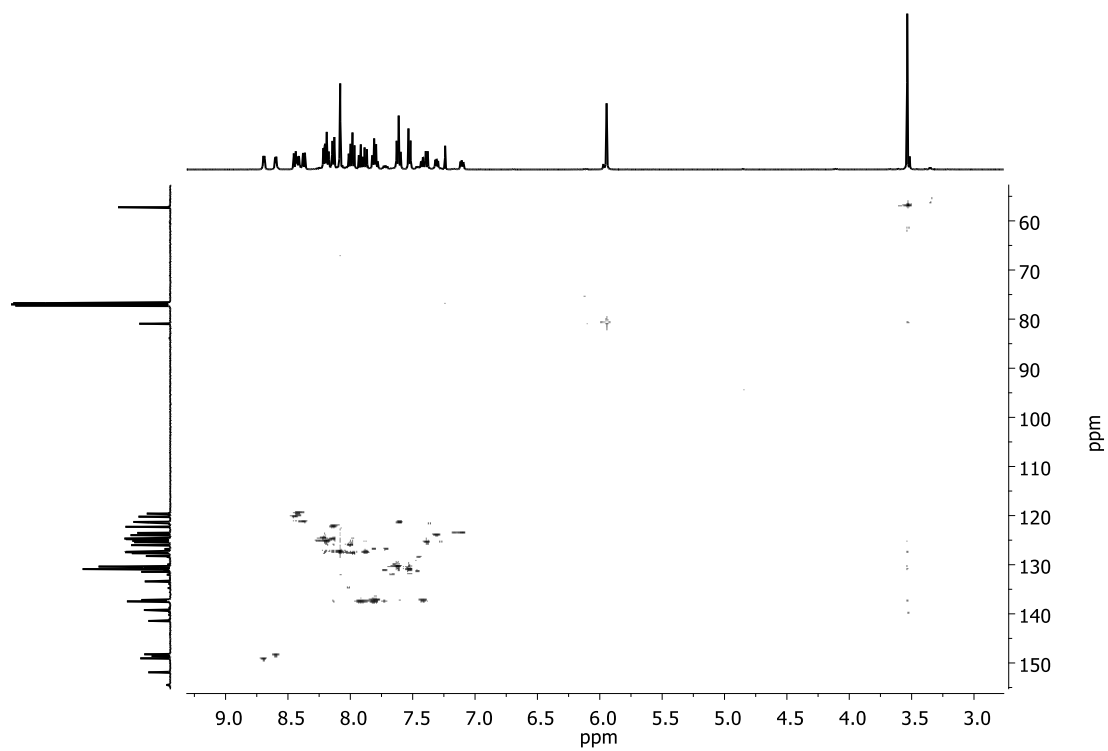
Figure A6. ^{1}H,^{13}C-HSQC NMR spectrum of ^{pyr}**bbp(MOM)** in CDCl$_3$.
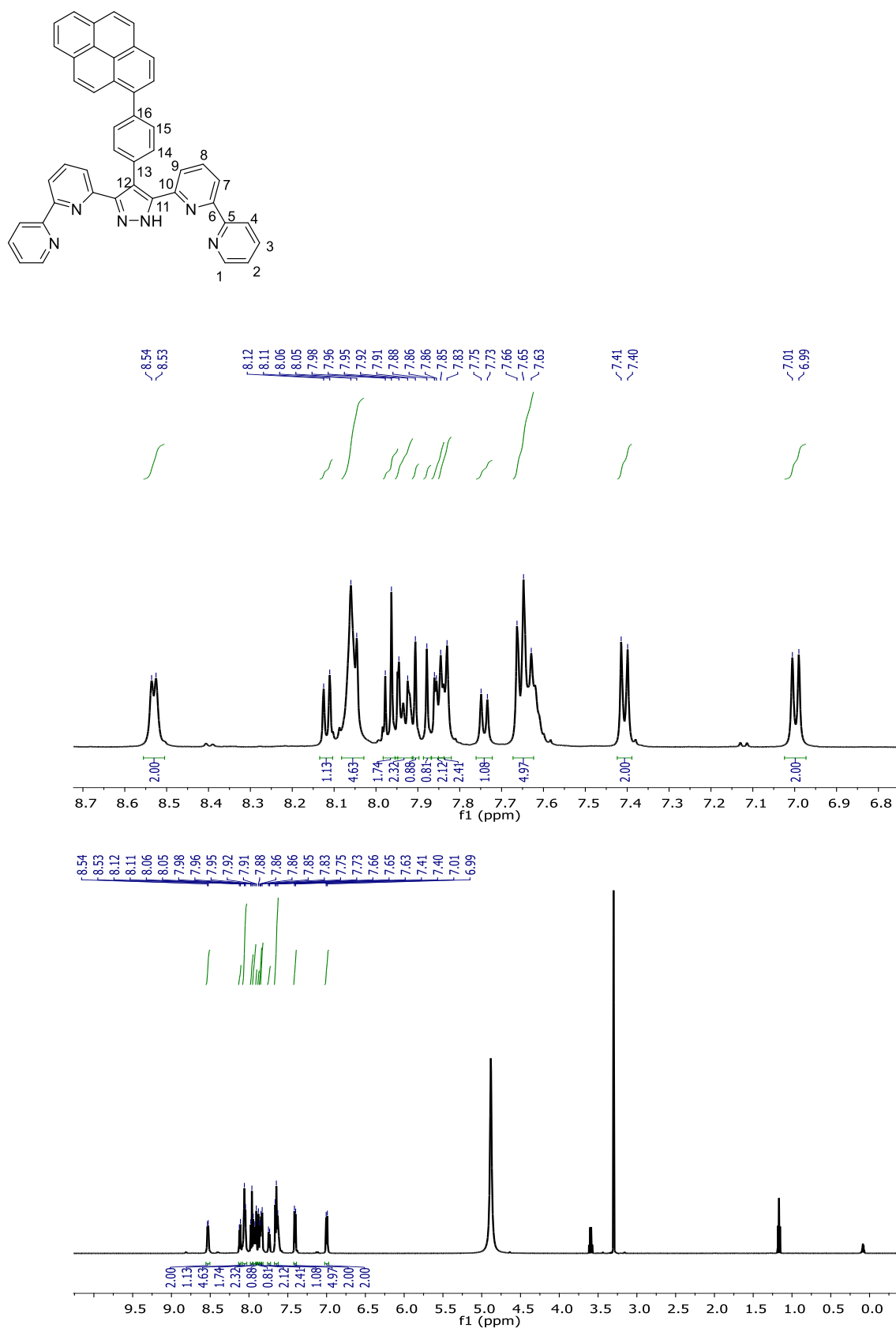
Figure A7. ¹H-NMR spectrum of **ᴾʸʳbbpH** in methanol-d_4.
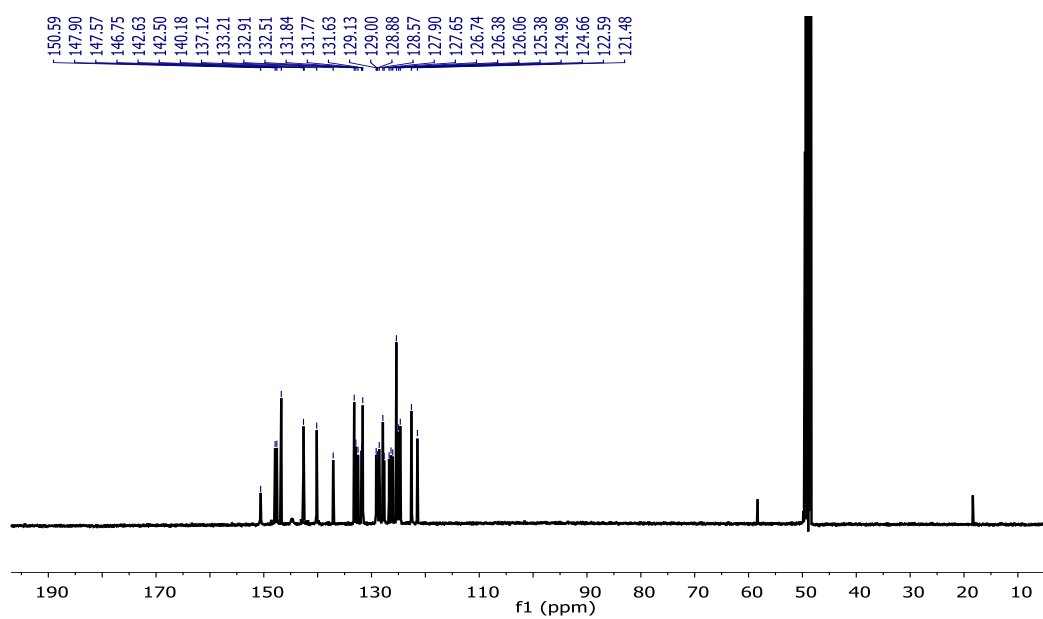
Figure A8. ^{13}C-NMR spectrum of ^{pyr}**bbpH** in methanol-d_4.
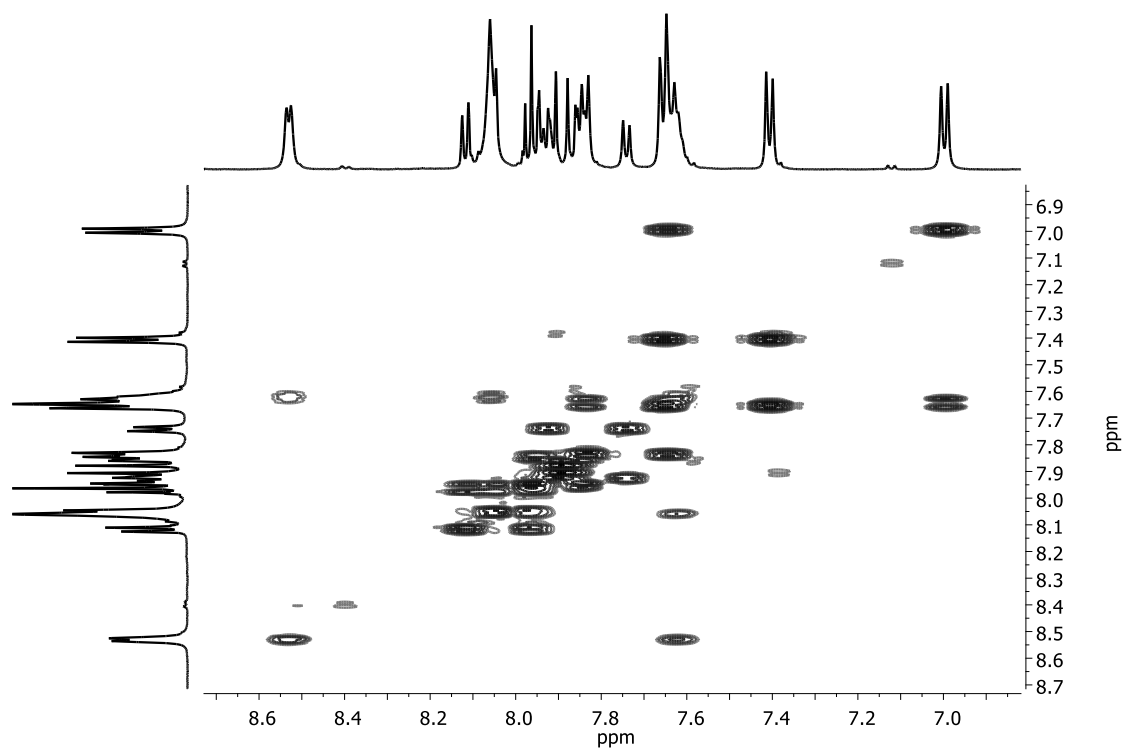
Figure A9. ^{1}H,^{1}H-COSY NMR spectrum of ^{pyr}**bbpH** in methanol-d_4.
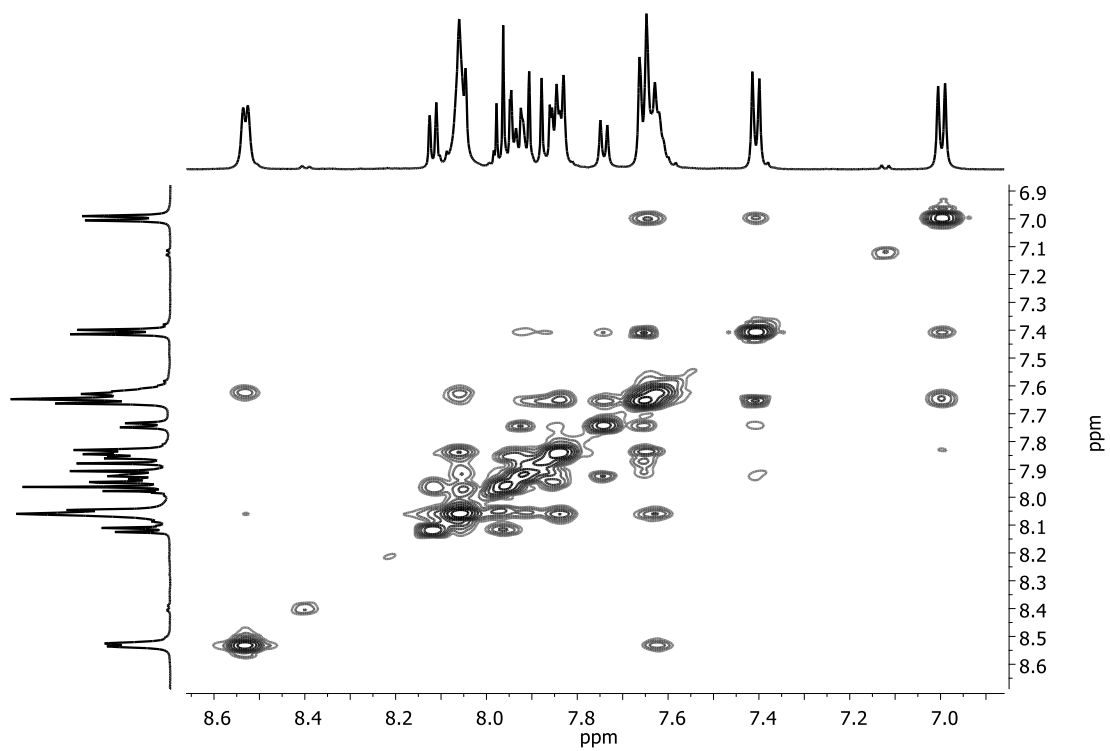
Figure A10. ^{1}H,^{1}H-NOESY NMR spectrum of ^{pyr}**bbpH** in methanol-d_4.
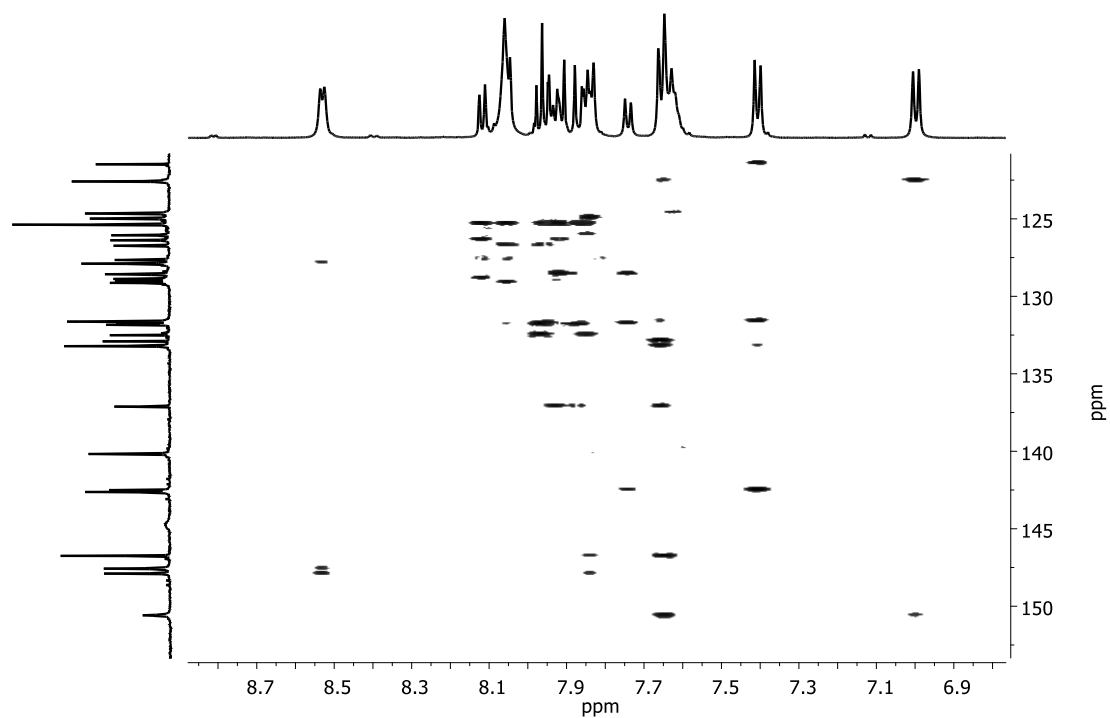
Figure A11. ^{1}H,^{13}C-HMBC NMR spectrum of ^{pyr}**bbpH** in methanol-d_4.
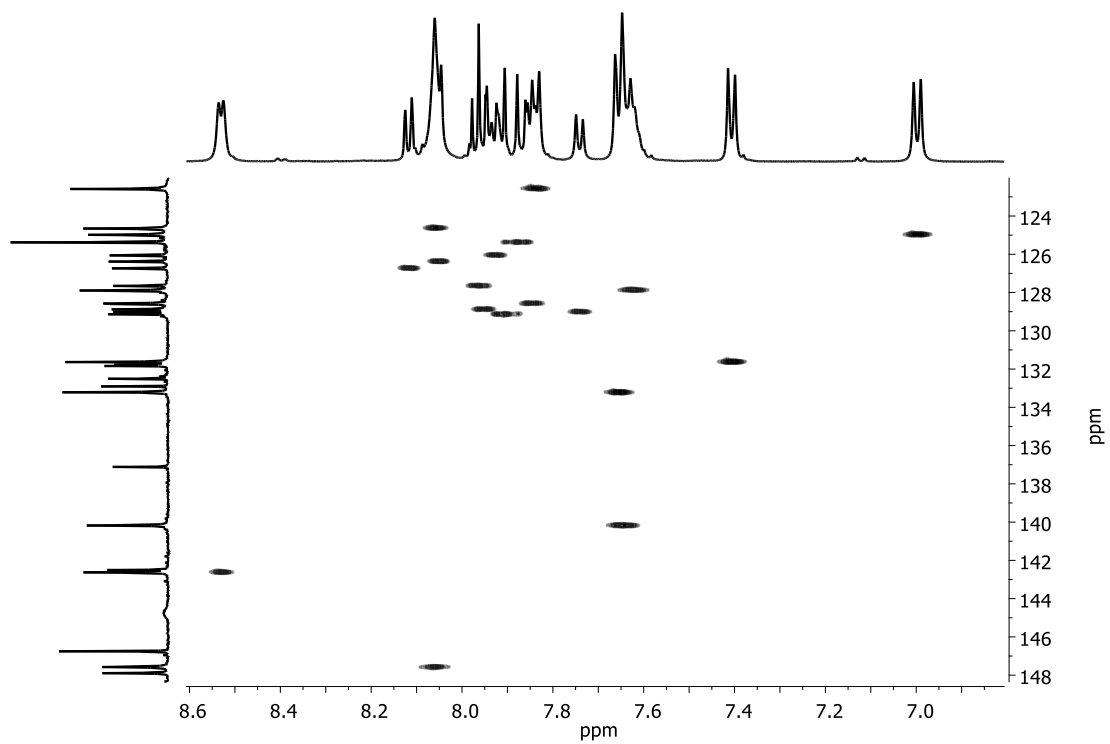
Figure A12. ^{1}H,^{13}C-HSQC NMR spectrum of ^{pyr}**bbpH** in methanol-d_4.
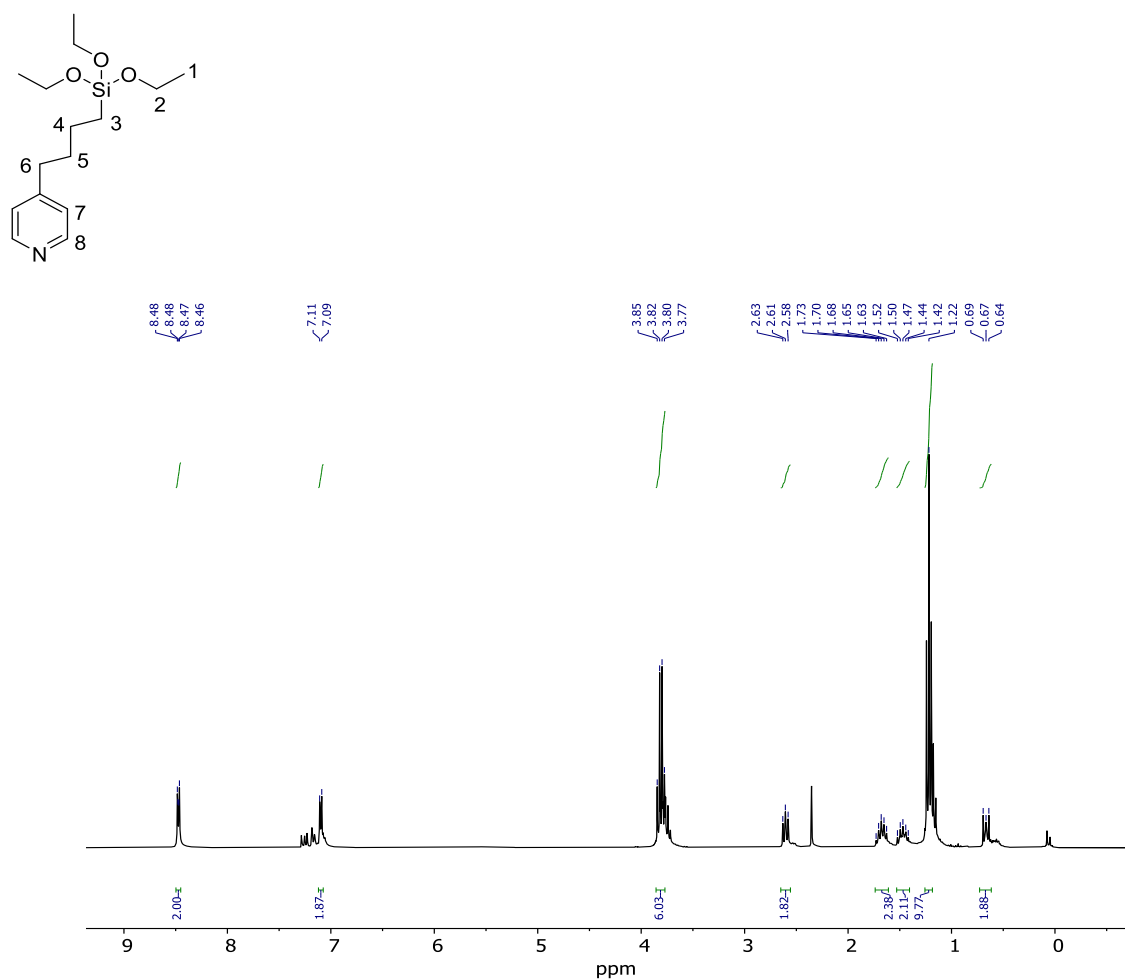
Figure A13. ^{1}H-NMR spectrum of **4-(4-(triethoxysilyl)butyl)pyridine** in CDCl$_3$
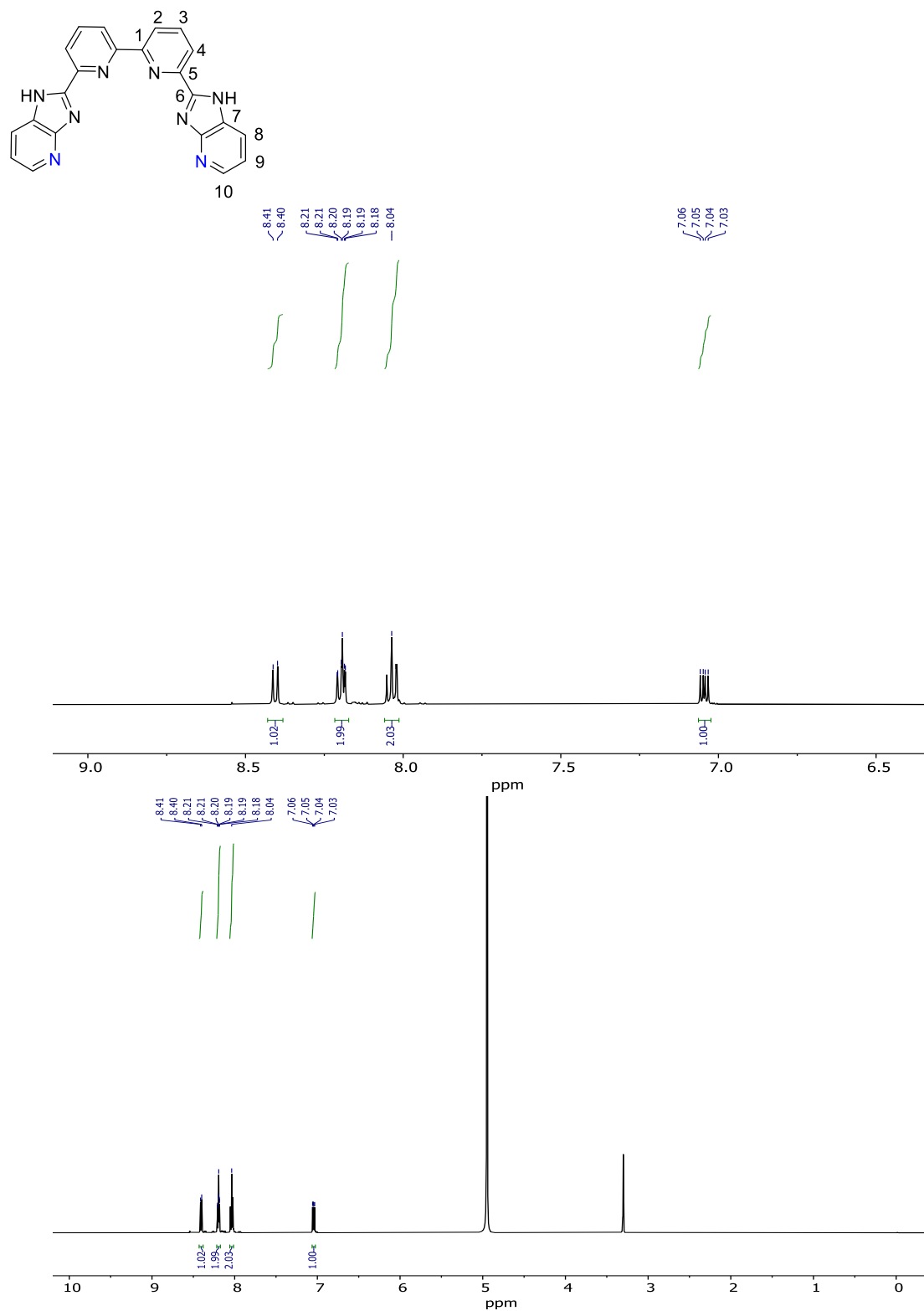
Figure A14. ^{1}H-NMR spectrum of **H₂L²** in methanol-d_4.
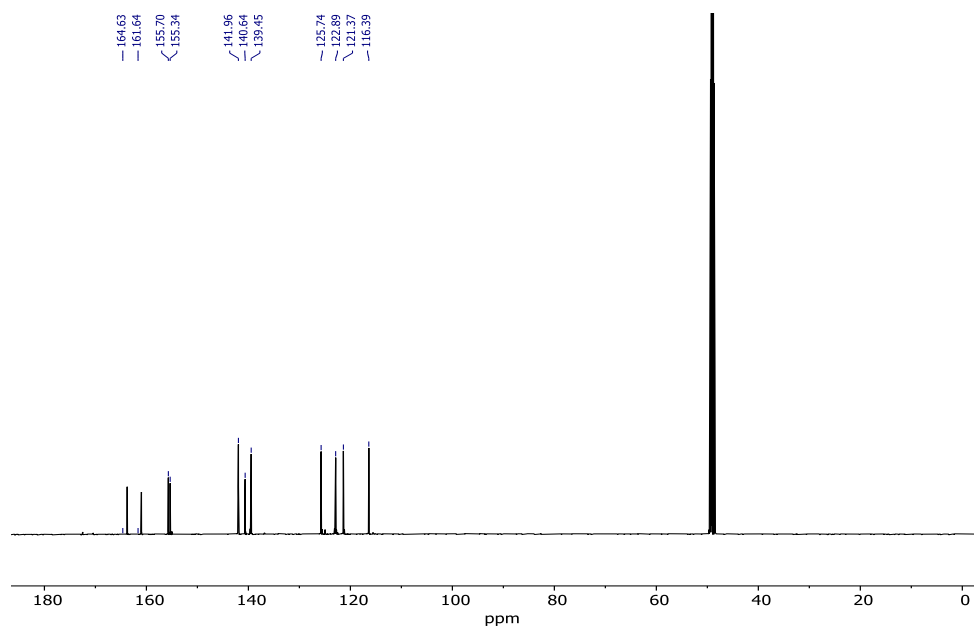
Figure A15. ^{13}C-NMR spectrum of **H₂L²** in methanol-d_4.
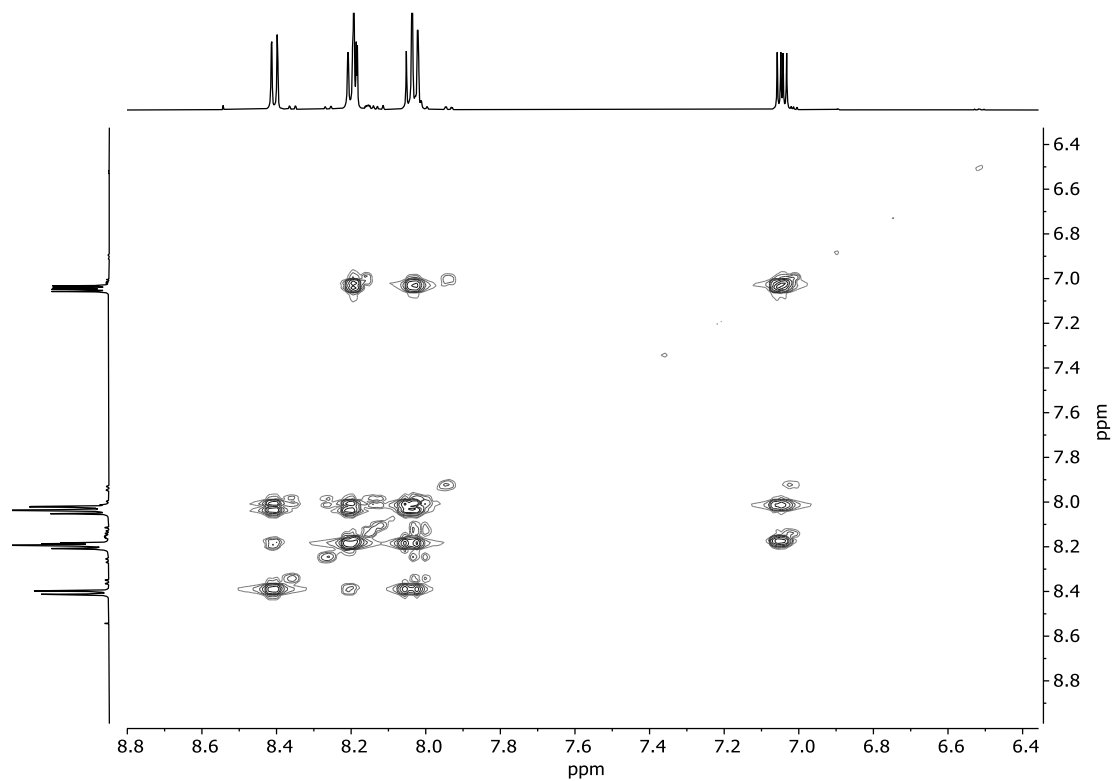
Figure A16. ^{1}H,^{1}H-COSY NMR spectrum of **H₂L²** in methanol-d_4.
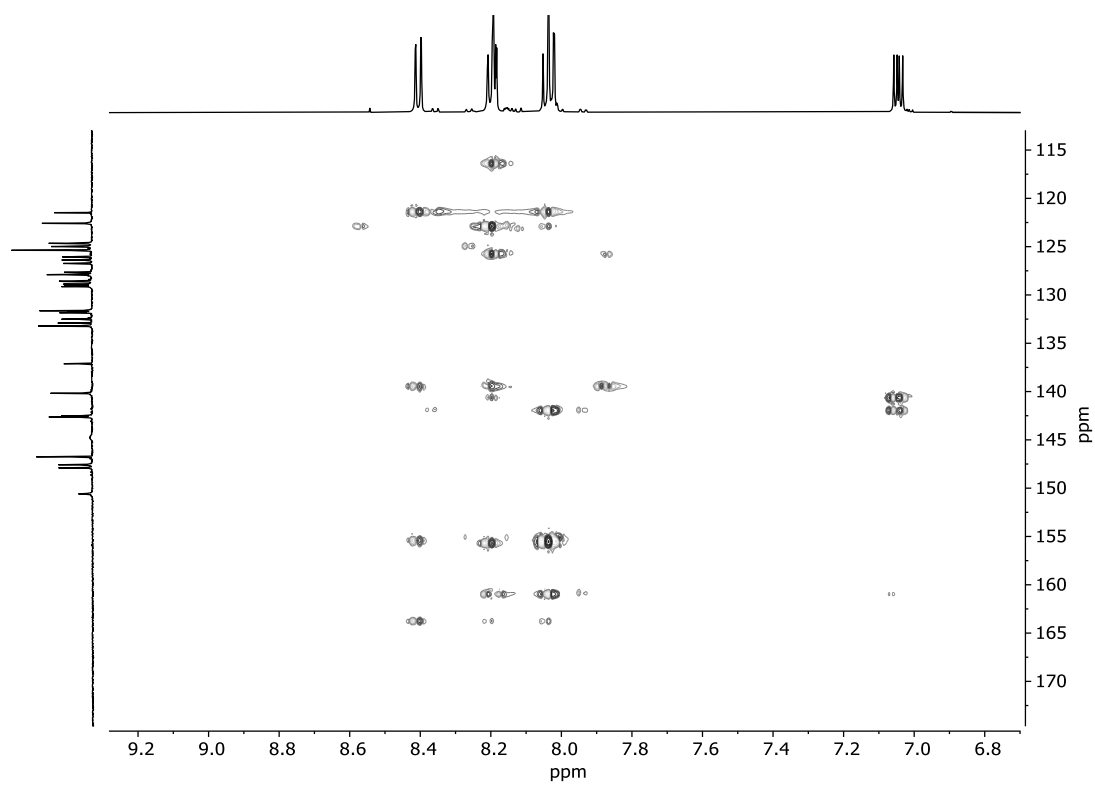
Figure A17. ^{1}H,^{13}C-HMBC NMR spectrum of **H₂L²** in methanol-d_4.
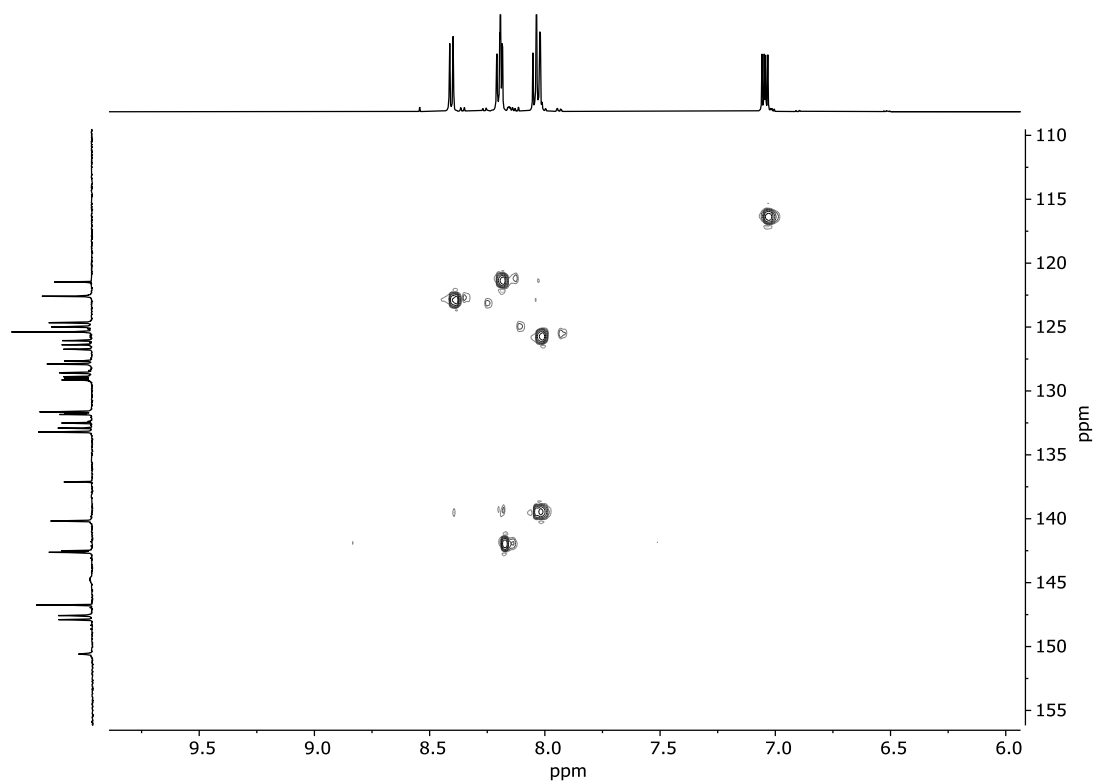
Figure A18. ^{1}H,^{13}C-HMBC NMR spectrum of **H₂L²** in methanol-d_4.
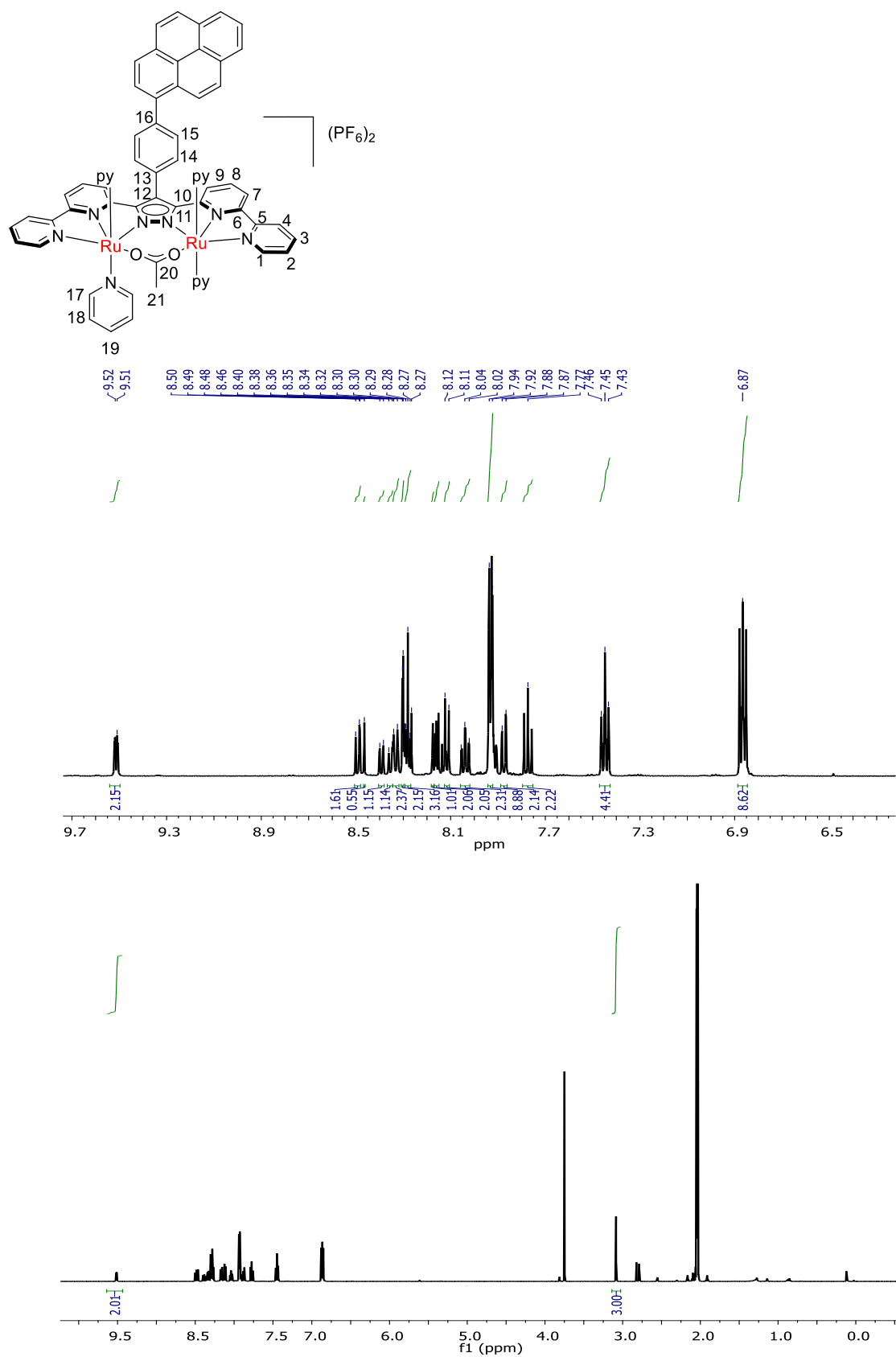
Figure A19. ^{1}H-NMR spectrum of **1^{pyr}** in acetone-d_6.
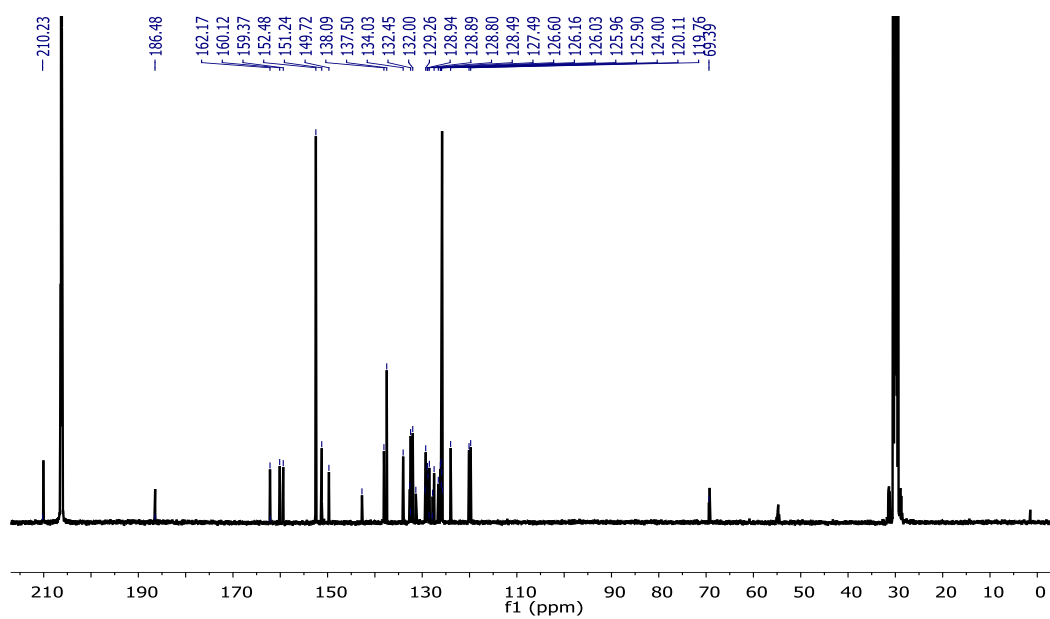
Figure A20. ^{13}C-NMR spectrum of **1^{pyr}** in acetone-d_6.
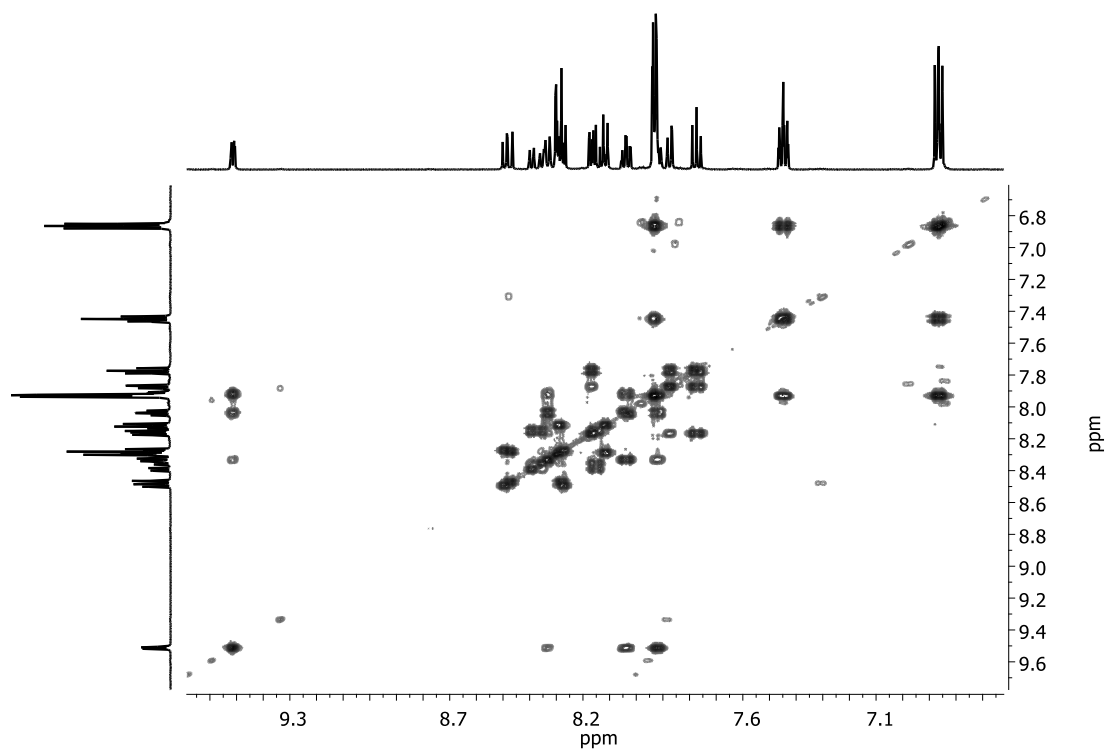
Figure A21. ^{1}H,^{1}H-COSY NMR spectrum of **1^{pyr}** in acetone-d_6.
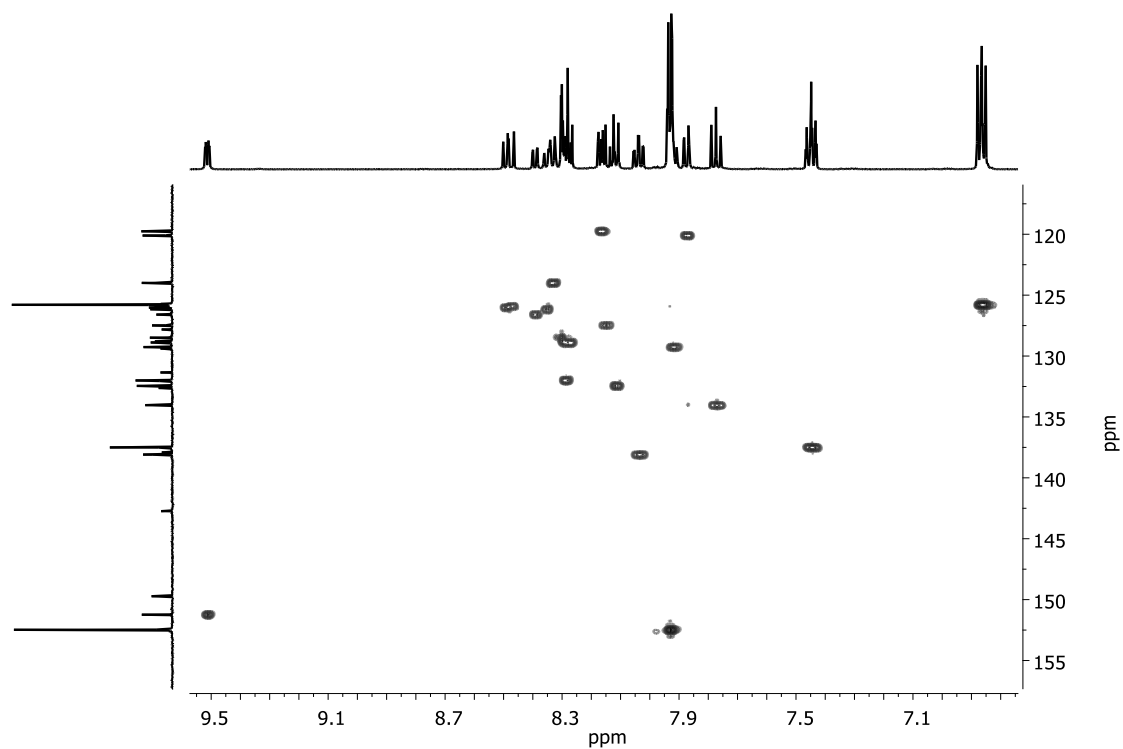
Figure A22. ^{1}H,^{13}C-HMBC NMR spectrum of **1^{pyr}** in acetone-d_6.
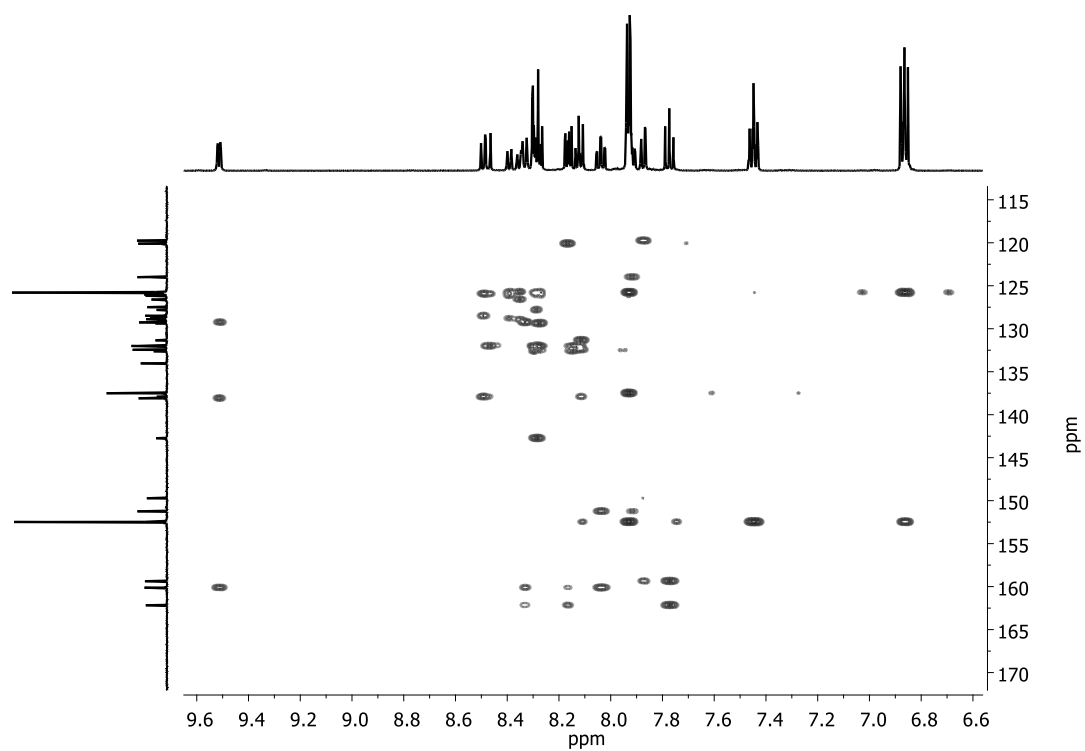
Figure A23. ^{1}H,^{13}C-HSQC NMR spectrum of **1^{pyr}** in acetone-d_6.
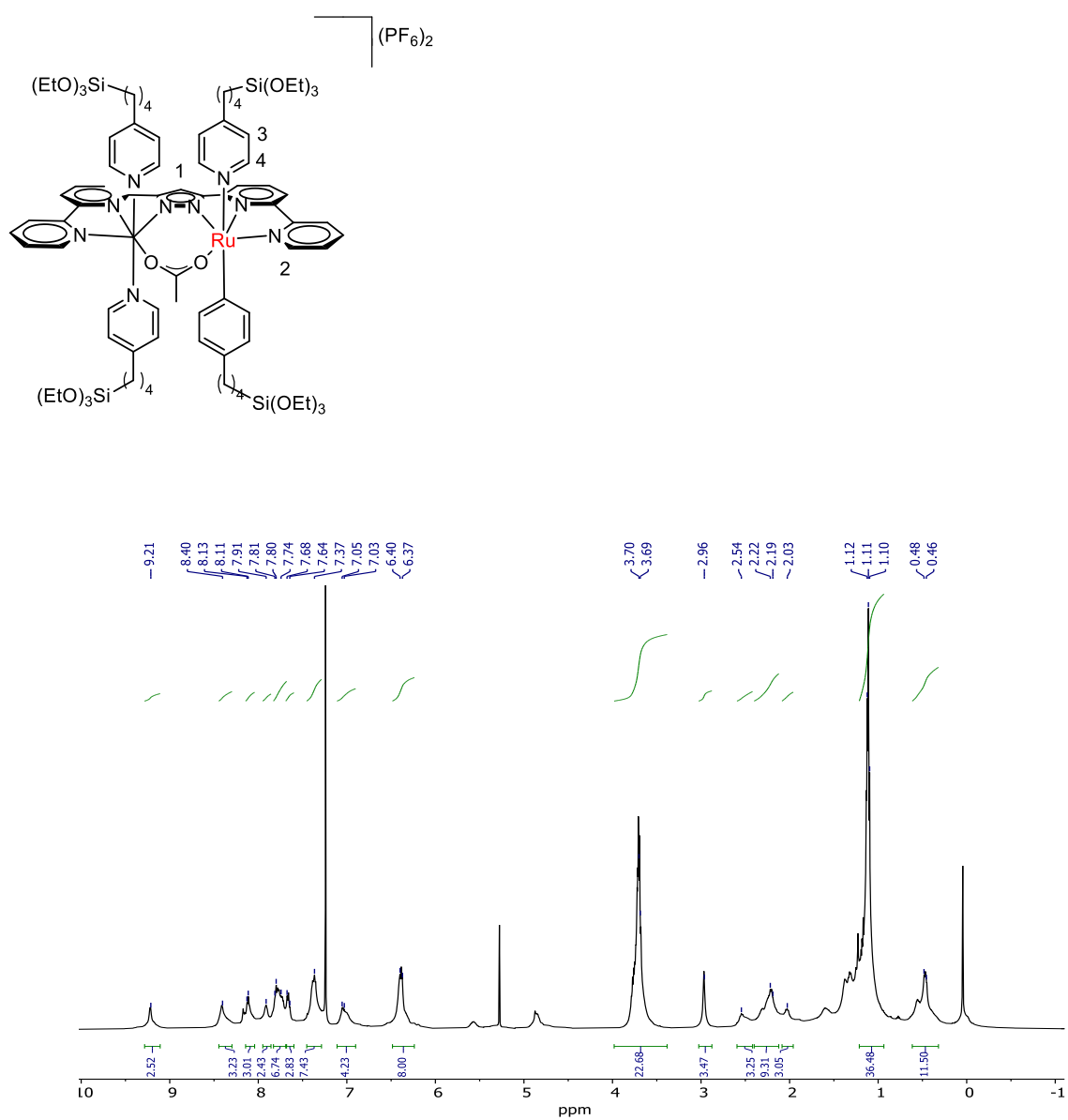
Figure A24. ^{1}H-NMR spectrum of **1$^{4Si(OEt)3}$** in CDCl$_3$.
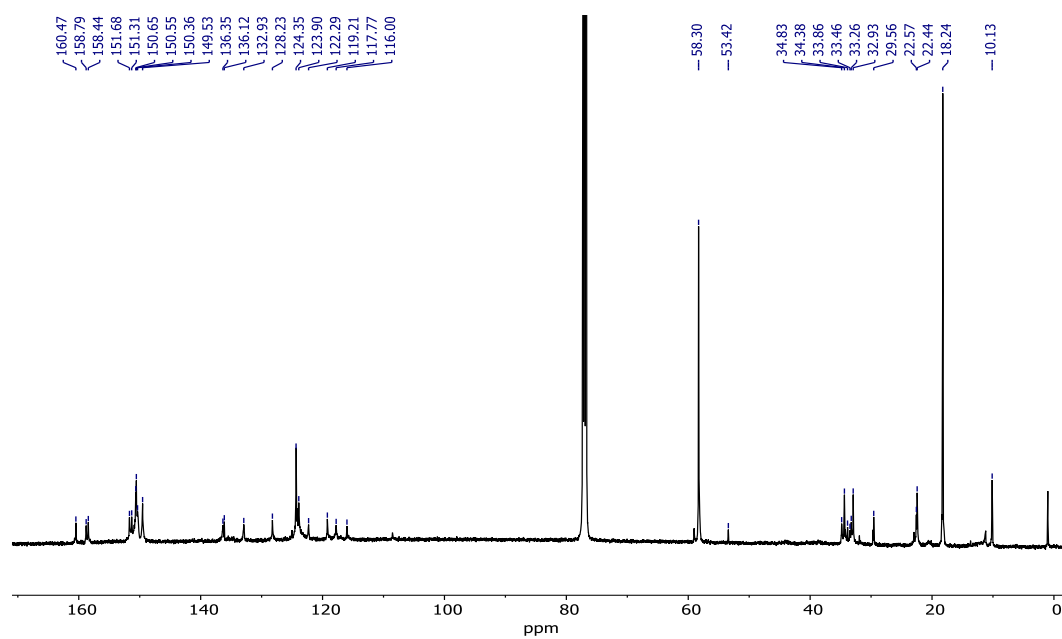
Figure A25. ^{13}C-NMR spectrum of **1$^{4Si(OEt)3}$** in CDCl$_3$.
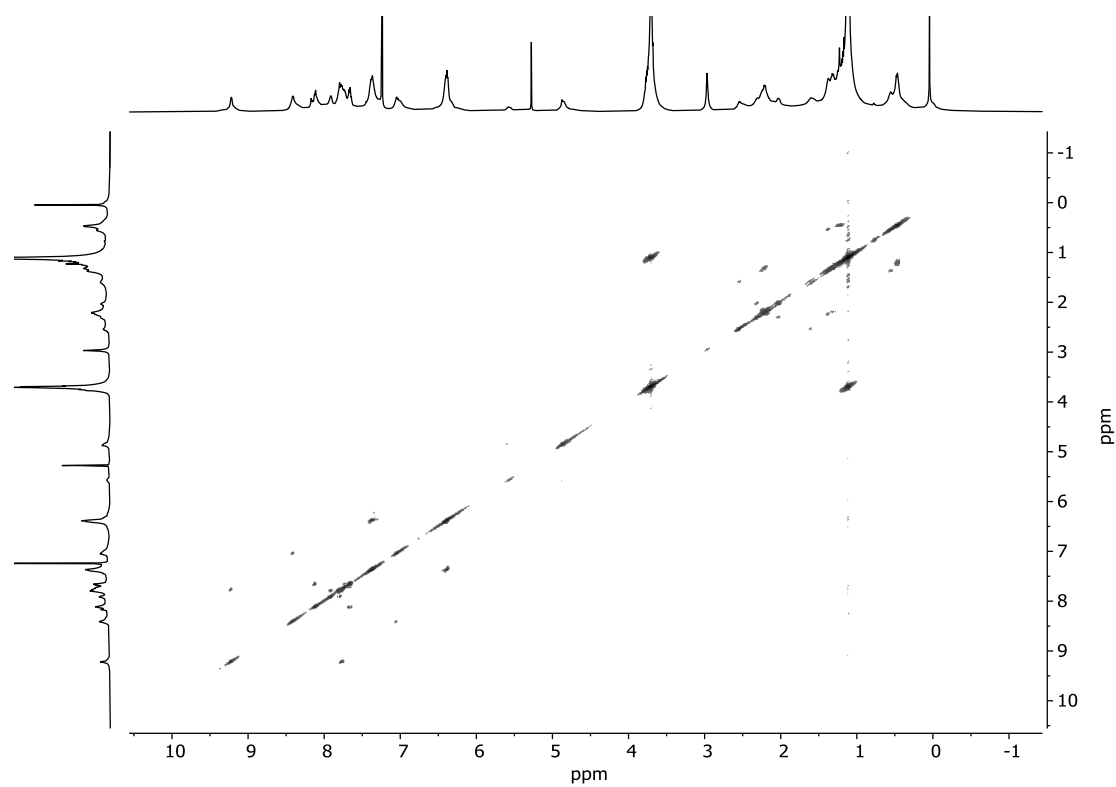
Figure A26. ^{1}H,^{1}H-COSY NMR spectrum of **1$^{4Si(OEt)3}$** in CDCl$_3$.
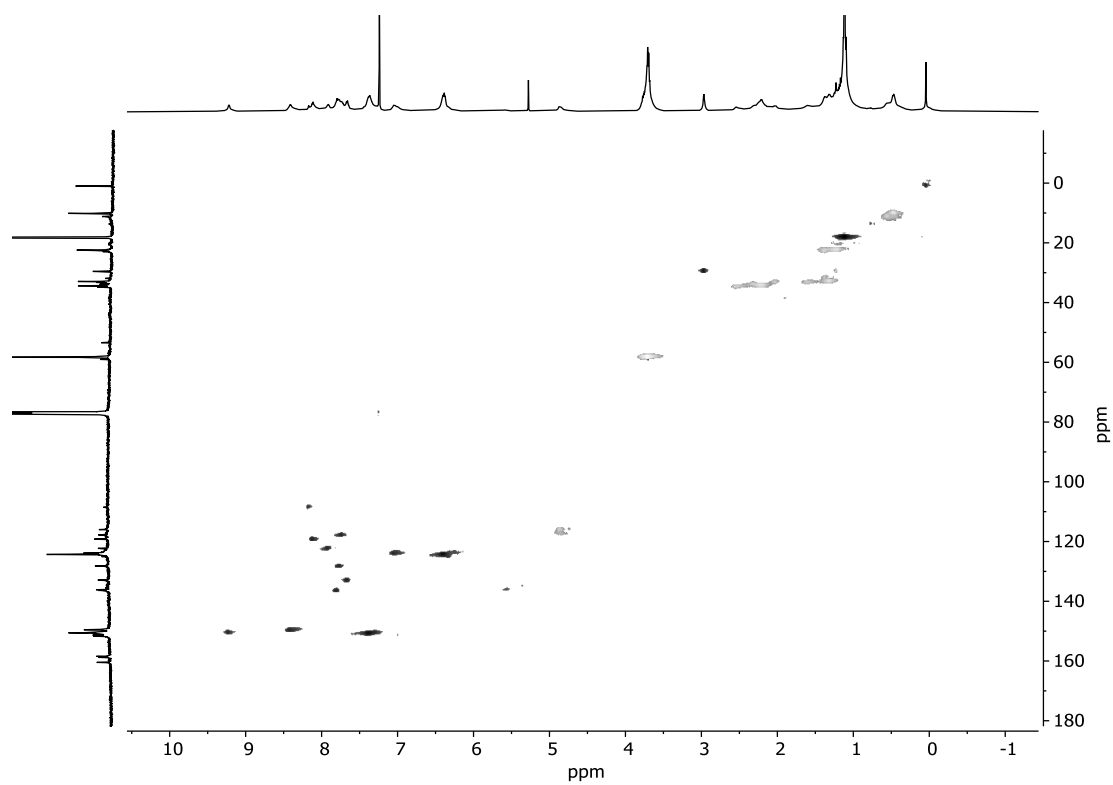
Figure A27. ^{1}H,^{13}C-HSQC NMR spectrum of **1**$^{4Si(OEt)3}$ in CDCl$_3$.
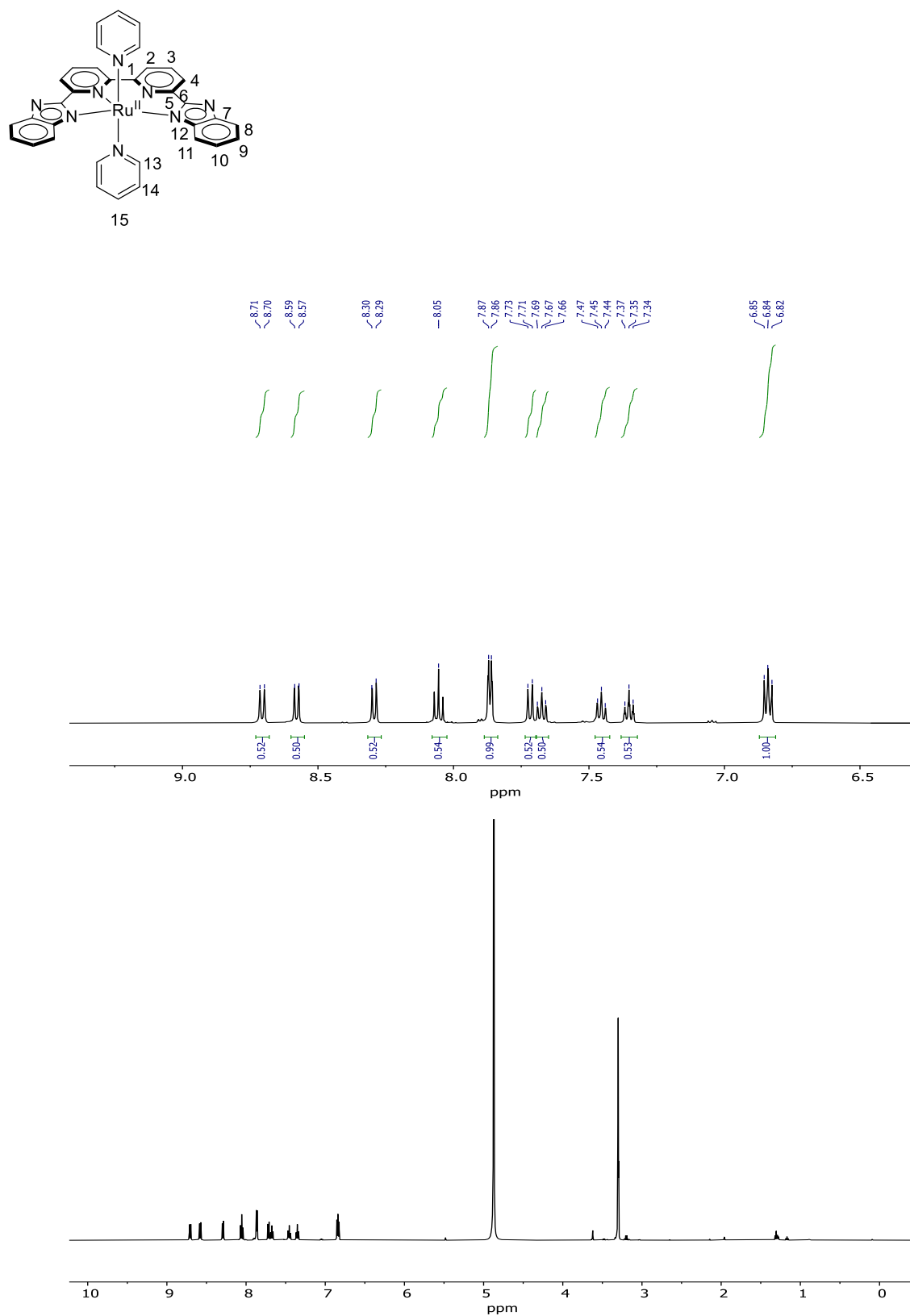
Figure A28. ^{1}H-NMR spectrum of **2** in methanol-d_4.
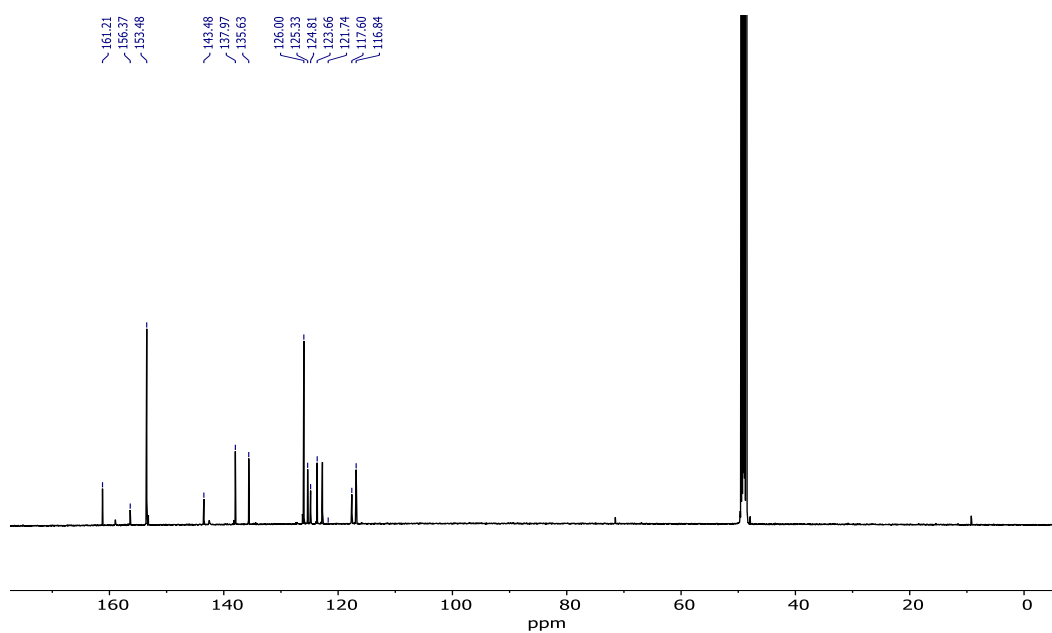
Figure A29. ^{13}C-NMR spectrum of **2** in methanol-d_4.
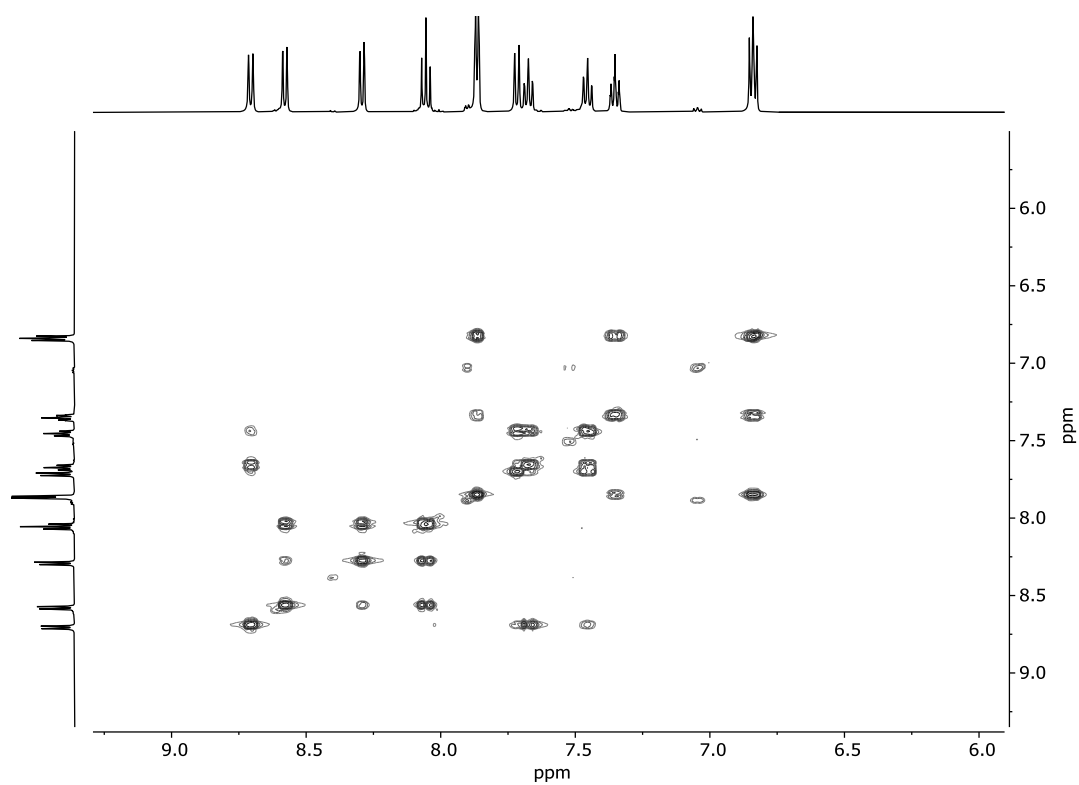
Figure A30. ^{1}H,^{1}H-COSY NMR spectrum of **2** in methanol-d_4.
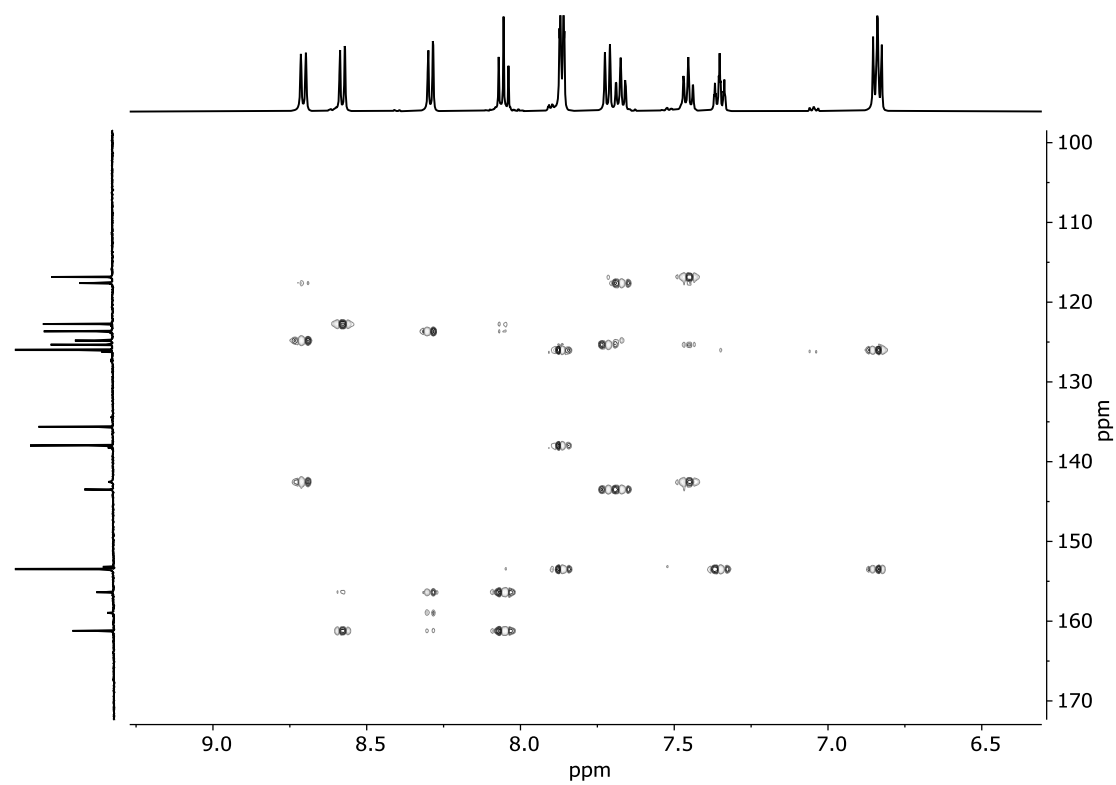
Figure A31. ^{1}H,^{13}C-HMBC NMR spectrum of **2** in methanol-d_4.
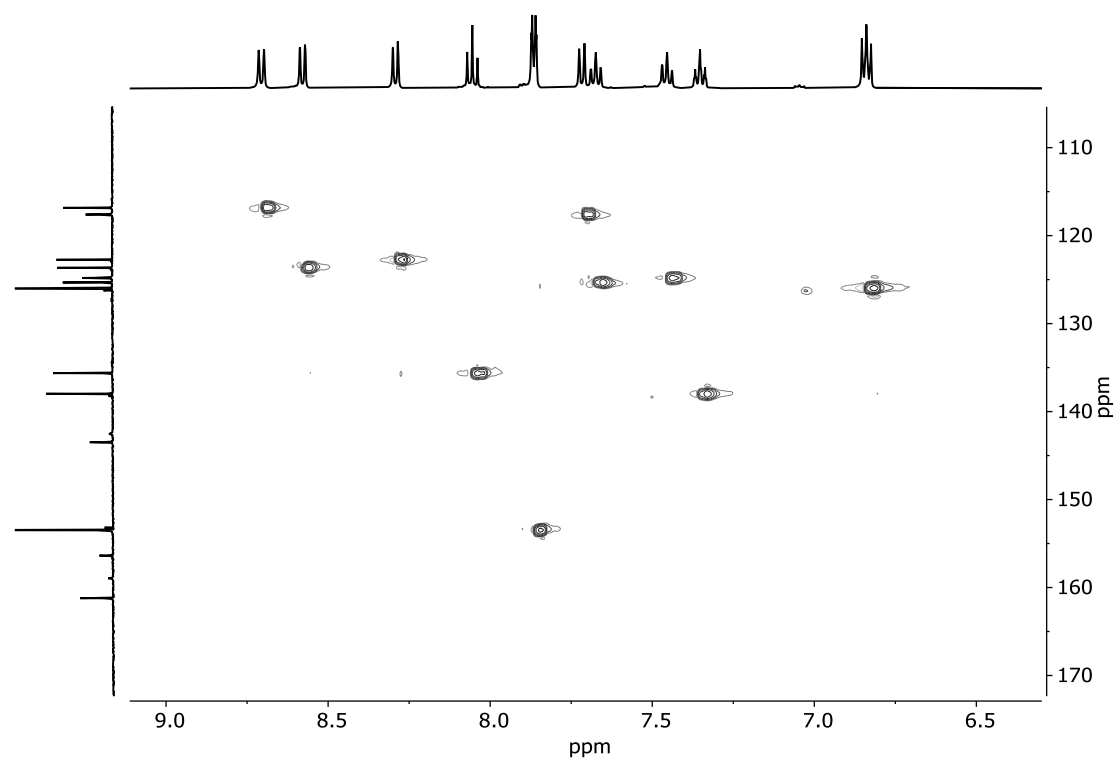
Figure A32. ^{1}H,^{13}C-HSQC NMR spectrum of **2** in methanol-d_4.
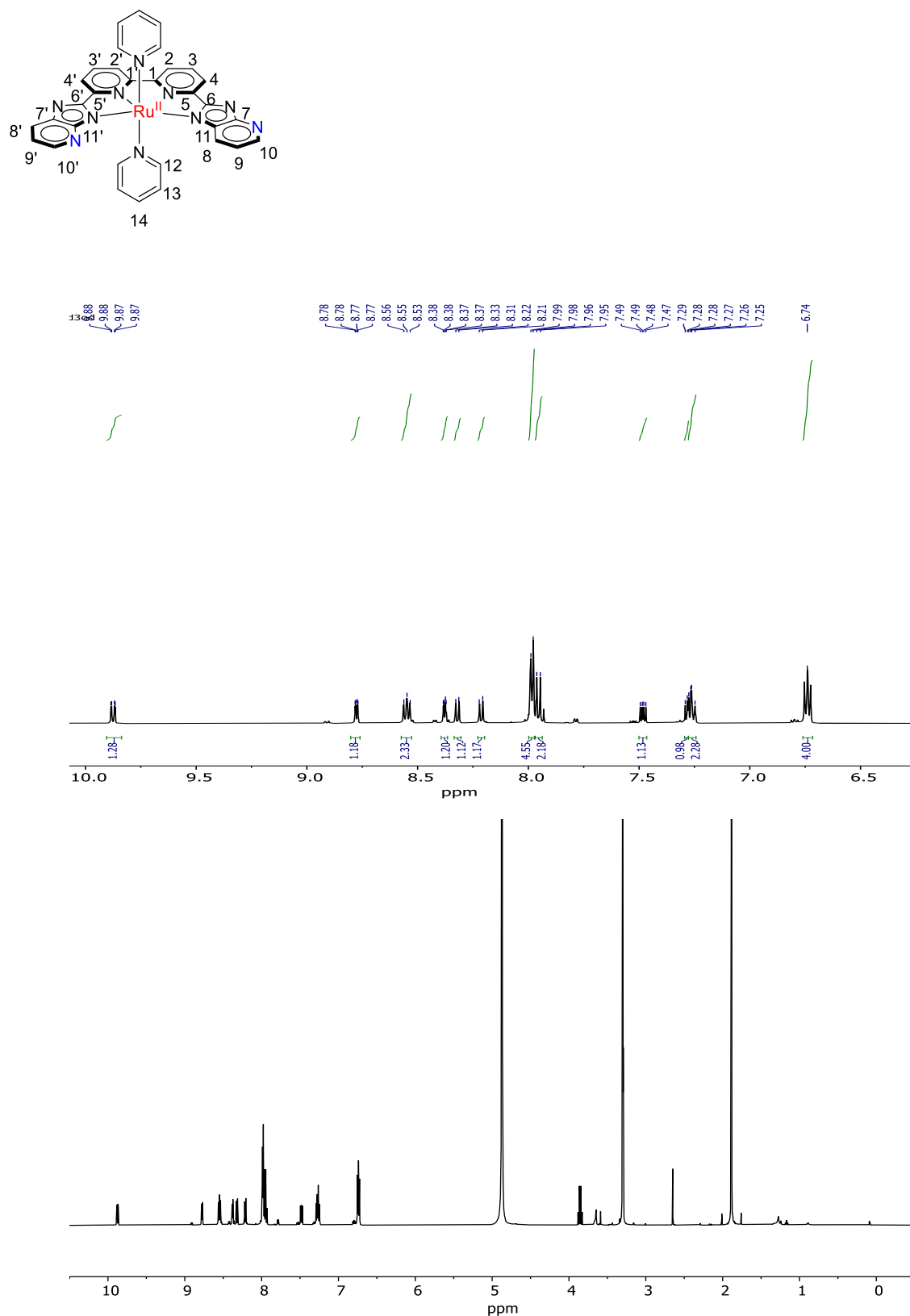
Figure A33. ^{1}H-NMR spectrum of **3** in methanol-d_4.
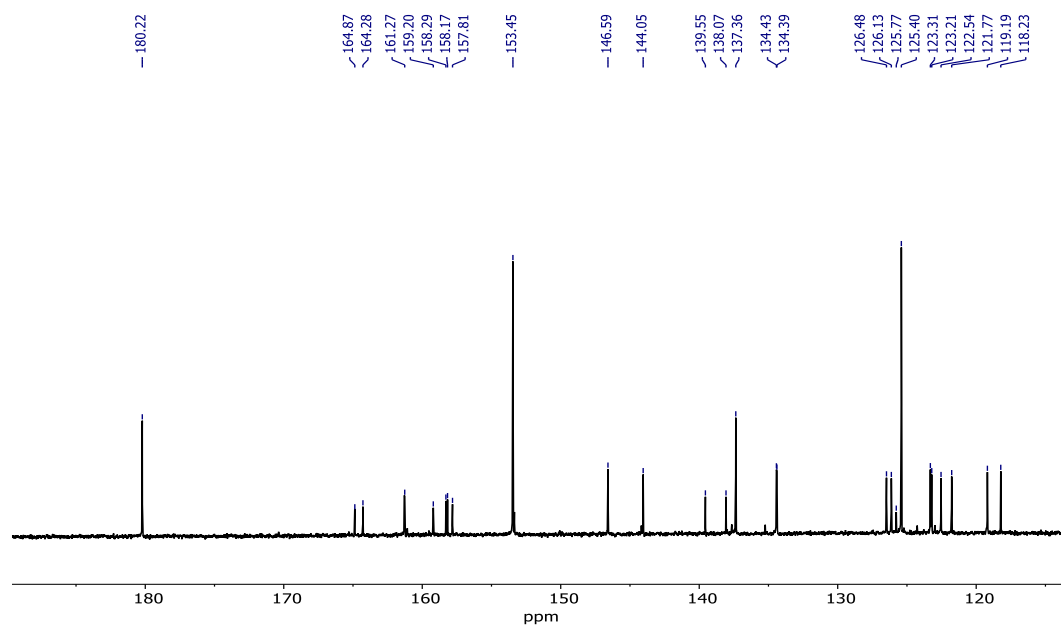
Figure A34. ^{13}C-NMR spectrum of **3** in methanol-d_4.
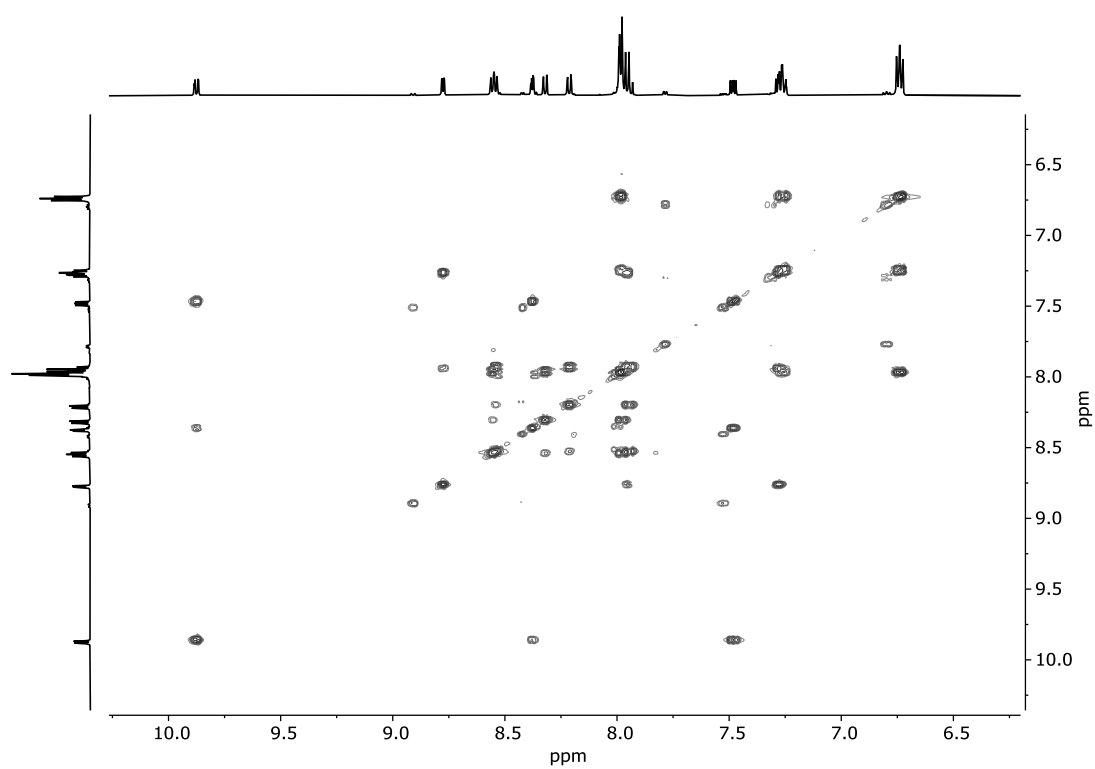
Figure A35. ^{1}H,^{1}H-COSY NMR spectrum of **3** in methanol-d_4.
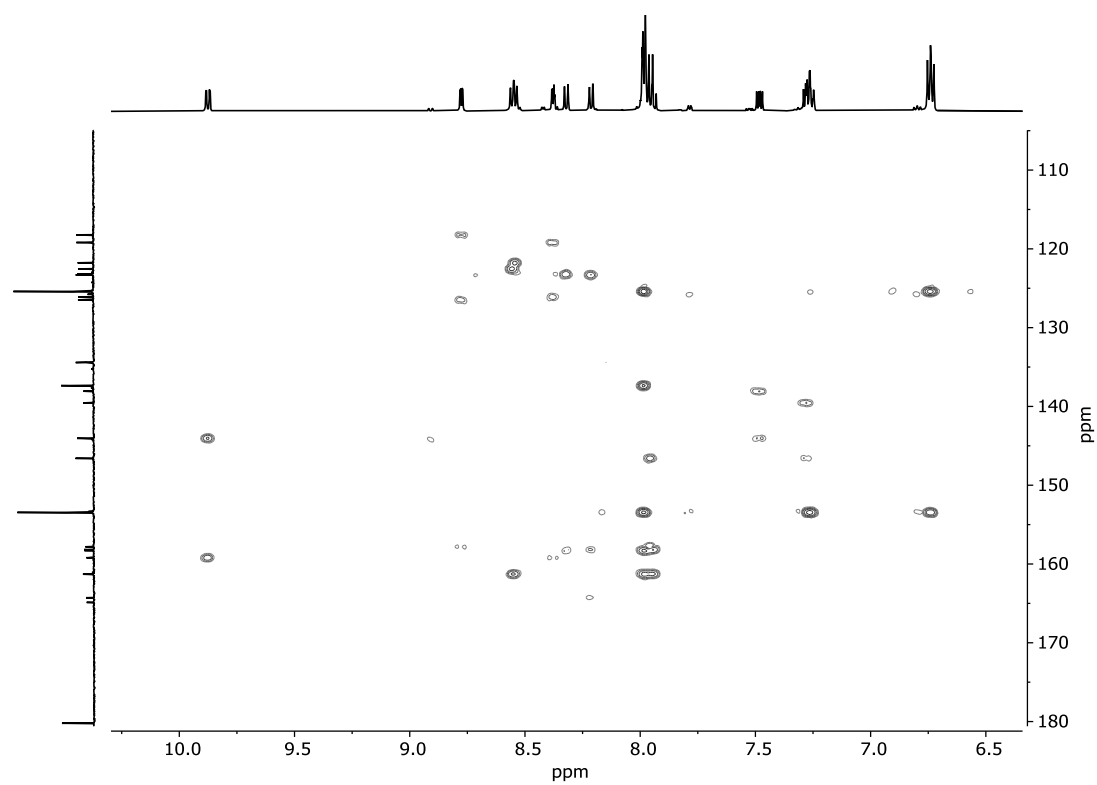
Figure A36. ^{1}H,^{13}C-HMBC NMR spectrum of **3** in methanol-d_4.
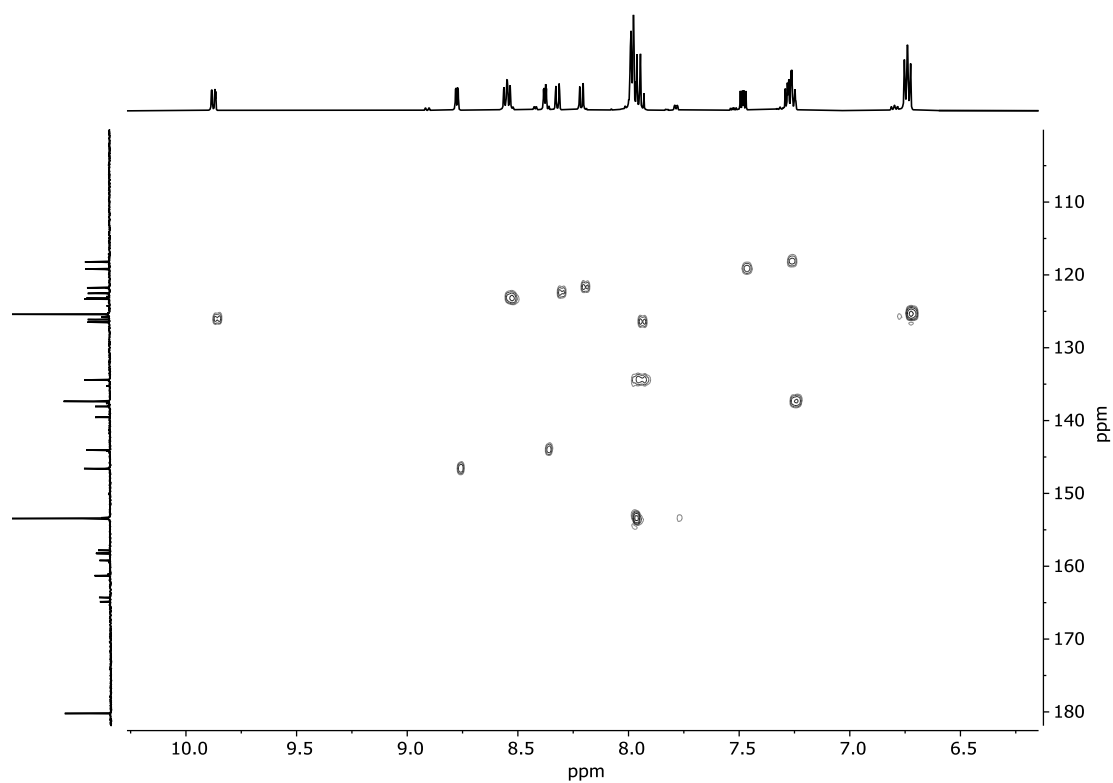
Figure A37. ^{1}H,^{13}C-HSQC NMR spectrum of **3** in methanol-d_4.
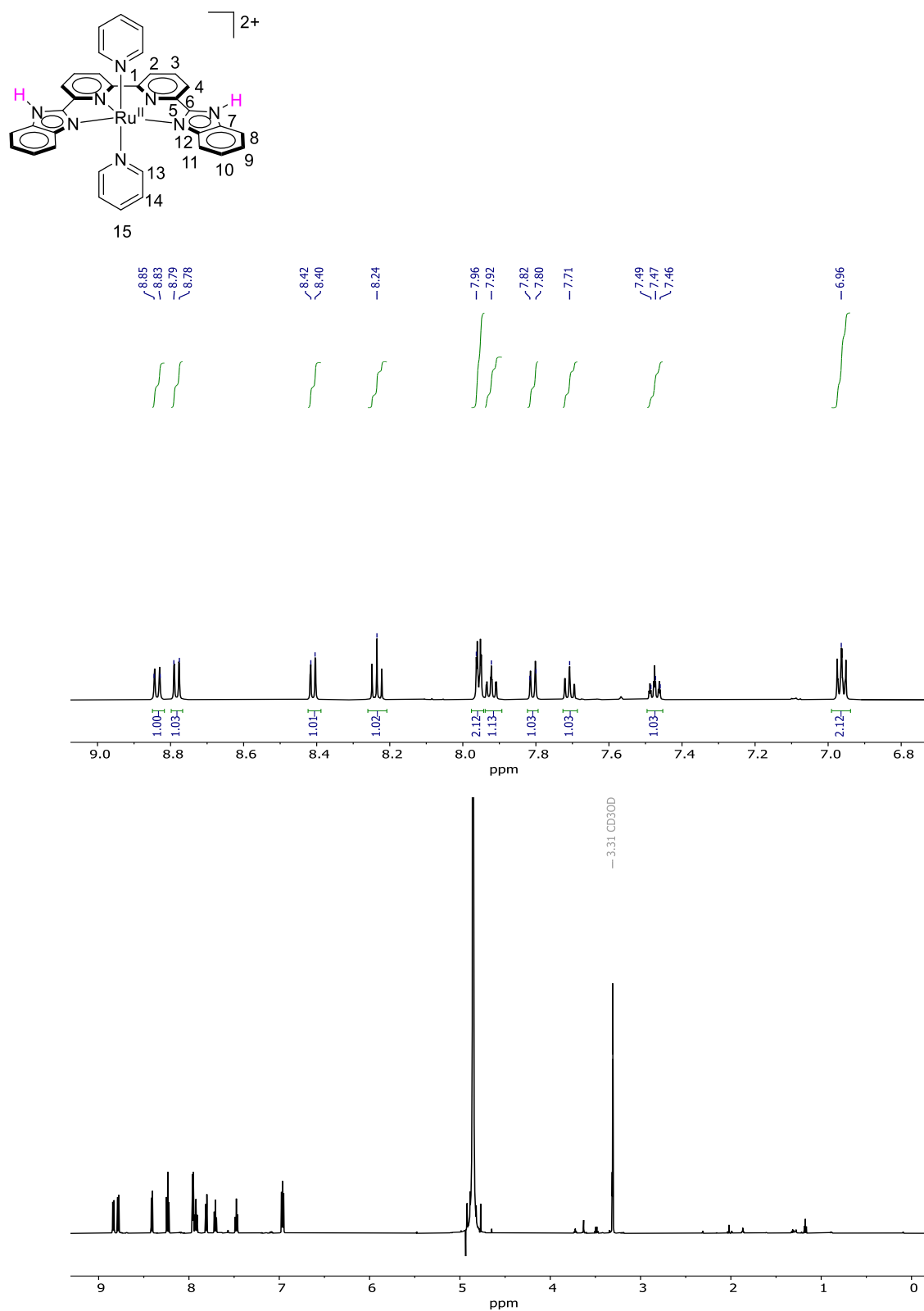
Figure A38. ¹HNMR spectrum of **[2H₂](CF₃SO₃)₂** in methanol-*d₄*.
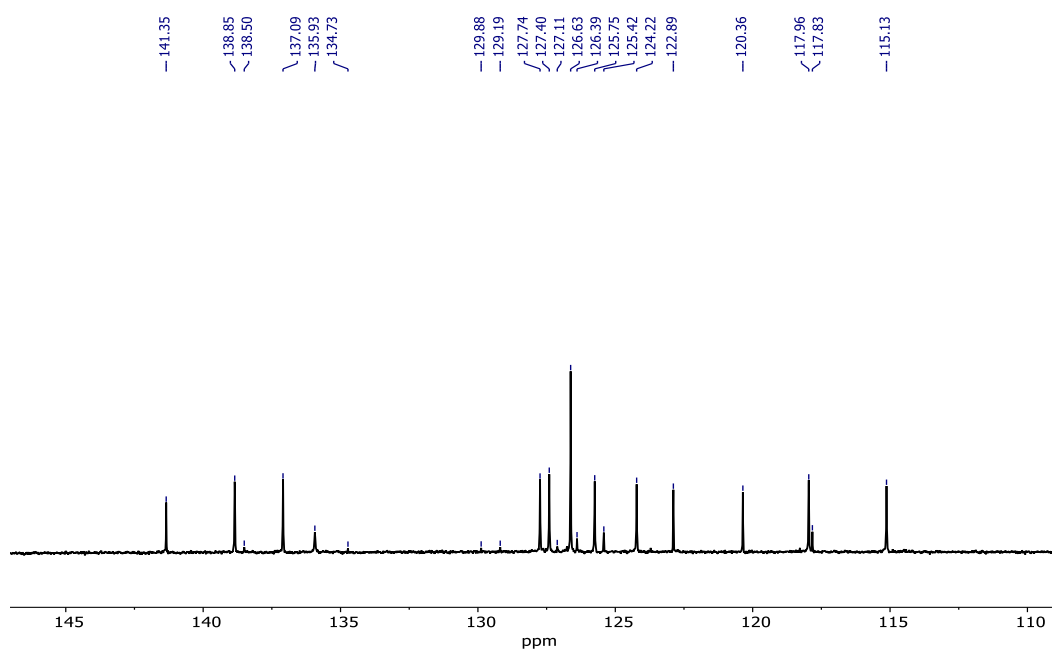
Figure A39. ^{13}C-NMR spectrum of **[2H$_2$](CF$_3$SO$_3$)$_2$** in methanol-d_4.
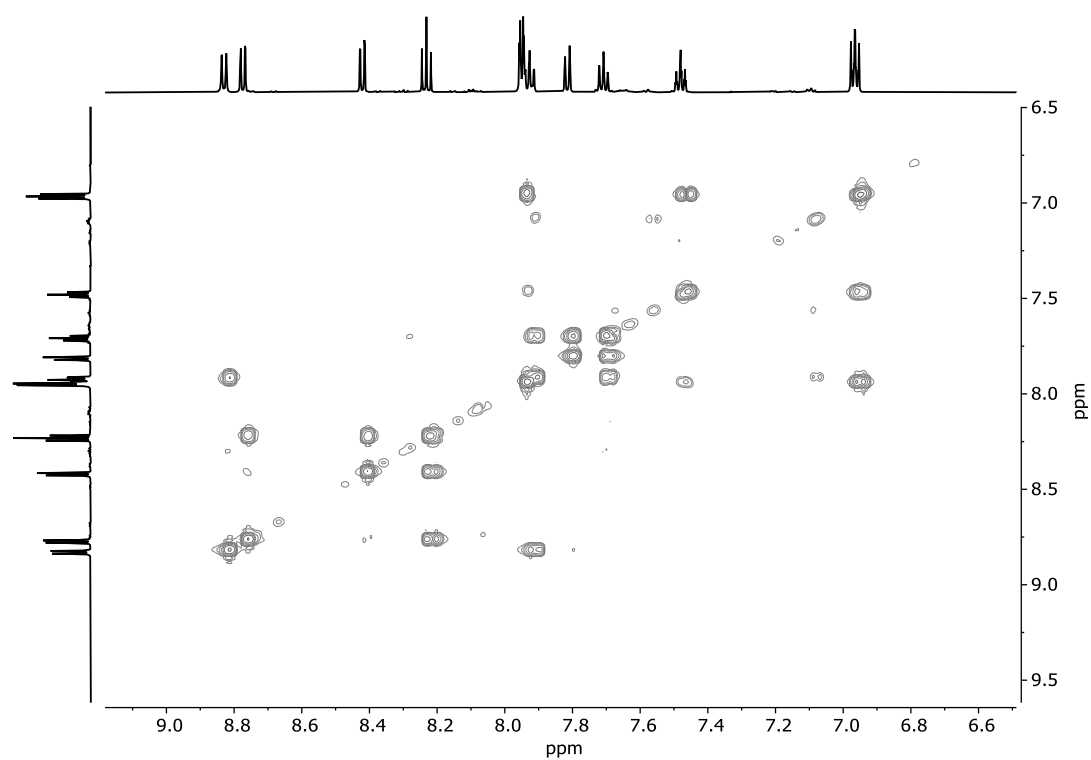
Figure A40. ^{1}H,^{1}H-COSY NMR spectrum of **[2H$_2$](CF$_3$SO$_3$)$_2$** in methanol-d_4.
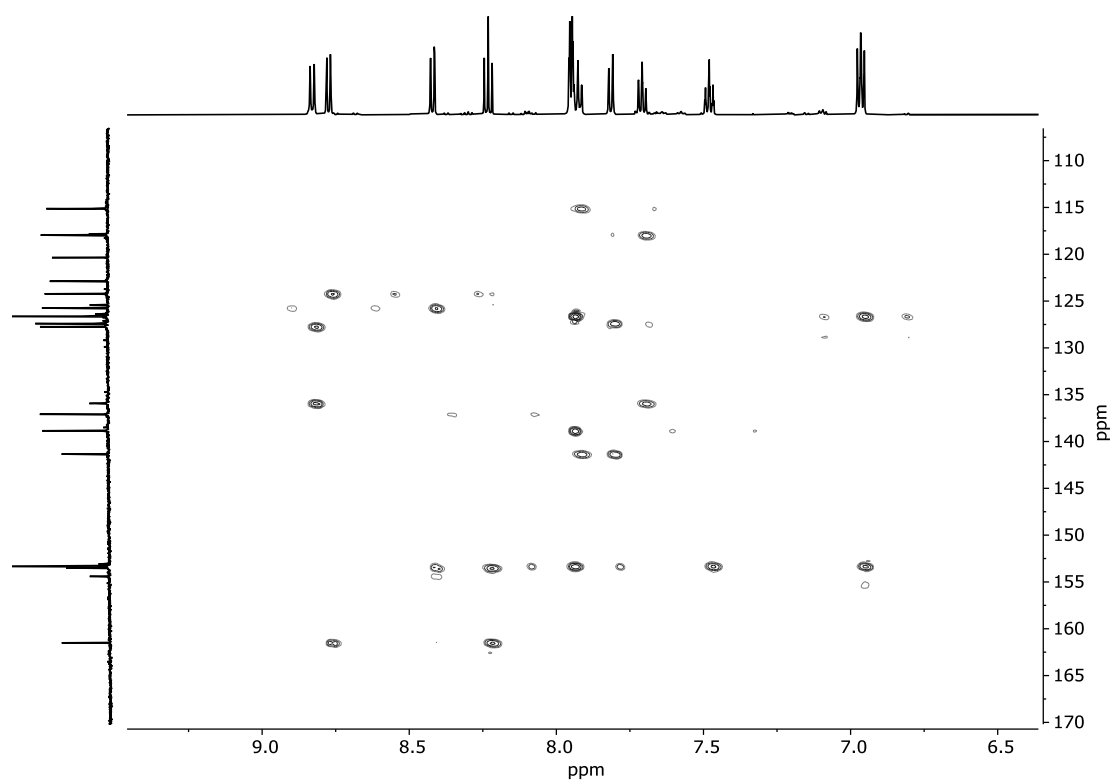
Figure A41. ^{1}H,^{13}C-HMBC NMR spectrum of **[2H$_2$](CF$_3$SO$_3$)$_2$** in methanol-d_4.
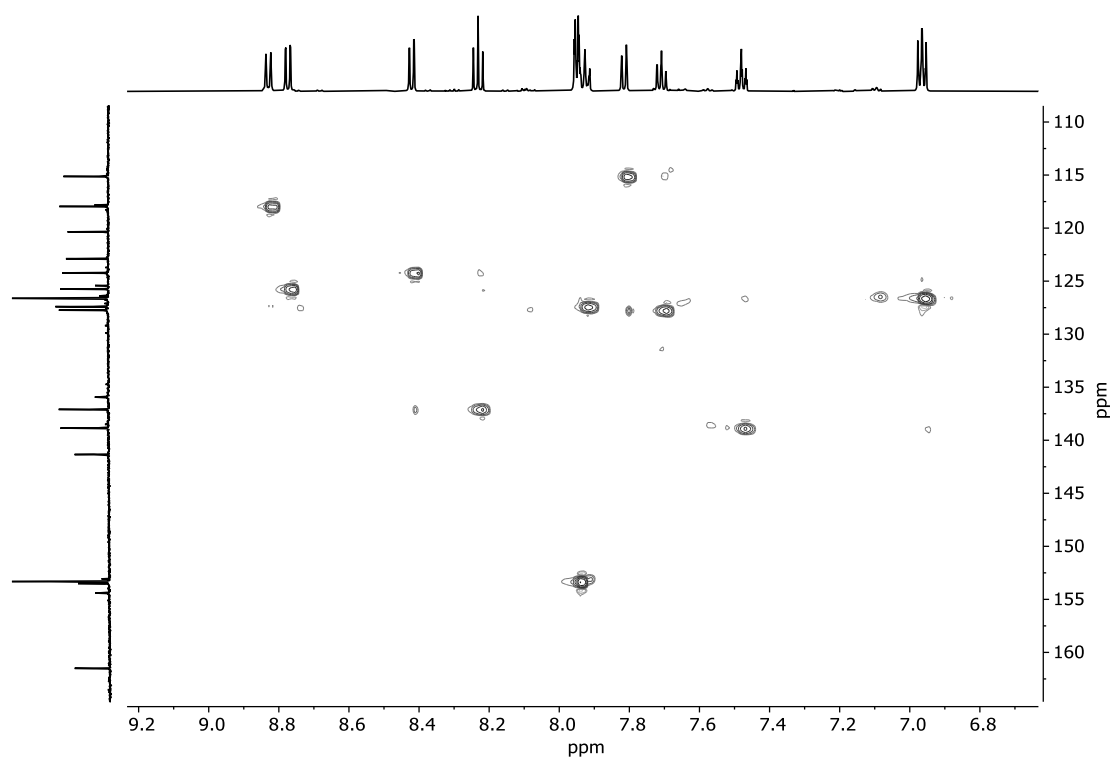
Figure A42. ^{1}H,^{13}C-HSQC NMR spectrum of **[2H$_2$](CF$_3$SO$_3$)$_2$** in methanol-d_4.
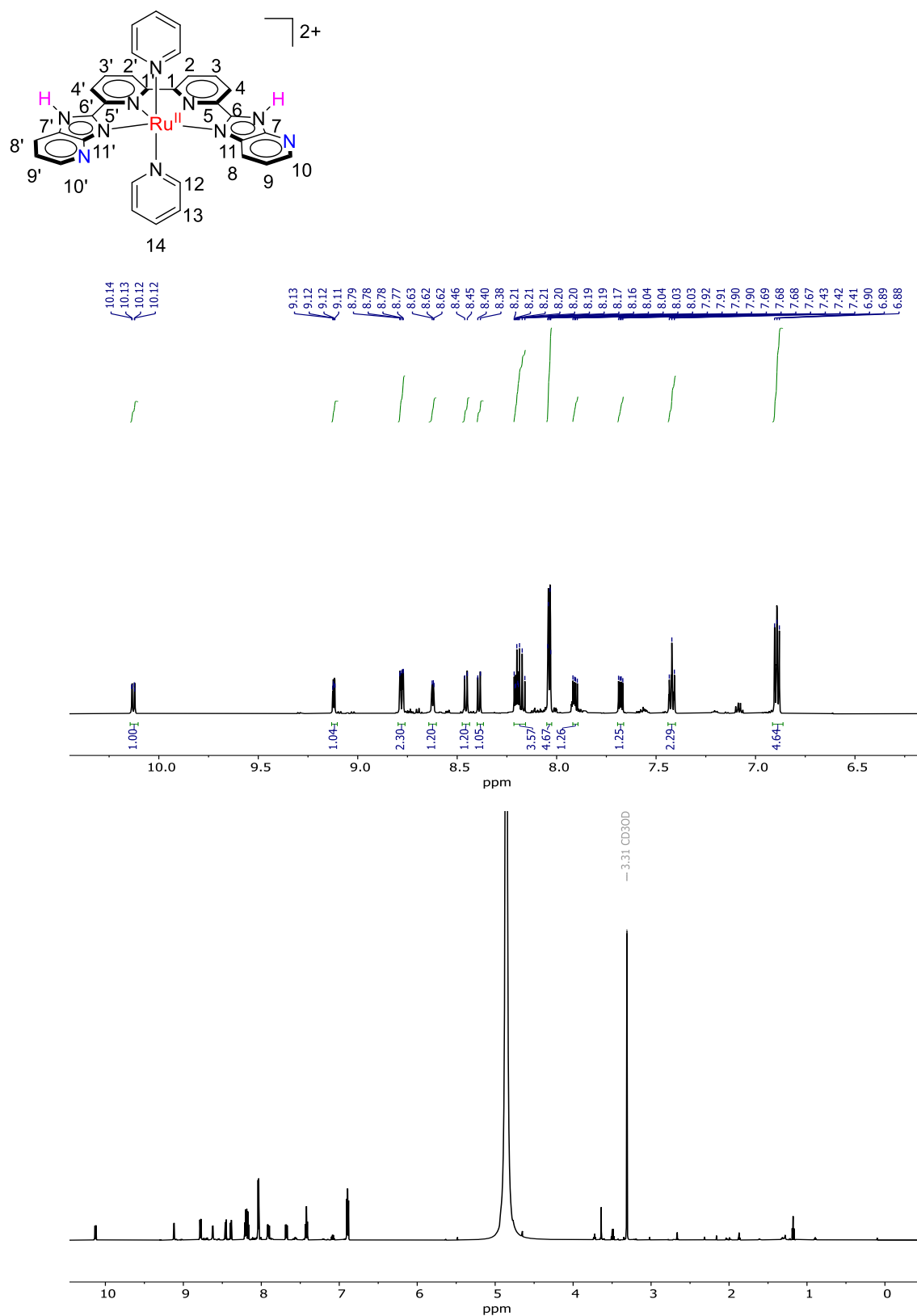
Figure A43. ^{1}HNMR spectrum of **[3H₂](CF₃SO₃)₂** in methanol-d_4.
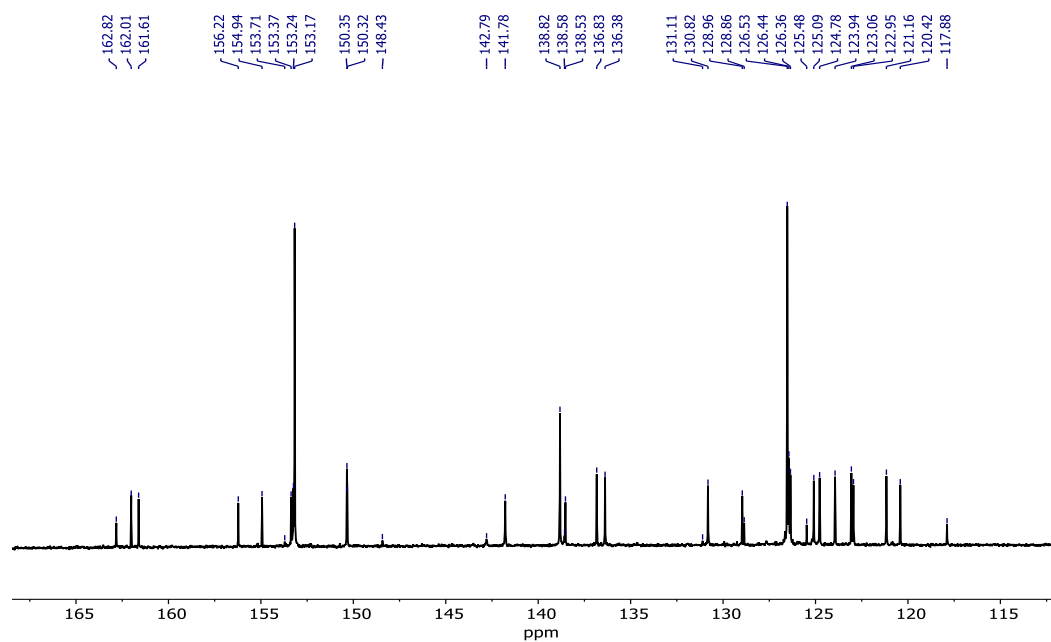
Figure A44. ^{13}CNMR spectrum of **[3H₂](CF₃SO₃)₂** in methanol-d_4.
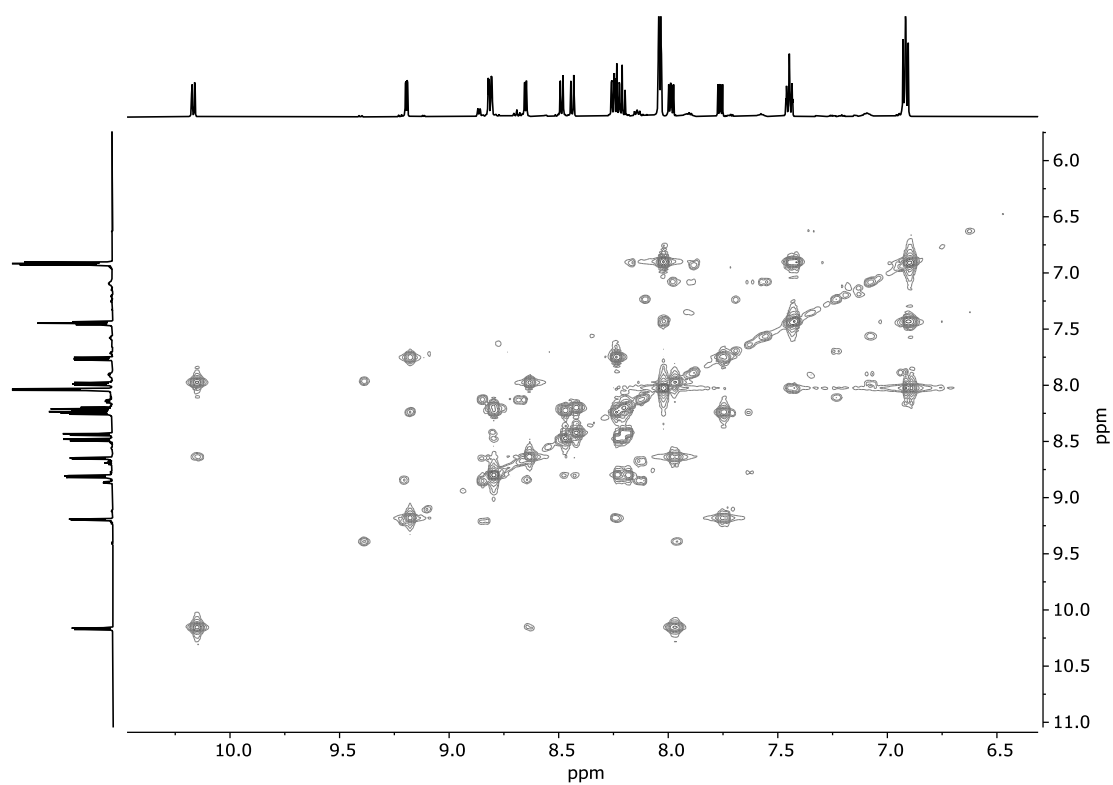
Figure A45. ^{1}H,^{1}H-COSY NMR spectrum of **[3H₂](CF₃SO₃)₂** in methanol-d_4.
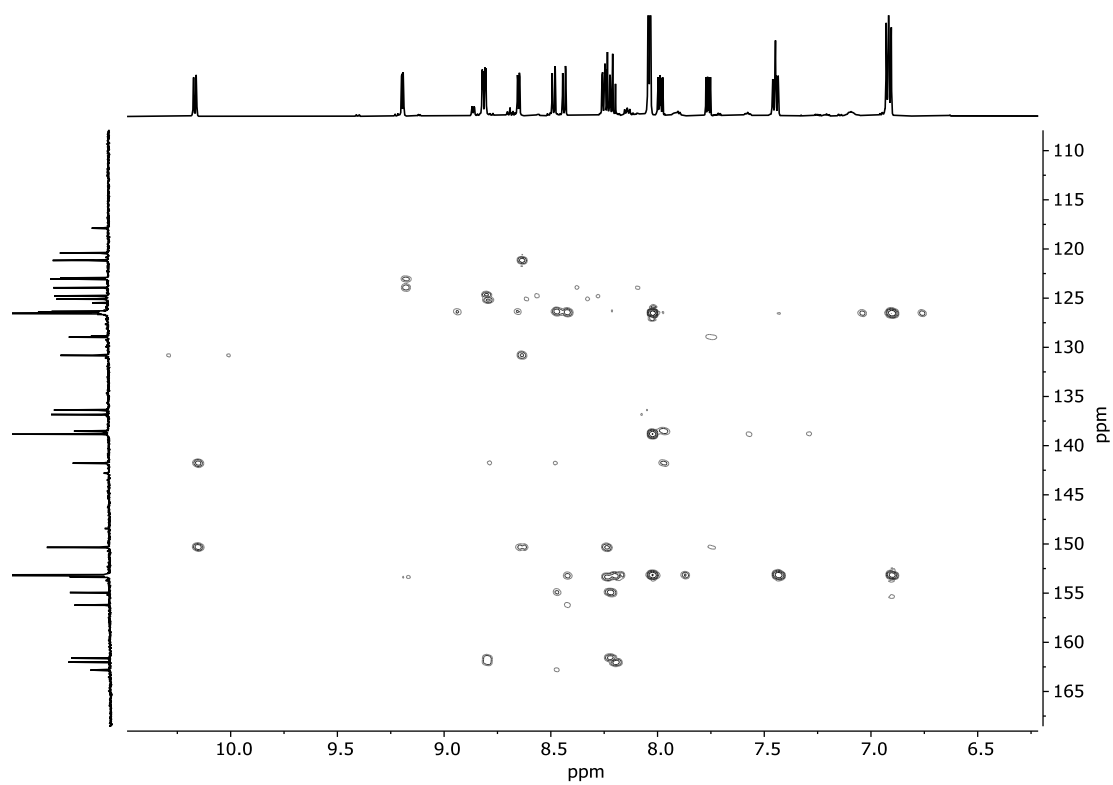
Figure A46. ^{1}H,^{13}C-HMBC NMR spectrum of **[3H$_2$](CF$_3$SO$_3$)$_2$** in methanol-d_4.
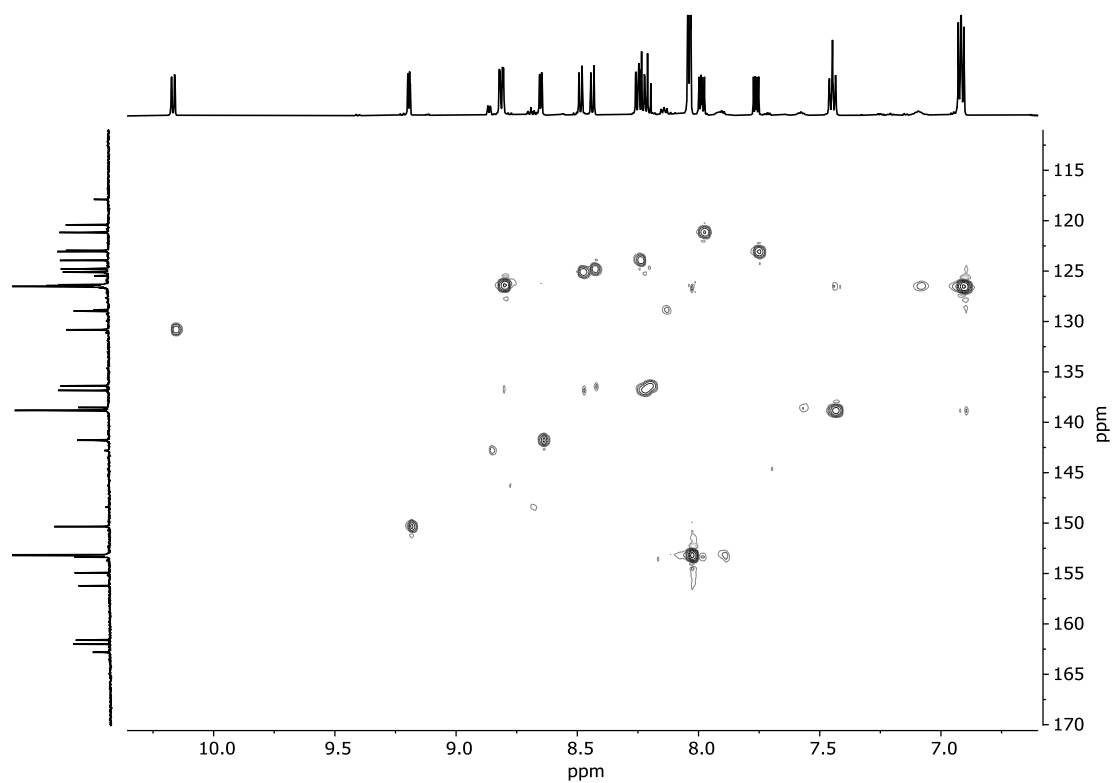
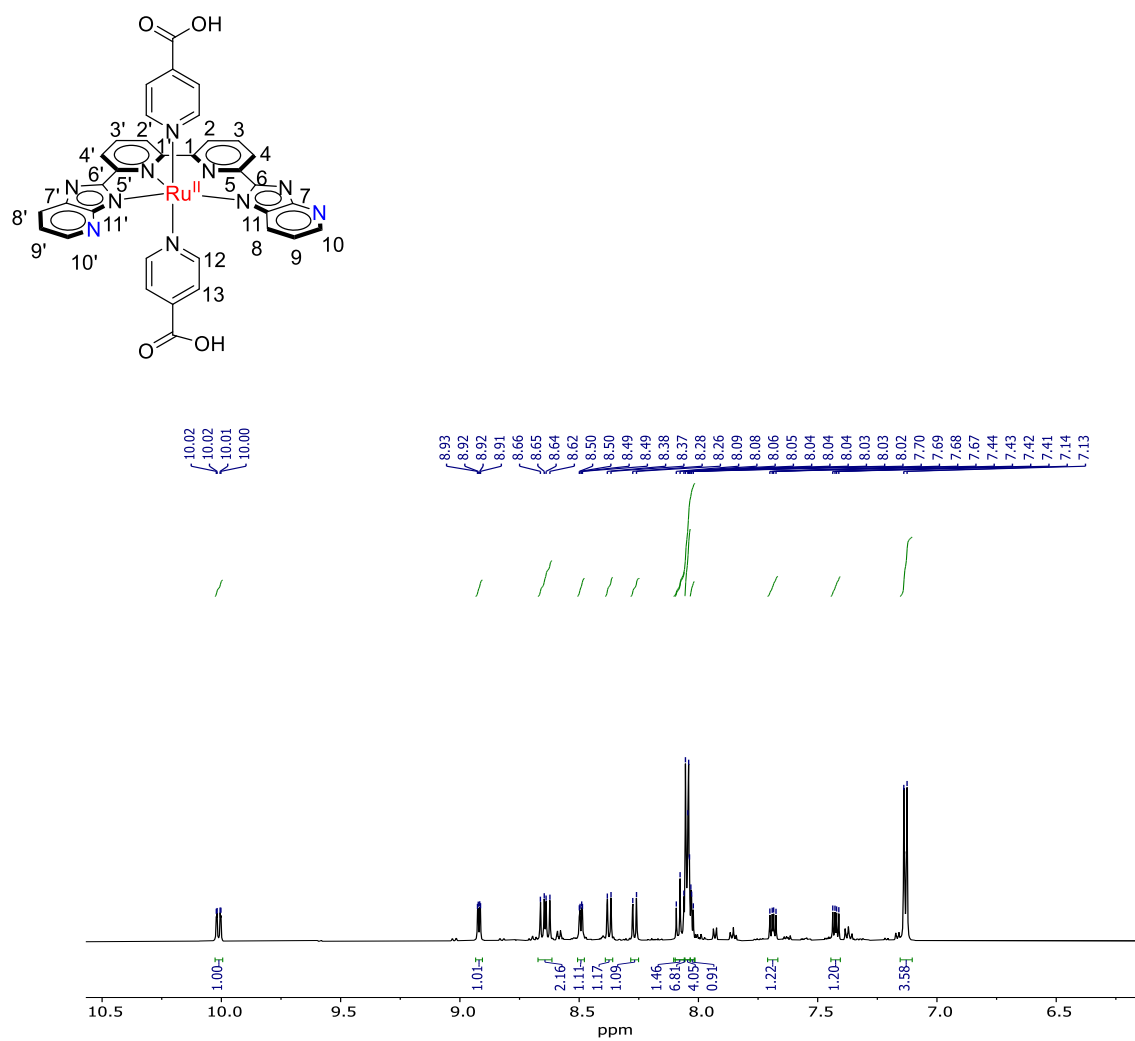**Figure A47.** ^{1}H,^{13}C-HSQC NMR spectrum of **[3H$_2$](CF$_3$SO$_3$)$_2$** in methanol-d_4.

Figure A48. ^{1}H-NMR spectrum of **4** in methanol-d_4.

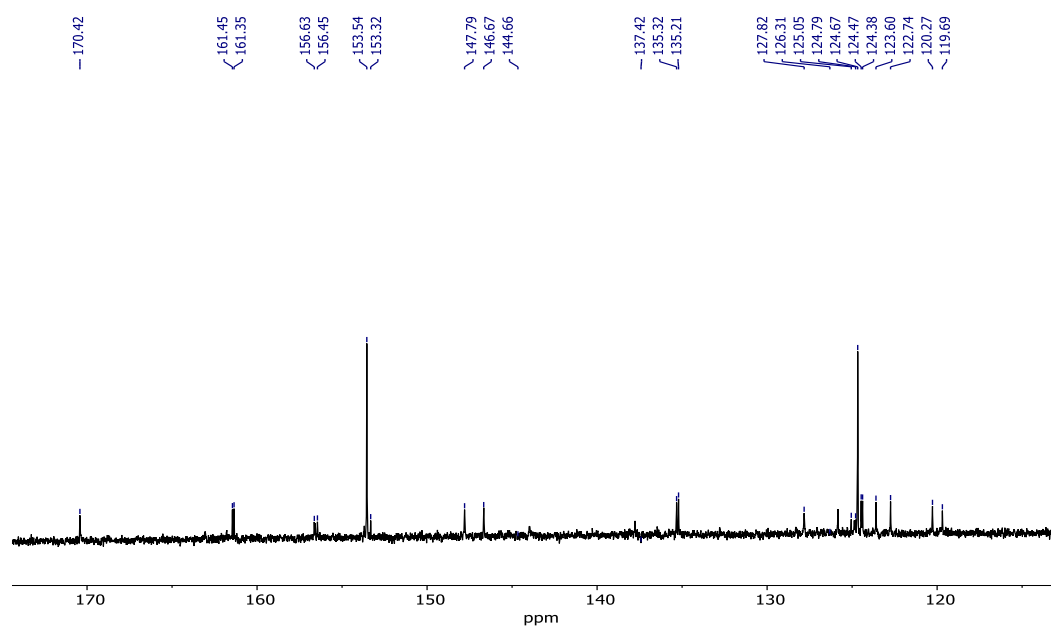**Figure A49.** ^{13}C-NMR spectrum of **4** in methanol-d_4..
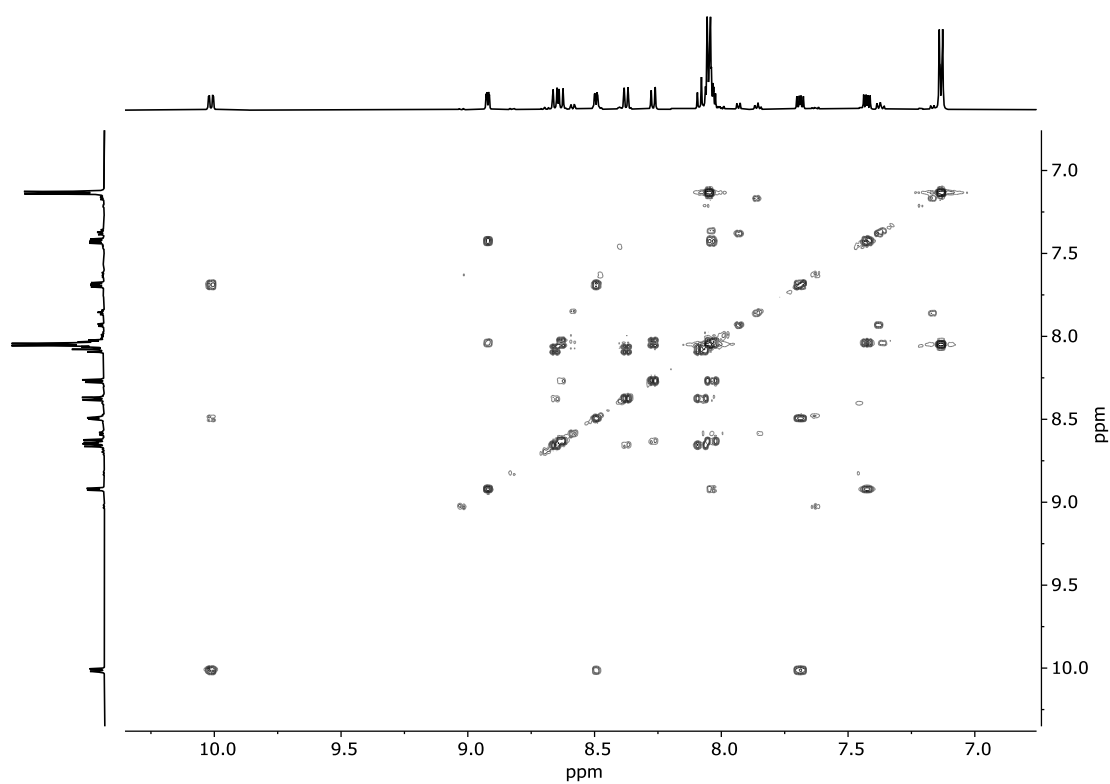
Figure A50. ^{1}H,^{1}H-COSY NMR spectrum of **4** in methanol-d_4.
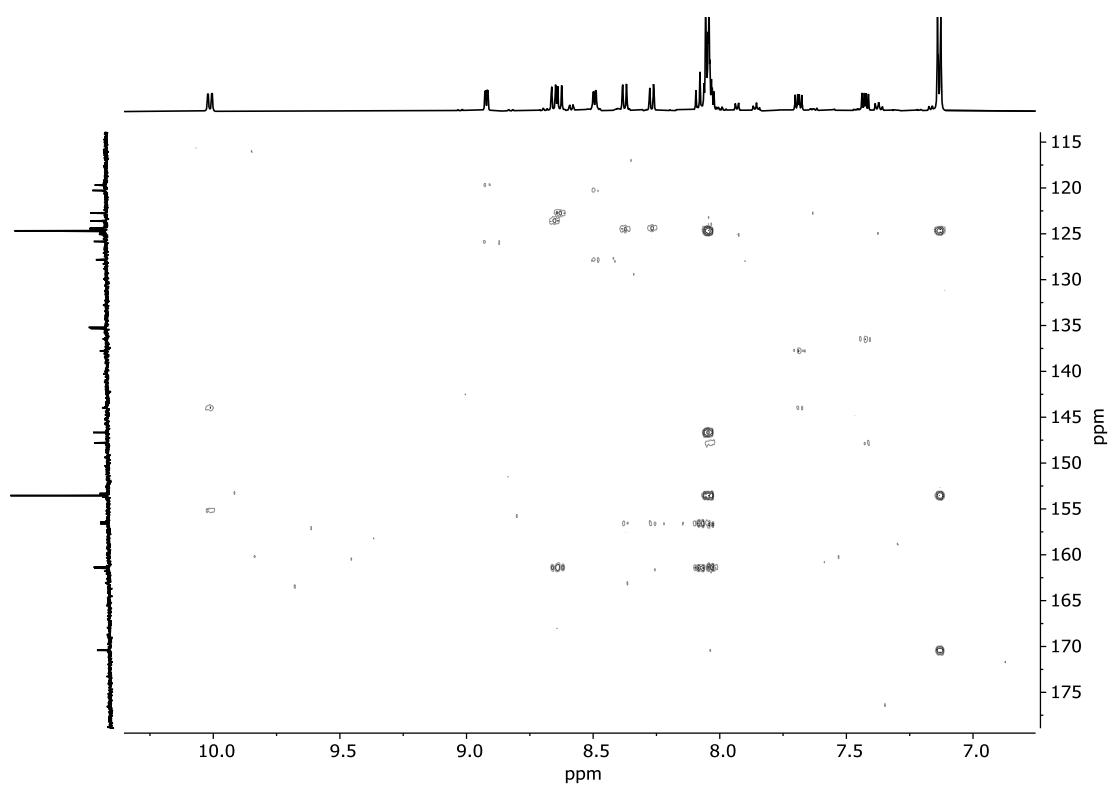
Figure A51. ^{1}H,^{13}C-HMBC NMR spectrum of **4** in methanol-d_4.
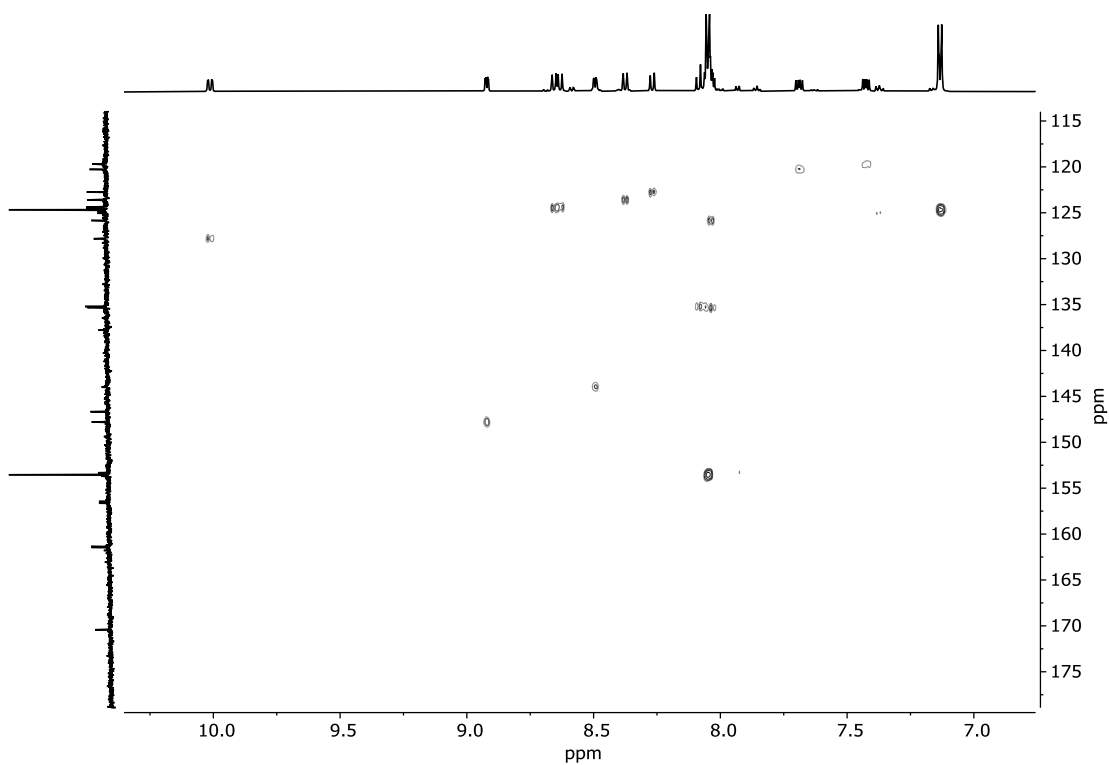
Figure A52. ^{1}H,^{13}C-HSQC NMR spectrum of **4** in methanol-d_4.
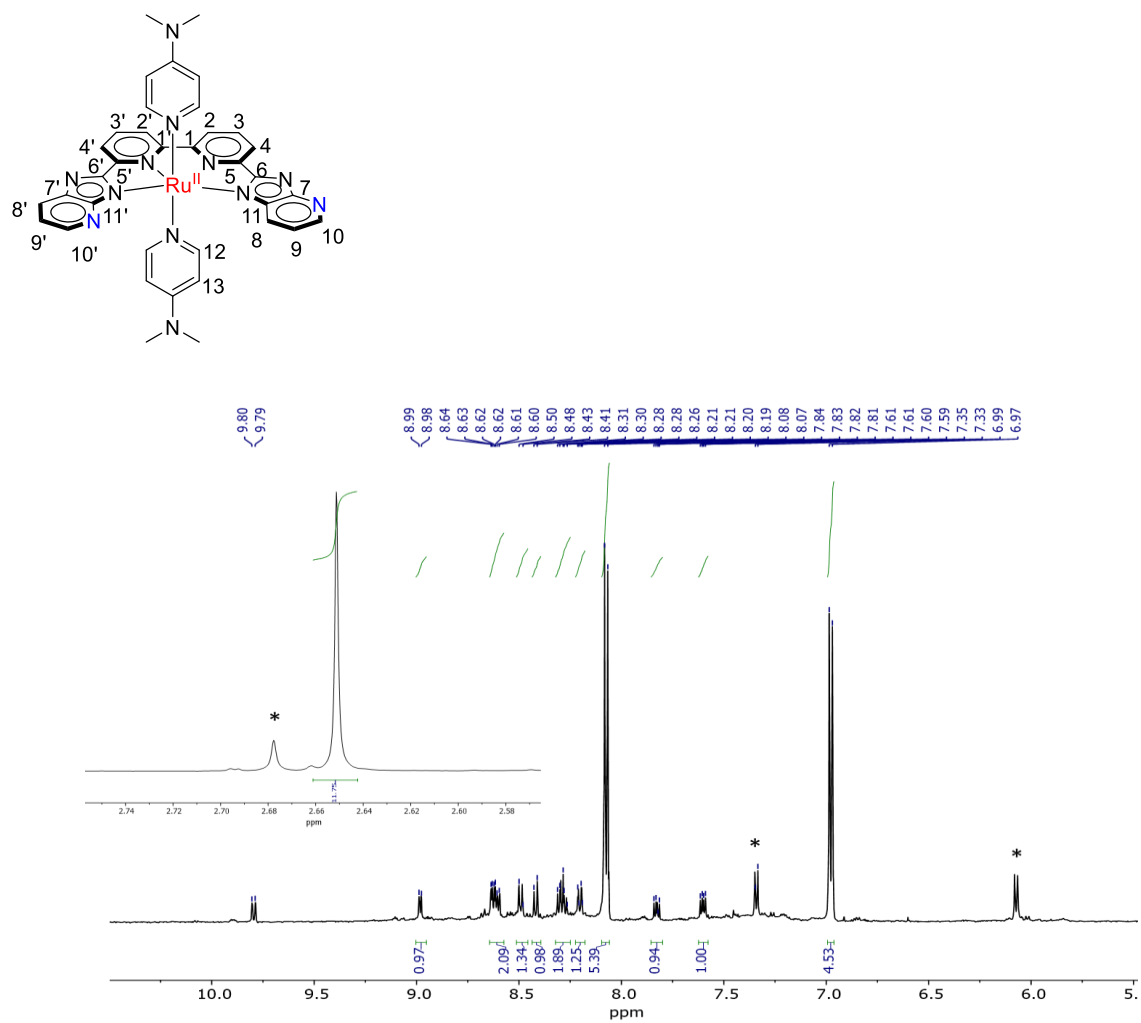
Figure A53. ^{1}H-NMR spectrum of **5** in methanol-d_4. The asterisks correspond to the free DMAP ligand.
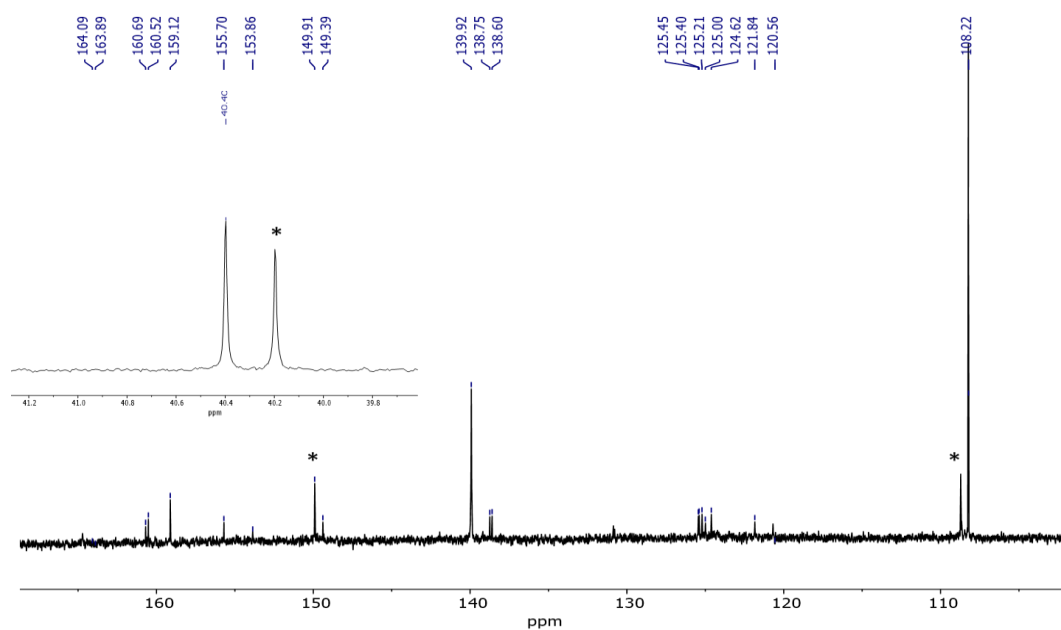
Figure A54. ^{13}C-NMR spectrum of **5** in methanol-d_4. The asterisks indicate the free DMAP ligand.
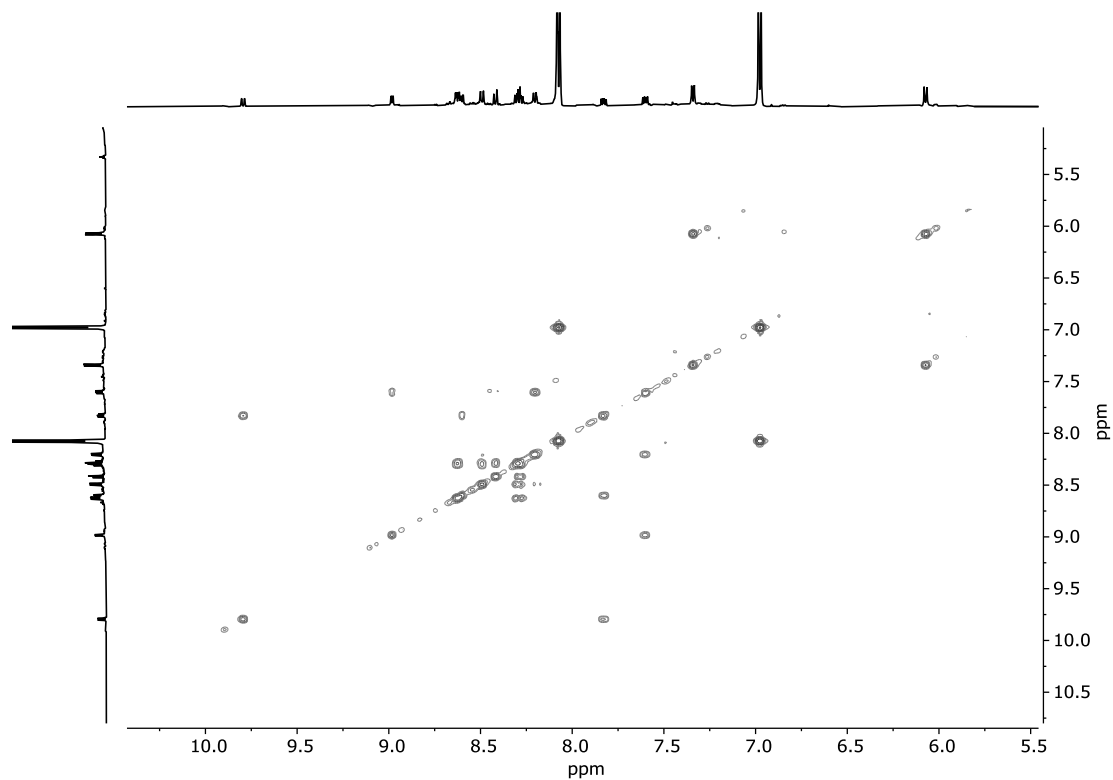
Figure A55. ^{1}H,^{1}H-COSY NMR spectrum of **5** in methanol-d_4.
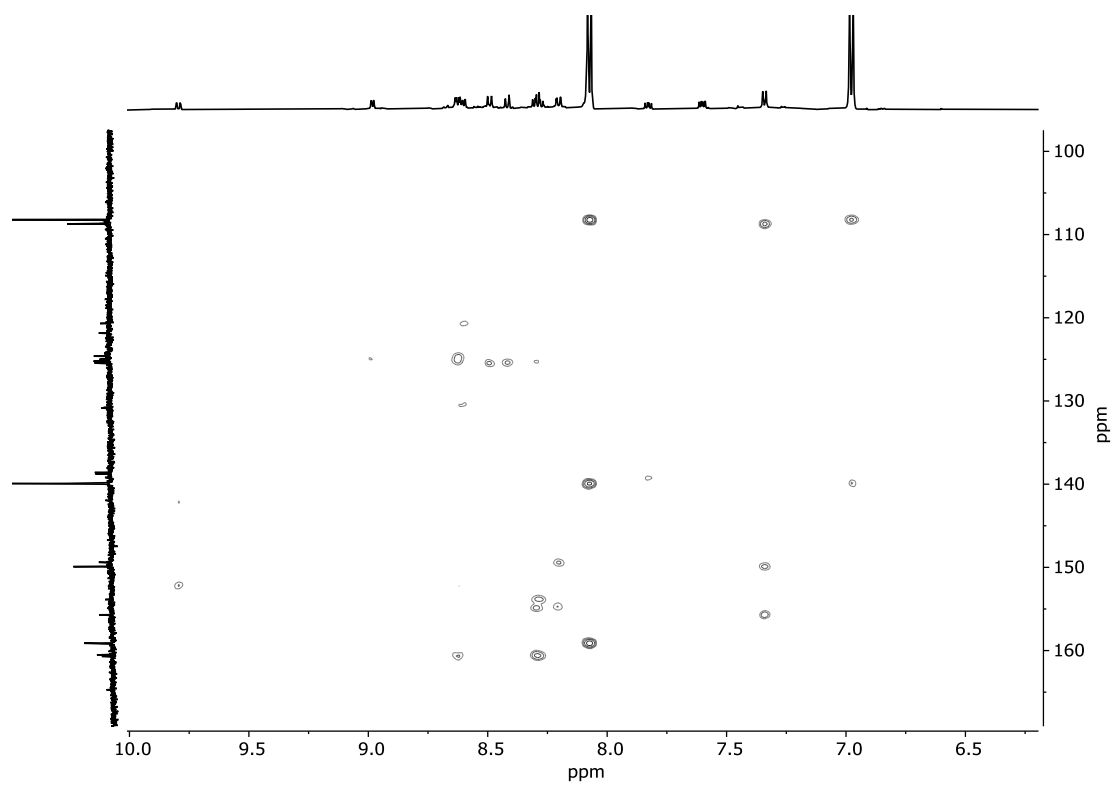
Figure A56. ^{1}H,^{13}C-HMBC NMR spectrum of **5** in methanol-d_4.
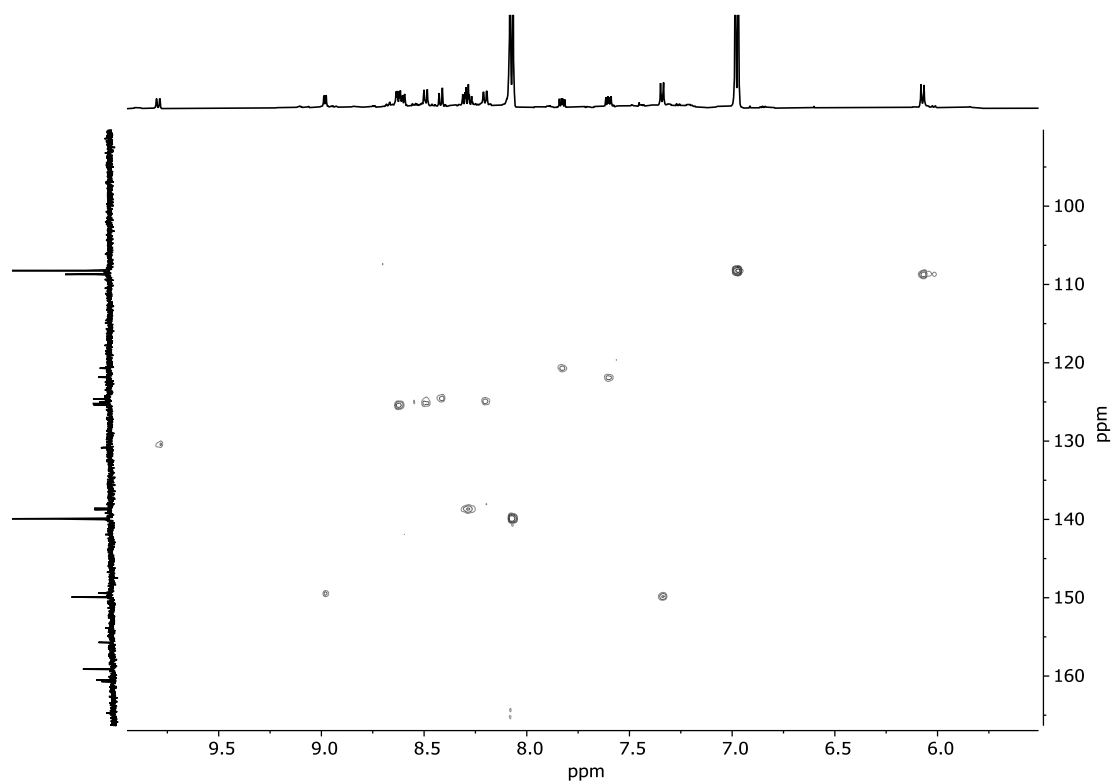
Figure A57. ^{1}H,^{13}C-HSQC NMR spectrum of **5** in methanol-d_4.
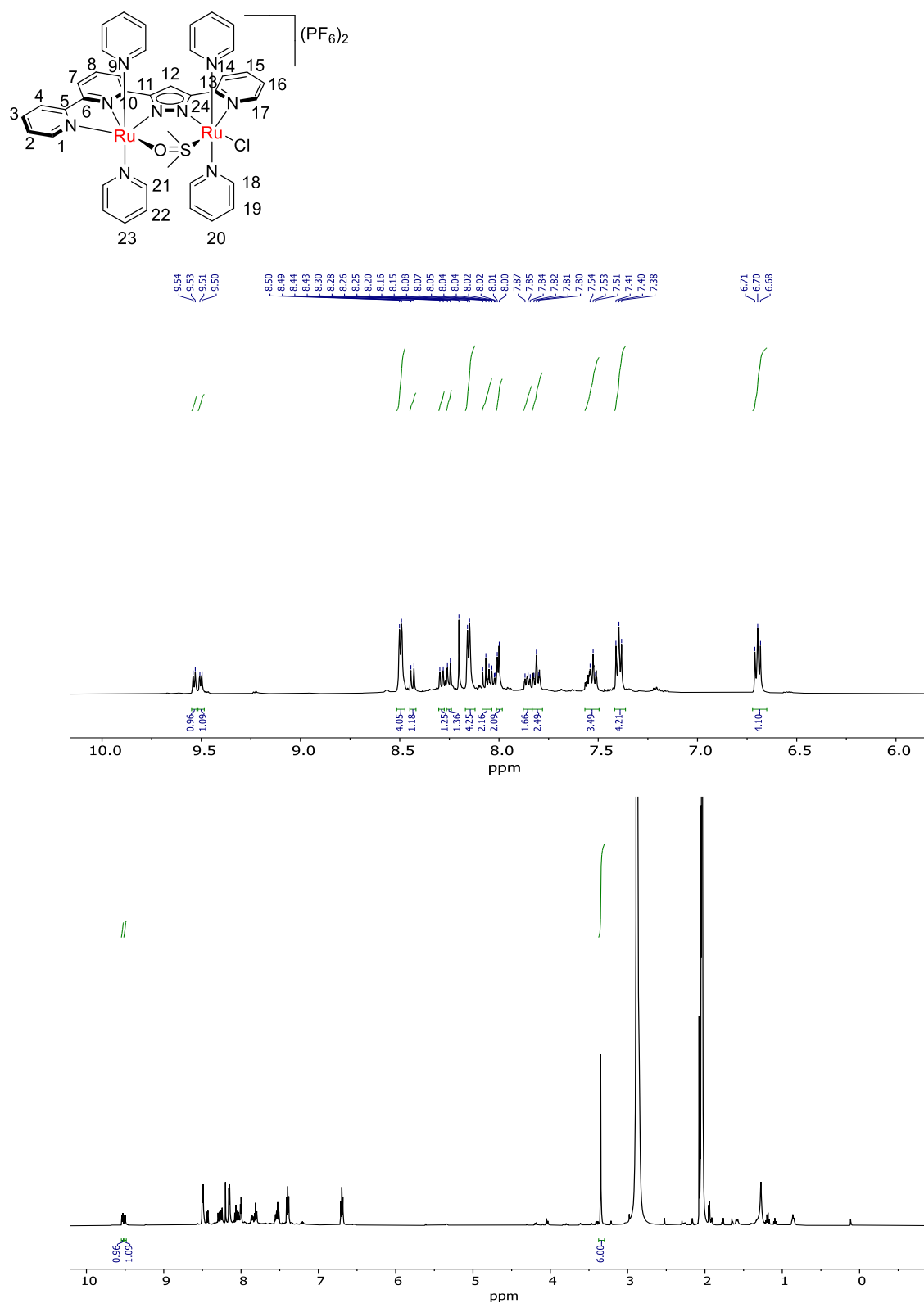
Figure A58. ^{1}H-NMR spectrum of **6** in acetone-d_6.
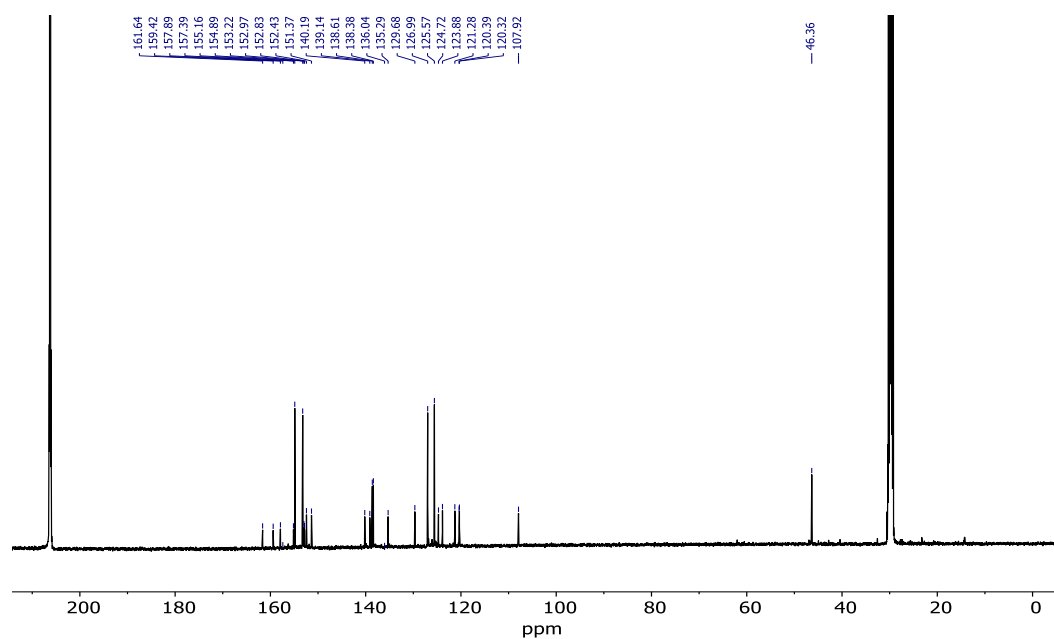
Figure A59. ^{13}C-NMR spectrum of **6** in acetone-d_6.
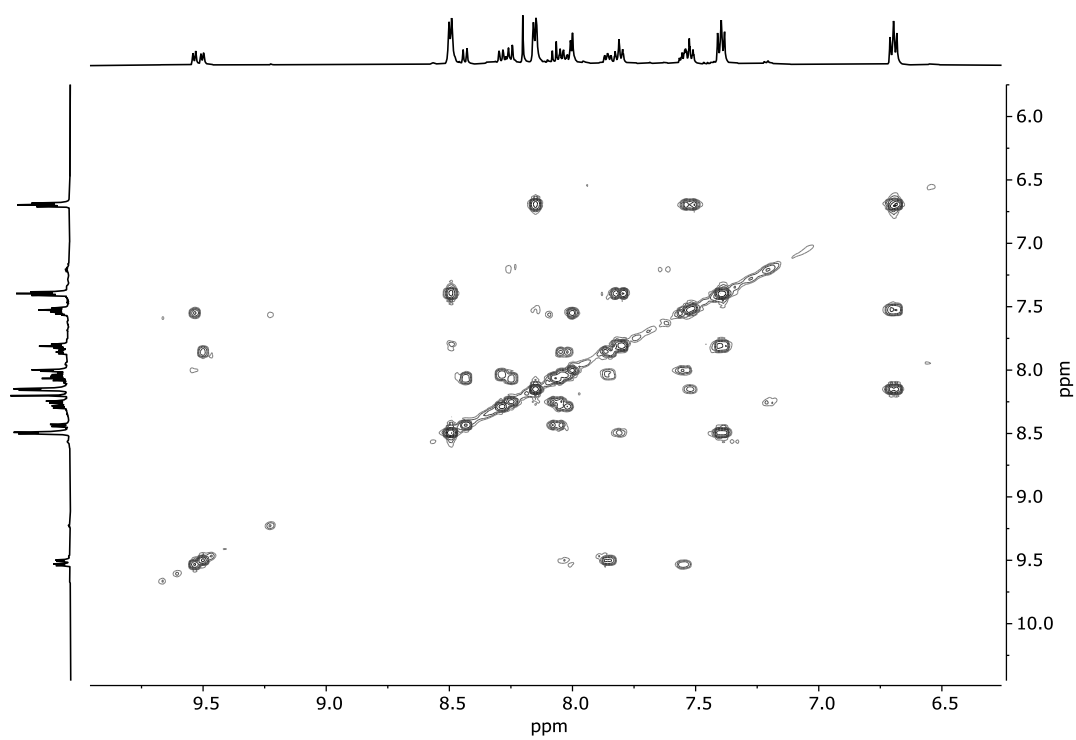
Figure A60. ^{1}H,^{1}H-COSY NMR spectrum of **6** in acetone-d_6.
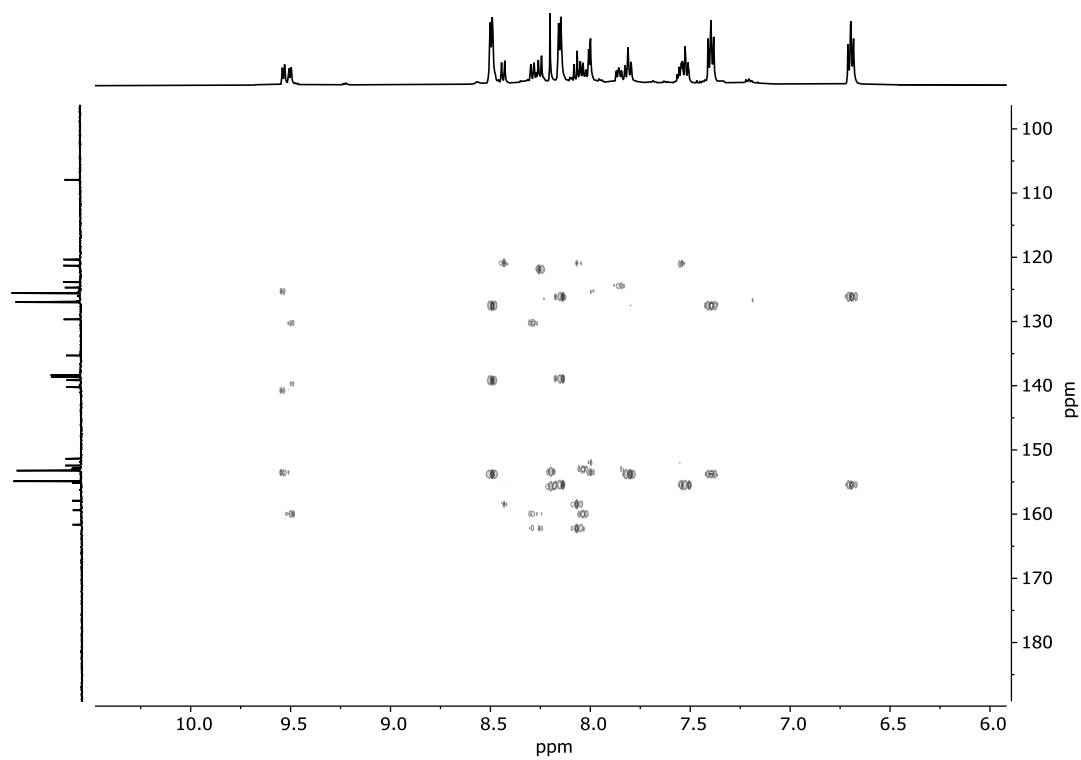
Figure A61. ^{1}H,^{13}C-HMBC NMR spectrum of **6** in acetone-d_6.
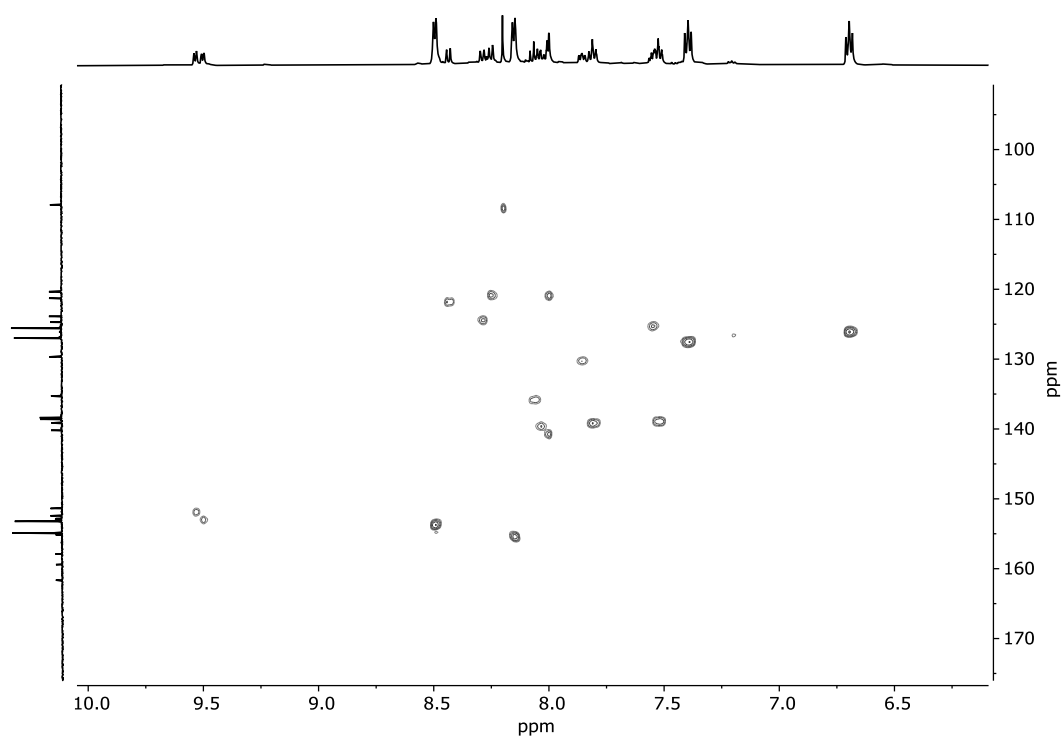
Figure A62. ^{1}H,^{13}C-HSQC NMR spectrum of **6** in acetone-d_6.
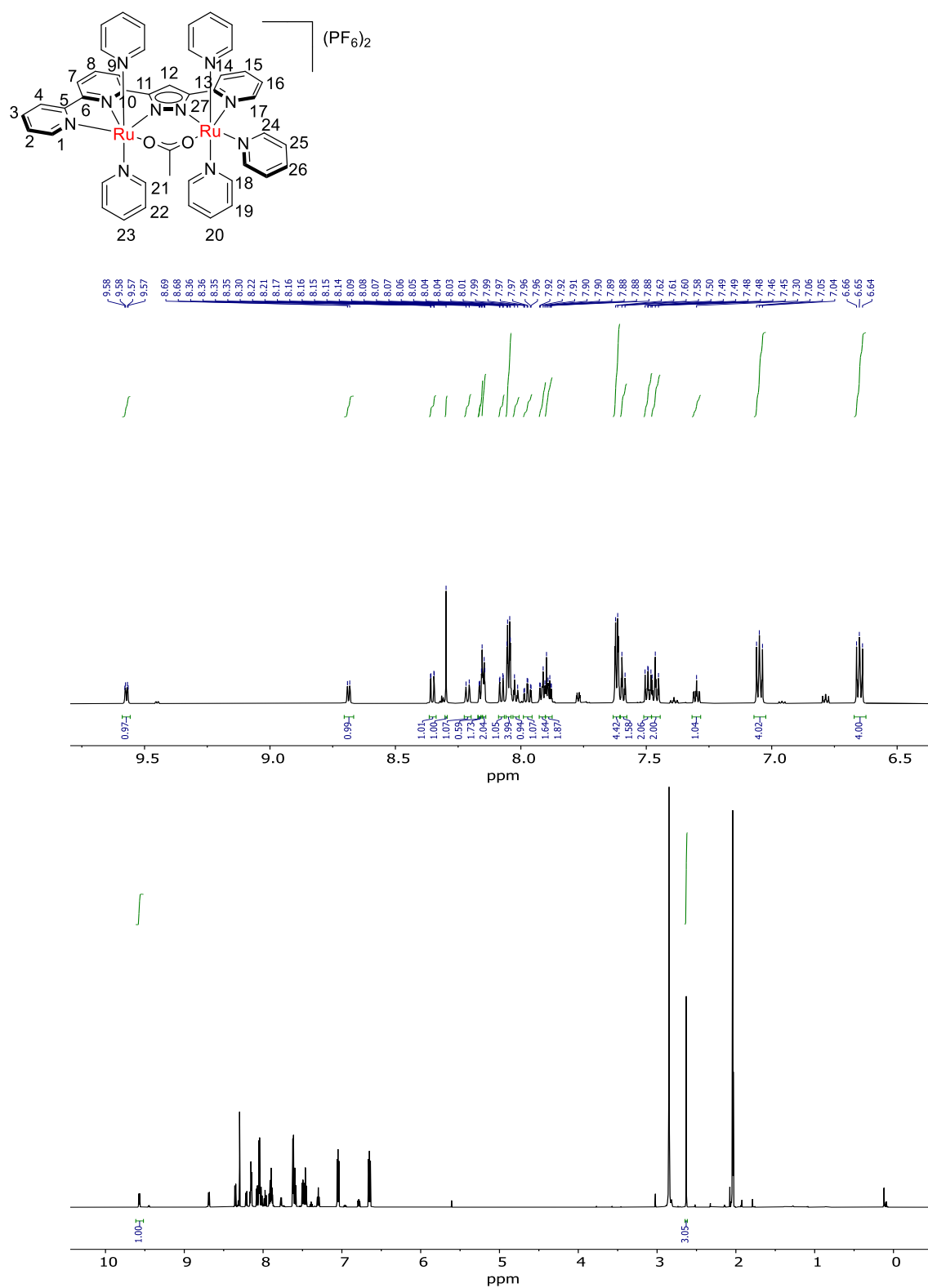
Figure A63. ^{1}H-NMR spectrum of **7** in acetone-d_6.
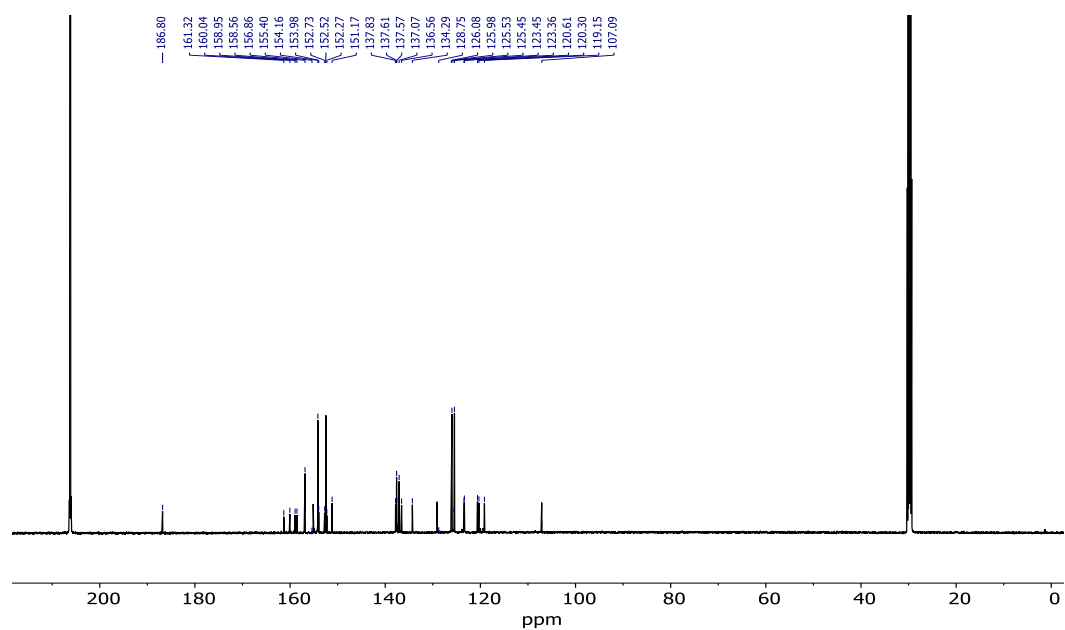
Figure A64. ^{13}C-NMR spectrum of **7** in acetone-d_6.
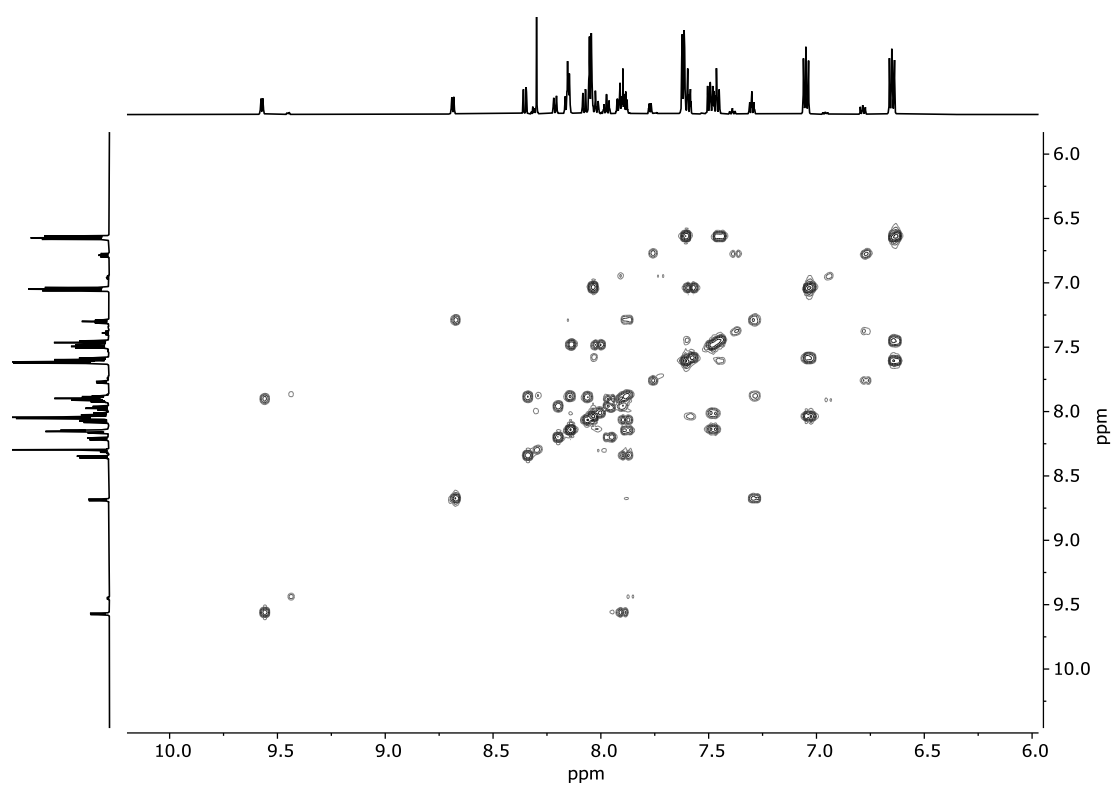
Figure A65. ^{1}H,^{1}H-COSY NMR spectrum of **7** in acetone-d_6.
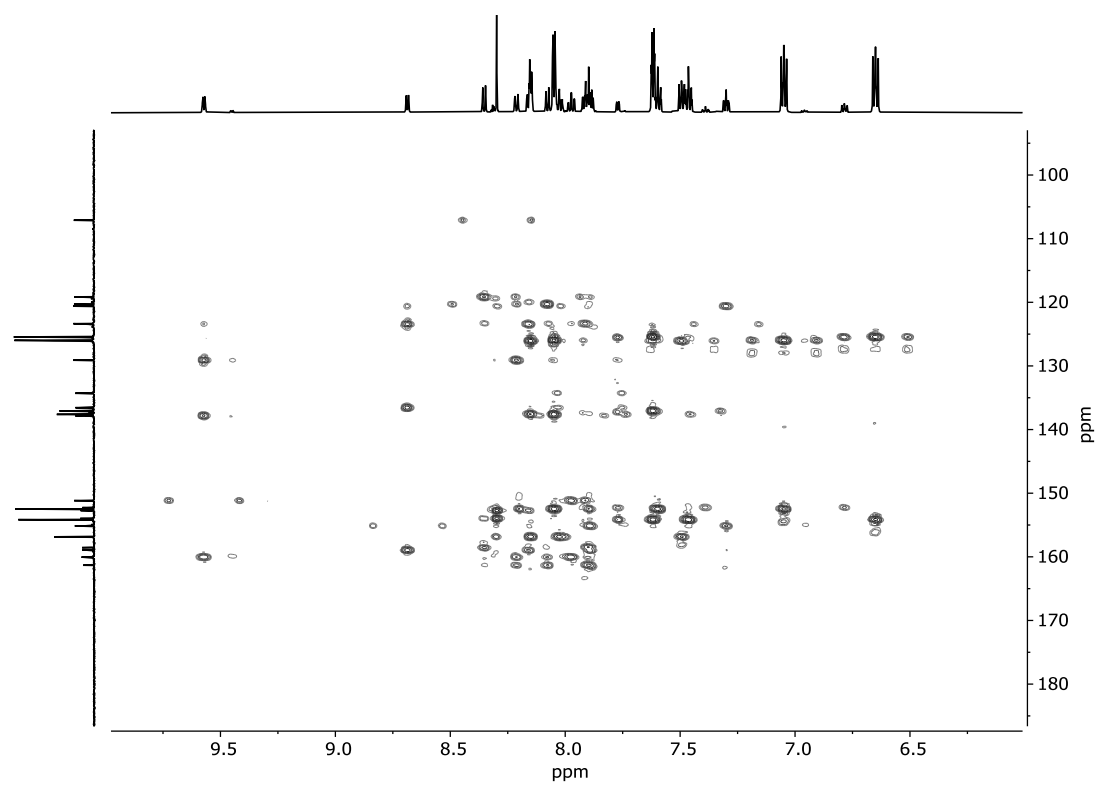
Figure A66. ^{1}H,^{13}C-HMBC NMR spectrum of **7** in acetone-d_6.
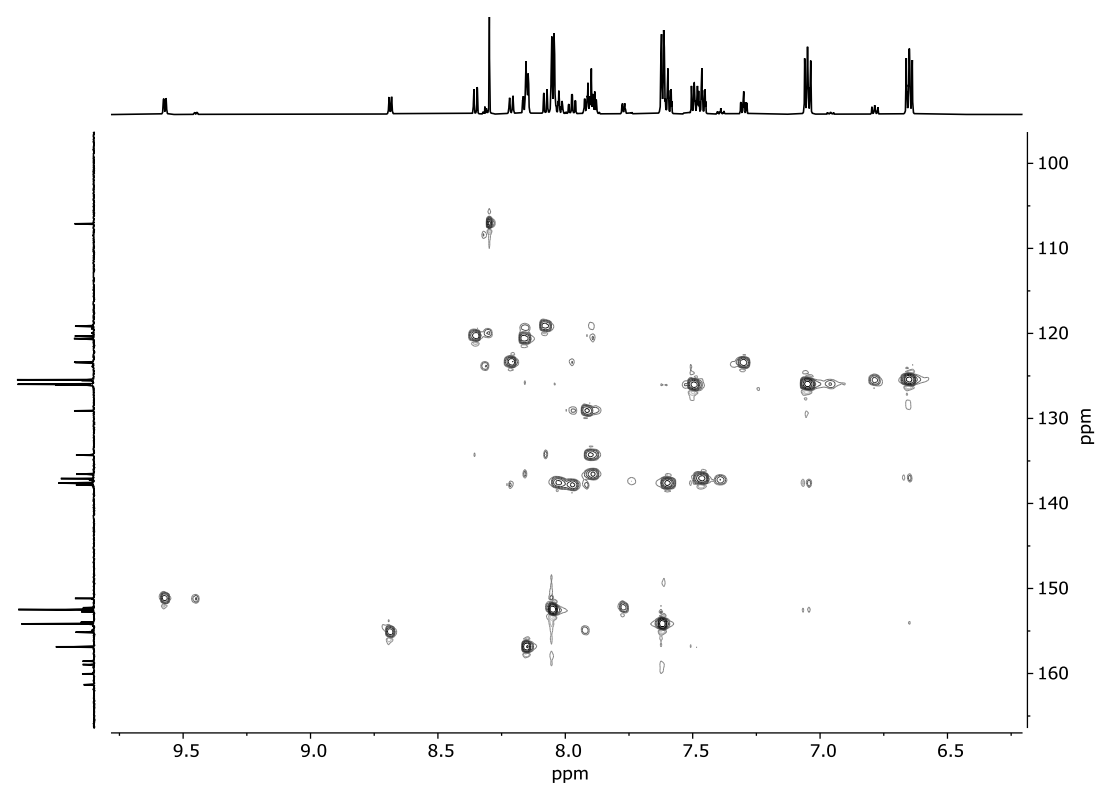
Figure A67. ^{1}H,^{13}C-HSQC NMR spectrum of **7** in acetone-d_6.
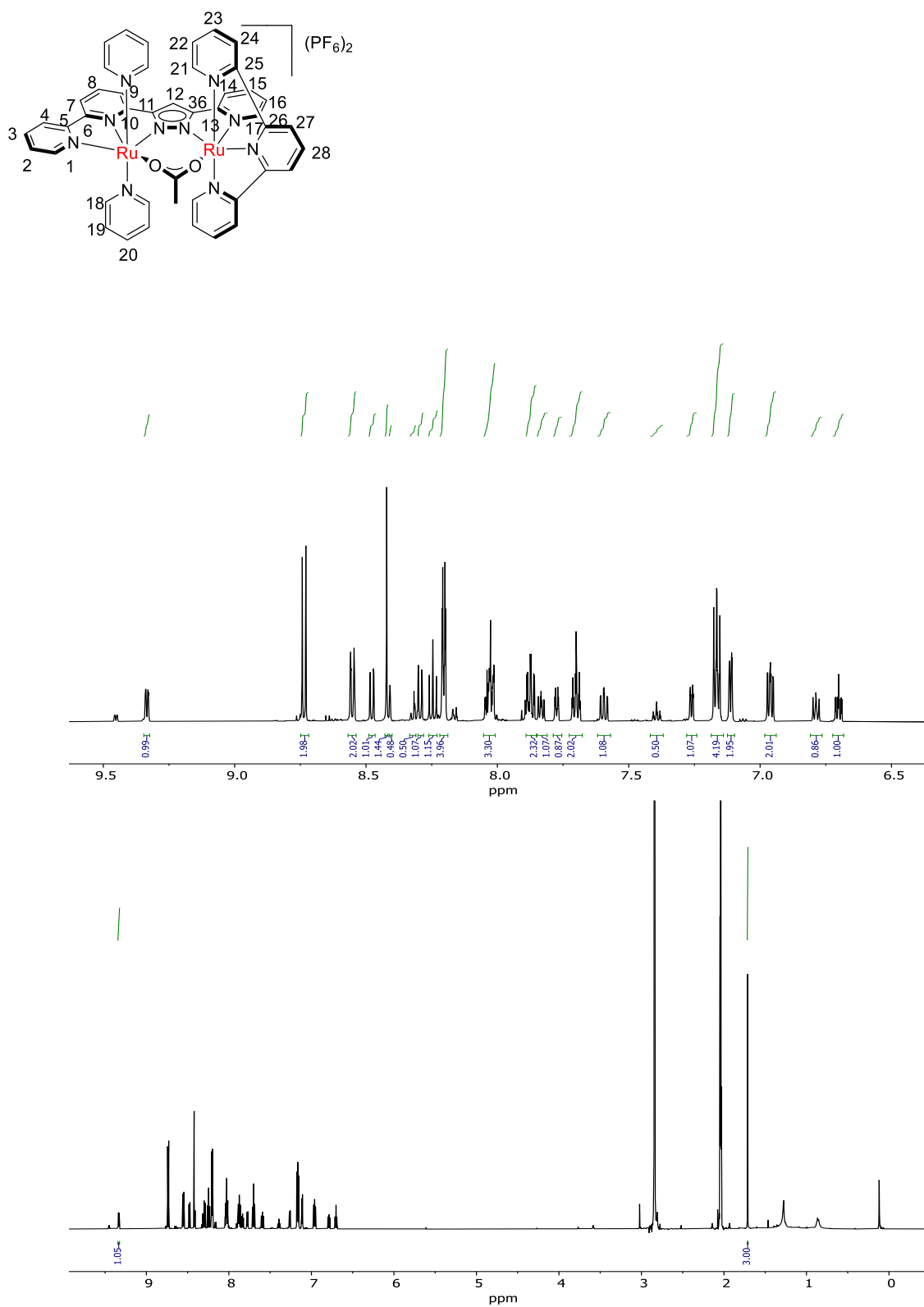
Figure A68. ^{1}H-NMR spectrum of **8** in acetone-d_6.
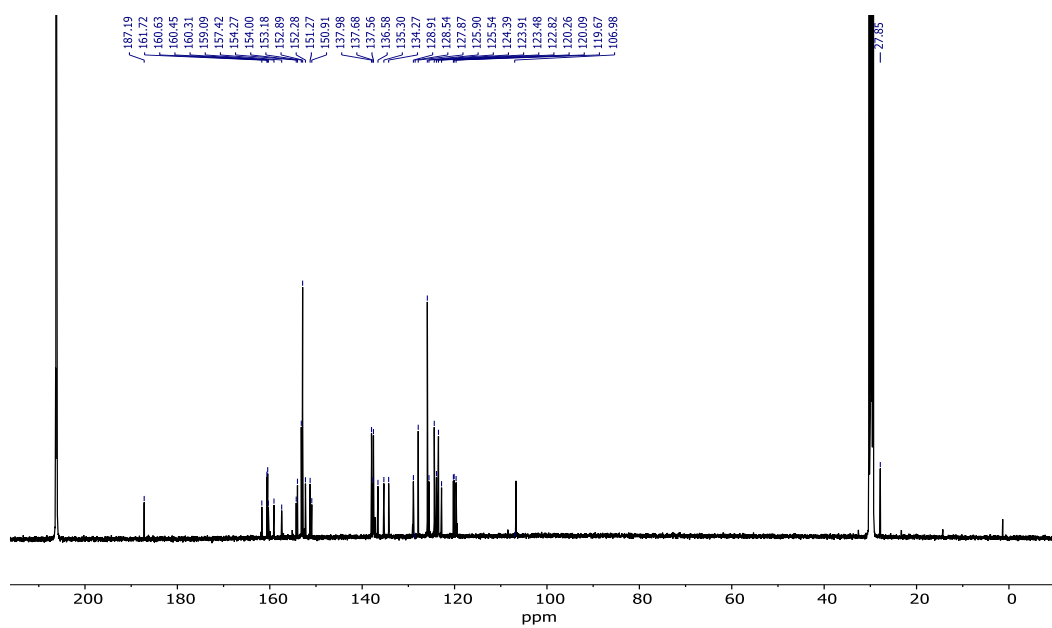
Figure A69. ^{13}C-NMR spectrum of **8** in acetone-d_6.
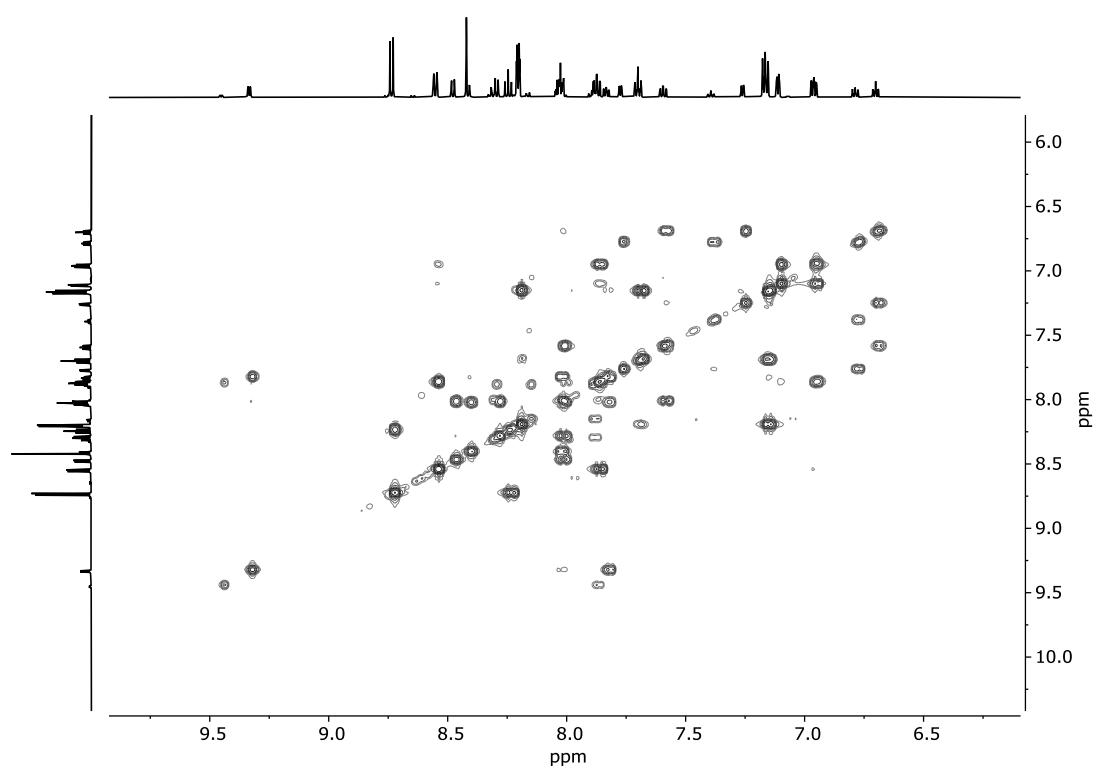
Figure A70. ^{1}H,^{1}H-COSY NMR spectrum of **8** in acetone-d_6.
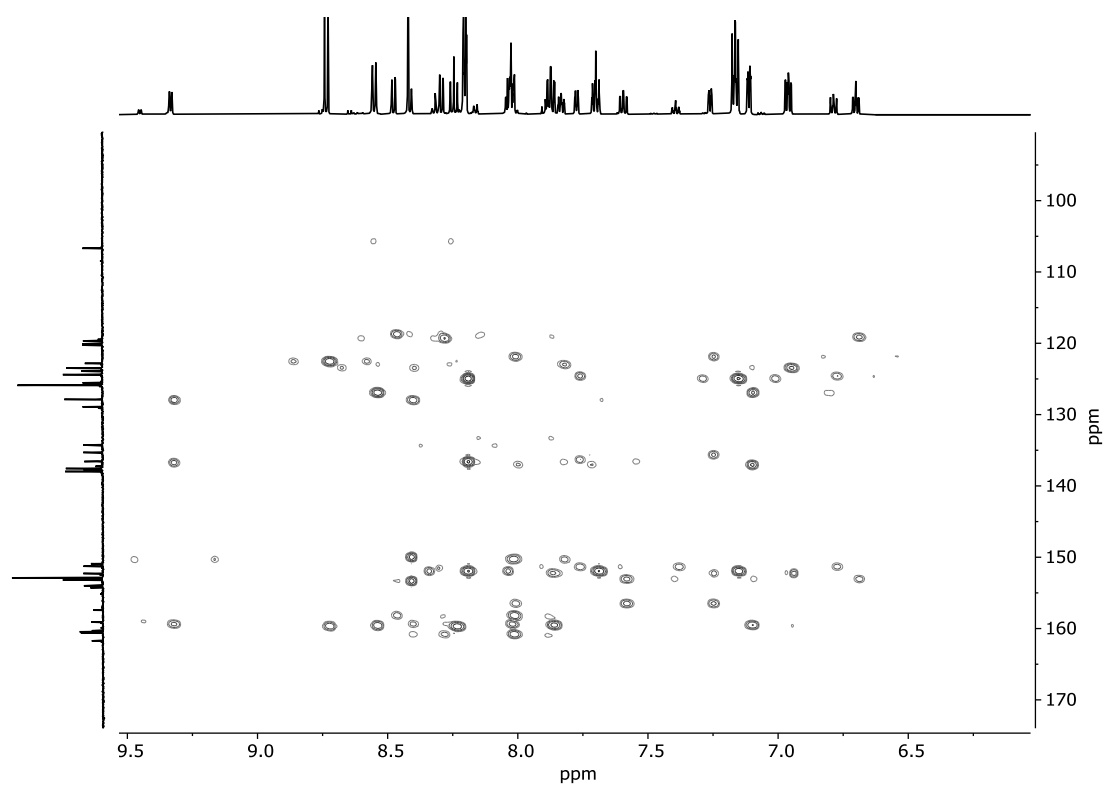
Figure A71. ^{1}H,^{13}C-HMBC NMR spectrum of **8** in acetone-d_6.
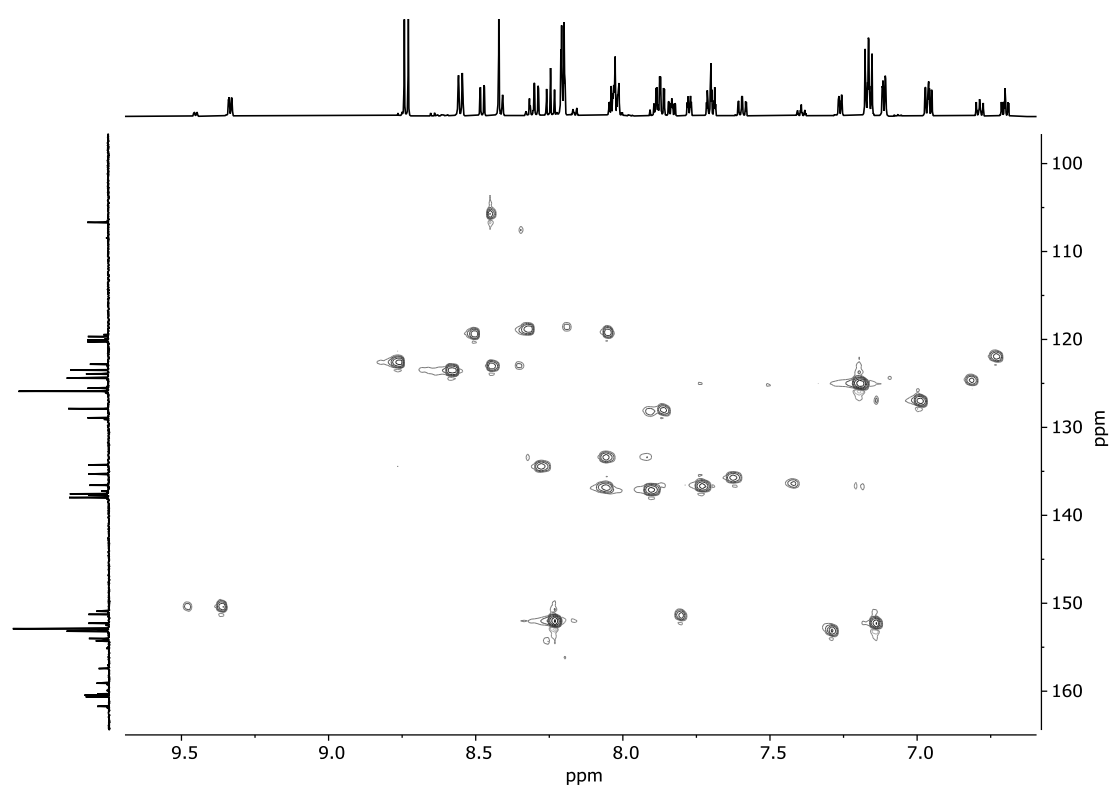
Figure A72. ^{1}H,^{13}C-HSQC NMR spectrum of **8** in acetone-d_6.

Mass Spectrometry
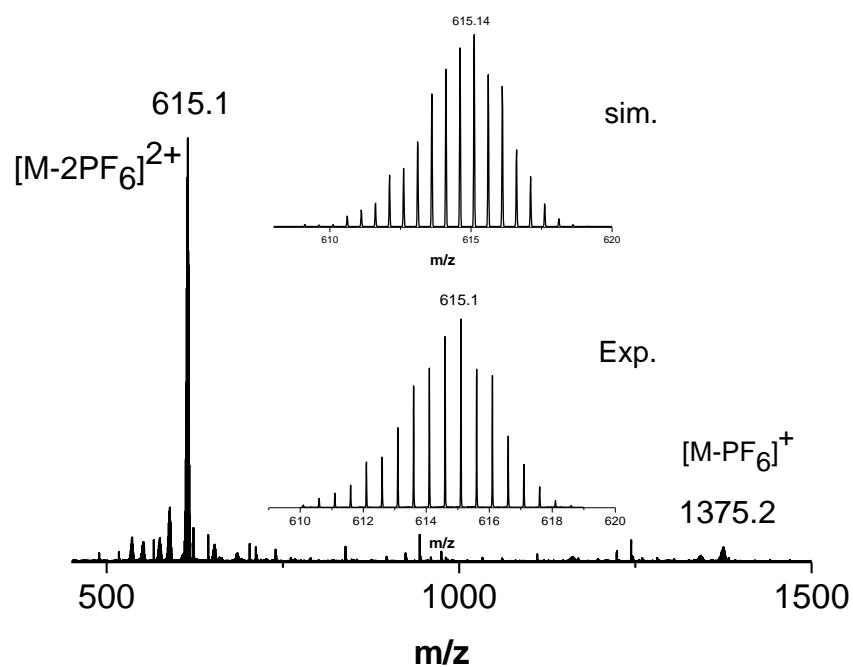
Figure A73. ESI-MS of **1^{pyr}** in methanol. The inset shows the expansion of the [M-2PF$_6$]$^{2+}$ peak and the simulation.*
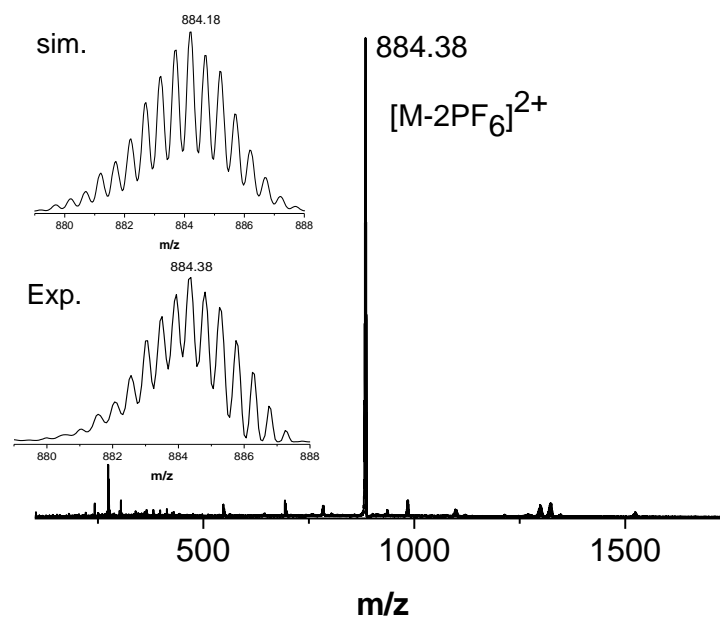
Figure A74. ESI-MS of **1^{4pyr}** in methanol. The inset shows the expansion of the [M-2PF$_6$]$^{2+}$ peak and the simulation.*
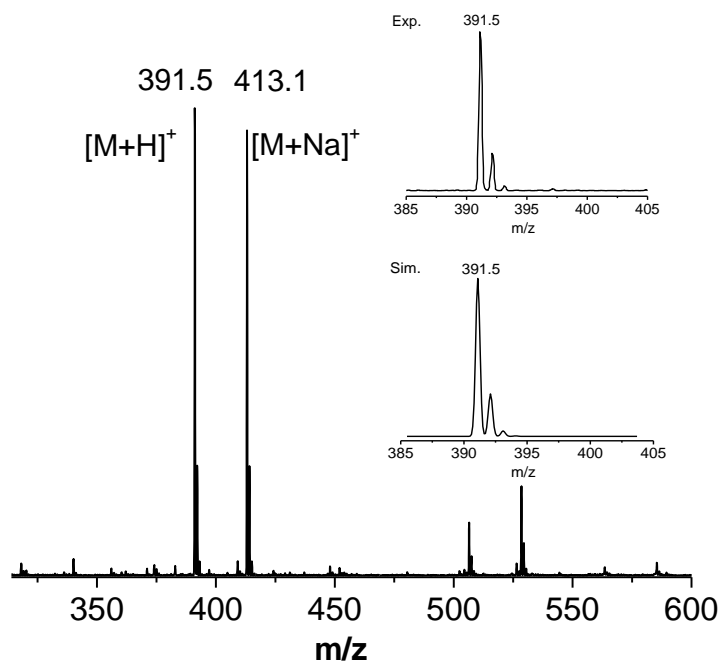
Figure A75. ESI(+)-MS of **H₂L²** in methanol. The isotopic patterns of the experimental and simulated corresponding to [M+H]⁺ signal is shown in inset.
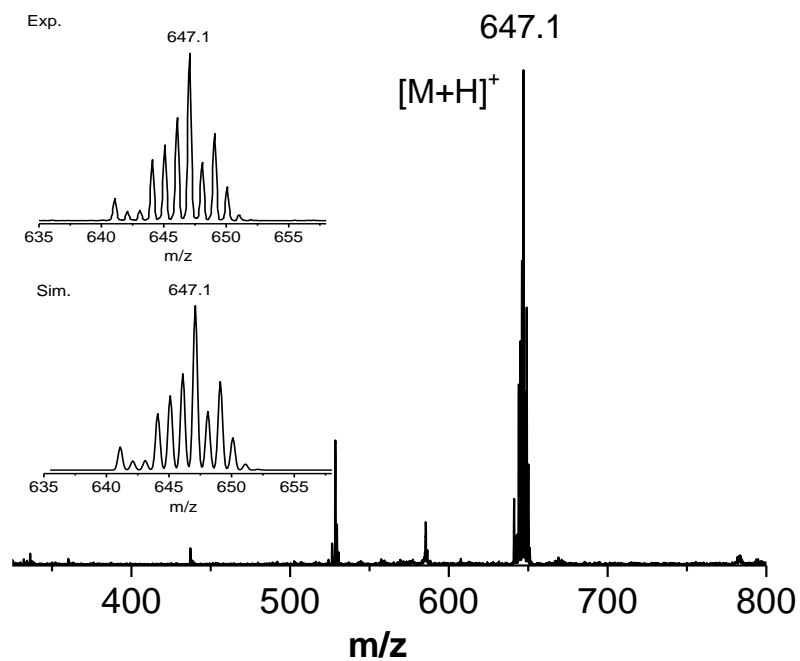
Figure A76. ESI-MS of **2** in methanol (positive mode). The inset displays the expansion of the [M+H]⁺ signal and the simulation.
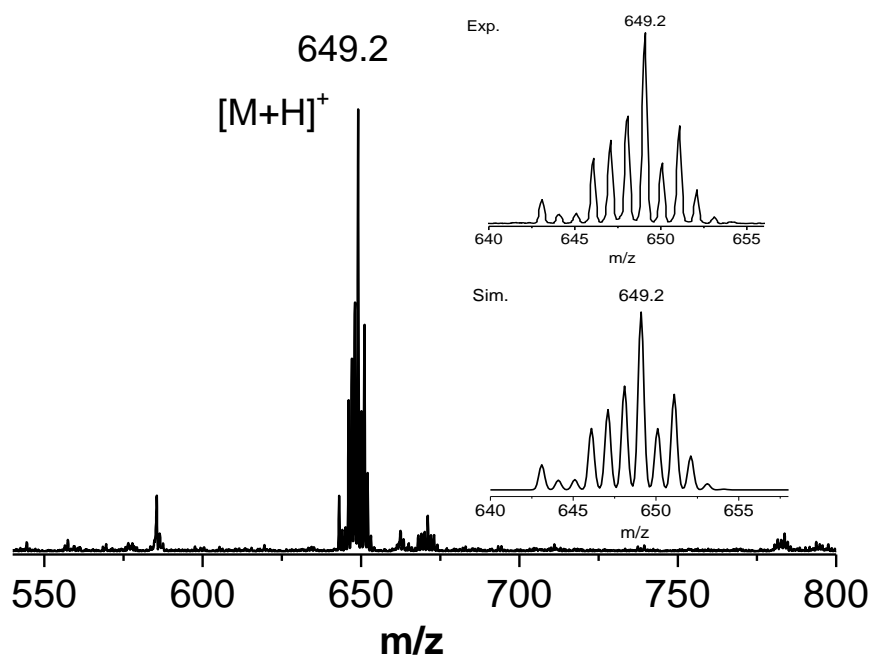
Figure A77. ESI-MS of **3** measured in methanol (positive mode). The inset exhibits the expansion of the [M+H]⁺ signal at 649.2 and the simulation.
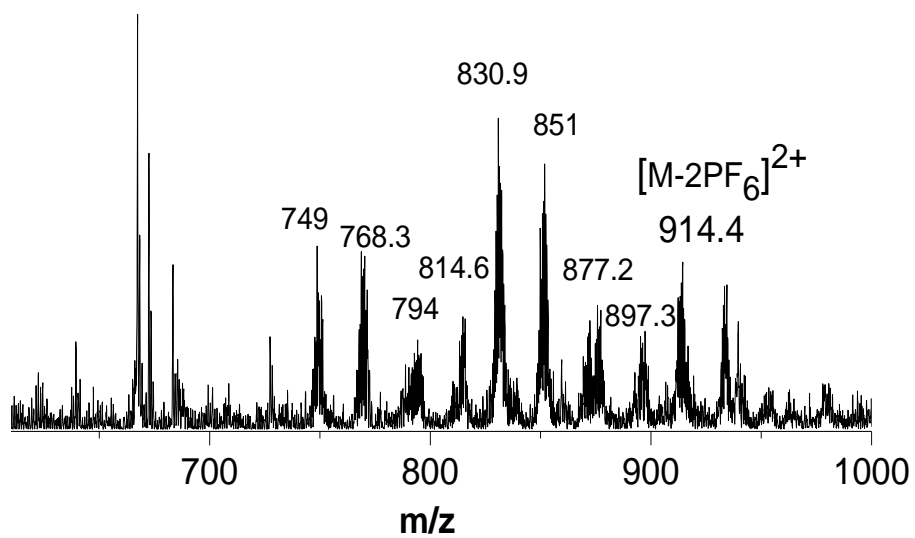
Figure A78. ESI-MS of **1^4Si(OEt)3** measured in THF (positive mode). Signals at *m/z* = 749, 768.3, 814, 830, 851, 877, and 897 are attributed to the hydrolyzed species.
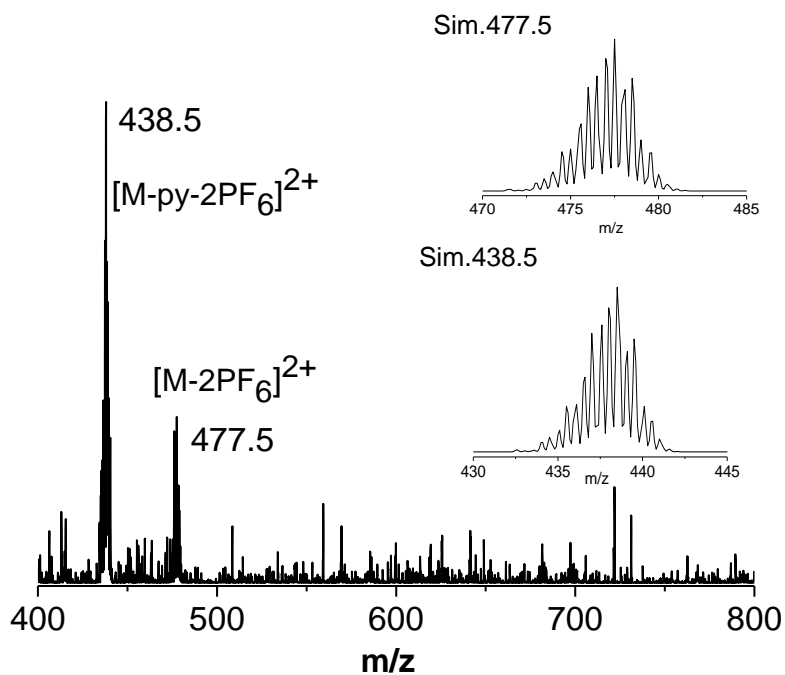
Figure A79. ESI(+)-MS of **7** in methanol displaying two dominant peaks at m/z= 438.5 and 477.5 corresponding to [M-py-2PF$_6$]$^{2+}$ and [M-2PF$_6$]$^{2+}$, respectively. Simulations are depicted in the inset.
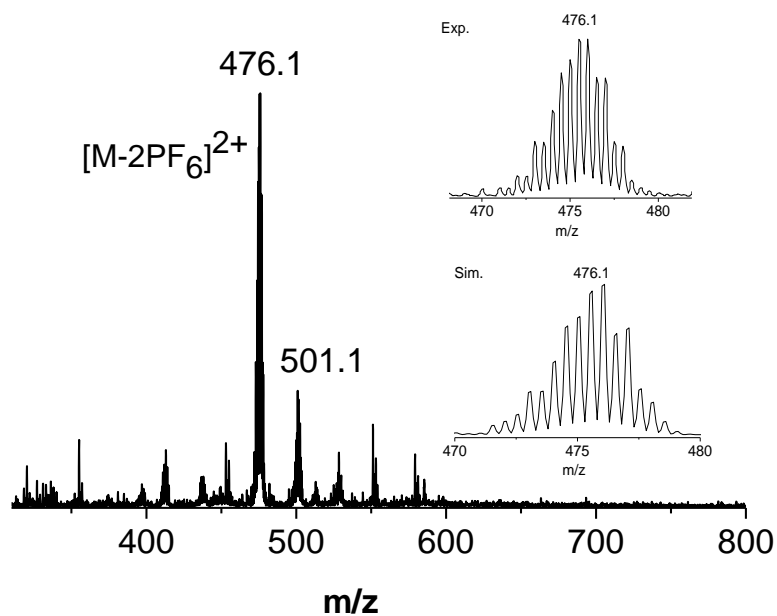
Figure A80. ESI(+)-MS of **8** in methanol displaying the dominant peak at m/z= 476.1 corresponding to [M-2PF$_6$]$^{2+}$. The peak at m/z= 501.1 could not be assigned. The Simulation is shown in the inset.

Electrochemical measurements
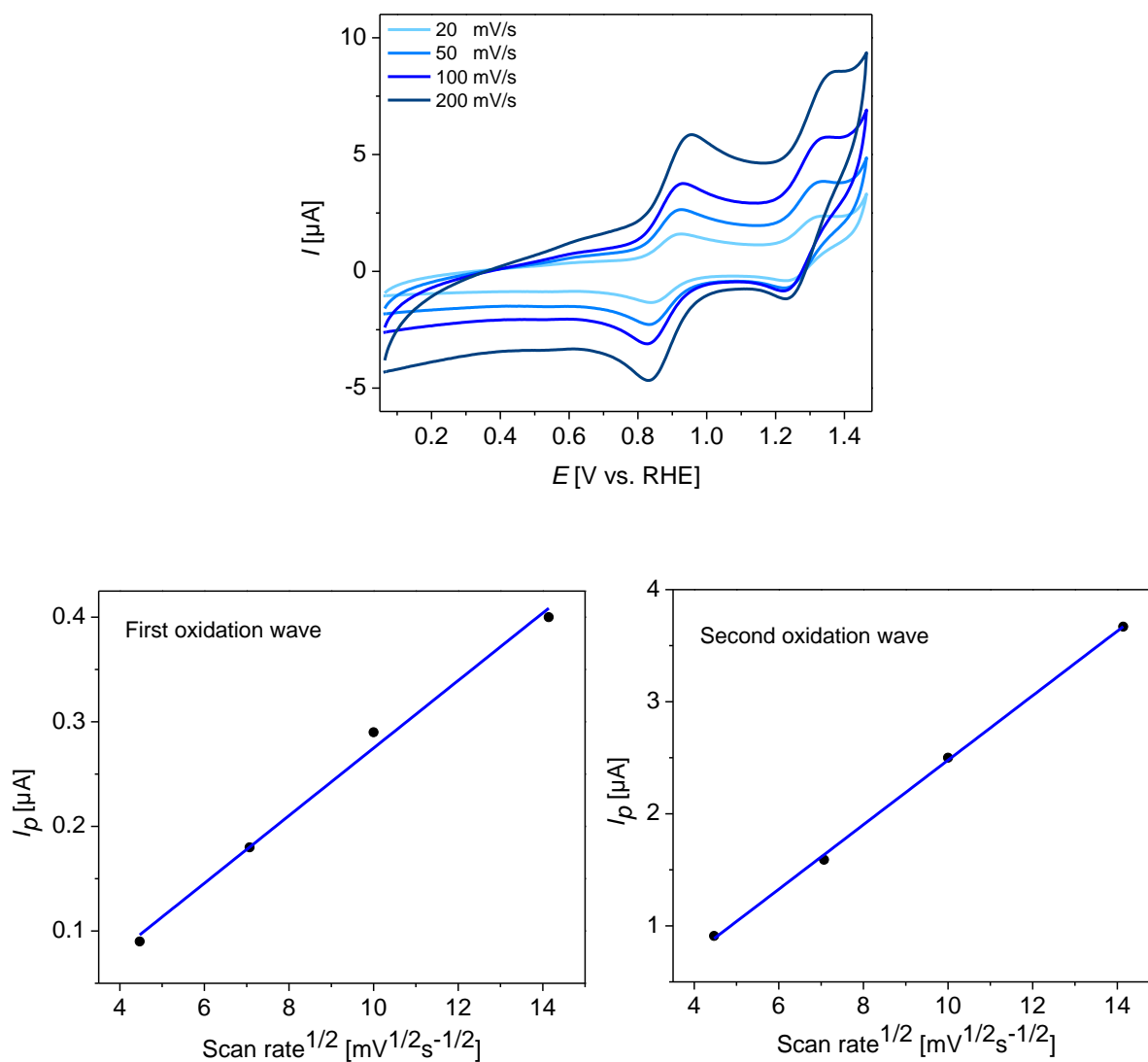
Figure A81. CV measurement of 1^{pyr} in PC (0.1M [$^nBu_4N$]PF_6) at four scan rates (20, 50, 100, 200 mV/s). WE: GC, CE: Pt, Ref. Ag wire (top).The dependency of the peak current to the square root of scan rate for the first and the second oxidation waves (bottom), indicating the reversibility of the two redox events. The potentials are reported versus RHE.
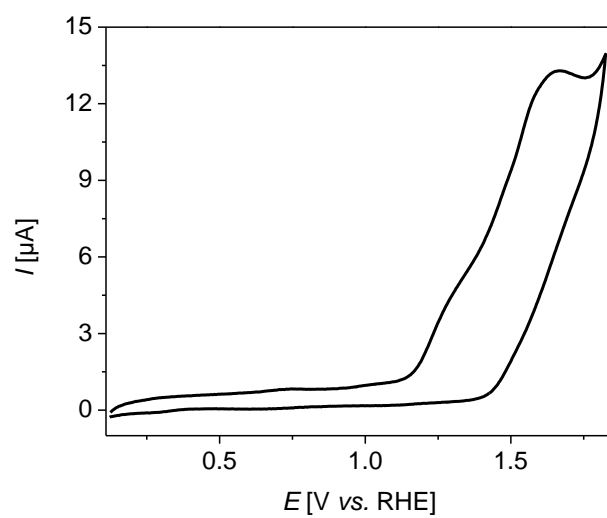
Figure A82. CV measurement of ^{pyr}**bbpH** measured in PC (0.1 M [^{n}Bu$_4$N]PF$_6$) at a scan rate of 50 mV/s. WE: GC, CE: Pt, Ref. MSE. The final potentials are reported versus RHE Scale.
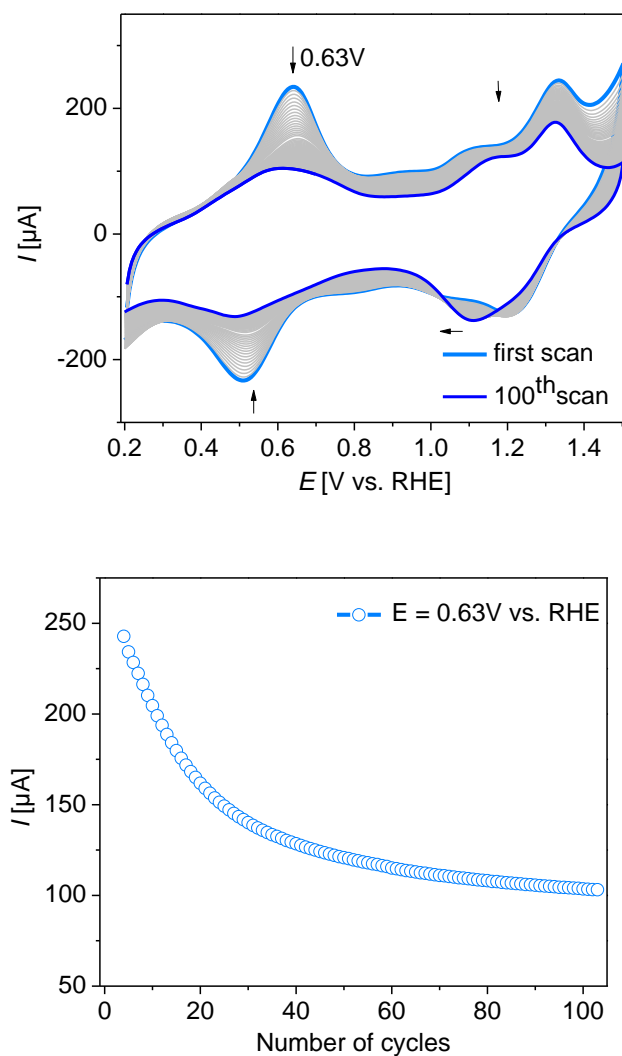
Figure A83. Repetitively measured CV of GC|MWCNTs|**1**^pyr (top) in aqueous HOTf (0.1 M, pH = 1) at a scan rate of 50 mV/s. leaching profile of the complex from the MWCNTs is plotted versus the number of CV cycles (bottom). CE: Pt, Ref. MSE. Final potentials are reported versus RHE scale.

196
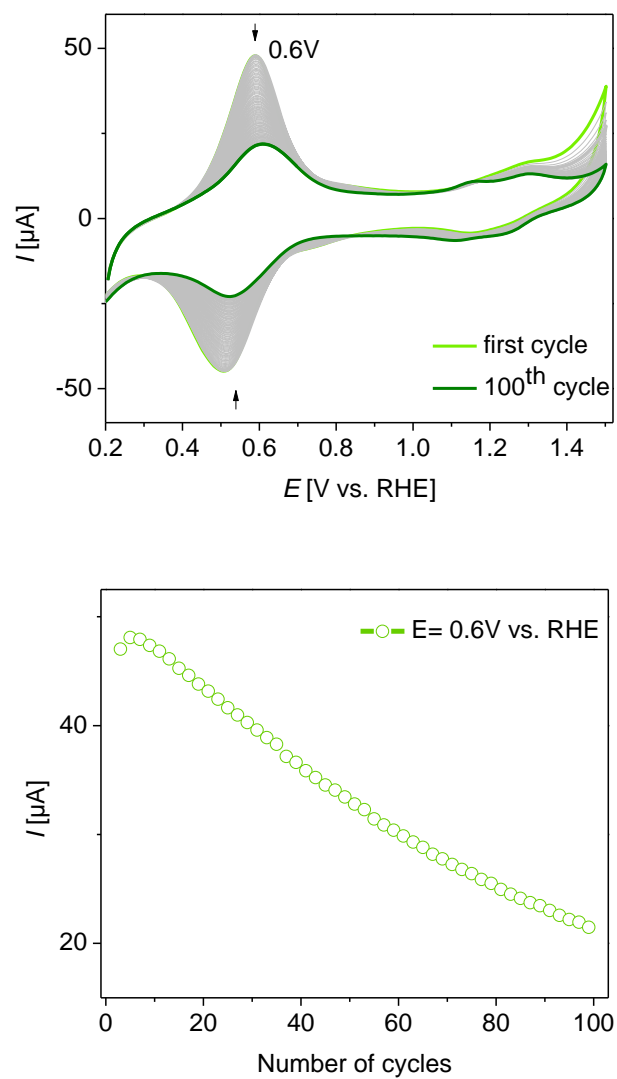
Figure A84. Repetitive CV measurement of GC|MWCNTs|**1**^{4pyr} (top) in aqueous HOTf (0.1 M, pH = 1) at a scan rate of 50 mV/s. The leaching profile of the complex from the surface is plotted versus the number of CV cycles (bottom). CE: Pt, Ref. MSE. Final potentials are reported versus RHE scale.
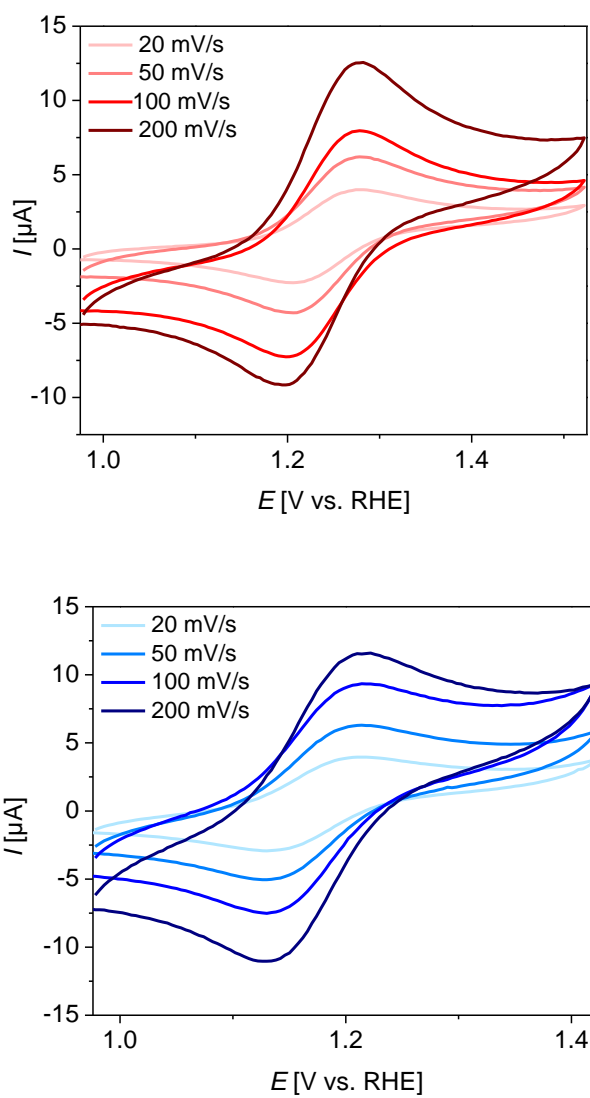
Figure A85. Cyclic voltammetry of **2** (top) and **3** (bottom) in 1:1 mixture of TFE and aqueous HOTf (pH = 1, 0.1 M) at various scan rates (20, 50, 100, 200 mV/s). WE: GC, CE: Pt, Ref. SCE. The final potentials are reported versus RHE Scale.
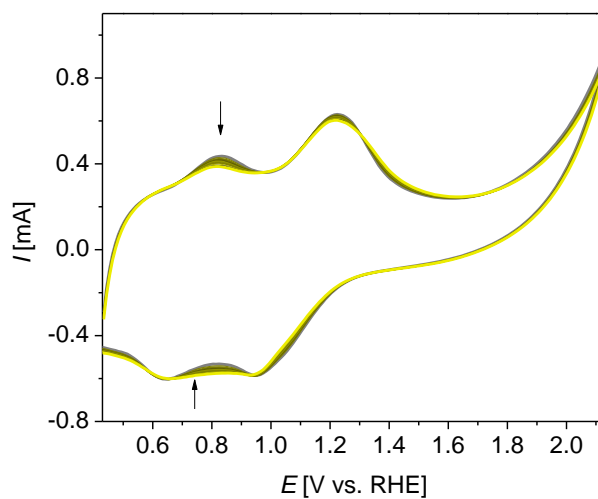
Figure A86. Repetitive CV measurement of ITO|*meso*ITO|**1**[4Si(OEt)3] implemented as working electrode at a scan rate of 50 mV/s in 0.1 M aqueous HOTf (pH = 1). CE: Pt, Ref. MSE. The final potentials are reported versus RHE Scale.
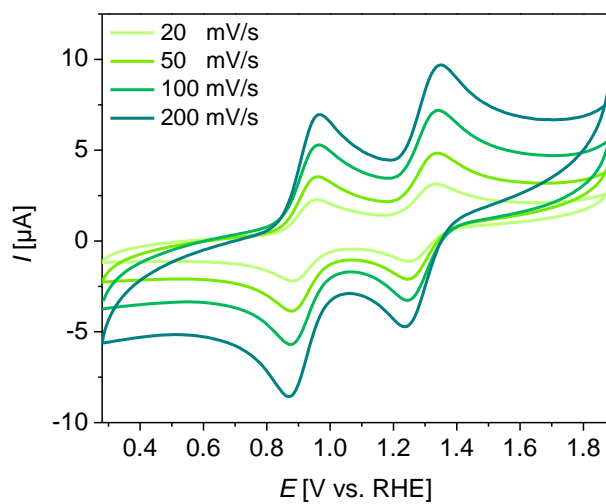
Figure A87. CV measurement of **8** in propylene carbonate (0.1M [^{n}Bu$_4$N]PF$_6$) at various scan rates (20, 50, 100, 200 mV/s). WE: GC, CE: Pt, Ref. Ag wire. The potentials are reported versus RHE.

X-ray Photoelectron Spectroscopy
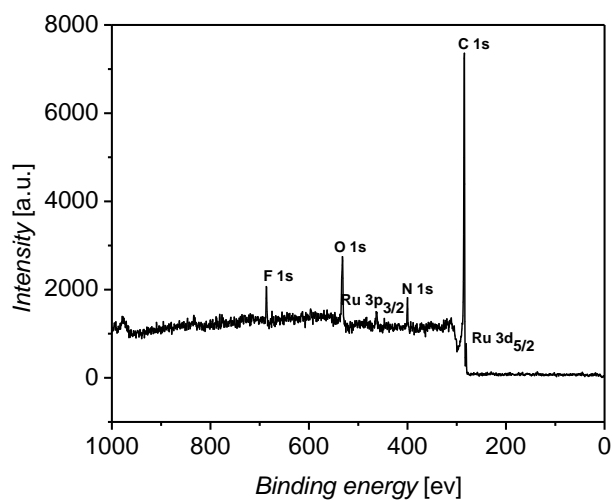
Figure A88. XPS survey spectra of complex **1**^{pyr} immobilized on MWCNT (GC|MWCNTs|**1**^{pyr}) before any electrochemical measurement (pristine sample).
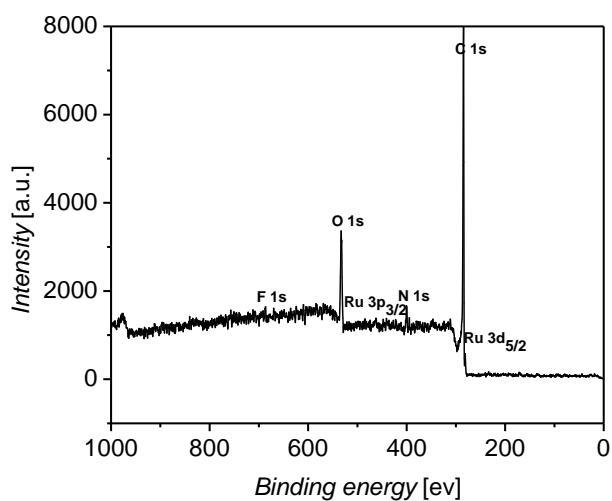
Figure A89. XPS survey spectra of complex **1**^{4pyr} immobilized on MWCNT (GC|MWCNTs|**1**^{4pyr}) before any electrochemical measurement (pristine sample).

Table A1. Stoichiometry determined by survey spectra of GC|MWCNTs|1^{pyr} and GC|MWCNTs|1^{4pyr}.

Element	GC|MWCNT|1^{4pyr} Pristine	GC|MWCNT|1^{4pyr} After CA	GC|MWCNT|1^{4pyr} Reference	GC|MWCNT |1^{pyr} Pristine	GC|MWCNT |1^{pyr} After 1min CA	GC|MWCNT|1^{pyr} Reference
O1s	12.93±0.47	13.88±0.42	13.93±0.60	8.86±0.42	13.12±0.48	12.10±0.80
C1s	84.74±0.52	83.88±0.48	77.83±0.74	85.90±0.6	82.82±0.61	80.25±1.38
Ru3d	0.31±0.04	0.28±0.03	0.59±0.07	0.73±0.06	0.58±0.06	0.69±0.20
N1s	1.59±0.22	1.53±0.23	3.67±0.48	3.91±0.44	3.51±0.43	5.04±1.28
F 1s	0.44±0.10	0.43±0.11	3.89±0.278	0.61±0.108	0.19±0.06	1.12±0.21
N/Ru	5.13±1.06	5.46±1.09	6.22±1.24	5.35±1.07	6.05±2.08	7.36±2.2
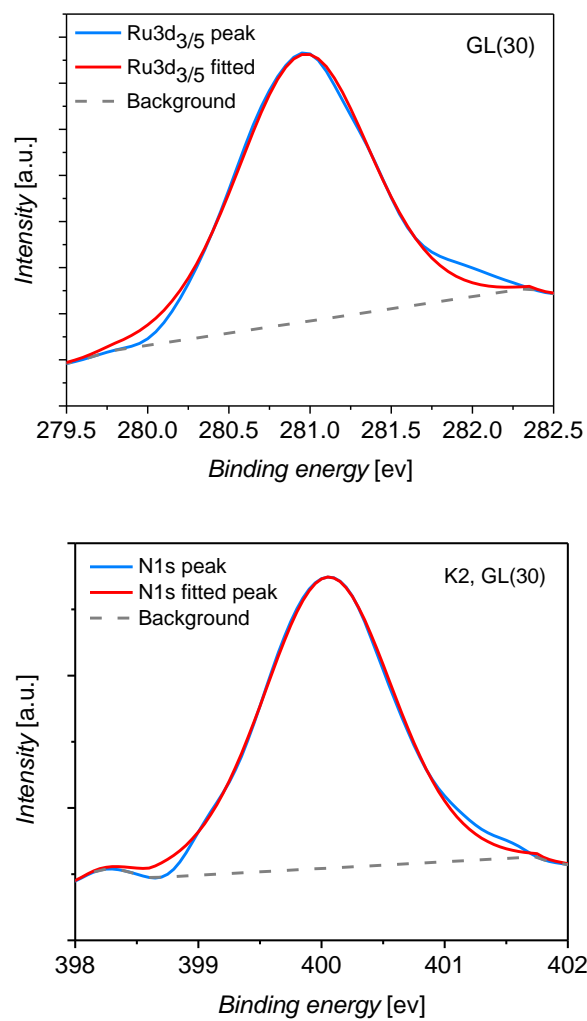
Figure A90. XPS detail scans of the core level spectra of the Ru(3d) (top) and N(1s) of GC|MWCNT|**1**^{pyr} with Gaussian lorentzian fitted curve and linear background.
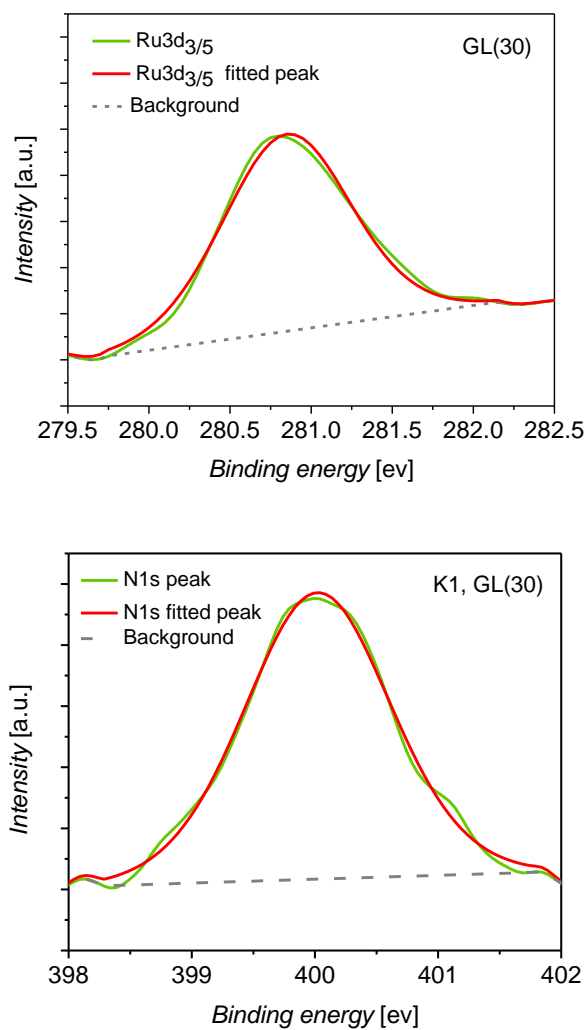
Figure A91. XPS detail scans of the core level spectra of the Ru(3d) (top) and N(1s) of GC|MWCNT|**1**[4pyr] with Gaussian lorentzian fitted curve and linear background.

GC Analysis
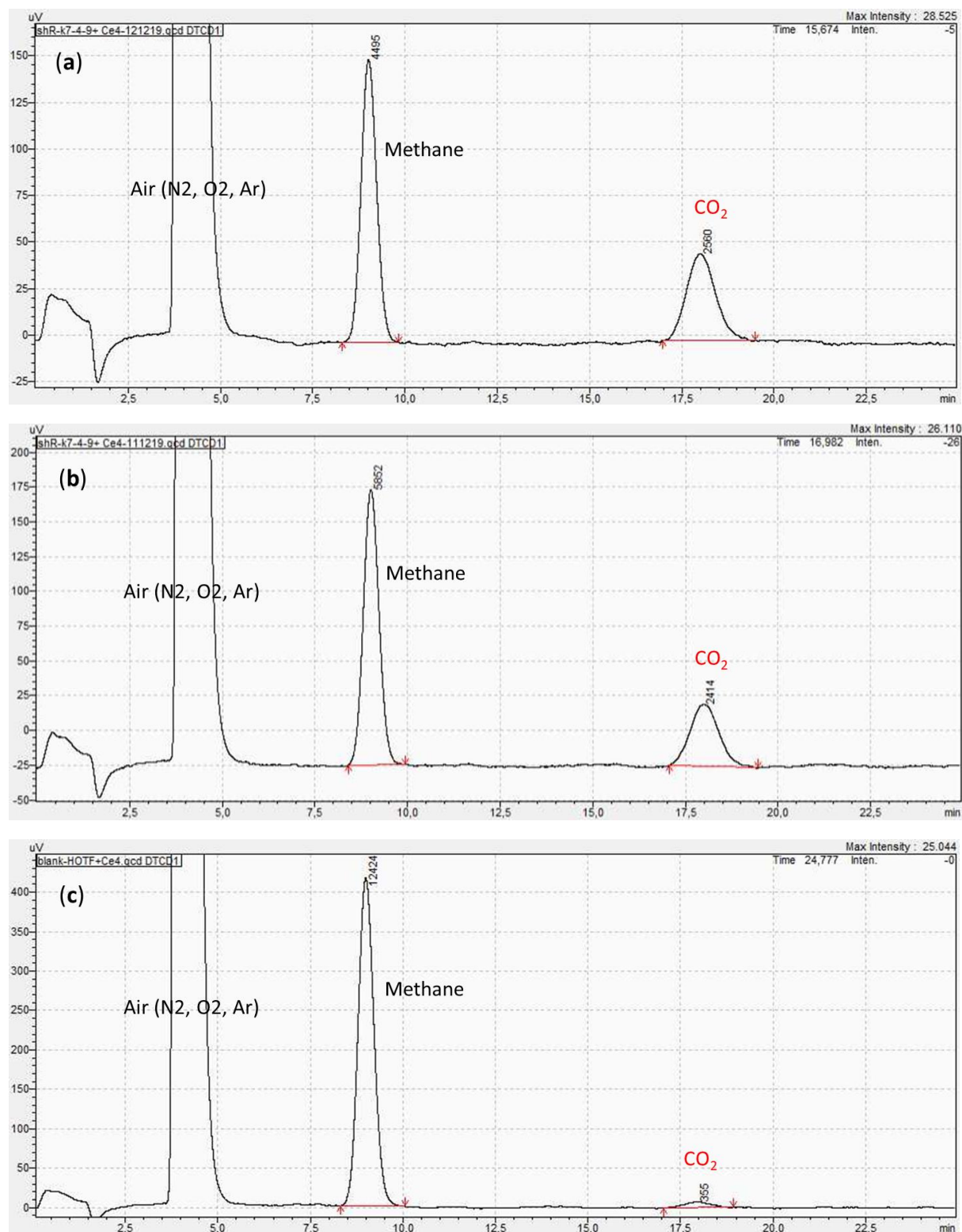
Figure A92. GC headspace analysis after chemical water oxidation experiment of **2** in aqueous HOTf (0.1 M, pH = 1) (a,b), of blank (without complex) (c). Methane has been added for calibration. The average values in experiments of a and b are reported as an amount of CO_2.

X-Ray crystallography
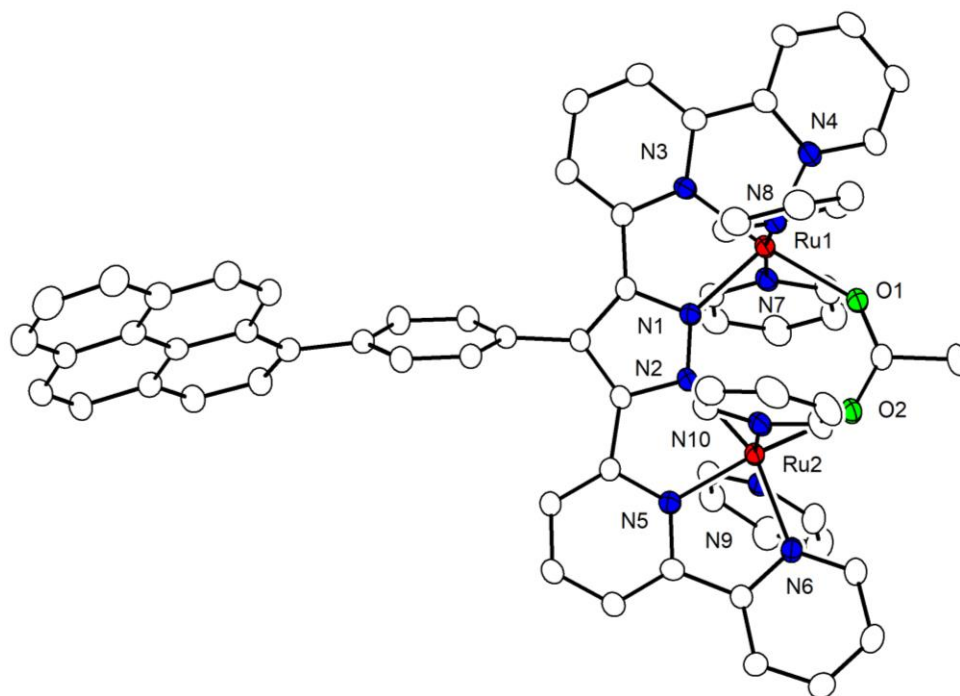
Figure A93. Plot (30% probability thermal ellipsoids) of the molecular structure of the cationic part of **1^pyr** (hydrogen atoms omitted for clarity). Only one of the two crystallographically independent molecules is shown. Selected bond lengths [Å] and angles [°]: Ru1–N3 1.954(3), Ru1–N1 2.021(3), Ru1–N4 2.074(3), Ru1–N8 2.080(3), Ru1–N7 2.092(3), Ru1–O1 2.122(2), Ru2–N5 1.947(3), Ru2–N2 2.012(3), Ru2–N6 2.074(3), Ru2–N10 2.089(3), Ru2–N9 2.096(3), Ru2–O2 2.110(2), Ru1···Ru2 4.2155(5); N3–Ru1–N1 78.44(11), N3–Ru1–N4 79.85(12), N1–Ru1–N4 158.25(12), N3–Ru1–N8 91.72(12), N1–Ru1–N8 90.71(12), N4–Ru1–N8 91.30(12), N3–Ru1–N7 96.35(12), N1–Ru1–N7 91.10(12), N4–Ru1–N7 89.93(12), N8–Ru1–N7 171.93(12), N3–Ru1–O1 173.52(11), N1–Ru1–O1 106.73(10), N4–Ru1–O1 95.02(11), N8–Ru1–O1 84.40(11), N7–Ru1–O1 87.55(11), N5–Ru2–N2 78.72(12), N5–Ru2–N6 80.42(12), N2–Ru2–N6 159.13(11), N5–Ru2–N10 91.39(12), N2–Ru2–N10 92.03(12), N6–Ru2–N10 88.13(12), N5–Ru2–N9 93.34(12), N2–Ru2–N9 91.45(12), N6–Ru2–N9 90.09(12), N10–Ru2–N9 174.60(12), N5–Ru2–O2 174.11(11), N2–Ru2–O2 107.15(10), N6–Ru2–O2 93.71(11), N10–Ru2–O2 87.94(11), N9–Ru2–O2 87.09(11).

Table A2. Crystal data and refinement details for **1^{pyr}**.

	1^{pyr}
empirical formula	$C_{70.50}H_{58}F_{12}N_{10}O_3P_2Ru_2$
moiety formula	$C_{67}H_{50}N_{10}O_2Ru_2^{2+}$, $2(F_6P^-)$, $0.5(C_4H_{10}O)$, $0.5(C_3H_6O)$
formula weight	1585.35
crystal size [mm³]	0.29 x 0.20 x 0.16
crystal system	triclinic
space group	*P*–1 (No. 2)
a [Å]	14.2194(3)
b [Å]	20.0432(4)
c [Å]	26.3213(6)
α [°]	83.352(2)
β [°]	79.323(2)
γ [°]	87.701(2)
V [Å³]	7320.9(3)
Z	4
ρ [g·cm⁻³]	1.438
F(000)	3204
μ [mm⁻¹]	0.539
T_{min} / T_{max}	0.8168 / 0.9260
θ-range [°]	1.223 - 25.774
hkl-range	–15 to 17, ±24, ±32
measured refl.	81052
unique refl. [R_{int}]	27613 [0.0351]
observed refl. ($I > 2\sigma(I)$)	21216
data / restr. / param.	27613 / 1251 / 1954
goodness-of-fit (*F*²)	1.012
*R*1, *wR*2 ($I > 2\sigma(I)$)	0.0437 / 0.1028
*R*1, *wR*2 (all data)	0.0637 / 0.1126
res. el. dens. [e·Å⁻³]	–0.772 / 1.143

Table A3. Selected distances [Å] and angles [°].

	1^{pyr}
Ru–N	1.947(3) - 2.101(3)
Ru–O	2.110(2) - 2.134(2)
Ru···Ru	4.2054(6) / 4.2155(5)
N/O–Ru–N (> 150°)	158.25(12) - 175.33(11)
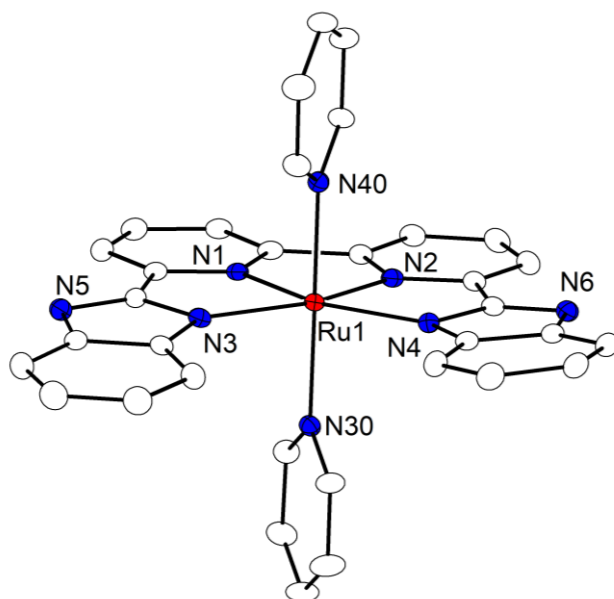
Figure A94. Plot (30% probability thermal ellipsoids) of the molecular structure of **2** (hydrogen atoms omitted for clarity). Selected bond lengths [Å] and angles [°]: Ru1–N1 1.967(3), Ru1–N2 1.963(3), Ru1–N3 2.133(3), Ru1–N4 2.145(3), Ru1–N30 2.092(3), Ru1–N40 2.086(3); N2–Ru1–N1 80.43(14), N2–Ru1–N40 91.54(13), N1–Ru1–N40 90.89(13), N2–Ru1–N30 92.11(13), N1–Ru1–N30 92.52(13), N40–Ru1–N30 175.37(13), N2–Ru1–N3 158.91(13), N1–Ru1–N3 78.49(13), N40–Ru1–N3 89.51(13), N30–Ru1–N3 88.11(12), N2–Ru1–N4 78.67(13), N1–Ru1–N4 159.06(14), N40–Ru1–N4 88.35(13), N30–Ru1–N4 89.58(13).

Table A4. Crystal data and refinement details for **2**.

	2
empirical formula	$C_{36}H_{26}Cl_6N_8Ru$
moiety formula	$C_{34}H_{24}N_8Ru$, $2(CHCl_3)$
formula weight	884.42
crystal size [mm³]	0.381 x 0.230 x 0.116
crystal system	monoclinic
space group	$P2_1/c$ (No. 14)
a [Å]	16.4139(14)
b [Å]	11.9008(5)
c [Å]	18.0764(14)
α [°]	90
β [°]	91.101(6)
γ [°]	90
V [Å³]	3530.4(4)
Z	4
ρ [g·cm⁻³]	1.664
$F(000)$	1776
μ [mm⁻¹]	0.940
T_{min} / T_{max}	0.5170 / 0.6811
θ-range [°]	2.049 – 26.880
hkl-range	±20, ±15, −20 to 22
measured refl.	41689
unique refl. [R_{int}]	7481 [0.0453]
observed refl. ($I > 2\sigma(I)$)	6252
data / restr. / param.	7481 / 0 / 460
goodness-of-fit (F^2)	1.086
$R1$, $wR2$ ($I > 2\sigma(I)$)	0.0480 / 0.1431
$R1$, $wR2$ (all data)	0.0603 / 0.1534
res. el. dens. [e·Å⁻³]	−1.478 / 1.793
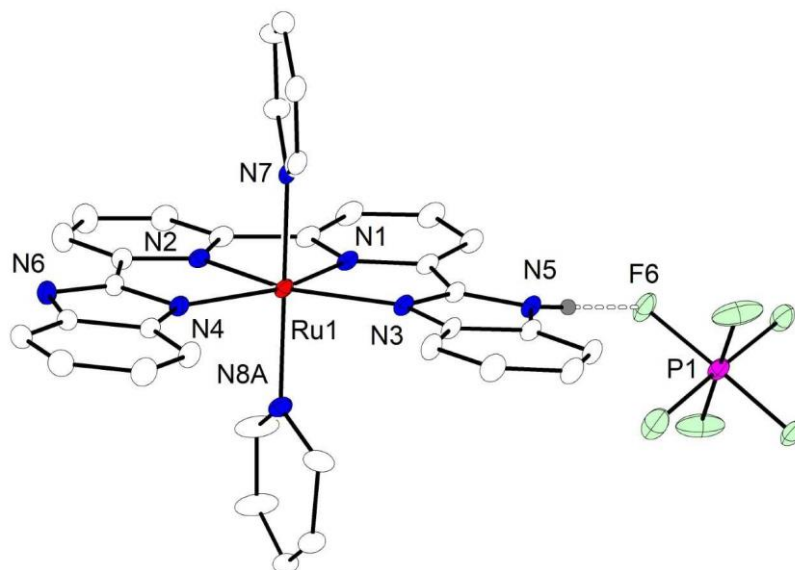
Figure A95. Molecular structure of **[2H]PF₆** (hydrogen atoms omitted for clarity except for the imidazole rings). Selected bond lengths [Å] and angles [°]: Ru(1)-N(1) 1.9545(16), Ru(1)-N(2) 1.9629(15), Ru(1)-N(7) 2.0838(15), Ru(1)-N(8A) 2.1085(17), Ru(1)-N(4) 2.1581(15), Ru(1)-N(3) 2.1791(15), N(1)-Ru(1)-N(2) 80.21(7), N(1)-Ru(1)-N(7) 93.25(6), N(2)-Ru(1)-N(7) 90.75(6), N(1)-Ru(1)-N(8A) 90.21(6), N(2)-Ru(1)-N(8A) 92.00(6), N(7)-Ru(1)-N(8A) 175.91(6), N(1)-Ru(1)-N(4) 158.30(6), N(2)-Ru(1)-N(4) 78.08(6), N(7)-Ru(1)-N(4) 86.97(6), N(8A)-Ru(1)-N(4) 90.63(6), N(1)-Ru(1)-N(3) 78.15(6), N(2)-Ru(1)-N(3) 158.25(6), N(7)-Ru(1)-N(3) 88.38(6), N(8A)-Ru(1)-N(3) 90.19(6), N(4)-Ru(1)-N(3) 123.54(6).

Table A5. Crystal data and refinement details for **[2H]PF$_6$**.

	[2H]PF$_6$
empirical formula	$C_{34}H_{25}F_6N_8PRu$
formula weight	791.66
T [K]	100(2) K
Wavelength	0.71073 Å
crystal size [mm³]	0.230 x 0.133 x 0.050
crystal system	monoclinic
space group	P2$_1$/c
a [Å]	10.4368(6)
b [Å]	14.2525(8)
c [Å]	24.3119(14)
α [°]	90
β [°]	96.107(2)°
γ[°]	90
V [Å³]	9276(2)
Z	4
ρ [g·cm^{-3}]	1.462
F(000)	1592
μ [mm^{-1}]	0.548
T_{min} / T_{max}	0.93 /0.97
θ-range [°]	2.257 – 27.279
Index ranges	-13<=h<=13, -18<=k<=18, -31<=l<=31
Reflections collected	88245
Independent reflections	8587 [R(int) = 0.0390]
Completeness to theta = 25.242°	100.0 %
Absorption correction	Semi-empirical from equivalents
Refinement method	Full-matrix least-squares on F^2
Data / restraints / parameters	8587 / 66 / 503
Goodness-of-fit on F^2	1.014
Extinction coefficient	n/a
Largest diff. peak and hole	0.678 and -0.706 e.Å^{-3}
Final R indices [I>2sigma(I)]	R1 = 0.0292, wR2 = 0.0702
R indices (all data)	R1 = 0.0343, wR2 = 0.0730
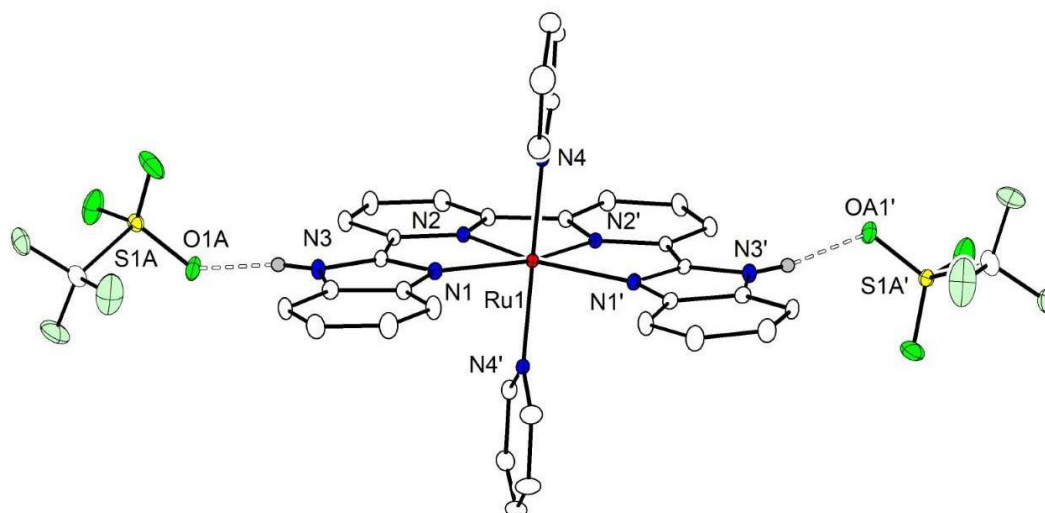
Figure A96. Molecular structure of **[2H₂](CF₃SO₃)₂** (hydrogen atoms omitted for clarity except for the imidazole rings). Selected bond lengths [Å] and angles [°]: Ru(1)-N(2) 1.959(3), Ru(1)-N(2)' 1.959(3), Ru(1)-N(4) 2.096(3), Ru(1)-N(4)' 2.096(3), Ru(1)-N(1) 2.169(3), Ru(1)-N(1)' 2.169(3), N(2)-Ru(1)-N(2)' 80.45(16), N(2)-Ru(1)-N(4) 93.41(12), N(2)' -Ru(1)-N(4) 91.05(11), N(2)-Ru(1)-N(4)' 91.05(11), N(2)'-Ru(1)-N(4)' 93.42(12), N(4)-Ru(1)-N(4)' 174.2(2), N(2)-Ru(1)-N(1) 78.20(12), N(2)'-Ru(1)-N(1) 158.65(11), N(4)Ru(1)-N(1) 89.72(11), N(4)'-Ru(1)-N(1) 87.50(11), N(2)-Ru(1)-N(1)' 158.65(11), N(2)'-Ru(1)-N(1)' 78.20(12), N(4)-Ru(1)-N(1)' 87.50(11), N(4)'-Ru(1)-N(1)' 89.72(11), N(1)-Ru(1)-N(1)' 123.15(15).

Table A6. Crystal data and refinement details for **[2H$_2$](CF$_3$SO$_3$)$_2$**.

	[2H$_2$](CF$_3$SO$_3$)$_2$
empirical formula	C$_{36}$H$_{26}$F$_6$N$_8$O$_6$RuS$_2$
formula weight	945.84
T [K]	100(2) K
Wavelength	0.71073 Å
crystal size	0.274 x 0.223 x 0.196 mm^3
crystal system	Orthorhombic
space group	Fdd2
a [Å]	16.3145(9)
b [Å]	37.428(2)
c [Å]	12.1759(7)
α [°]	90
β [°]	90
γ[°]	90
V [Å^3]	7434.9(7)
Z	8
ρ[g·cm^{-3}]	1.690
Absorption coefficient [mm^{-1}]	0.624 mm^{-1}
F(000)	3808
μ [mm^{-1}]	0.548
T_{min} / T_{max}	0.93 /0.97
θ-range [°]	2.157-27.882
Index ranges	-21<=h<=21, -47<=k<=49, -12<=l<=16
Reflections collected	16721
Independent reflections	3896 [R(int) = 0.0254]
Completeness to theta = 25.242°	99.5 %
Max. and min. transmission	0.89 and 0.81
Absorption correction	Semi-empirical from equivalents
Refinement method	Full-matrix least-squares on F^2
Data / restraints / parameters	3896 / 20 / 332
Goodness-of-fit on F^2	1.112
Extinction coefficient	n/a
Largest diff. peak and hole	0.550 and -0.477 e.Å^{-3}
Final R indices [I>2sigma(I)]	R1 = 0.0245, wR2 = 0.0580

|	
R indices (all data)	R1 = 0.0246, wR2 = 0.0581
Absolute structure parameter	0.023(8)
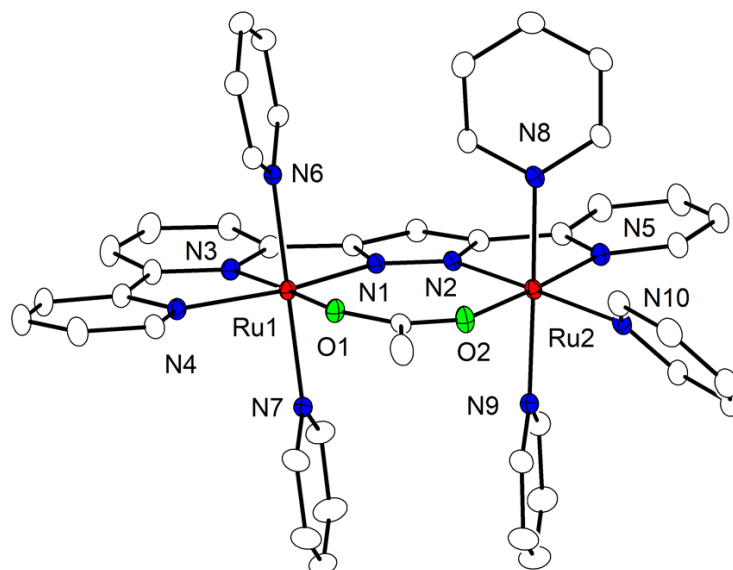
Figure A97. Plot (30% probability thermal ellipsoids) of the molecular structure of **7** (hydrogen atoms omitted for clarity). Selected bond lengths [Å] and angles [°]: Ru1–N3 1.9467(17), Ru1–N1 2.0329(16), Ru1–N4 2.0555(17), Ru1–N7 2.0930(18), Ru1–N6 2.0949(18), Ru1–O1 2.0990(14), Ru2–N2 2.0226(17), Ru2–N5 2.0556(17), Ru2–N8 2.0763(18), Ru2–N9 2.0909(19), Ru2–N10 2.1055(18), Ru2–O2 2.1097(15), Ru1···Ru2 4.2614(6); N3–Ru1–N1 79.58(7), N3–Ru1–N4 80.15(7), N1–Ru1–N4 159.73(7), N3–Ru1–N7 93.67(7), N1–Ru1–N7 89.64(7), N4–Ru1–N7 91.81(7), N3–Ru1–N6 89.46(7), N1–Ru1–N6 92.47(7), N4–Ru1–N6 87.18(7), N7–Ru1–N6 176.50(7), N3–Ru1–O1 172.46(6), N1–Ru1–O1 107.62(6), N4–Ru1–O1 92.63(6), N7–Ru1–O1 88.68(6), N6–Ru1–O1 88.03(6), N2–Ru2–N5 78.21(7), N2–Ru2–N8 90.73(7), N5–Ru2–N8 89.00(7), N2–Ru2–N9 89.84(7), N5–Ru2–N9 93.28(7), N8–Ru2–N9 177.72(7), N2–Ru2–N10 175.75(7), N5–Ru2–N10 98.80(7), N8–Ru2–N10 92.24(7), N9–Ru2–N10 87.31(7), N2–Ru2–O2 102.02(6), N5–Ru2–O2 177.15(7), N8–Ru2–O2 88.16(7), N9–Ru2–O2 89.57(7), N10–Ru2–O2 81.12(6).

Table A7. Crystal data and refinement details for **7**.

	7
empirical formula	$C_{50.50}H_{53}F_{12}N_{10}O_{3.50}P_2Ru_2$
moiety formula	$C_{45}H_{40}N_{10}O_2Ru_2^{2+}$, $2(F_6P^-)$, $C_4H_{10}O$, $0.5(C_3H_6O)$
formula weight	1348.11
T [K]	120(2)
crystal size [mm³]	0.253 x 0.205 x 0.177
crystal system	monoclinic
space group	$P2_1/n$ (No. 14)
a [Å]	12.6619(5)
b [Å]	18.5301(7)
c [Å]	23.1578(9)
α [°]	90
β [°]	99.5880(10)
γ [°]	90
V [Å³]	99.5880(10)
Z	4
ρ [g·cm⁻³]	1.671
$F(000)$	2720
μ [mm⁻¹]	0.720
T_{min} / T_{max}	0.82 / 0.88
θ-range [°]	2.044 – 27.902
hkl-range	±16, ±24, ±30
measured refl.	157201
unique refl. [R_{int}]	12808 [0.0547]
observed refl. ($I > 2\sigma(I)$)	10974
data / restr. / param.	12808 / 259 / 856
goodness-of-fit (F^2)	1.077
$R1$, $wR2$ ($I > 2\sigma(I)$)	0.0298 / 0.0668
$R1$, $wR2$ (all data)	0.0399 / 0.0733
res. el. dens. [e·Å⁻³]	−0.615 / 0.700
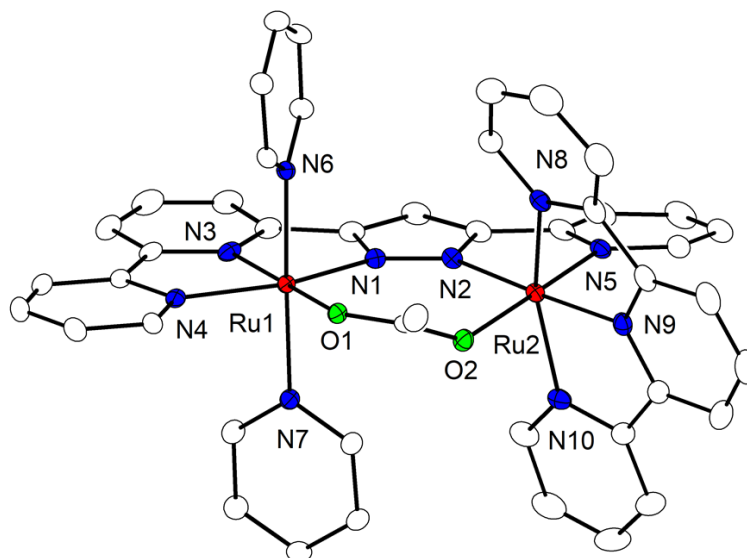
Figure A98. Plot (30% probability thermal ellipsoids) of the molecular structure of shr_k10_10 (hydrogen atoms omitted for clarity). Selected bond lengths [Å] and angles [°]: Ru1–N3 1.944(3), Ru1–N1 2.044(3), Ru1–N4 2.051(3), Ru1–N7 2.097(3), Ru1–N6 2.099(3), Ru1–O1 2.117(2), Ru2–N9 1.956(3), Ru2–N5 2.046(3), Ru2–N2 2.057(3), Ru2–N8 2.061(3), Ru2–N10 2.068(3), Ru2–O2 2.115(3), Ru1···Ru2 4.3195(13); N3–Ru1–N1 79.37(13), N3–Ru1–N4 80.37(14), N1–Ru1–N4 159.74(13), N3–Ru1–N7 92.68(12), N1–Ru1–N7 89.97(12), N4–Ru1–N7 90.62(12), N3–Ru1–N6 90.56(12), N1–Ru1–N6 90.88(12), N4–Ru1–N6 89.67(12), N7–Ru1–N6 176.75(12), N3–Ru1–O1 173.12(12), N1–Ru1–O1 106.29(11), N4–Ru1–O1 93.94(12), N7–Ru1–O1 91.24(11), N6–Ru1–O1 85.51(11), N9–Ru2–N5 95.83(13), N9–Ru2–N2 173.66(13), N5–Ru2–N2 77.98(13), N9–Ru2–N8 79.80(14), N5–Ru2–N8 99.06(13), N2–Ru2–N8 102.34(13), N9–Ru2–N10 80.08(14), N5–Ru2–N10 85.36(13), N2–Ru2–N10 97.93(13), N8–Ru2–N10 159.73(14), N9–Ru2–O2 86.72(12), N5–Ru2–O2 176.94(13), N2–Ru2–O2 99.44(11), N8–Ru2–O2 83.04(12), N10–Ru2–O2 93.43(12).

Table A8. Crystal data and refinement details for **8**.

	8
empirical formula	$C_{45}H_{36}F_{12}N_{10}O_2P_2Ru_2$
moiety formula	$C_{45}H_{36}N_{10}O_2Ru_2^{2+}$, $2(F_6P^-)$
formula weight	1240.92
T [K]	133(2)
crystal size [mm³]	0.456 x 0.421 x 0.114
crystal system	monoclinic
space group	*C2/c (No. 15)*
a [Å]	51.417(6)
b [Å]	10.6713(13)
c [Å]	17.145(2)
α [°]	90
β [°]	99.580(4)
γ [°]	90
V [Å³]	9276(2)
Z	8
ρ [g·cm⁻³]	1.777
$F(000)$	4944
μ [mm⁻¹]	0.821
T_{min} / T_{max}	0.74 / 0.91
θ-range [°]	2.257 – 27.279
hkl-range	−66 to 65, ±13, ±21
measured refl.	71051
unique refl. [R_{int}]	10247 [0.0503]
observed refl. ($I > 2\sigma(I)$)	9010
data / restr. / param.	10247 / 0 / 672
goodness-of-fit (F^2)	1.135
$R1$, $wR2$ ($I > 2\sigma(I)$)	0.0484 / 0.0953
$R1$, $wR2$ (all data)	0.0573 / 0.0988
res. el. dens. [e·Å⁻³]	−1.500 / 0.878

DFT Calculations

The calculations were performed by Dr. Sebastian Dechert. The ORCA program package (version 4.2.1) was used for all calculations.[183] Geometry optimization and frequency calculation was performed starting from the crystallographic data (BP86 functional, def2-tzvp basis set,[184,185] RI approximation using the auxiliary def2/J basis set, D3 dispersion correction with Becke-Johnson damping,[186] tight convergence and optimization criteria). Energy calculation on the optimized coordinates was performed with the B3LYP functional under otherwise same conditions using the RIJCOSX approximation.

Table A9. Geometry optimized coordinates of **8**.

Ru	2140391	-0.070841	-0.319109
Ru	-2.078530	0.093083	0.103545
O	1.097923	0.682798	-1.930777
O	-1.144181	0.307498	-1.759360
N	0.771533	-0.627845	1.078636
N	3.316372	-0.757070	1.092118
N	3.980936	0.297366	-1.169031
N	2.208742	1.872222	0.446984
N	2.008955	-1.966399	-1.183426
N	-0.548834	-0.489890	1.266233
N	-3.020064	-0.216438	1.891912
N	-2.069908	2.132038	0.383979
N	-3.668031	0.625204	-0.962625
N	-2.799964	-1.753405	-0.482105
C	2.760119	-1.297028	2.223589
C	4.666907	-0.665095	0.918553
C	-0.091545	0.610228	-2.400476
C	1.316749	-1.186009	2.219860
C	5.042068	-0.048576	-0.361742
C	4.222315	0.846391	-2.375497
C	2.312210	2.110292	1.776772

C	2.211297	2.933245	-0.394745
C	0.798686	-2.433145	-1.573688
C	3.094679	-2.745625	-1.398854
C	3.591990	-1.803216	3.227566
C	5.521773	-1.158623	1.904580
C	-0.239491	0.915160	-3.870026
C	-0.869313	-0.939315	2.532721
C	0.294669	-1.394940	3.161839
C	6.355470	0.173117	-0.778063
C	5.513924	1.086730	-2.836638
C	2.435901	3.393502	2.297776
C	2.328231	4.242223	0.058366
C	0.642847	-3.665809	-2.193659
C	3.010057	-3.992666	-2.006744
C	4.974909	-1.733324	3.058563
C	-3.049927	2.804162	-0.310308
C	-3.944572	1.947217	-1.100322
C	-4.363651	-0.336690	-1.620342
C	-2.257308	-0.773128	2.892631
C	6.598085	0.749213	-2.024729
C	2.452366	4.484630	1.427348
C	1.764243	-4.466426	-2.419626
C	-4.329441	0.025710	2.125460
C	-1.219521	2.827002	1.165422
C	-3.891407	-1.693924	-1.317103
C	-2.339645	-2.956572	-0.082864
C	-3.160112	4.192301	-0.220728
C	-4.997282	2.351186	-1.925313
C	-5.421175	0.026456	-2.458865
C	-2.821929	-1.100834	4.129072
C	-4.935411	-0.273124	3.338388

C	-1.290803	4.210051	1.290094
C	-4.498624	-2.862925	-1.777779
C	-2.914272	-4.149659	-0.508487
C	-2.274718	4.906211	0.585596
C	-5.735579	1.379350	-2.605390
C	-4.171092	-0.851964	4.357019
C	-4.007321	-4.104056	-1.376025
H	3.337951	1.075151	-2.969626
H	2.303846	1.240406	2.430495
H	2.111283	2.699410	-1.452663
H	-0.050304	-1.781081	-1.380750
H	4.053908	-2.346828	-1.077016
H	3.160515	-2.242047	4.126061
H	6.602067	-1.102282	1.780423
H	-1.287869	0.874600	-4.177938
H	0.346455	0.193314	-4.456144
H	0.171516	1.911160	-4.085584
H	0.393901	-1.797637	4.163661
H	7.185881	-0.103229	-0.129961
H	5.660427	1.528747	-3.821080
H	2.533009	3.525692	3.375191
H	2.336446	5.057959	-0.663794
H	-0.352136	-3.985949	-2.499693
H	3.916797	-4.577011	-2.157816
H	5.636282	-2.125230	3.830787
H	7.620025	0.927571	-2.358092
H	2.569020	5.499885	1.806777
H	1.671670	-5.435844	-2.908757
H	-4.891298	0.469733	1.306072
H	-0.472096	2.239644	1.695700
H	-1.485987	-2.940174	0.593835

H	-3.942602	4.711841	-0.771527
H	-5.240892	3.405944	-2.042682
H	-5.993345	-0.730011	-2.993263
H	-2.195887	-1.544197	4.902341
H	-5.993122	-0.054905	3.477523
H	-0.586580	4.726288	1.940487
H	-5.363637	-2.802177	-2.436843
H	-2.509129	-5.097191	-0.156100
H	-2.360658	5.989720	0.669576
H	-6.558964	1.678264	-3.253560
H	-4.623204	-1.102036	5.316406
H	-4.481111	-5.021271	-1.724400

List of Ligands and Complexes
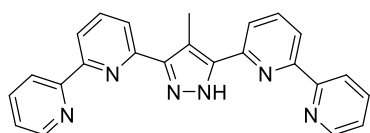
^{Me}**bbpH**
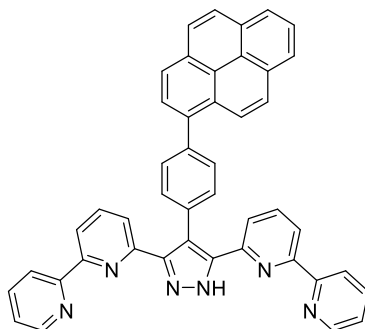
^{pyr}**bbpH**
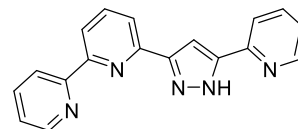
HL^3
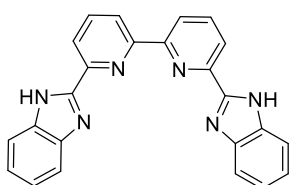
H$_2$L^1
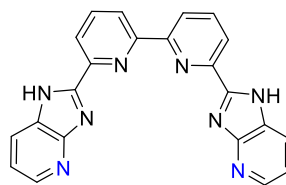
H$_2$L^2
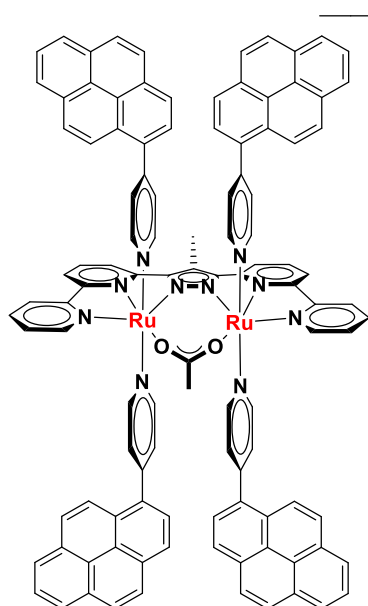
1^{4pyr}
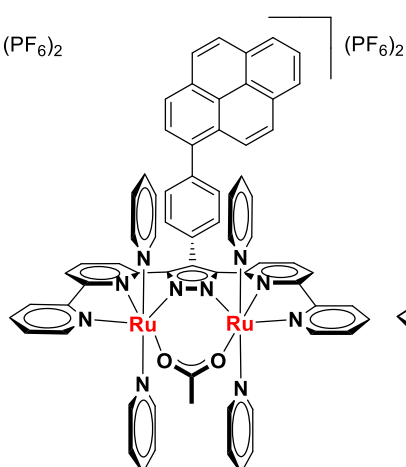
1^{pyr}
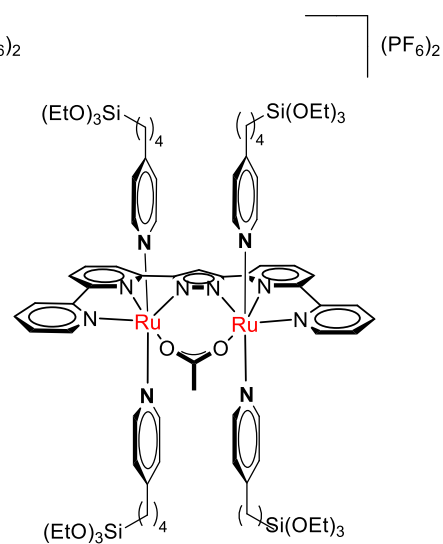
1$^{(Si(OEt)3)4}$
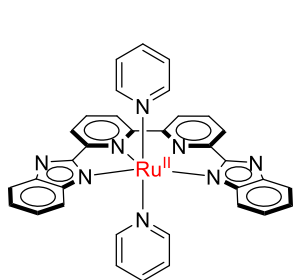
2
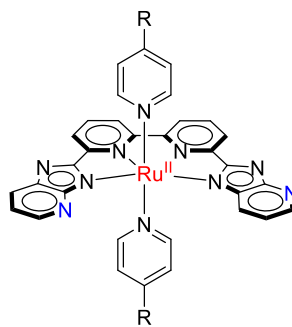
3 : R = -H
4 : R = -COOH
5 : R = -N(Me)$_2$

[2H]PF$_6$

[2H$_2$](CF$_3$SO$_3$)$_2$

6

7

8

225
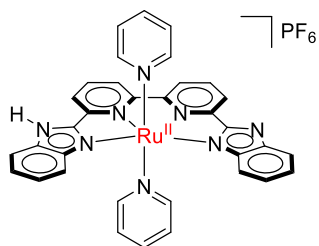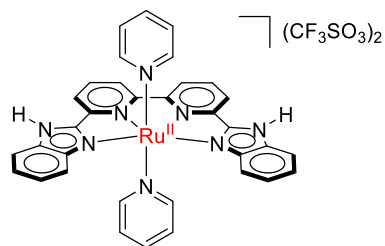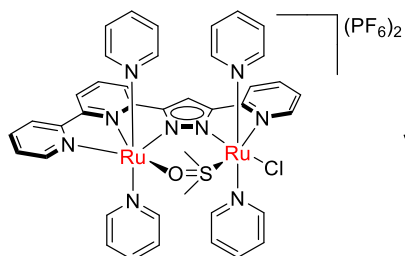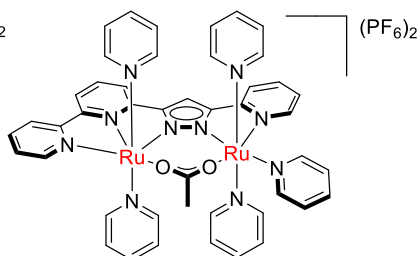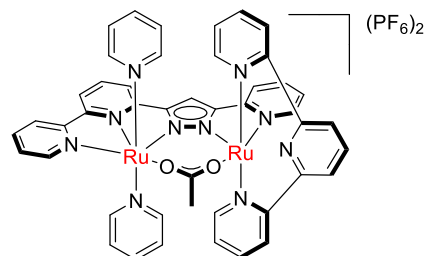
Abbreviation

AP	Artificial photosynthesis
ATP	Adenosine triphosphate
ALOX	Aluminum oxide
bpy	Bipyridine
bda^{2-}	2,2'-bipyridine-6,6'-dicarboxylate
^{H}bbp^{-}	3,5-Bis{6-(2,2'-bipyridyl)}pyrazolate
^{H}bpp^{-}	3,5-bis(2-pyridyl)pyrazolate
CAN	Ceric ammonium nitrate
CE	Counter electrode
CN	Coordination number
COSY	Correlated spectroscopy
CSM	Continuous Symmetry Measures
CV	Cyclic voltammetry
Cyt b$_6$f	Cytochrome b$_6$f complex
CNT	Carbon nanotubes
CD$_2$Cl$_2$	Dichloromethane-d$_2$
CA	Chronoamperometry
CRR	Complex reduction reaction
CPE	controlled potential electrolysis
d	Doublet (NMR)
damp	2,6-Bis[(dimethylamino)methyl]pyridine)
DCM	Dichloromethane
DFT	Density functional theory
DMSO	Dimethyl sulphoxide
DSSC	Dye Sensitised Solar Cells
eq	Equivalent
ESI	Electrospray ionization
Et	Ethyl
EtOH	Ethanol
Et$_2$O	Diethylether

EELS	Electron energy loss spectroscopy
et al.	*et alii*, to complete a list
Fc	Ferrocene
FTO	Fluorine doped tin oxide
FOWA	Foot of the wave analysis
freq.	Frequency
FD	Ferredoxin
FE	Faradaic efficiency
FeS	Iron-sulfur cluster
FNR	Ferredoxin-NADP$^+$ reductase
GC	Glassy carbon
HEC	Hydrogen evolution catalyst
HMBC	Heteronuclear multiple-bond correlation spectroscopy
$E_{1/2}$	Half wave potential
HAT	Hydrogen atom transfer
HOTf	Trifluoro methane sulfonic acid
HSQC	Heteronuclear single quantum coherance
H$_3$tpha$^-$	2,2':6',2''-terpyridine-6,6''-diphosphononic acid
HRTEM	High-resolution transmission electron microscopy
I2M	Interaction of two metal-oxo units
IRI	Infrared
NIS	N-Iodosuccinimide
IPCC	Intergovernmental panel on climate change
Isoq	Isoquinoline
IVCT	Intervalence charge transfer
J	Coupling constant (NMR)
LMCT	Ligand-metal charge transfer
m	Multiplet (NMR)
Me	Methyl
MeCN	Acetonitrile, CH3CN
MeOH	Methanol
MLCT	Metal-ligand charge transfer

MS	Mass spectrometry
MO	Molecular orbital
MSE	Mercury sulfate electrode
m/z	Mass-to-charge ratio
meso-ITO	Mesoporous indium tin oxide
MOM	Methoxymethylether
MWCNT	Multi-walled carbon nanotubes
N	Collection efficiency
NADPH	Nicotinamide adenine dinucleotide phosphate
NaOAc	Sodium acetate
Na^{t}OBu	Sodium tert-butoxide
NEt$_3$	Triethyl amine
NHE	Normal hydrogen electrode
NMR	Nuclear magnetic resonance
NIR	Near infrared
nb	Non bonding
NOESY	Nuclear overhauser enhancement spectroscopy
OEC	Oxygen evolving complex
OER	Oxygen evolution reaction
ORR	Oxygen reduction reaction
ΔE_p	Peak potential separation
PSI	Photosystem I
PSII	Photosystem II
PVE	Photovoltaic-coupled electrolyzer
PEC	Photo electrochemical cell
PC	Propylene carbonate
PCET	Proton coupled electron transfer
PEM	Proton exchange membrane
ppm	Part per million
py	Pyridine
Pheo	Pheophytin
pic	Picoline

q	Quartet (NMR)
ref.	Reference electrode
RRDE	Rotating ring disc electrode
RHE	Reversible hydrogen electrode
s	Second
SCE	Saturated calomel electrode
SWV	Square wave voltammetry
SEM	Scanning electron microscopy
SWCNT	Single-walled carbon nanotubes
t	Triplet (NMR)
TOF	Turnover frequency
TBD	1,5,7-Triazabicyclo[4.4.0]dec-5-en
TON	Turnover number
trpy	2,2';6',2"-terpyridine
THF	Tetrahydrofuran
TEM	Transmission electron microscopy
TMSCN	Trimethylsilyl cyanide
UV-vis	Ultraviolet and visible
viz.	Namely
WNA	Water nucleophilic attack
WOC	Water oxidation catalyst
WE	Working electrode
XRD	X-ray diffraction
XPS	X-ray photoelectron spectroscopy

References

(1) Governments must take heed of latest IPCC assessment. *Nature* **2018**, *562*, 163.

(2) D'Amato, G.; Holgate, S. T.; Pawankar, R.; Ledford, D. K.; Cecchi, L.; Al-Ahmad, M.; Al-Enezi, F.; Al-Muhsen, S.; Ansotegui, I.; Baena-Cagnani, C. E.; Baker, D. J.; Bayram, H.; Bergmann, K. C.; Boulet, L.-P.; Buters, J. T. M.; D'Amato, M.; Dorsano, S.; Douwes, J.; Finlay, S. E.; Garrasi, D.; Gómez, M.; Haahtela, T.; Halwani, R.; Hassani, Y.; Mahboub, B.; Marks, G.; Michelozzi, P.; Montagni, M.; Nunes, C.; Oh, J. J.-W.; Popov, T. A.; Portnoy, J.; Ridolo, E.; Rosário, N.; Rottem, M.; Sánchez-Borges, M.; Sibanda, E.; Sienra-Monge, J. J.; Vitale, C.; Annesi-Maesano, I. Meteorological conditions, climate change, new emerging factors, and asthma and related allergic disorders. A statement of the World Allergy Organization. *World Allergy Organ. J.* **2015**, *8*, 25.

(3) Haines, A.; Ebi, K. The Imperative for Climate Action to Protect Health. *N. E. J. M.* **2019**, *380*, 263–273.

(4) *Bundesministerium für Wirtschaft und Energie*:*Renewable energy*. https://www.bmwi.de/Redaktion/DE/Dossier/erneuerbare-energien.html.

(5) *Bundesministerium für Wirtschaft und Energie*:*Solar Energy*. https://www.erneuerbare-energien.de/EE/Navigation/DE/Technologien/Solarenergie-Photovoltaik/solarenergie-photovoltaik.html.

(6) Ashok. *Solar energy*. S://www.britannica.com/science/solar-energy.

(7) Inoue, H.; Shimada, T.; Kou, Y.; Nabetani, Y.; Masui, D.; Takagi, S.; Tachibana, H. The water oxidation bottleneck in artificial photosynthesis: how can we get through it? An alternative route involving a two-electron process. *ChemSusChem* **2011**, *4*, 173–179.

(8) Styring, S. Artificial photosynthesis for solar fuels. *Faraday Discuss.* **2012**, *155*, 357–376.

(9) Crabtree, R. H. *Energy Production and Storage: Inorganic Chemical Strategies for a Warming World*; Wiley, 2013.

(10) WHATLEY, F. R.; TAGAWA, K.; ARNON, D. I. Separation of the light and dark reactions in electron transfer during photosynthesis. *PNAS* **1963**, *49*, 266–270.

(11) Barber, J.; Tran, P. D. From natural to artificial photosynthesis. *J. R. Soc. Interface* **2013**, *10*, 20120984.

(12) McEvoy, J. P.; Brudvig, G. W. Water-splitting chemistry of photosystem II. *Chem. Rev.* **2006**, *106*, 4455–4483.

(13) Nelson, N.; Ben-Shem, A. The complex architecture of oxygenic photosynthesis. *Nat. Rev.* **2004**, *5*, 971–982.

(14) Baniulis, D.; Yamashita, E.; Zhang, H.; Hasan, S. S.; Cramer, W. A. Structure-function of the cytochrome b_6f complex. *Photochem. Photobiol.* **2008**, *84*, 1349–1358.

References

(15) Croce, R.; van Amerongen, H. Natural strategies for photosynthetic light harvesting. *Nat. Chem. Biol.* **2014**, *10*, 492–501.

(16) Barber, J. Photosynthetic energy conversion: natural and artificial. *Chem. Soc. Rev.* **2009**, *38*, 185–196.

(17) Ferreira, K. N.; Iverson, T. M.; Maghlaoui, K.; Barber, J.; Iwata, S. Architecture of the photosynthetic oxygen-evolving center. *Science* **2004**, *303*, 1831–1838.

(18) Cox, N.; Retegan, M.; Neese, F.; Pantazis, D. A.; Boussac, A.; Lubitz, W. Photosynthesis. Electronic structure of the oxygen-evolving complex in photosystem II prior to O-O bond formation. *Science* **2014**, *345*, 804–808.

(19) Cook, S. A.; Borovik, A. S. Inorganic chemistry: Deconstructing water oxidation. *Nat. chem.* **2013**, *5*, 259–260.

(20) Najafpour, M. M.; Moghaddam, A. N.; Yang, Y. N.; Aro, E.-M.; Carpentier, R.; Eaton-Rye, J. J.; Lee, C.-H.; Allakhverdiev, S. I. Biological water-oxidizing complex: a nano-sized manganese-calcium oxide in a protein environment. *Photosynth. Res.* **2012**, *114*, 1–13.

(21) Umena, Y.; Kawakami, K.; Shen, J.-R.; Kamiya, N. Crystal structure of oxygen-evolving photosystem II at a resolution of 1.9 Å. *Nature* **2011**, *473*, 55–60.

(22) Kok, B.; Forbush, B.; McGloin, M. Cooperation of charges in photosynthetic O_2 evolution-I. A linear four step mechanism. *Photochem. Photobiol.* **1970**, *11*, 457–475.

(23) Gust, D.; Moore, T. A.; Moore, A. L. Solar fuels via artificial photosynthesis. *Acc. Chem. Res.* **2009**, *42*, 1890–1898.

(24) Berardi, S.; Drouet, S.; Francàs, L.; Gimbert-Suriñach, C.; Guttentag, M.; Richmond, C.; Stoll, T.; Llobet, A. Molecular artificial photosynthesis. *Chem. Soc. Rev.* **2014**, *43*, 7501–7519.

(25) Zhang, B.; Sun, L. Artificial photosynthesis: opportunities and challenges of molecular catalysts. *Chem. Soc. Rev.* **2019**, *48*, 2216–2264.

(26) Ager, J. W.; Shaner, M. R.; Walczak, K. A.; Sharp, I. D.; Ardo, S. Experimental demonstrations of spontaneous, solar-driven photoelectrochemical water splitting. *Energy Environ. Sci.* **2015**, *8*, 2811–2824.

(27) An, J.; Tian, Z.; Zhang, L.; Yang, X.; Cai, B.; Yu, Z.; Zhang, L.; Hagfeldt, A.; Sun, L. Supramolecular Co-adsorption on TiO_2 to enhance the efficiency of dye-sensitized solar cells. *J. Mater. Chem. A* **2021**, *9*, 13697–13703.

(28) Ding, X.; Zhang, L.; Wang, Y.; Liu, A.; Gao, Y. Design of photoanode-based dye-sensitized photoelectrochemical cells assembling with transition metal complexes for visible light-induced water splitting. *Coord. Chem. Rev.* **2018**, *357*, 130–143.

(29) Gao, B.; Wang, T.; Xue, H.; Jiang, C.; Sheng, L.; Huang, X.; He, J. A nano-surface monocrystalline $BiVO_4$ nanoplate photoanode for enhanced photoelectrochemical performance. *New J. Chem.* **2021**, *45*, 7069–7073.

References

(30) Gafney, H. D.; Adamson, A. W. Excited state Ru(bipyr)$_3^{2+}$ as an electron-transfer reductant. *J. Am. Chem. Soc.* **1972**, *94*, 8238–8239.

(31) Adamson, A. W.; Demas, J. N. New photosensitizer. Tris(2,2'-bipyridine)ruthenium(II) chloride. *J. Am. Chem. Soc.* **1971**, *93*, 1800–1801.

(32) Forster, L. S. Intersystem crossing in transition metal complexes. *Coord. Chem. Rev.* **2006**, *250*, 2023–2033.

(33) Galán-Mascarós, J. R. Water Oxidation at Electrodes Modified with Earth-Abundant Transition-Metal Catalysts. *ChemElectroChem* **2015**, *2*, 37–50.

(34) Weinberg, D. R.; Gagliardi, C. J.; Hull, J. F.; Murphy, C. F.; Kent, C. A.; Westlake, B. C.; Paul, A.; Ess, D. H.; McCafferty, D. G.; Meyer, T. J. Proton-coupled electron transfer. *Chem. Rev.* **2012**, *112*, 4016–4093.

(35) Blakemore, J. D.; Crabtree, R. H.; Brudvig, G. W. Molecular Catalysts for Water Oxidation. *Chem. Rev.* **2015**, *115*, 12974–13005.

(36) Savini, A.; Belanzoni, P.; Bellachioma, G.; Zuccaccia, C.; Zuccaccia, D.; Macchioni, A. Activity and degradation pathways of pentamethyl-cyclopentadienyl-iridium catalysts for water oxidation. *Green Chem.* **2011**, *13*, 3360.

(37) Tong, L.; Thummel, R. P. Mononuclear ruthenium polypyridine complexes that catalyze water oxidation. *Chem. Sci.* **2016**, *7*, 6591–6603.

(38) Binstead, R. A.; Moyer, B. A.; Samuels, G. J.; Meyer, T. J. Proton-coupled electron transfer between [Ru(bpy)$_2$(py)OH$_2$]$^{2+}$ and [Ru(bpy)$_2$(py)O]$^{2+}$. A solvent isotope effect (kH$_2$O/kD$_2$O) of 16.1. *J. Am. Chem. Soc.* **1981**, *103*, 2897–2899.

(39) Gagliardi, C. J.; Vannucci, A. K.; Concepcion, J. J.; Chen, Z.; Meyer, T. J. The role of proton coupled electron transfer in water oxidation. *Energy Environ. Sci.* **2012**, *5*, 7704.

(40) Betley, T. A.; Wu, Q.; van Voorhis, T.; Nocera, D. G. Electronic design criteria for O-O bond formation via metal-oxo complexes. *Inorg. Chem.* **2008**, *47*, 1849–1861.

(41) Kryatov, S. V.; Rybak-Akimova, E. V.; Schindler, S. Kinetics and mechanisms of formation and reactivity of non-heme iron oxygen intermediates. *Chem. Rev.* **2005**, *105*, 2175–2226.

(42) Abu-Omar, M. M.; Loaiza, A.; Hontzeas, N. Reaction mechanisms of mononuclear non-heme iron oxygenases. *Chem. Rev.* **2005**, *105*, 2227–2252.

(43) Zhang, R.; Horner, J. H.; Newcomb, M. Laser flash photolysis generation and kinetic studies of porphyrin-manganese-oxo intermediates. Rate constants for oxidations effected by porphyrin-Mn(V)-oxo species and apparent disproportionation equilibrium constants for porphyrin-Mn(IV)-oxo species. *J. Am. Chem. Soc.* **2005**, *127*, 6573–6582.

(44) Gersten, S. W.; Samuels, G. J.; Meyer, T. J. Catalytic oxidation of water by an oxo-bridged ruthenium dimer. *J. Am. Chem. Soc.* **1982**, *104*, 4029–4030.

(45) Gray, H. B.; Winkler, J. R. Living with Oxygen. *Acc. Chem. Res.* **2018**, *51*, 1850–1857.

References

(46) Winkler, J. R.; Gray, H. B. Electronic Structures of Oxo-Metal Ions. In *Molecular Electronic Structures of Transition Metal Complexes I*; Mingos, D. M. P., Day, P., Dahl, J. P., Eds.; Structure and Bonding; Springer Berlin Heidelberg, 2012; pp 17–28.

(47) Shaffer, D. W.; Xie, Y.; Concepcion, J. J. O-O bond formation in ruthenium-catalyzed water oxidation: single-site nucleophilic attack vs. O-O radical coupling. *Chem. Soc. Rev.* **2017**, *46*, 6170–6193.

(48) Sala, X.; Maji, S.; Bofill, R.; García-Antón, J.; Escriche, L.; Llobet, A. Molecular water oxidation mechanisms followed by transition metals: state of the art. *Acc. Chem. Res.* **2014**, *47*, 504–516.

(49) Wasylenko, D. J.; Palmer, R. D.; Berlinguette, C. P. Homogeneous water oxidation catalysts containing a single metal site. *Chem. Commun.* **2013**, *49*, 218–227.

(50) Meyer, T. J.; Sheridan, M. V.; Sherman, B. D. Mechanisms of molecular water oxidation in solution and on oxide surfaces. *Chem. Soc. Rev.* **2017**, *46*, 6148–6169.

(51) Casadevall, C.; Martin-Diaconescu, V.; Browne, W. R.; Fernández, S.; Franco, F.; Cabello, N.; Benet-Buchholz, J.; Lassalle-Kaiser, B.; Lloret-Fillol, J. Isolation of a Ru(IV) side-on peroxo intermediate in the water oxidation reaction. *Nat. chem.* **2021**, *13*, 800–804.

(52) Romain, S.; Bozoglian, F.; Sala, X.; Llobet, A. Oxygen-oxygen bond formation by the Ru-Hbpp water oxidation catalyst occurs solely via an intramolecular reaction pathway. *J. Am. Chem. Soc.* **2009**, *131*, 2768–2769.

(53) Neudeck, S.; Maji, S.; López, I.; Meyer, S.; Meyer, F.; Llobet, A. New powerful and oxidatively rugged dinuclear Ru water oxidation catalyst: control of mechanistic pathways by tailored ligand design. *J. Am. Chem. Soc.* **2014**, *136*, 24–27.

(54) Liu, F.; Concepcion, J. J.; Jurss, J. W.; Cardolaccia, T.; Templeton, J. L.; Meyer, T. J. Mechanisms of water oxidation from the blue dimer to photosystem II. *Inorg. Chem.* **2008**, *47*, 1727–1752.

(55) Bianco, R.; Hay, P. J.; Hynes, J. T. Theoretical study of O-O single bond formation in the oxidation of water by the ruthenium blue dimer. *J. Phys. Chem. A* **2011**, *115*, 8003–8016.

(56) Bozoglian, F.; Romain, S.; Ertem, M. Z.; Todorova, T. K.; Sens, C.; Mola, J.; Rodríguez, M.; Romero, I.; Benet-Buchholz, J.; Fontrodona, X.; Cramer, C. J.; Gagliardi, L.; Llobet, A. The Ru–Hbpp Water Oxidation Catalyst. *J. Am. Chem. Soc.* **2009**, *131*.

(57) Duan, L.; Bozoglian, F.; Mandal, S.; Stewart, B.; Privalov, T.; Llobet, A.; Sun, L. A molecular ruthenium catalyst with water-oxidation activity comparable to that of photosystem II. *Nat. chem.* **2012**, *4*, 418–423.

(58) Muckerman, J. T.; Polyansky, D. E.; Wada, T.; Tanaka, K.; Fujita, E. Water oxidation by a ruthenium complex with noninnocent quinone ligands: possible formation of an O-O bond at a low oxidation state of the metal. *Inorg. Chem.* **2008**, *47*, 1787–1802.

(59) Nyhlén, J.; Duan, L.; Akermark, B.; Sun, L.; Privalov, T. Evolution of O_2 in a seven-coordinate Ru(IV) dimer complex with a HOHOH- bridge: a computational study. *Angew. Chem. Int. Ed.* **2010**, *49*, 1773–1777.

References

(60) Romero, I.; Rodríguez, M.; Sens, C.; Mola, J.; Rao Kollipara, M.; Francàs, L.; Mas-Marza, E.; Escriche, L.; Llobet, A. Ru complexes that can catalytically oxidize water to molecular dioxygen. *Inorg. Chem.* **2008**, *47*, 1824–1834.

(61) Privalov, T.; Åkermark, B.; Sun, L. The O-O bonding in water oxidation: the electronic structure portrayal of a concerted oxygen atom-proton transfer pathway. *Chemistry (Weinheim an der Bergstrasse, Germany)* **2011**, *17*, 8313–8317.

(62) Neudeck, S. Establishing Dinuclear Ruthenium Complexes Based on the Bis(bipyridyl)pyrazolate Ligand System for CatalyticWater Oxidation: Synthetic Access, Catalytic Activity and Mechanistic Investigations, Göttingen, 2015.

(63) Kohl, S. W.; Weiner, L.; Schwartsburd, L.; Konstantinovski, L.; Shimon, L. J. W.; Ben-David, Y.; Iron, M. A.; Milstein, D. Consecutive Thermal H_2 and Light-Induced O_2 Evolution from Water Promoted by a Metal Complex. *Science* **2009**, *324*, 74–77.

(64) Maji, S.; Vigara, L.; Cottone, F.; Bozoglian, F.; Benet-Buchholz, J.; Llobet, A. Ligand Geometry Directs O⬚O Bond-Formation Pathway in Ruthenium-Based Water Oxidation Catalyst. *Angew. Chem.* **2012**, *124*, 6069–6072.

(65) Vigara, L.; Ertem, M. Z.; Planas, N.; Bozoglian, F.; Leidel, N.; Dau, H.; Haumann, M.; Gagliardi, L.; Cramer, C. J.; Llobet, A. Experimental and quantum chemical characterization of the water oxidation cycle catalysed by $[Ru^{II}(damp)(bpy)(H_2O)]^{2+}$. *Chem. Sci.* **2012**, *3*, 2576.

(66) Matheu, R.; Neudeck, S.; Meyer, F.; Sala, X.; Llobet, A. Foot of the Wave Analysis for Mechanistic Elucidation and Benchmarking Applications in Molecular Water Oxidation Catalysis. *ChemSusChem* **2016**, *9*, 3361–3369.

(67) Zhang, L.-H.; Mathew, S.; Hessels, J.; Reek, J. N. H.; Yu, F. Homogeneous Catalysts Based on First-Row Transition-Metals for Electrochemical Water Oxidation. *ChemSusChem* **2021**, *14*, 234–250.

(68) P. Atkins, T. Overton, J. Rourke, M. Weller, F. Armstrong, Shriver and. *Inorganic Chemistry*, 2010.

(69) Garrido-Barros, P.; Gimbert-Suriñach, C.; Matheu, R.; Sala, X.; Llobet, A. How to make an efficient and robust molecular catalyst for water oxidation. *Chem. Soc. Rev.* **2017**, *46*, 6088–6098.

(70) Zong, R.; Thummel, R. P. A new family of Ru complexes for water oxidation. *J. Am. Chem. Soc.* **2005**, *127*, 12802–12803.

(71) Tseng, H.-W.; Zong, R.; Muckerman, J. T.; Thummel, R. Mononuclear ruthenium(II) complexes that catalyze water oxidation. *Inorg. Chem.* **2008**, *47*, 11763–11773.

(72) Duan, L.; Fischer, A.; Xu, Y.; Sun, L. Isolated seven-coordinate Ru(IV) dimer complex with HOHOH(-) bridging ligand as an intermediate for catalytic water oxidation. *J. Am. Chem. Soc.* **2009**, *131*, 10397–10399.

(73) Duan, L.; Wang, L.; Li, F.; Li, F.; Sun, L. Highly efficient bioinspired molecular Ru water oxidation catalysts with negatively charged backbone ligands. *Acc. Chem. Res.* **2015**, *48*, 2084–2096.

References

(74) Zhan, S.; Mårtensson, D.; Purg, M.; Kamerlin, S. C. L.; Ahlquist, M. S. G. Capturing the Role of Explicit Solvent in the Dimerization of Ru^V(bda) Water Oxidation Catalysts. *Angew. Chem. Int. Ed.* **2017**, *56*, 6962–6965.

(75) Wang, L.; Duan, L.; Wang, Y.; Ahlquist, M. S. G.; Sun, L. Highly efficient and robust molecular water oxidation catalysts based on ruthenium complexes. *Chem. Commun.* **2014**, *50*, 12947–12950.

(76) Duan, L.; Araujo, C. M.; Ahlquist, M. S. G.; Sun, L. Highly efficient and robust molecular ruthenium catalysts for water oxidation. *PNAS* **2012**, *109*, 15584–15588.

(77) Duan, L.; Wang, L.; Inge, A. K.; Fischer, A.; Zou, X.; Sun, L. Insights into Ru-based molecular water oxidation catalysts: electronic and noncovalent-interaction effects on their catalytic activities. *Inorg. Chem.* **2013**, *52*, 7844–7852.

(78) Yi, J.; Zhan, S.; Chen, L.; Tian, Q.; Wang, N.; Li, J.; Xu, W.; Zhang, B.; Ahlquist, M. S. G. Electrostatic Interactions Accelerating Water Oxidation Catalysis via Intercatalyst O-O Coupling. *J. Am. Chem. Soc.* **2021**, *143*, 2484–2490.

(79) Matheu, R.; Ertem, M. Z.; Benet-Buchholz, J.; Coronado, E.; Batista, V. S.; Sala, X.; Llobet, A. Intramolecular Proton Transfer Boosts Water Oxidation Catalyzed by a Ru Complex. *J. Am. Chem. Soc.* **2015**, *137*, 10786–10795.

(80) Muckerman, J. T.; Kowalczyk, M.; Badiei, Y. M.; Polyansky, D. E.; Concepcion, J. J.; Zong, R.; Thummel, R. P.; Fujita, E. New water oxidation chemistry of a seven-coordinate ruthenium complex with a tetradentate polypyridyl ligand. *Inorg. Chem.* **2014**, *53*, 6904–6913.

(81) Vereshchuk, N.; Matheu, R.; Benet-Buchholz, J.; Pipelier, M.; Lebreton, J.; Dubreuil, D.; Tessier, A.; Gimbert-Suriñach, C.; Ertem, M. Z.; Llobet, A. Second Coordination Sphere Effects in an Evolved Ru Complex Based on Highly Adaptable Ligand Results in Rapid Water Oxidation Catalysis. *J. Am. Chem. Soc.* **2020**, *142*, 5068–5077.

(82) Liu, Y.; Ng, S.-M.; Yiu, S.-M.; Lam, W. W. Y.; Wei, X.-G.; Lau, K.-C.; Lau, T.-C. Catalytic water oxidation by ruthenium(II) quaterpyridine (qpy) complexes: evidence for ruthenium(III) qpy-N,N'''-dioxide as the real catalysts. *Angew. Chem. Int. Ed.* **2014**, *53*, 14468–14471.

(83) Gilbert, J. A.; Eggleston, D. S.; Murphy, W. R.; Geselowitz, D. A.; Gersten, S. W.; Hodgson, D. J.; Meyer, T. J. Structure and redox properties of the water-oxidation catalyst [(bpy)$_2$(OH$_2$)RuORu(OH$_2$)(bpy)$_2$]$^{4+}$. *J. Am. Chem. Soc.* **1985**, *107*, 3855–3864.

(84) Nagoshi, K.; Yamashita, S.; Yagi, M.; Kaneko, M. Catalytic activity of [(bpy)$_2$(H$_2$O)Ru–O–Ru(H$_2$O)(bpy)$_2$]$^{4+}$ for four-electron water oxidation. *J. Mol. Catal. A Chem.* **1999**, *144*, 71–76.

(85) Llobet, A.; Curry, M. E.; Evans, H. T.; Meyer, T. J. Synthesis, spectral, and redox properties of three triply bridged complexes of ruthenium. *Inorg. Chem.* **1989**, *28*, 3131–3137.

(86) Sala, X.; Romero, I.; Rodríguez, M.; Escriche, L.; Llobet, A. Molecular catalysts that oxidize water to dioxygen. *Angew. Chem. Int. Ed.* **2009**, *48*, 2842–2852.

(87) Binstead, R. A.; Chronister, C. W.; Ni, J.; Hartshorn, C. M.; Meyer, T. J. Mechanism of Water Oxidation by the μ-Oxo Dimer [(bpy)$_2$ (H$_2$O)Ru^{III}ORu^{III}(OH$_2$)(bpy)$_2$]$^{4+}$. *J. Am. Chem. Soc.* **2000**, *122*, 8464–8473.

References

(88) Yamada, H.; Siems, W. F.; Koike, T.; Hurst, J. K. Mechanisms of water oxidation catalyzed by the cis,cis-[(bpy)$_2$Ru(OH$_2$)]$_2$O^{4+} ion. *J. Am. Chem. Soc.* **2004**, *126*, 9786–9795.

(89) Chronister, C. W.; Binstead, R. A.; Ni, J.; Meyer, T. J. Mechanism of Water Oxidation Catalyzed by the μ-Oxo Dimer [(bpy)$_2$(OH$_2$)Ru^{III}ORu^{III}(OH$_2$)(bpy)$_2$]$^{4+}$. *Inorg. Chem.* **1997**, *36*, 3814–3815.

(90) Stull, J. A.; Stich, T. A.; Hurst, J. K.; Britt, R. D. Electron paramagnetic resonance analysis of a transient species formed during water oxidation catalyzed by the complex ion (bpy)$_2$Ru(OH$_2$)$_2$O^{4+}. *Inorg. Chem.* **2013**, *52*, 4578–4586.

(91) Cape, J. L.; Hurst, J. K. Detection and mechanistic relevance of transient ligand radicals formed during Ru(bpy)2(OH2)2O4+-catalyzed water oxidation. *J. Am. Chem. Soc.* **2008**, *130*, 827–829.

(92) Hurst, J. K. Water oxidation catalyzed by dimeric μ-oxo bridged ruthenium diimine complexes. *Coord. Chem. Rev.* **2005**, *249*, 313–328.

(93) Sens, C.; Romero, I.; Rodríguez, M.; Llobet, A.; Parella, T.; Benet-Buchholz, J. A New Ru Complex Capable of Catalytically Oxidizing Water to Molecular Dioxygen. *J. Am. Chem. Soc.* **2004**, *126*, 7798–7799.

(94) Sens, C.; Rodríguez, M.; Romero, I.; Llobet, A.; Parella, T.; Benet-Buchholz, J. Synthesis, structure, and acid-base and redox properties of a family of new Ru(II) isomeric complexes containing the trpy and the dinucleating Hbpp ligands. *Inorg. Chem.* **2003**, *42*, 8385–8394.

(95) Roeser, S.; Ertem, M. Z.; Cady, C.; Lomoth, R.; Benet-Buchholz, J.; Hammarström, L.; Sarkar, B.; Kaim, W.; Cramer, C. J.; Llobet, A. Synthesis, structure, and electronic properties of RuN$_6$ dinuclear Ru-Hbpp complexes. *Inorg. Chem.* **2012**, *51*, 320–327.

(96) Deng, Z.; Tseng, H.-W.; Zong, R.; Wang, D.; Thummel, R. Preparation and study of a family of dinuclear Ru(II) complexes that catalyze the decomposition of water. *Inorg. Chem.* **2008**, *47*, 1835–1848.

(97) Neudeck, S.; Maji, S.; López, I.; Dechert, S.; Benet-Buchholz, J.; Llobet, A.; Meyer, F. Establishing the Family of Diruthenium Water Oxidation Catalysts Based on the Bis(bipyridyl)pyrazolate Ligand System. *Inorg. Chem.* **2016**, *55*, 2508–2521.

(98) Planas, N.; Christian, G. J.; Mas-Marzá, E.; Sala, X.; Fontrodona, X.; Maseras, F.; Llobet, A. Through-space ligand interactions in enantiomeric dinuclear Ru complexes. *Chemistry (Weinheim an der Bergstrasse, Germany)* **2010**, *16*, 7965–7968.

(99) Brennaman, M. K.; Dillon, R. J.; Alibabaei, L.; Gish, M. K.; Dares, C. J.; Ashford, D. L.; House, R. L.; Meyer, G. J.; Papanikolas, J. M.; Meyer, T. J. Finding the Way to Solar Fuels with Dye-Sensitized Photoelectrosynthesis Cells. *J. Am. Chem. Soc.* **2016**, *138*, 13085–13102.

(100) Hammarström, L. Accumulative charge separation for solar fuels production: coupling light-induced single electron transfer to multielectron catalysis. *Acc. Chem. Res.* **2015**, *48*, 840–850.

(101) Ernstorfer, R.; Gundlach, L.; Felber, S.; Storck, W.; Eichberger, R.; Willig, F. Role of molecular anchor groups in molecule-to-semiconductor electron transfer. *J. Phys. Chem. B* **2006**, *110*, 25383–25391.

References

(102) Martini, L. A.; Moore, G. F.; Milot, R. L.; Cai, L. Z.; Sheehan, S. W.; Schmuttenmaer, C. A.; Brudvig, G. W.; Crabtree, R. H. Modular Assembly of High-Potential Zinc Porphyrin Photosensitizers Attached to TiO_2 with a Series of Anchoring Groups. *J. Phys. Chem. C* **2013**, *117*, 14526–14533.

(103) Jiang, J.; Swierk, J. R.; Materna, K. L.; Hedström, S.; Lee, S. H.; Crabtree, R. H.; Schmuttenmaer, C. A.; Batista, V. S.; Brudvig, G. W. High-Potential Porphyrins Supported on SnO_2 and TiO_2 Surfaces for Photoelectrochemical Applications. *J. Phys. Chem. C* **2016**, *120*, 28971–28982.

(104) Materna, K. L.; Crabtree, R. H.; Brudvig, G. W. Anchoring groups for photocatalytic water oxidation on metal oxide surfaces. *Chem. Soc. Rev.* **2017**, *46*, 6099–6110.

(105) Ginley, D. S., Ed. *Handbook of Transparent Conductors*; Springer US, 2011.

(106) Ginley, D. S.; Bright, C. Transparent Conducting Oxides. *MRS Bull.* **2000**, *25*, 15–18.

(107) Gao, Y.; Zhang, L.; Ding, X.; Sun, L. Artificial photosynthesis--functional devices for light driven water splitting with photoactive anodes based on molecular catalysts. *Phys. Chem. Chem. Phys.* **2014**, *16*, 12008–12013.

(108) Moore, G. F.; Blakemore, J. D.; Milot, R. L.; Hull, J. F.; Song, H.; Cai, L.; Schmuttenmaer, C. A.; Crabtree, R. H.; Brudvig, G. W. A visible light water-splitting cell with a photoanode formed by codeposition of a high-potential porphyrin and an iridium water-oxidation catalyst. *Energy Environ. Sci.* **2011**, *4*, 2389.

(109) Materna, K. L.; Brennan, B. J.; Brudvig, G. W. Silatranes for binding inorganic complexes to metal oxide surfaces. *Dalton trans.* **2015**, *44*, 20312–20315.

(110) McNamara, W. R.; Snoeberger III, R. C.; Li, G.; Richter, C.; Allen, L. J.; Milot, R. L.; Schmuttenmaer, C. A.; Crabtree, R. H.; Brudvig, G. W.; Batista, V. S. Hydroxamate anchors for water-stable attachment to TiO_2 nanoparticles. *Energy Environ. Sci.* **2009**, *2*, 1173.

(111) Brennan, B. J.; Koenigsmann, C.; Materna, K. L.; Kim, P. M.; Koepf, M.; Crabtree, R. H.; Schmuttenmaer, C. A.; Brudvig, G. W. Surface-Induced Deprotection of THP-Protected Hydroxamic Acids on Titanium Dioxide. *J. Phys. Chem. C* **2016**, *120*, 12495–12502.

(112) Liu, F.; Cardolaccia, T.; Hornstein, B. J.; Schoonover, J. R.; Meyer, T. J. Electrochemical oxidation of water by an adsorbed mu-oxo-bridged Ru complex. *J. Am. Chem. Soc.* **2007**, *129*, 2446–2447.

(113) Mola, J.; Mas-Marza, E.; Sala, X.; Romero, I.; Rodríguez, M.; Viñas, C.; Parella, T.; Llobet, A. Ru-hbpp-based water-oxidation catalysts anchored on conducting solid supports. *Angew. Chem. Int. Ed.* **2008**, *47*, 5830–5832.

(114) Odrobina, J.; Scholz, J.; Risch, M.; Dechert, S.; Jooss, C.; Meyer, F. Chasing the Achilles' Heel in Hybrid Systems of Diruthenium Water Oxidation Catalysts Anchored on Indium Tin Oxide: The Stability of the Anchor. *ACS Catal.* **2017**, *7*, 6235–6244.

(115) Odrobina, J.; Scholz, J.; Pannwitz, A.; Francàs, L.; Dechert, S.; Llobet, A.; Jooss, C.; Meyer, F. Backbone Immobilization of the Bis(bipyridyl)pyrazolate Diruthenium Catalyst for Electrochemical Water Oxidation. *ACS Catal.* **2017**, *7*, 2116–2125.

References

(116) Wu, L.; Eberhart, M.; Nayak, A.; Brennaman, M. K.; Shan, B.; Meyer, T. J. A Molecular Silane-Derivatized Ru(II) Catalyst for Photoelectrochemical Water Oxidation. *J. Am. Chem. Soc.* **2018**, *140*, 15062–15069.

(117) Creus, J.; Matheu, R.; Peñafiel, I.; Moonshiram, D.; Blondeau, P.; Benet-Buchholz, J.; García-Antón, J.; Sala, X.; Godard, C.; Llobet, A. A Million Turnover Molecular Anode for Catalytic Water Oxidation. *Angew. Chem.* **2016**, *128*, 15608–15612.

(118) Garrido-Barros, P.; Gimbert-Suriñach, C.; Moonshiram, D.; Picón, A.; Monge, P.; Batista, V. S.; Llobet, A. Electronic π-Delocalization Boosts Catalytic Water Oxidation by Cu(II) Molecular Catalysts Heterogenized on Graphene Sheets. *J. Am. Chem. Soc.* **2017**, *139*, 12907–12910.

(119) Matheu, R.; Moreno-Hernandez, I. A.; Sala, X.; Gray, H. B.; Brunschwig, B. S.; Llobet, A.; Lewis, N. S. Photoelectrochemical Behavior of a Molecular Ru-Based Water-Oxidation Catalyst Bound to TiO2-Protected Si Photoanodes. *J. Am. Chem. Soc.* **2017**, *139*, 11345–11348.

(120) Bandaru, P. R. Electrical properties and applications of carbon nanotube structures. *J. Nanosci. Nanotechnol.* **2007**, *7*, 1239–1267.

(121) Grau, S.; Berardi, S.; Moya, A.; Matheu, R.; Cristino, V.; Vilatela, J. J.; Bignozzi, C. A.; Caramori, S.; Gimbert-Suriñach, C.; Llobet, A. A hybrid molecular photoanode for efficient light-induced water oxidation. *Sustainable Energy Fuels* **2018**, *2*, 1979–1985.

(122) Li, F.; Zhang, B.; Li, X.; Jiang, Y.; Chen, L.; Li, Y.; Sun, L. Highly Efficient Oxidation of Water by a Molecular Catalyst Immobilized on Carbon Nanotubes. *Angew. Chem.* **2011**, *123*, 12484–12487.

(123) Koelewijn, J. M.; Lutz, M.; Detz, R. J.; Reek, J. N. H. Anode Preparation Strategies for the Electrocatalytic Oxidation of Water Based on Strong Interactions between Multiwalled Carbon Nanotubes and Cationic Acetylammonium Pyrene Moieties in Aqueous Solutions. *ChemPlusChem* **2016**, *81*, 1098–1106.

(124) Bélanger, D.; Pinson, J. Electrografting: a powerful method for surface modification. *Chem. Soc. Rev.* **2011**, *40*, 3995–4048.

(125) Matheu, R.; Francàs, L.; Chernev, P.; Ertem, M. Z.; Batista, V.; Haumann, M.; Sala, X.; Llobet, A. Behavior of the Ru-bda Water Oxidation Catalyst Covalently Anchored on Glassy Carbon Electrodes. *ACS Catal.* **2015**, *5*, 3422–3429.

(126) Li, F.; Li, L.; Tong, L.; Daniel, Q.; Göthelid, M.; Sun, L. Immobilization of a molecular catalyst on carbon nanotubes for highly efficient electro-catalytic water oxidation. *Chem. Commun.* **2014**, *50*, 13948–13951.

(127) Zhan, S.; Ahlquist, M. S. G. Dynamics and Reactions of Molecular Ru Catalysts at Carbon Nanotube-Water Interfaces. *J. Am. Chem. Soc.* **2018**, *140*, 7498–7503.

(128) Hoque, M. A.; Gil-Sepulcre, M.; Aguirre, A. de; Elemans, J. A. A. W.; Moonshiram, D.; Matheu, R.; Shi, Y.; Benet-Buchholz, J.; Sala, X.; Malfois, M.; Solano, E.; Lim, J.; Garzón-Manjón, A.; Scheu, C.; Lanza, M.; Maseras, F.; Gimbert-Suriñach, C.; Llobet, A. Water oxidation electrocatalysis using ruthenium coordination oligomers adsorbed on multiwalled carbon nanotubes. *Nat. chem.* **2020**, *12*, 1060–1066.

References

(129) Schulze, M.; Kunz, V.; Frischmann, P. D.; Würthner, F. A supramolecular ruthenium macrocycle with high catalytic activity for water oxidation that mechanistically mimics photosystem II. *Nat. chem.* **2016**, *8*, 576–583.

(130) Schindler, D.; Gil-Sepulcre, M.; Lindner, J. O.; Stepanenko, V.; Moonshiram, D.; Llobet, A.; Würthner, F. Efficient Electrochemical Water Oxidation by a Trinuclear Ru(bda) Macrocycle Immobilized on Multi-Walled Carbon Nanotube Electrodes. *Adv. Energy Mater.* **2020**, *10*, 2002329.

(131) Gil-Sepulcre, M.; Lindner, J. O.; Schindler, D.; Velasco, L.; Moonshiram, D.; Rüdiger, O.; DeBeer, S.; Stepanenko, V.; Solano, E.; Würthner, F.; Llobet, A. Surface-Promoted Evolution of Ru-bda Coordination Oligomers Boosts the Efficiency of Water Oxidation Molecular Anodes. *J. Am. Chem. Soc.* **2021**.

(132) Wadsworth, E.; Duke, F. R.; Goetz, C. A. Present Status of Cerium(IV)-Cerium(III) Potentials. *Anal. Chem.* **1957**, *29*, 1824–1825.

(133) Parent, A. R.; Crabtree, R. H.; Brudvig, G. W. Comparison of primary oxidants for water-oxidation catalysis. *Chem. Soc. Rev.* **2013**, *42*, 2247–2252.

(134) Rensmo, H.; Lunell, S.; Siegbahn, H. Absorption and electrochemical properties of ruthenium(II) dyes, studied by semiempirical quantum chemical calculations. *J. Photochem. Photobiol.* **1998**, *114*, 117–124.

(135) F. P. Rotzinger, S. Munavalli, P. Comte, J. K. Hurst. Molecular water oxidation catalysts. *J. Am. Chem. Soc.* **1987**, 6619–6626.

(136) Robert, A.; Meunier, B. *New J. Chem.* **1988**, 885.

(137) Weavers, L. K.; Hua, I.; Hoffmann, M. R. Degradation of triethanolamine and chemical oxygen demand reduction in wastewater by photoactivated periodate. *Water Environ. Res.* **1997**, *69*, 1112–1119.

(138) Limburg, J.; Crabtree, R. H.; Brudvig, G. W. *Inorg. Chim. Acta.* **2000**, 301.

(139) Lee, K. J.; Elgrishi, N.; Kandemir, B.; Dempsey, J. L. Electrochemical and spectroscopic methods for evaluating molecular electrocatalysts. *Nat. Rev. Chem.* **2017**, *1*.

(140) Nakagawa, T.; Beasley, C. A.; Murray, R. W. Efficient Electro-Oxidation of Water near Its Reversible Potential by a Mesoporous IrO_x Nanoparticle Film. *J. Phys. Chem. C* **2009**, *113*, 12958–12961.

(141) Nakagawa, T.; Bjorge, N. S.; Murray, R. W. Electrogenerated IrO_x nanoparticles as dissolved redox catalysts for water oxidation. *J. Am. Chem. Soc.* **2009**, *131*, 15578–15579.

(142) Concepcion, J. J.; Binstead, R. A.; Alibabaei, L.; Meyer, T. J. Application of the rotating ring-disc-electrode technique to water oxidation by surface-bound molecular catalysts. *Inorg. Chem.* **2013**, *52*, 10744–10746.

(143) Bagotsky, V. S. Fundamentals of Electrochemistry, **2006**.

(144) Hamann, C. H.; Hamnett, A.; Vielstich, W. Electrochemistry. *Wiley-VCH* **2007**.

References

(145) Rajabi, S.; Ebrahimi, F.; Lole, G.; Odrobina, J.; Dechert, S.; Jooss, C.; Meyer, F. Water Oxidizing Diruthenium Electrocatalysts Immobilized on Carbon Nanotubes: Effects of the Number and Positioning of Pyrene Anchors. *ACS Catal.* **2020**, *10*, 10614–10626.

(146) van der Vlugt, J. I.; Demeshko, S.; Dechert, S.; Meyer, F. Tetranuclear CoII, MnII, and CuII complexes of a novel binucleating pyrazolate ligand preorganized for the self-assembly of compact 2 x 2-grid structures. *Inorg. Chem.* **2008**, *47*, 1576–1585.

(147) Chen, J.-L.; Song, P.; Liao, J.; Wen, H.-R.; Hong, R.; Chen, Z.-N.; Chi, Y. Luminescent homodinuclear copper(I) halide complexes based on the 3,5-bis{6-(2,2'-dipyridyl)}pyrazole ligand. *Inorg. Chem. Commun.* **2010**, *13*, 1057–1060.

(148) Steinert, M. Defektgitter und Gitterkomplexe – Einflüsse von Gegenionen und Lösungsmitteln auf ihre magnetischen Eigenschaften. Cuvillier Verlag:, göttingen, 2016.

(149) Modrakowski, C.; Flores, S. C.; Beinhoff, M.; Schlüter, A. D. Synthesis of Pyrene Containing Building Blocks for Dendrimer Synthesis. *Synthesis* **2001**, *2001*, 2143–2155.

(150) Odrobina. Jann. Immobilization and Characterization Strategies for Dinuclear Ruthenium Water Oxidation Catalyts on Solid Supports, Göttingen, 2017.

(151) Bachman, J. C.; Kavian, R.; Graham, D. J.; Kim, D. Y.; Noda, S.; Nocera, D. G.; Shao-Horn, Y.; Lee, S. W. Electrochemical polymerization of pyrene derivatives on functionalized carbon nanotubes for pseudocapacitive electrodes. *Nat. Commun.* **2015**, *6*, 7040.

(152) Barathi, P.; Kumar, A. S. Electrochemical conversion of unreactive pyrene to highly redox-active 1,2-quinone derivatives on a carbon nanotube-modified gold electrode surface and its selective hydrogen peroxide sensing. *Langmuir* **2013**, *29*, 10617–10623.

(153) Uchimiya, M.; Stone, A. T. Reversible redox chemistry of quinones: impact on biogeochemical cycles. *Chemosphere* **2009**, *77*, 451–458.

(154) Ma, L.; Dong, X.; Chen, M.; Zhu, L.; Wang, C.; Yang, F.; Dong, Y. Fabrication and Water Treatment Application of Carbon Nanotubes (CNTs)-Based Composite Membranes: A Review. *Membranes* **2017**, *7*.

(155) Liao, Y. *Practical Electron Microscopy and Database*, 2018.

(156) Suenaga, K.; Colliex, C.; Iijima, S. In situ electron energy-loss spectroscopy on carbon nanotubes during deformation. *Appl. Phys. Lett.* **2001**, *78*, 70–72.

(157) Beig, R.; Beiglböck, W.; Domcke, W.; Englert, B.-G.; Frisch, U.; Hänggi, P.; Hasinger, G.; Hepp, K.; Hillebrandt, W.; Imboden, D.; Jaffe, R. L.; Lipowsky, R.; Löhneysen, H. v.; Ojima, I.; Sornette, D.; Theisen, S.; Weise, W.; Wess, J.; Zittartz, J.; Loiseau, A.; Launois, P.; Petit, P.; Roche, S.; Salvetat, J.-P. *Understanding Carbon Nanotubes*, Vol. 677; Springer Berlin Heidelberg, 2006.

(158) Ducastelle, F.; Blase, X.; Bonard, J.-M.; Charlier, J.-C.; Petit, P. Electronic Structure. In *Understanding Carbon Nanotubes*; Beig, R., Beiglböck, W., Domcke, W., Englert, B.-G., Frisch, U., Hänggi, P., Hasinger, G., Hepp, K., Hillebrandt, W., Imboden, D., Jaffe, R. L., Lipowsky, R., Löhneysen, H. v., Ojima, I., Sornette, D., Theisen, S., Weise, W., Wess, J., Zittartz, J., Loiseau, A., Launois, P., Petit,

P., Roche, S., Salvetat, J.-P., Eds.; Lecture Notes in Physics; Springer Berlin Heidelberg, 2006; pp 199–276.

(159) Koh, A. L.; Gidcumb, E.; Zhou, O.; Sinclair, R. Observations of carbon nanotube oxidation in an aberration-corrected environmental transmission electron microscope. *ACS nano* **2013**, *7*, 2566–2572.

(160) Scholz, J.; Risch, M.; Stoerzinger, K. A.; Wartner, G.; Shao-Horn, Y.; Jooss, C. Rotating Ring–Disk Electrode Study of Oxygen Evolution at a Perovskite Surface: Correlating Activity to Manganese Concentration. *J. Phys. Chem. C* **2016**, *120*, 27746–27756.

(161) Wang, L.; Fan, K.; Daniel, Q.; Duan, L.; Li, F.; Philippe, B.; Rensmo, H.; Chen, H.; Sun, J.; Sun, L. Electrochemical driven water oxidation by molecular catalysts in situ polymerized on the surface of graphite carbon electrode. *Chem. Commun.* **2015**, *51*, 7883–7886.

(162) Bard, A. J.; Faulkner, L. R. *Electrochemical methods: fundamentals and applications*, 2001.

(163) Murthi, V. S.; Urian, R. C.; Mukerjee, S. Oxygen Reduction Kinetics in Low and Medium Temperature Acid Environment: Correlation of Water Activation and Surface Properties in Supported Pt and Pt Alloy Electrocatalysts. *J. Phys. Chem. C* **2004**, *108*, 11011–11023.

(164) Zhou, R.; Zheng, Y.; Jaroniec, M.; Qiao, S.-Z. Determination of the Electron Transfer Number for the Oxygen Reduction Reaction: From Theory to Experiment. *ACS Catal.* **2016**, *6*, 4720–4728.

(165) Rooij, M. R. de. Electrochemical Methods: Fundamentals and Applications. *Anti-Corrosion Meth & Material* **2003**, *50*.

(166) Zhang, B.; Sun, L. Ru-bda: Unique Molecular Water-Oxidation Catalysts with Distortion Induced Open Site and Negatively Charged Ligands. *J. Am. Chem. Soc.* **2019**, *141*, 5565–5580.

(167) Moonshiram, D.; Pineda-Galvan, Y.; Erdman, D.; Palenik, M.; Zong, R.; Thummel, R.; Pushkar, Y. Uncovering the Role of Oxygen Atom Transfer in Ru-Based Catalytic Water Oxidation. *J. Am. Chem. Soc.* **2016**, *138*, 15605–15616.

(168) Ertem, M. Z.; Concepcion, J. J. Oxygen Atom Transfer as an Alternative Pathway for Oxygen-Oxygen Bond Formation. *Inorg. Chem.* **2020**, *59*, 5966–5974.

(169) Dutta, S.; Baitalik, S.; Ghosh, M.; Flörke, U.; Nag, K. Structural, photophysical and electrochemical studies of $[RuN_6]^{2+}$ complexes having polypyridine and azole mixed-donor sites. *Inorganica Chim. Acta.* **2011**, *372*, 227–236.

(170) Francàs, L.; Sala, X.; Benet-Buchholz, J.; Escriche, L.; Llobet, A. A Ru-Hbpp-based water-oxidation catalyst anchored on rutile TiO_2. *ChemSusChem* **2009**, *2*, 321–329.

(171) Lücken, J. Transformations of Energy-Related Small Molecules at Dinuclear Complexes. Dissertation, Göttingen, 2020.

(172) Schneider, B.; Demeshko, S.; Neudeck, S.; Dechert, S.; Meyer, F. Mixed-spin [2 × 2] Fe_4 grid complex optimized for quantum cellular automata. *Inorg. Chem.* **2013**, *52*, 13230–13237.

(173) Schneider, B. Multistabile Gitterkomplexe. Dissertation, göttingen, 2017.

References

(174) Zabrodsky, H.; Peleg, S.; Avnir, D. Continuous symmetry measures. *J. Am. Chem. Soc.* **1992**, *114*, 7843–7851.

(175) Zabrodsky, H.; Peleg, S.; Avnir, D. Continuous symmetry measures. 2. Symmetry groups and the tetrahedron. *J. Am. Chem. Soc.* **1993**, *115*, 8278–8289.

(176) Alvarez, S.; Avnir, D.; Llunell, M.; Pinsky, M. Continuous symmetry maps and shape classification. The case of six-coordinated metal compounds. *New J. Chem.* **2002**, *26*, 996–1009.

(177) Evans, I. P.; Spencer, A.; Wilkinson, G. Dichlorotetrakis(dimethyl sulphoxide)ruthenium(II) and its use as a source material for some new ruthenium(II) complexes. *J. Chem. Soc., Dalton Trans.* **1973**, 204.

(178) Sheldrick, G. M. Crystal structure refinement with SHELXL. *Acta Cryst.* **2015**, *71*, 3–8.

(179) Sheldrick, G. M. SHELXT - integrated space-group and crystal-structure determination. *Acta Cryst.* **2015**, *71*, 3–8.

(180) Spek, A. L. PLATON SQUEEZE: a tool for the calculation of the disordered solvent contribution to the calculated structure factors. *Acta Cryst.* **2015**, *71*, 9–18.

(181) X-RED; STOE & CIE GmbH, Darmstadt, Germany, 2002.

(182) SADABS; BRUKER AXS GmbH, Karlsruhe, Germany, 2016.

(183) Neese, F. The ORCA program system. *WIREs. Comput. Mol. Sci.* **2012**, *2*, 73–78.

(184) Schäfer, A.; Horn, H.; Ahlrichs, R. Fully optimized contracted Gaussian basis sets for atoms Li to Kr. *J. Chem. Phys.* **1992**, *97*, 2571–2577.

(185) Weigend, F.; Ahlrichs, R. Balanced basis sets of split valence, triple zeta valence and quadruple zeta valence quality for H to Rn: Design and assessment of accuracy. *Phys. Chem. Chem. Phys.* **2005**, *7*, 3297–3305.

(186) Grimme, S.; Antony, J.; Ehrlich, S.; Krieg, H. A consistent and accurate ab initio parametrization of density functional dispersion correction (DFT-D) for the 94 elements H-Pu. *J. Chem. Phys.* **2010**, *132*, 154104.

Acknowledgments